Displacement pile installation effects in sand

An experimental study

Displacement pile installation effects in sand

An experimental study

Proefschrift

ter verkrijging van de graad van doctor
aan de Technische Universiteit Delft,
op gezag van de Rector Magnificus prof. ir. K. C. A. M. Luyben,
voorzitter van het College voor Promoties,
in het openbaar te verdedigen op 6 Januari om 10 uur

door

Anders Beijer-Lundberg

Civilingenjör
geboren te Härlanda, Zweden.

Dit proefschrift is goedgekeurd door de promotor:

Prof. ir. A. F. van Tol

Copromotor: Dr. J. Dijkstra

Samenstelling promotiecommissie:

Rector Magnificus,	Technische Universiteit Delft, voorzitter
Prof. ir. A. F. van Tol,	Technische Universiteit Delft, promotor
Dr. J. Dijkstra,	Chalmers Tekniska Högskola, copromotor
Prof. Dr. M. A. Hicks,	Technische Universiteit Delft
Prof. Dr. J. G. Rots	Technische Universiteit Delft
Prof. Dr. A. Bezuijen	Universiteit Gent
Univ. Prof. Dr. Ing. J. Grabe	Technische Universität Hamburg Harburg
Dr. K. Gavin.	University College Dublin

The research presented in this thesis was funded by STW.

ISBN 978-94-6295-061-0

Cover designed by BoxPress, s'Hertogenbosch
Printed by BoxPress, s'Hertogenbosch

This thesis is dedicated to Her Royal Highness,
Crown Princess Estelle of Sweden

Surtout, par trop de zèle - Talleyrand

Door meten tot weten - Kammerlingh Onnes

Vad våldet må skapa är vanskligt och kort,
det dör som en stormvind i öknen bort - Tegnér

Abstract

Displacement pile installation causes large displacements and stress changes in the soil. Consequently the subsequent load-deformation response is partly governed by the installation effects. Analysis of piles and pile groups therefore needs to include the installation effects to produce realistic simulations of the behaviour of piles. The installation effects are currently not completely understood, because of the large deformation character of the installation, which is not straight-forward to model with standard laboratory and numerical methods. A fuller understanding of installation effects would therefore lead to more efficient design methods and techniques for analysis of piled structures.

Physical models that mimic the behaviour of the prototype installation at correct initial and boundary conditions simulate the prototype mechanism of the installation. In the current thesis displacement pile installation effects are modelled in the centrifuge for correct scaling of the stress conditions in the soil. A small scale model pile was realized for Small-scale contact stress measurements. Deformation measurements were made in-flight during the installation.

Continuous and incremental installation in dry sand were modelled in order to assess the effect of cyclic loading during installation with an impact hammer. Loose, medium dense and dense initial relative densities were tested. After installation, the model was subjected to a static load test and a subsequent extraction test.

The experimental measurements show that the installation effects strongly depend on the initial relative density of the soil. The friction fatigue effect, which is caused by a gradual decline of horizontal contact stress with further penetration of the pile at a fixed soil horizon, was confirmed in the model tests. The link between friction fatigue and horizontal deformations during installation was also observed in the deformation measurements. The behaviour of the pile in tension during the extraction tests showed a more brittle response for the loose and medium dense samples. The deformation measurements showed that both the displacements path of the soil continuum and the development of strain during installation depends on the initial relative density.

The current explanation of installation effects is shown to be relatively accurate for comparable types of soil. During installation, the repeated loading cycles results in a gradual change in horizontal stress, at the same time as the stress conditions around the pile changes as a result of the soil displacements. The installation effects are shown to govern the pile soil interaction when the pile is loaded, and recommendations for future research are given.

Samenvatting

Installatie effecten bepalen het gedrag na de installatie van grondverdringende palen in zand. Deze effecten worden nog niet volledig begrepen. Geschikte experimentele technieken om deze installatie effecten te modelleren omvatten veld-, laboratorium- en experimentele modellen. In dit proefschrift wordt een laboratorium model op kleine schaal gebruikt om installatie effecten van grondverdringende palen in zand te onderzoeken, als aanvulling op een numerieke studie van hetzelfde onderwerp.

Allereerst wordt de huidige kennis over installatie effecten toegelicht. De verdeling van de schachtwrijving ten gevolge van cyclische belasting en het effect van de initile relatieve dichtheid op de installatie effecten zijn hierbij van bijzonder belang. Vervolgens worden de doelstellingen en strekking van het voorliggend proefschrift besproken welke het onderzoek naar het effect van de installatiewijze (continue of stapsgewijze installatie) en het effect van de initile relatieve dichtheid van de grond voor de installatie omvatten.

De experimenten zijn uitgevoerd in de geotechnische centrifuge waarbij aanzienlijke inspanning is ondernomen om de overeenstemming tussen het schaalmodel en het prototype te verzekeren. Dit betreft het model zelf, de grootte van de zandkorrels, evenals de randen van de grondbak. Dit proces wordt bepaald door zowel theoretische als ook empirische overwegingen.

Vervolgens wordt het experimentele model verder uitgewerkt. Dit betreft de geotechnische centrifuge zelf, alsmede de genstalleerde elektrische en communicatie systemen om de elektrische stapmotoren aan te drijven en de meet- en besturingsgegevens door te geven. Het besturingssysteem van het model wordt beschreven inclusief de computerprogramma's die de modelproeven aansturen. Vervormingsmetingen zijn uitgevoerd met een in-flight camera. De vervormingsmetingen zijn vervolgens door een reeks computerprogramma's geanalyseerd en aangepast om met de lensvervorming rekening te houden en verplaatsingsincrementen te verkijgen met een Particle Image Velocimetry (PIV) programma. De procedure om het grondmonster voor te bereiden wordt beschreven inclusief de voorbereiding met verschillende initile relatieve dichtheden.

Daarna wordt de kleine schaal modelpaal beschreven. In deze modelpaal zijn horizontale contact- en axiale spannings-meetsensoren opgenomen die zich in kleine membranen binnen de modelpaal bevinden. De modelpaal werd geanalyseerd met een FE-programma om het effect van de belastingscondities in te kunnen schatten. Kalibratie werd uitgevoerd in op maat gemaakte kalibratie-apparatuur voor de horizontale en axiale spanningssensoren.

De experimentele meetresultaten bestaan uit spannings- en vervormingsmetingen. De spanningsmetingen bestaan zowel uit de horizontale contactspanningen en de axiale spanning als ook hun onderlinge verhoudingen. De vervormingsmetingen worden gepresenteerd als verplaatsingpaden waarin zowel de grondverplaatsing is geanalyseerd als ook de incrementele rekken.

De interpretatie van de metingen is gericht op het effect van de initile relatieve dichtheid en het effect van belastingscycli. Het wordt aangetoond dat de initile relatieve dichtheid een groot effect heeft op de horizontale contactspanning tijdens installatie en tijdens trekken van de paal. De vervormingsmetingen tonen een soortgelijk effect waarbij de dichtere grondmonsters grotere horizontale verplaatsing laten zien. Het effect van stapsgewijze installatie op de spannings- en vervormingsmetingen is geanalyseerd en geeft aan dat de verdichting van de grond tijdens cyclische belasting leidt tot lagere contactspanningen. De metingen zijn vergeleken met numerieke modellen die een vergelijkbaar resultaat geven. Hierdoor is meer vertrouwen ontstaan in de huidige theorie van installatie effecten die in empirische ontwerpmethoden gebruikt wordt.

Summary

Installation effects govern the post-installation behaviour of displacement piles in sand. These effects are currently not completely understood. Suitable experimental techniques to model these installation effects include field, laboratory and experimental models. In the current thesis a small-scale laboratory model is used to investigate the installation effect of displacement piles in sand, to complement a numerical study of the same subject.

The current knowledge of installation effects is initially discussed. The distribution of shaft friction, resulting from cyclic loading, and the effect of initial relative density on the installation effects are of particular interest. Aims and scope for the current thesis are subsequently discussed, and consist of investigating the effect of installation mode (continuous or incremental installation), and the effect of the initial relative density of the soil before installation.

The experiments are carried out in the geotechnical centrifuge, and considerable effort is taken to ensure that the similarity between the scale model and the prototype is assured. This concerns the model itself, the size of the soil grains, as well as the boundaries of the soil container. This process is guided both by theoretical and empirical consideration.

The experimental model is then elaborated. This includes the geotechnical centrifuge, as well as the electrical and communications system installed to drive electric control motors and transmit measurement and control data. The model control system is described, including the computer programs that control the model tests. Deformation measurements are carried out by an in-flight camera. The deformation measurements are subsequently analysed with a series of computer programs to adjust for lens distortion and to retain displacement increments with a Particle Image Velocimetry (PIV) program. The soil sample preparation procedure is described, including preparation at different initial relative densities.

The small scale model pile is described. This model pile included horizontal contact stress and axial stress measurement sensors that were included in the small membranes inside the model pile. The model pile was analysed with a FE-program to estimate the effect of the loading conditions. Calibration was carried out in custom-made calibration equipment for the horizontal stress sensors and the axial stress sensor.

The experimental measurement results consisted of stress measurements and deformation measurements. The stress measurements consisted of the horizontal contact stress and the axial stress, as well ratios between these. The deformation measurements were presented as displacement paths in which the soil displacements were analysed, as well as incremental

strains.

The interpretation of the measurement focused on the effect of initial relative density, and the effect of load cycles. The initial relative effect was shown to have a large effect on the horizontal contact stress during installation, and during extraction of the pile. The deformation measurements showed a similar effect in which the denser soil samples exhibited more horizontal displacement. The effect of incremental installation was analysed in the stress and deformation measurements, and indicates that the compaction of the soil during cyclic loading results in lower horizontal contact stress. The measurements were compared to numerical models that display a similar result, giving more confidence in the current theory of installation effects that is included in empirical design methods.

Contents

Chapter 1

Introduction

1.1 Modelling of displacement pile installation effects

Structures built on soft soils are frequently underpinned by deep foundations consisting of piles. The design of these piles is governed by soil conditions and experience of the specific construction method. A common pile type, worldwide and especially in the Netherlands, is the displacement pile. This pile type displaces the soil around the pile during installation, which leads to changes in the structure of the soil. These changes in soil state and soil structure after installation, including stress and strain, are often defined as the displacement pile installation effects.

The installation effects make practical analysis of the load-deformation behaviour of piles complicated, since the properties of the soil around the pile are not known. Axial pile design is traditionally based on empirical methods, which are calibrated through a pile load test database to produce predictions based on input data. The advent of fast computers makes it possible to conduct numerical analysis of piles and pile groups with an advanced numerical framework and various non-linear constitutive models. Much more accurate predictions of load capacity and load-deformation behaviour are therefore possible, if the soil is modelled correctly.

Such advanced models are governed by the input data which is put into the model. This includes properly defined model parameters, boundary values and initial conditions of the soil, which are determined from laboratory and in-situ tests. The presence of the installation effects make evaluation of such soil parameters complicated, since the state of the soil is significantly different from the initial conditions. A more detailed description of the installation effects, and how these evolve in sand for different types of initial conditions, is therefore of practical interest.

Further insight into the installation effects would be helpful for improvement of the current empirical design methods. These are often based on the Cone Penetration Test (CPT). There is still not complete agreement over the accuracy of these methods, especially for large diameter piles, and for very loose and very dense initial conditions. Extrapolation of these methods consequently leads to large variations in prediction of bearing capacity. The effect of initial relative density and stress level are especially of interest, since these govern the mechanical response of the pile during installation and subsequent loading.

Both the empirical prediction methods as well as behaviour of soil parameters in numerical analysis would consequently be possible to improve by more accurate description of the displacement pile installation effects. Further experimental and numerical research with the aim of capturing the installation effects is therefore needed. This thesis is restricted to experimental research into pile installation effects, and is complemented by a study of numerical simulations of installation effects, [76].

1.2 Aims and scope

The research aims of the thesis consist of capturing the governing mechanisms in the soil adjacent to a displacement pile during pile installation through experiments. This should allow for validation of numerical simulations of the installation process with correct soil parameters. The aim was to study the effect of the initial relative soil density as well as of the installation mode. Measurements were made of pile behaviour during and after installation. This includes the resulting stress-strain paths during installation, which required stress and deformation measurements of the soil during pile installation.

The experimental model was simplified in order to provide practical and reliable measurements. Piles are commonly installed as part of pile groups, in which the piles interact. The behaviour of such a pile group is very complicated, and suitable simplifications are needed to approach the problem of installation effects. This thesis is restricted to experimental analysis of installation effects for single piles in dry sand, and therefore excludes inertial and consolidation effects. The experimental tests were carried out in the TU Delft geotechnical centrifuge, and the displacement pile installation was simulated with a mechanical actuator conducting continuous and incremental pile installation.

1.3 Outline of the thesis

The thesis presents the experimental research, as well as the underlying considerations and idealizations. In chapter 2, installation effects are defined, and suitable prototype parameters for experimental tests are summarized. The installation procedure is discussed, and the installation is divided into installation stages to clarify the soil behaviour.

In chapter 3, the experimental methodology is presented, and similitude of the physical model is discussed. The adaption of pile installation to a small scale model is elaborated in detail, and suitable measurement techniques are summarized.

Chapter 4 presents the experimental test set-up, sample preparation methods and the properties of the experimental soil type. The control system for the experimental setup is discussed in detail, and the experimental model capabilities are described.

In chapter 5, the realization of an instrumented model pile for horizontal contact stress measurements is described, including numerical simulation of the sensor and calibration method.

Chapter 6 presents the experimental results.

In chapter 7, the experimental measurements and the interpretation of these results are discussed and put in a conceptual framework for pile installation.

Finally, chapter 8 presents the conclusions of the research presented in this thesis as well as recommendations for further research.

1.4 A note on the sign convention

The x-axis is defined the horizontal axis with origin in the center of the pile and directed outward. The installation effects are mostly symmetrical around the pile axis. The y-axis is defined as the vertical axis and has its origin at the soil surface and is directed into the soil mass.

The stress convention consists of the standard system in soil mechanics, in which the tensile stresses have a negative sign, and compressive stresses have a positive sign.

Chapter 2

Physical modeling of installation effects

2.1 Introduction

Pile foundations transfer loads from the top soft soil layers down to strata with higher bearing capacity. There are many different pile types, [82]. A common type worldwide and in the Netherlands is the displacement pile, which is installed by displacing the soil around the pile through impact driving, jacking or vibrating the pile. After installation, the soil surrounding the pile will have undergone large deformations and stress changes. These installation effects change the subsequent load-deformation behaviour of the soil-pile system when the pile is eventually loaded.

In this chapter the motivation for a closer study of installation effects is presented. The pile installation effects are described by a conceptual framework consisting of various components which have been verified by experimental measurements and numerical simulations. A simplified description of the behaviour of sands is delineated to assist the study, and the most significant soil parameters are outlined. Installation effects are defined in order to limit the current experimental study, and typical values of prototype parameters are summarized. The different phases of displacement pile installation are subsequently considered to assist an structured study. This includes description of initial soil conditions, the installation phase and the post-installation phase.

Various methods of analysing installation effects are then discussed. Based on the conceptual framework of soil behaviour, a combination of a numerical and experimental methods to study these installation effects is proposed. The installation effects are modelled experimentally in the current thesis, and the research complements a separate numerical study of pile installation effect in sand carried out by numerical simulations with the hypoplastic constitutive model, [76].

The conceptual framework consists of the model of pile installation described in [159], [128], [130], [148], as well as the detail description in [241]. The realization of the experimental model is governed by the types of measurements needed to expand this conceptual framework. A relatively detailed description of pervious types of measurements and finding is therefore presented in the current chapter.

2.2 Motivation

Design of axially loaded displacement piles comprises prediction of the pile bearing capacity, and the pile load-deformation response. Displacement pile installation effects alter the soil state, hence the behaviour of the soil, and should therefore be taken into account in practical design. Ideally, these installation effects should also be included in the analysis of piles subjected to load combinations, and to pile groups. For these types of structures, empirical methods are not particularly accurate, and numerical methods seem more appropriate, especially for soil-structure interaction (e.g. small-deformation dynamic analysis of structures). So far there is no consistent framework to create realistic models including installation effects, which is why the installation stage is not explicitly included in most analytical and numerical analyses.

2.2.1 Design of axially loaded single piles

Pile foundations have a long history, [82], [233]. Consequently a vast amount of practical experience has been gained which governs practical designs, [187]. The total pile axial bearing capacity of a single pile, Q_{tot}, is defined as:

$$Q_{tot} = Q_{base} + Q_{shaft} - W_{Pile} \tag{2.2.1}$$

where W_{Pile} is the self-weight of the pile, and Q_{base} and Q_{shaft} are the bearing capacity of the pile base and the pile shaft, respectively. An idealized loaded axially loaded pile is shown in Figure 2.1. The components of the axial pile bearing capacity may subsequently be calculated as:

$$Q_{base} = q_{base} A_{base} \tag{2.2.2}$$

$$Q_{shaft} = C_{Pile} \int^{z_{Pile}} \tau_s(z) dz \tag{2.2.3}$$

where q_{base} is the pile base resistance, A_{base} is the area of the pile base, C_{Pile} is the circumference of the pile, and $\tau_s(z)$ is the shaft friction along the length z_{Pile} of the pile.

It is possible to estimate the base resistance following the method of limit analysis or cavity expansion methods, in which a bearing capacity factor is calculated, e.g. [25], [82], [187]. In this method, the pile base resistance q_{base} is correlated to the effective vertical stress level σ'_v through a bearing capacity factor N_q, [163]:

$$q_{base} = N_q \sigma'_v \tag{2.2.4}$$

The shaft capacity τ_s can be predicted by the effective stress approach in sand, [82], [163]:

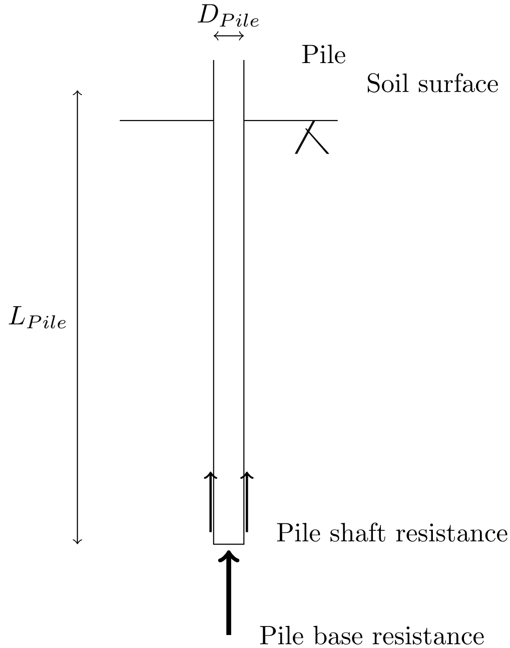

Figure 2.1: Pile base and shaft resistance.

$$\tau_s = \beta \sigma'_v \tag{2.2.5}$$

where β is expressed as:

$$\beta = K_{Pile} \tan \delta' \tag{2.2.6}$$

where K_{Pile} is the earth pressure factor against the pile shaft including the installation effects, and $\tan \delta'$ is the drained pile-soil interface friction coefficient. The β-method consequently constitutes an estimate of the axial capacity of the pile shaft based on Mohr-Coulomb friction.

The interface friction $\tan \delta'$ is measured in shear tests or inferred from pile load tests. Guidelines to determine $\tan \delta'$ in such tests have been established, e.g. [121], [124]. The earth pressure is more cumbersome to describe, [178]. Estimations for various relative densities have been established, e.g. [141]. In these estimates, the earth pressure factor K_{Pile} depends on the relative density R_d of the soil and p' is the mean stress level before installation:

$$K_{pile} = f(R_d, p') \tag{2.2.7}$$

where p' is defined as

$$p' = (\sigma'_1 + \sigma'_2 + \sigma'_3)/3 \tag{2.2.8}$$

where σ'_1, σ'_2 and $\sigma_3.'$ are the major, intermediate and minor principal stresses.

The pressure coefficient K_{Pile} is evaluated from the cone resistance q_c, [141]:

$$K_{Pile} = f(q_c) \tag{2.2.9}$$

Experimental verification has shown that there are large inaccuracies in these correlations, [122], [178]. An alternative simplified design method consists of empirical correlations between in-situ measurements and axial pile bearing capacity, e.g. [40], [50], [64]. [77], [123], [138], [150], [208]. These direct methods provide formulas for calculating the axial bearing capacity Q_{tot} of a single pile as a ratio to an in-situ measurement, such as the cone resistance q_c:

$$Q_{tot} = Q_{base} + Q_{shaft} = f(q_c, p', D_{Pile}, h_y) \tag{2.2.10}$$

where D_{Pile} is the pile diameter and h_y is the distance from the pile tip. For the constant design coefficients α_b and α_s, the base and shaft resistance are estimated as [40], [64], [77], [173]:

$$Q_{base} = \alpha_b q_c \tag{2.2.11}$$

and

$$Q_{base} = \alpha_s q_c \tag{2.2.12}$$

Some recent methods include a variation in shaft friction with the normalized distance from the pile tip h_y/D_{Pile}, shown in Figure 2.2, [123], [138], [150].

These empirical methods contain correlation coefficients derived from databases of axial pile loads tests carried out in different conditions for various pile geometries, [122]. The accuracy of these empirical methods is therefore dependent on these pile load test databases, [178]. Some of the tests were carried out in very loose sands [97], or very dense sands [256]. The installation effects are therefore implicitly included in these empirical design methods, since the database consists of displacement piles with a stress history related to the cone resistance. Not all of the piles in these databases have similar dimensions, [148], [187], [256]. These correlations give more accurate predictions of load capacity compared to the traditional methods, i.e. Eq. 2.2.4 and 2.2.5 [41].

The settlement of axially loaded piles in Servicebility Limit State (SLS), is estimated with a variety of methods, including both analytical and numerical approaches where the soil and pile materials are simplified, e.g. [81], [184]. For onshore foundation design, settlement analysis dominates the design, while load capacity frequently governs design in offshore constructions, [173], [187].

2.2.2 Modelling installation effects for axially loaded single piles

The pile installation effects make it cumbersome to analyse the load-deformation response of piles, [104], [141], [148]. During pile installation, the soil conditions change, thereby influencing the pile-soil interaction response, [173], [187]. The empirical design formulas previously presented do not take the governing mechanisms of the pile into account, and could therefore result in inaccurate estimations of axial pile bearing capacity when the soil properties or the

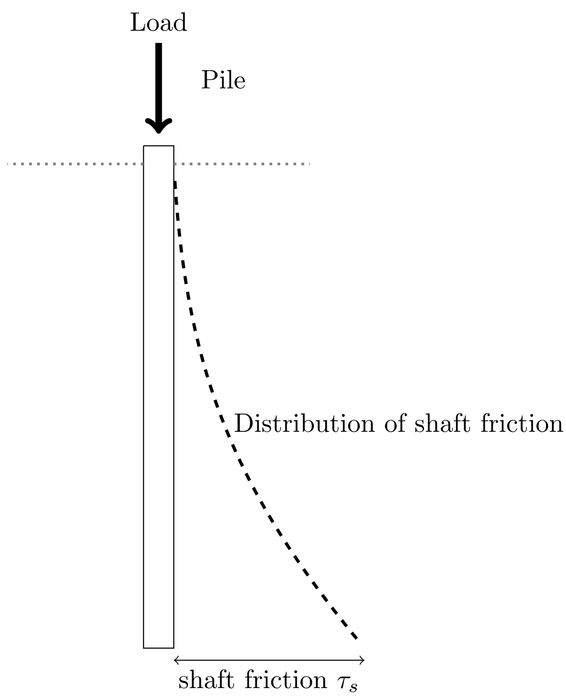

Figure 2.2: Idealized distribution of shaft friction in recent design models.

pile type are different from those in the pile load test database, [241].

Especially the behaviour of skin friction degradation, which governs the distribution of the shaft friction, reduces the accuracy of predictions, [103], [148], [231]. The reduction in shaft friction at any depth y with increasing pile penetration is assumed to be a result of the installation effects, [104]. A possible explanation is that the installation cycles during driving and jacking change the relative density R_d of the soil adjacent to the shaft, [103], [104]. This volumetric change results in lower normal stresses at the pile shaft, [148]. This effect is combined with reduction in interface friction angle δ' as the large shear strains at the pile surface reduces the roughness of the pile by grinding down the asperities at the pile surface, [109], [120]. The horizontal contact stresses have been shown to recover over time. This is assumed to be a result of more immediate stress relaxation and long-time creep in the soil surrounding the pile, [11], [47], [48], [95], [139], [140], [120].

Empirical methods may also not be accurate for soil types which exhibit unusual properties. These soils include soils with very angular grains, calcareous soils, and soils with a high silt or mica content, [149], [210], [216], [225]. In-situ measurements are also affected by the properties of these soils, which means that empirical design methods do not properly incorporate the soil response, [49].

It would therefore be of interest to more fully understand the behaviour (i.e. the stress and strain paths) of the soil during pile installation of axially loaded single piles. If the stress history and deformation behaviour during the installation of the pile are described and included in subsequent analysis, empirical, analytical and numerical methods will improve, [122], [241].

2.2.3 Design of pile group foundations in general VHM load conditions

Even though empirical methods are available for the design of axially loaded single piles, such load conditions comprise a significant simplification of normal pile foundation load-settlement behaviour. Actual conditions include vertical, horizontal and moment (VHM) loads, shown in Figure 2.3a. The load capacity and load-deformation behaviour of a pile at these general load conditions are much more cumbersome to predict than for the axially loaded pile, [82], [122].

Combination of piles into pile groups also makes empirical design methods more complicated, [173]. Since the total load is distributed between the piles in the group, each pile will carry loads of different type and magnitude, [82], [182]. Other types of load effects on the pile group include consolidation of the ground around the piles following installation, which results in negative skin friction, shown in Figure 2.3b, [27], [78].

Empirical methods are therefore generally not a suitable option for analyzing pile groups loaded with general VHM-conditions, shown in Figure 2.3b, since load testing of pile groups is complicated and not practical for large structures. Some load tests have been carried out on pile groups, but only for small group configurations, [199]. Pile groups are frequently very large structures, and field tests are therefore not feasible, [64].

2.2.4 Including installation effects in advanced numerical models

Analysis of pile groups subjected to general loads is therefore preferably carried out in advanced numerical models, e.g. [185], and more recently, [193]. Many other types of pile group analysis include significant simplifications of the soil conditions, e.g. [185]. Numerical implementations include the finite element method, the boundary element method and the material point method, e.g. [15], [14], [255]. These methods are more accurate and flexible compared to traditional analytical methods, such as those presented in [184] and [185] as long as the soil properties are correctly modelled. This gives the possibility of more accurate design in comparison to simplified analytical and empirical models, [96], [186], [228].

Realistic simulations by an advanced constitutive model and numerical framework require estimation of suitable input parameters for the settings of initial and boundary conditions in the model, [159], [184], [228]. Many numerical models assume that the soil parameters are unchanged after the installation of the structure, i.e. the pile. This method is sometimes called *wished in place*, since the structure is placed into the soil without changing the soil properties, [34]. These initial conditions result in significant simplifications of the pile-soil interaction, [173].

This assumption is not realistic for analysis of displacement piles, and to increase the accuracy of the simulation, installation effect should be included in the model. Simulations of

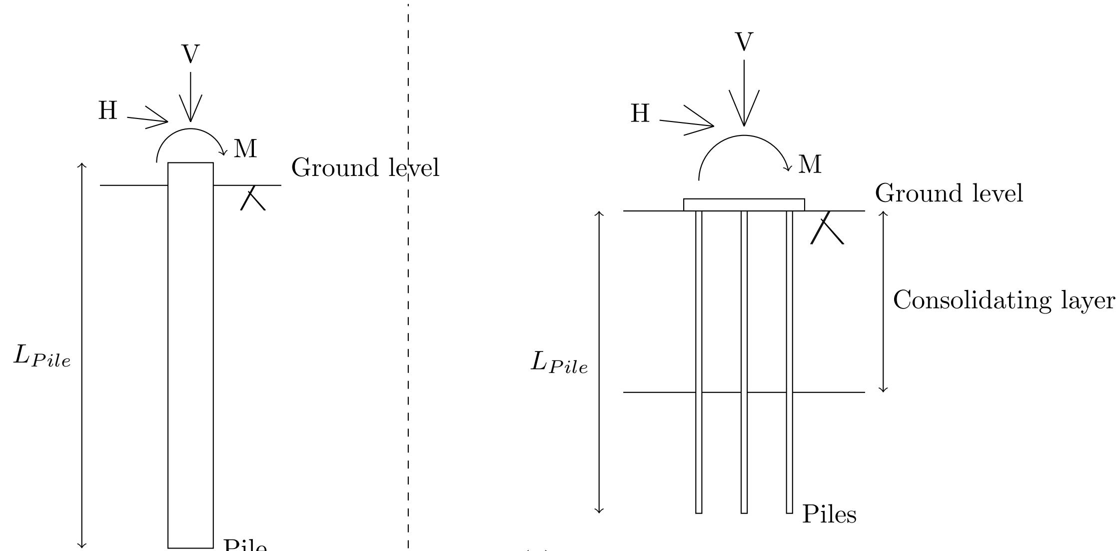

(a) Pile loaded with vertical, horizontal and moment load (VHM) at pile head.

(b) General load conditions on pile group with consolidating layer

Figure 2.3: General loading conditions on single pile and pile group

installation and penetration mechanisms are generally time-consuming, and may probably not be carried out for routine projects. Instead, it would be of interest to develop a method in which the installation effects can be directly included into the initial conditions of the numerical model, in which realistic simulations could be conducted.

To establish such a method through a conceptual framework, numerical and experimental research is needed to estimate installation effects for various initial conditions. So far, similar types of research have been primarily aimed at developing empirical design methods, e.g. [121], [148], [256]. The behaviour of the soil during installation should therefore be modelled and subsequently efficiently included in the numerical simulations.

2.3 A conceptual framework for pile installation effects

Pile installation effects should be included in simplified empirical design methods or in advanced numerical analysis for realistic modelling of displacement piles. The components of a design method or numerical model are based on a conceptual framework of the pile installation effects. This needs to be described before the practical design method or method of analysis can be devised. The aim of the current research is to contribute to this conceptual framework by experimental measurements of displacement pile installation effects. The conceptual framework is the result of the accumulated scientific research about the topic, and the formulation obviously depends on the selection of empirical data. For displacement piles such models are presented in [121], [122], and [241].

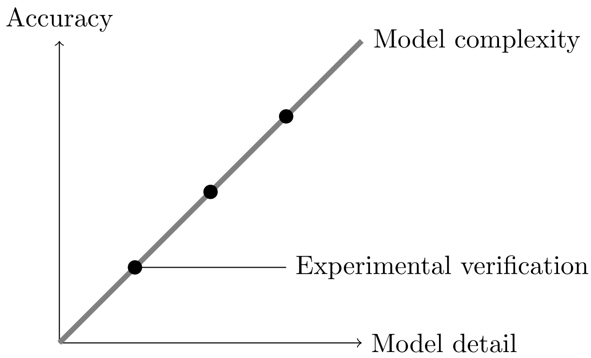

Figure 2.4: Idealized description of increasing accuracy and detail in conceptual model.

The scientific method governs the construction of such a conceptual framework, which consists of conjectures that are verified by which experimental measurements, [143]. The conceptual framework is subdivided into separate parts in practical research, and these isolated parts are simplified and studied by experiments and analysis, [67]. A more detailed model is possible to construct based on experimental verification. An idealized relation between number of components and accuracy of a conceptual model is shown in Figure 2.4, in which the conceptual framework is describing the phenomena in more detail by verification of the smaller parts.

For installation effects of displacements piles, there are several components of interest in the construction of an experimental model, [241]. For single piles, components such as horizontal stress σ'_h, and the distribution of stress along the pile, the effect of friction fatigue r_{ff}, and also long-term changes in the structure of the soil are possible to include by suitable measurements of the experimental model, [11], [104], [148]. For pile groups, interaction effects on load-deformation behaviour and pile group bearing capacity are also of interest, [184], [185].

The conceptual framework itself is not sufficient to result in prediction for design purposes. It can guide the construction of a design method, but the precise formulation of such a method should be based on experience, practical judgment, and the availability of input data. Figure 2.5 shows the route from conceptual framework to a simplified model, which then is supplied with soil parameters and subsequently presents a prediction for the particular load effect. Accurate prediction in soil mechanics is often governed by the practical need for soil parameters, [122], [182], [250]. For design of single axially loaded piles, many methods are based on the Cone Penetration Test (CPT), e.g. [16], [25], [40], [50], [64], [123], [138], [150]. Prediction can also be made by numerical models, e.g. [76] with suitable soil parameters. This thesis is limited to the discussion of the conceptual framework of pile installation.

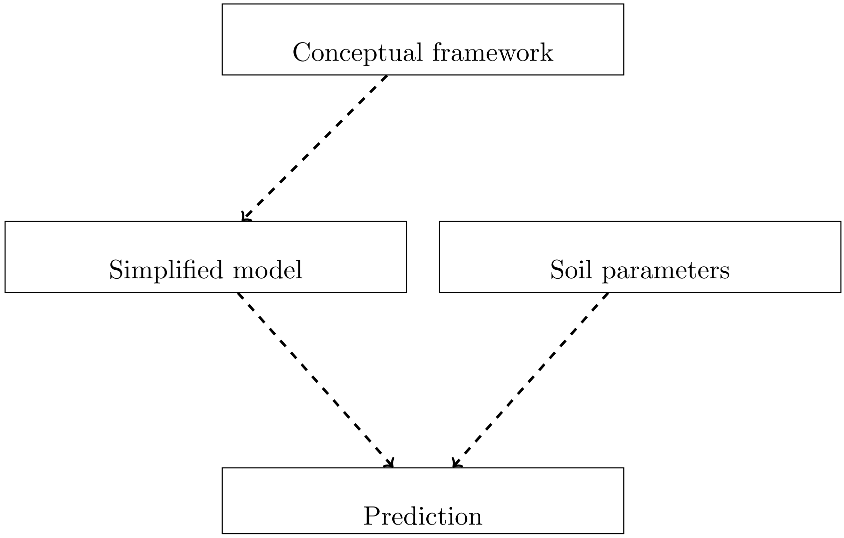

Figure 2.5: The route from conceptual model to prediction based on soil parameters.

2.4 Practical simplifications of real soil behaviour

Modelling of installation effects includes suitable simplification of behaviour of the soil. Conclusions from model experiments are subsequently integrated into the conceptual framework for describing installation effects and for conducting experimental tests. This specific framework is then valid for soil and pile types which are comparable to the prototype behaviour in the framework. The soil parameters and the scale on which they govern the behaviour of the soil should also be accurately measured in laboratory or in-situ tests, [250]. A flowchart describing the governing parameters is shown in Figure 2.6. The flowchart begins at the grain scale level, proceeds through the soil composition, the state of the soil and the load type. This description is a significant simplification of real soil, but is still helpful for modelling purposes. An extensive discussion of advanced laboratory modelling for analysis of these effects is given in [120].

Drained experiments on sand (without excess pore pressures) have shown that sands respond to loads and displacements through normal and shear stresses, which restrain displacements and rotations of the grains, [74], [205]. The effective stress state of the soil consists of the total effect of these forces, integrated over a specified boundary, [74], [169]. A sufficient number of grains are therefore required to constitute a homogenous stress state $V_{hom,soil}$, [58]. The approximate number of grains relative to model size need in experiments is discussed in the following chapter. The size of the volume $V_{hom,soil}$ depends on the grain size and grain shape, [43], [74], [203]. Furthermore, experiments show that grain shape has an impact on the soil-structure load and deformation response, e.g. [49], [149], [216]. Grain shape may be described by sphericity, roundness and the roughness of the soil grains. These expressions describe the 3D shape of the grains, [43], [149].

The mineral composition of the soil contributes to the soil properties as well. Brittle grains

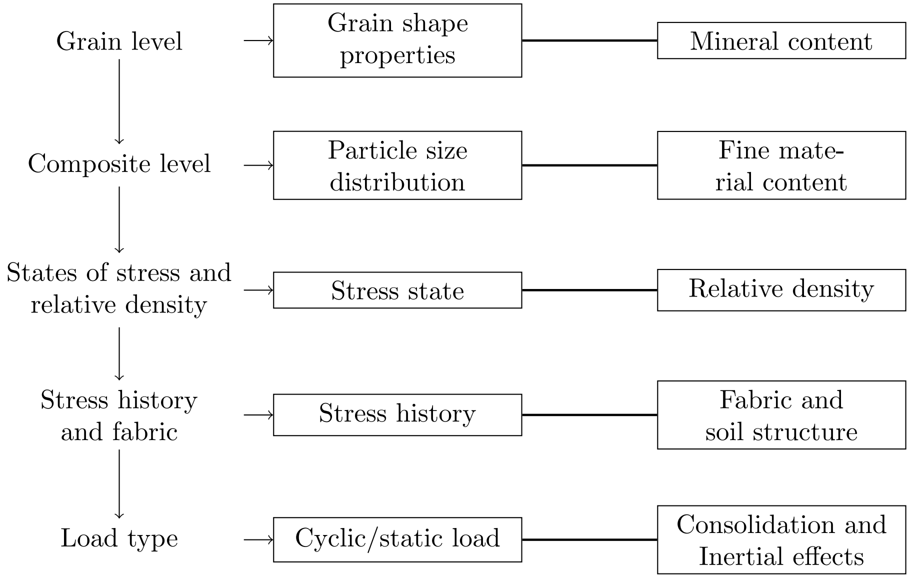

Figure 2.6: Parameters that govern the behaviour of sands.

in the soil mass fracture at higher stress levels, [31], [51], [132], [250]. The mineral content likewise influences the possibility of grain cementation and transition into a different behaviour, [51],[221].

Natural soils have large variations in particle size distribution, e.g. [90], [169], [250]. The particle size distribution has an effect on the packing of the grains, and therefore the range of the relative density of the soil, expressed as the maximum and minimum void ratios e_{max} and e_{min} (which are difficult to consistently obtain in experimental tests), [20], [22], [100], [170], [203]. Inclusion of clay and silt in sands changes the behaviour of the soil, and has been observed to change the mechanical behaviour of the soil, and consequently the bearing capacity of piles, e.g. [21], [22], [210].

The state of soil is described by parameters such as the stress and void ratio, [250]. Experiments on soils of different void ratios or relative densities have shown the influence of the evolution of the state of the soil, [42], [116], [194], [195]. The behaviour of the soil is also determined by the stress state, [19], [212], [250]. Such observations of the effect of relative density and stress level were formalized into critical state soil mechanics, [202], [250].

Natural soils have a stress history and contain soil structure, or fabric, that is observed both in the field and in the laboratory. These in-situ conditions are cumbersome to recreate in experiments, [136], [250]. The soil fabric depends on the geological history of the soil, [39], [152], [228]. It is also complicated to separate overconsolidation effects and fabric, and the term yield strength ratio (YSR) has therefore been adopted in design procedures, [122]. Pile installation has been observed to influence the response of the soil over longer periods, which is assumed to a result of the change in fabric, as well as the stress distribution, [11], [95], [139], [140], [120].

Parameters		Standard ranges	
Water-cement ratio	(vcr)	0.4	(-)
One-month cubic compressive strength	σ_c	60	MPa
Diameter	D_{Pile}	250 to 600	mm
Length	L_{Pile}	10 to 30	m
Young 's modulus	E_{Pile}	35	GPa
Poissons ratio	ν_{Pile}	0.2	(-)

Table 2.1: Properties of prototype concrete piles, [235], [82].

Possible load effects include static loads as well as cyclic loads at different frequencies, e.g. [64], [120]. Load cycles alters the soil state, especially on soil-structure boundaries, e.g. [103]. Depending on the mean stress level and the cyclic load variation, the cyclic behaviour of the soil may not be stable, [120], [130]. These loads frequently result in consolidation effects and inertial effects in the soil. Saturated soils subjected to dynamic loads (including inertial effects) experience pore pressure generation and dissipation as well as stress wave propagation, both in the soil and the structure, e.g. [7], [247], [248].

Because of the variability of the soil properties, an experimental model of soil-structure interaction should be a compromise between realistic description of soil behaviour and the number of model parameters. The accuracy of the model depends on how well the model simplifies the prototype behaviour, which cannot be inferred from the model itself, [142]. The prototype should therefore be studied in detail, so that suitable simplifications can be made, and the governing mechanisms be included in a practical but still realistic realization, [200], [250].

2.5 Description of prototype for modelling

This thesis is restricted to modelling displacement pile installation effects in rounded, clean silica sand, with no clay or silt content. This type of soil therefore has a relatively high permeability, resulting in some generation of excess pore pressures during installation and relatively quick dissipation after the installation in the prototype. The behaviour of this type of material is therefore not directly applicable to other types of soils, such as sands with a high silt content or calcareous sands that exhibit a different load-deformation response, e.g. [49], [132], [216], [225].

Piles are classified as either displacement piles or non-displacement piles, [82], [173], [187]. This thesis is restricted to square closed-ended displacement piles. The prototype pile is here defined as a square full-displacement concrete pile with rectangular cross-section. These piles have limited steel reinforcement, which does not directly influence the behaviour of the pile in compression, [173]. Some prototype parameters for such concrete piles are shown in Table 2.1.

This type of displacement piles are installed by impact driving, jacking or vibrating, e.g. [159]. The most common method of installation is by impact driving, in which the pile is driven into the soil by repeated blows by an impact load provided from the pile hammer, with a typical rate of ca. 1 Hz, [173], [235]. Hammer types include steam, hydraulic and diesel hammers, [64]. Piles may also be installed by jacking, although this method is most common for tubular piles and sheet piles, [93]. The hammer energy for a blow may ranges from 18 to 600 kNm for diesel and hydraulic hammers, [235].

This type of simplification helps to constrain the large variation of pile length (2 m -100 m), and pile diameters (0.2 m- 2.5 m) to a prototype which is developed into a model. The model is consequently not replicating all prototypes, but a limited type which is possible to simulate in numerical and physical models. The following dimensions are considered: 4 - 10 m pile with 250 - 500 mm diameter.

In the following text, results of previous experimental and numerical studies are discussed in the detail, to provide an argument for the design of the experimental model.

2.6 Modelling installation effects

Natural soils show large variability in composition and behaviour, and their mechanical response is consequently diverse, depending on many characteristics of the soil. These aspects are often formalized as soil parameters, e.g. [169], [202], [212], [250].

In experimental tests on prototype soil with accurate initial conditions and stress paths, the soil behaviour is directly included, [1], [189]. Careful experimental preparation in the laboratory has been shown to give relatively consistent reproduction of experimental conditions, [8].

In contrast, analytical and experimental models are based on constitutive material formulations and produces simulations of the material behaviour based on parameters determined in experiments. Formulations range from elastic models to advanced models such as the Cam clay or the Severn-Trent model [58], [87]. The basis of these constitutive models is experimental evidence from laboratory tests. The models should therefore not be extended to simulations where these conditions are not valid, [230].

2.6.1 Analytical models

Analytical models include elastic models, suitable for small deformations, and perfectly plastic models, which are used in limit analysis, [58], [59], [250]. Simplified elastic solutions of deformation around a pile have been formulated, but modelling pile installation procedure requires much larger deformations, e.g. [166], [190], [191]. Analytical models of plastic deformations also require significant simplifications, e.g. [59], [189]. The flow of soil around the pile during installation has been simulated in cavity expansion models which also results in large simplifications of the soil behaviour, e.g. [187], [232]. Although analytical methods result in rigorous solutions, they are probably not the most suitable options way to model the pile installation effects.

2.6.2 Numerical models

Material behaviour in numerical models is described by a constitutive framework for sand, e.g. [87]. Well-known numerical codes include the finite element method, the boundary element method and the finite difference method, [14], [56], [255].

Numerical simulations of installation effects include [26], [37], [71], [72], [96], [186], [159], [157]. The numerical approach to modelling installation effects is very promising, and will give valuable additional information about the simulated stress-strain behaviour of soil due to installation effects. A disadvantage is the practical limitations of the method, such as the large number of parameters required in more advanced constitutive models. This results in large variations in the input data into the models, since the quality of the parameter determination process is highly dependent both on the operator of the laboratory experiments and the type of analysis carried out to obtain soil parameters. These procedures are also dependent on the analysis and laboratory procedure, [169].

2.6.3 Experimental modelling

Experimental modelling of installation effects comprises field and laboratory measurements. The big advantage of field measurements is the direct inclusion of ground conditions. There is therefore no need for scaling of the soil properties, e.g. [28], [78], [97]. Most physical models contain normally or isotropically consolidated soil, since complicated features of the soil behaviour such as fabric and stress history are cumbersome to include in physical models such as centrifuge tests, [136], [222].

The laboratory gives the possibility to perform experiments in a variety of configurations in a controlled environment. Geotechnical centrifuge models scale the mechanical behaviour accurately, [201], [242]. Alternatively, simulated stress conditions may be carried out in calibration chamber models, e.g. [49], [85], [128].

An advantage of small scale model tests is the lower cost of laboratory scale models compared to field models, [242]. A larger number of experimental tests can therefore be conducted, e.g. [49], [136]. In contrast, large scale field models are frequently restricted to a small number of field tests with relatively limited measurement possibilities (resulting in less information from the tests), due to the cost and practical considerations, e.g. [256].

2.6.4 A combined modelling approach

A suitable compromise includes field, laboratory and numerical models, combining the strengths of the different types of modelling, [188]. Field tests provide information about the prototype, laboratory measurements show the detailed behaviour of the mechanisms of the soil, and numerical methods offer the possibility of combining these results. The research carried out in the line of this thesis consists of laboratory modelling, and is part of a project containing simulations of pile installation effects by numerical modelling, [76], with a suitable constitutive model, [234].

2.7 Description of the prototype installation phases

It is useful to separate the installation procedure into installation phases. A pile is installed in soil with a specific geological history, and consequently the installation effects are influenced by the initial properties of the soil, such as the relative density R_d, the stress state p' and the soil fabric. The installation is here divided into installation stage 1 and installation stage 2. The stages are related to an arbitrary soil element, shown in Figure 2.7. In stage 1, the pile approaches the soil element, followed by installation stage 2 in which the soil is cyclically loaded at lower stress levels but with a high shear strain at the pile-soil interface, [109]. After installation the structure of the soil changes due to the stress relaxation and creep, [11], [48], [47], [95], [139], [140], [120].

2.7.1 Pre-installation stage and normalization of installation effects

Before installation of displacement piles, the soil is normally characterized by in-situ tests or tests on retrieved soil samples in the laboratory, [82]. Sands are often disturbed during sampling, and special methods are needed to obtain soil samples that give an accurate representation of the soil properties, e.g. soil freezing, [110]. In-situ methods, such as the cone penetration test (CPT), or the standard penetration test (SPT) (which is not recommended, [82]) are therefore frequently used to characterize sands. Many types of correlations have been established between soil parameters and in-situ tests, e.g. [18], [49].

It is possible to prepare soil samples at a specified relative density in the laboratory according to correlations between cone resistance q_c and relative density R_d, [8], [136], [250].

2.7.2 Installation stage 1

The penetration mechanism in installation stage 1 results in very large deformations and changes in effective stresses as well as stress rotations when the pile is installed into the ground, [119], [136], [148]. This has also been modelled in numerical models, e.g. [96]. It should be pointed out that the stress and strain paths of the soil depend on the location of the soil relative to the pile, [119]. Figure 2.8 shows elements a, b and c at the depth y at various initial radial distances r. The soil follows stress and strain paths represented by functional relations, [85], [119]:

$$\sigma'_{ij} = f(r/D_{Pile}, h_y/D_{Pile}, p') \tag{2.7.1}$$

$$\varepsilon_{ij} = f(r/D_{Pile}, h_y/D_{Pile}, p') \tag{2.7.2}$$

where σ_{ij} and ε_{ij} are the effective stress and the strain components, r is the initial distance from the pile, D_{Pile} is the pile diameter, and h_y is the vertical distance from the pile base. The complete stress and strain path of a homogenous element of soil consequently consists of the evolution of σ_{ij} and ε_{ij} during the installation. For large strain gradients in soil samples with relative large grains, which is common in model tests, [85], [88], the concept of homogenous soil element V_{hom} is also doubtful, since the theoretical size of the homogenous element of soil depends on the homogeniety of the stress field, [58], [74]. The distribution of

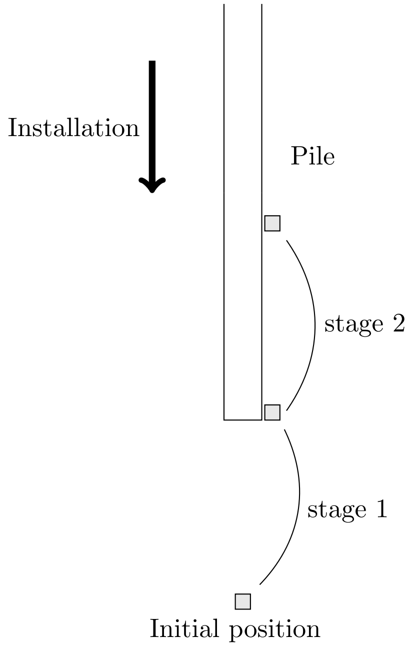

Figure 2.7: Installation stage 1 and 2.

stress during large deformation is therefore complicated to describe.

To replicate a collection of heterogeneous stress paths in homogenous soil tests, e.g. the tri-axial apparatus, a large number of samples should be tested for different stress paths. Based on these tests, the total system response could be estimated from the measurements. In traditional experimental analysis of slope stability, such types of suitable stress paths are tested to recreate the system response to deformation, e.g. [8]. A series of different tests, such as triaixal test in compression, simple shear test, and triaixal test in extension, recreate the governing mechanism at each part of the prototype accurately, [250]. Alternatively the soil response is modelled by a consitutive model with a numerical framework based on such experiments, e.g. [234], [250].

Similar modelling of displacement pile installation is more cumbersome. The deformation and stress levels during installation are also very different and include large stress rotations, [62], [148]. This makes experiments in tests with fixed principal stresses, such as the triaxial apparatus, not a practical method to model the prototype behaviour. The soil response during pile installation is consequently not easy to measure in element level laboratory tests.

The large variation in stress level makes it also complicated to conduct accurate measurements, so the experimental measurements system should both have a large range and a very fine resolution during the installation. The penetration mechanism of a displacement pile is comparable to that of a cone penetrometer, [122]. The cone penetrometer friction in sand is around 1% of the cone resistance, [49], [158]. A friction angle δ' of e.g. 25 degrees, results in

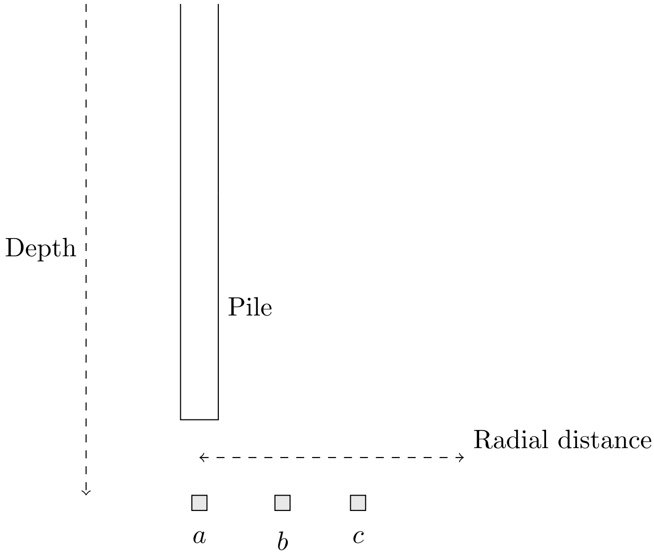

Figure 2.8: Soil element at various radial distances from the pile.

a horizontal normal stress corresponding to around 2% - 2.5% of the cone resistance, [124]. This is a relatively small fraction of the total stress range, which governs the accuracy of the measurements. If any stress measurement system used to measure the total stress path has a resolution of less than 1% of the total stress range, the variation in the horizontal normal stress in installation stage 2 will therefore be around ± 50%. Measurements of the total stress path must consequently have a very high resolution and precision, as well as total range, if both installation stage 1 and 2 are to be captured simultaneously.

The installation effects consist of the change of the initial soil state as a result of the installation, [141]. The installation effects are consequently a function of pre-installation parameters such as relative density R_d, mean stress level p', [29],[141]. The installation effects have also been described based on normalization with the state parameter ψ, [136]. The state parameter is defined as, [22], [250]:

$$\psi = e_{soil} - e_{cs} \tag{2.7.3}$$

where e_{soil} is the void ratio of the soil, and e_{cs} is the void ratio at critical state at the mean stress level p', [22], [250]. Installation effects have been analysed in the same way, in which similar normalizations of the installation response were carried out, [136]. These show large variations, possibly as a result of the variation in stress and strain path during displacement pile installation. It is therefore not conclusive whether it is possible to use the state parameter to characterize displacement pile installation effects.

The soil-pile stress during installation has been measured both at the surface of the pile or penetrometer, as well as in the soil mass. Measurements in the soil itself are more tedious to conduct, and a large number of stress transducers are required for accurate measurements, [85], [119]. Measurements of installation effects on the surrounding soil include measurements of heave around the pile, and driving resistance for subsequent pile installation, [23], [173].

Field investigations of the installation effects include penetrometer measurements carried out before and after a displacement pile was installed, [180]. These measurements show a large increase of penetration resistance close to the pile, which is reduced at larger distances. It is also notable that the change in penetrometer resistance in the test was dependent on the initial void ratio and mean stress level, with a larger increase in the penetration resistance in dense sand layers. Similar types of measurements have been carried out with dynamic sounding apparatus, showing a similar pattern, [23]. These field tests are relatively old and it is possible that this specific and sensitive experimental test set-up results in measurement uncertainty.

Stress change measurements on installed piles during subsequent pile installation nearby has also been carried out, showing stress redistribution in the soil as the subsequent pile advances, [24], [46]. The previously installed pile was observed to lift slightly in the vertical direction during the installation of the next pile. In turn, this resulted in reduction of the pile base resistance as a result of the disturbance of the stress field, [24].

Soil stress measurements during pile installation have also been carried out in the laboratory, where accurate sample control is possible. These studies display similar behaviour as the field measurements, with a stress peak at the location of the pile base, [38], [83], [85], [119], [128]. Measurements of the stress components σ'_r, σ'_z and σ'_θ have been carried out at several layers with embedment stress sensors in the calibration chamber and compared to the cone resistance q_c, [119], [128]:

$$\frac{\sigma'_i}{q_c} = f(h_y/R_{Pile}, r/R_{Pile}) \tag{2.7.4}$$

where σ_i is a stress component (i = r, z or θ), h_y is the distance between the soil and the pile in y-level, and R_{Pile} is the radius of the pile. These types of relationships are very valuable for analysis of the stress change during installation on structures close to the piles, [183]. The post installation stresses are however very small in comparison to the maximum stresses, which makes a complete description of the stress and strain paths of the soil difficult, [241].

Field measurements of penetration resistance, replicating pile base resistance include [16], [180]. These measurements showed a correlation between the cone resistance, mean stress level p' and the relative density R_d. Later, explicit correlations calculated from experiments in pressure controlled calibration chambers were formulated, [18], [22], [49], [158], [207]:

$$q_c = f(R_d, p') \tag{2.7.5}$$

Measurements of pile installation in the field and in the laboratory have shown similar types of response, [83], [85], [119], [128], [136], [148], [256]. Many experiments have been carried out in dry sand where pore pressure generation and dissipation does not change the effective stress state, e.g. [34], [83], [85], [119]. A typical penetration resistance is shown in Figure 2.9a, which shows increased penetration resistance in dense sand layers, and at higher mean stress levels p' which occurs at greater depth in the soil. Numerical models have shown the

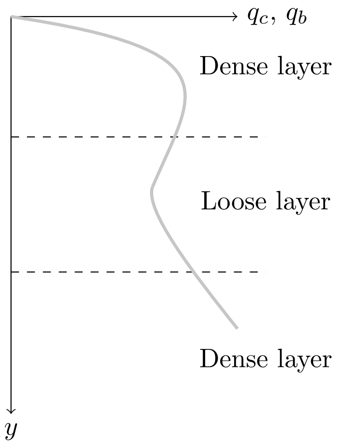

(a) Variation of base resistance with relative density.

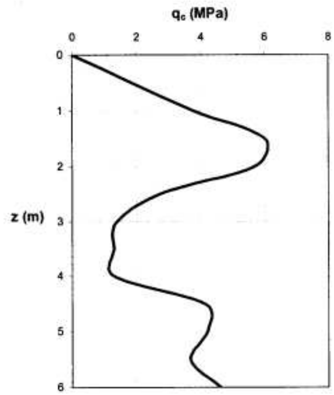

(b) Measurements from [151].

Figure 2.9: Change in cone resistance and relative density with depth.

same result, [159].

The stress distribution in the pile is sometimes determined by dynamic testing methods, [64], [227]. The most likely distribution of stress in the pile is found through signal matching of measurements of the acceleration and force at the top of the pile using analysis software such as CAPWAP, [94]. These measurements have relatively low resolution, and cannot describe the evolution of the stress distribution in the pile with high levels of accuracy, [227]. The installation method (including vibrations) influences the stress distribution around the pile, and it is there not possible to evaluate different pile types with the same method, [159].

The displacements of the soil around the pile during installation by a transparent surface have been measured in various experimental settings, e.g. [69], [70], [162], [165], [246], [252]. The behaviour of the soil was shown to depend on the relative density R_d and the mean stress level p', as well as the mineral content of the soil, [162], [243]. Idealized displacements are shown in Figure 2.10.

The deep penetration mode has been compared to the strain path method in undrained soil, which presents similar displacement paths but with a larger vertical rebound mechanism in installation stage 2, [13], as well as other experimental methods, [171], [243], [246]. Centrifuge modelling of a similar deep penetration mechanism in a two-layer material has been carried out in [54]. Experimental modelling of deep penetration mechanisms in sand has been carried out by [99].

Measurements of soil deformation and soil density change in 3D conditions have been conducted with X-ray measurements, in which the soil deformation was tracked with pre-placed metal spheres in the soil mass. The soil sample was prepared in loose conditions and the tests carried out at low stress, in which qualitative measurements of the soil flow mechanisms

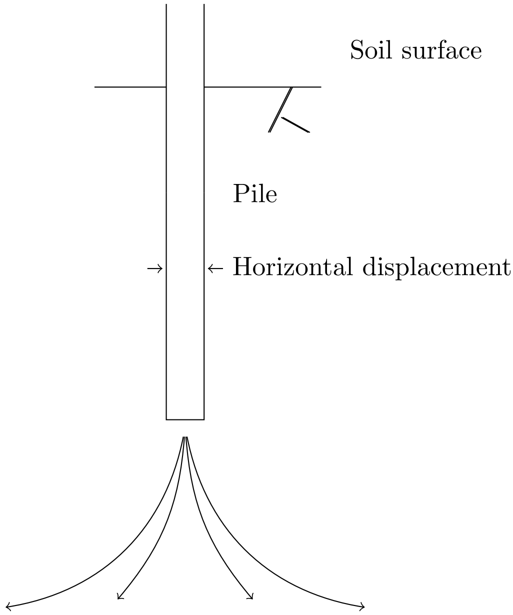

Figure 2.10: Idealized displacement of soil around the pile during installation.

were carried out, [197], [198]. From these measurements the specific mechanisms which governed the installation process were described, including a deep penetration flow mechanism, which included large magnitudes of vertical deformations of the soil around the pile, [197]. A special nose-cone, which does not deform and is displaced along with the soil in isotropic compression, was also found, [197], [243], [246].

Other measurements of soil deformation and strain levels during pile installation include [25], [44], [57], [63], [137], [213], [252]. These measurements show the steady state deformation mechanism in which the soil flows around the pile base during installation, Figure 2.10.

2.8 Installation stage 2

Installation stage 2 commences when the soil element has reached the same depth y as the pile tip, shown in Figure 2.7. The pile installation resistance is composed of the pile base resistance and the pile shaft resistance, [96]. For the study of interface shaft friction, the most interesting part of the soil mass is positioned adjacent to the pile shaft, shown in Figure 2.11. The behavior of the soil at the interface is governed by the whole soil mass extending from the pile, [82], [187]. The stress history of the soil is a result of the stress and strain paths in this volume of soil during installation stage 1. The behaviour of the soil in stage 2 is consequently cumbersome to model since the stress history is heterogeneous and largely unknown, even though some measurements of installation stage 1 are available, e.g. [119].

During installation with an impact pile hammer, the soil-pile interface is cyclically loaded by

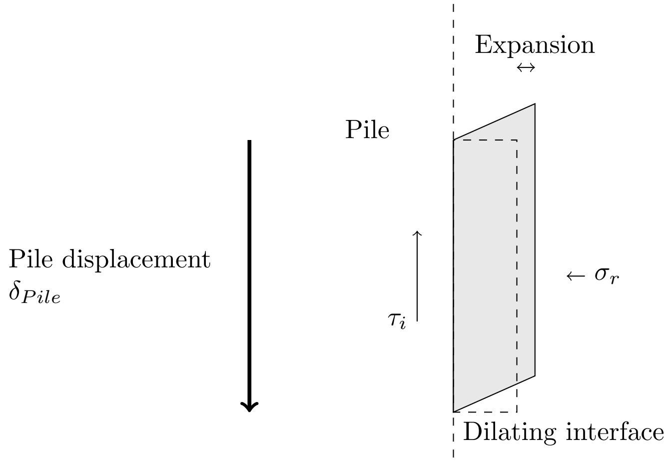

Figure 2.11: Dilating soil at pile-soil interface.

the displacement increments in the two-way installation cycles, shown in Figure 2.13a, [124], [109]. These load cycles have been shown to cause changes in the peak shear and normal stress, e.g. [89], [148], [256]. This is believed to result from densification of the loose soil, degradation of the interface friction angle, and stress redistribution in the soil, [84], [120], [148], [251]. This phenomenon is shown in Figure 2.13a to 2.13c in the $\tau_s - \sigma'_n$-space.

The cyclic loading mechanism at the pile-soil interface depends on the displacement, Δz, the roughness of the pile R_{CLA} (the average height of the troughs and the peaks of the material surface, defined in Appendix A), the mean grain size d_{50}, as well as the relative density R_d and the mean stress level p', [124], [148]. The loading type (i.e. one- or two way loading), and the loading frequency also influence the interface mechanism, [66], [118], [120].

In installation stage 2, averaged shaft friction has been captured through measurements of the axial stress distribution during the installation itself, e.g. [97], [256]. Measurements of the shaft friction through axial stress distribution have relatively low accuracy and these measurements consequently show some variation, but confirm the effect of initial relative density on the horizontal contact stress, with a horizontal contact stress correlated with the cone resistance, [148], [256].

More detailed information is gained in local horizontal normal stress measurements, e.g. [29], [136], carried out in the laboratory, and [89], [148], [256] carried out in field tests. The local horizontal normal stress is in these experimental models measured by special sensors at the pile shaft. Measurements such as these have shown the effect of the pile roughness R_{CLA}, mean stress level p' and the relative density of the soil R_d, [97], [148], [256], again with correlation between the horizontal contact stress and the measured cone resistance.

Experimental measurements have shown that the effective horizontal normal stress σ'_h clearly follows the cone resistance q_c in clean silica sand, [148], [256]. The direct correlation between relative density and shaft friction is consequently not a correct description, since the

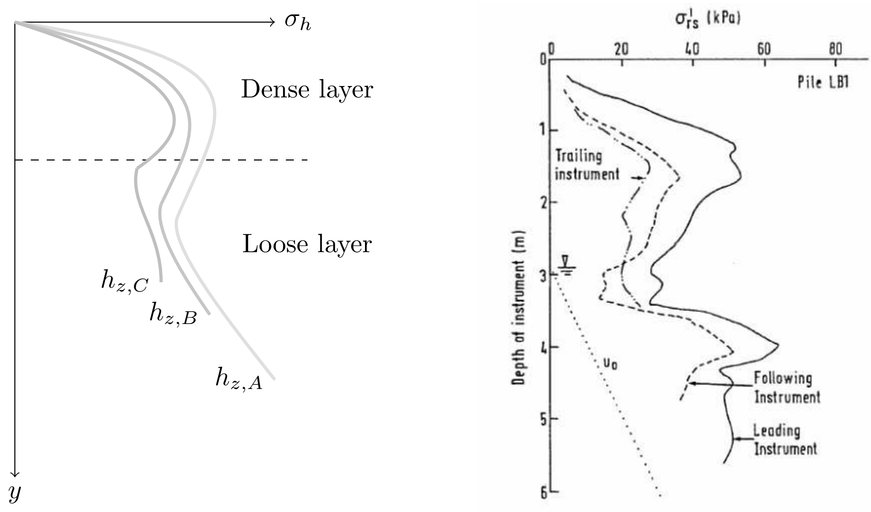

(a) Idealized model.

(b) Measurements from [151].

Figure 2.12: Distribution of horizontal normal stress σ_h resulting from friction fatigue.

mean stress level p' is not included, [178]. The correlation between shaft friction and cone resistance is significantly different in carbonate soils, and standard design methods are not accurate in such soils, [132], [225].

Field and laboratory experiments also show that the distribution of horizontal normal stress depends on the location of the measurement relative to the pile tip, h_y/D, and changes with increasing penetration. This effect has been observed in the field, [97], [103]. Such measurements of the horizontal normal stress at different distance h_y/D from the pile base show a reduction in σ_h' at increasing h_y/D, which has also been reported as friction fatigue, [103].

Laboratory measurements show that the most significant changes in interface horizontal stress (and the shaft friction) occur after a relatively small number of loading-unloading cycles, [65], [89], [154], [245]. This effect is partly caused by the volumetric response of the soil during shear loading, [65]. The friction fatigue mechanism is consequently also present in jacked piles, since the jacked piles are also loaded cyclically, but with a much smaller but still significant number of load cycles, [93]. The ideal continuous jacking modelled in the current thesis and e.g. [159] is not possible to achieve in the field in most cases. The mechanism of friction fatigue was previously presented as a critical depth, in which the average shear stress reached a constant value, e.g. [231]. Instrumented model pile experiments show that the local horizontal stress variation with increasing penetration causes the change in average horizontal stress, [155].

Interface behaviour between the soil and the pile has been modelled in the constant normal stiffness (CNS) test, [218], [241]. It has also been modelled in ring shear tests, in which very large strain levels may be modeled, e.g. [134], [148], [218]. Laboratory and field measurements have shown that the interface shaft friction τ_s between the soil and the pile can be described by the Mohr-Coulomb friction, [34], [124], [109], [148]:

$$\tau_s = \sigma'_{h,tot} \tan \delta' \quad (2.8.1)$$

where δ' is the drained interface friction angle and $\sigma'_{h,tot}$ is the total horizontal normal stress. The total horizontal contact stress $\sigma'_{tot,h}$ between the soil and the pile is approximated as the sum of the horizontal contact stress when the pile is not loaded $\sigma'_{h,n}$ and the increase in normal stress during deformation resulting from dilation, $\Delta\sigma'_h$:

$$\sigma'_{tot,h} = \sigma'_{n,h} + \Delta\sigma'_h \quad (2.8.2)$$

The change in normal stress during deformation is a result of the change in the dilatory expansion Δh. Based on cavity expansion theory, the change in normal horizontal stress $\Delta\sigma'_n$ is simplified as, [34], [148], [147]:

$$\Delta\sigma'_h = \frac{4G}{D_{Pile}} \Delta h \quad (2.8.3)$$

An alternative formulation includes the extra space of the dilating interface Δy_{soil}, which normally is around 10 soil grains, [34], [134]:

$$\Delta\sigma'_n = \frac{4G}{D_{Pile} + \Delta y_{soil}} \Delta h \quad (2.8.4)$$

where G is the shear modulus of the soil, and D_{Pile} is the pile diameter. The shear modulus is a function of the mean stress level, as well as the deformation level, [117], [126], [151]. It may be assumed that the soil reaches a stable stiffness level at around $0.4G_{in}$ after large deformations, where G_{in} is the initial shear stiffness before installation, [151]. Laboratory measurements on pre-installed piles loaded in tension show that the back-calculated shear modulus is a smaller fraction of G_{in}, [147]. Some experimental measurements show that reversals in loading direction may result in very high stiffness levels, something which also could result in higher shear modulus resulting from the many installation cycles, [214], [247].

The interface friction angle δ' also changes during installation, since the soil friction at high stress levels decreases the roughness of the pile during installation, thereby lowering the Mohr-Coulomb failure envelope, shown in Figure 2.13c, [109]. In field and calibration chamber experiments, piles which have been retrieved from the soil were covered with a layer of soil, increasing the roughness R_{CLA} of the pile [109], [149]. In other experiments the interface roughness have been lower, [251]. Geological processes may also influence the pile roughness, [114]. The effects of aging and as well as grinding are complicated to assess, and also occur over different timescales, and depends on the properties of the soil.

The properties of the soil at the pile-soil interface have also been observed to change as a result of the installation process. Laboratory experiments have shown that the particle size distribution may change close to the pile, with a layer of small particles reducing the interface friction angle at large deformations, [109], [251]. These processes may also be time-dependent, and influenced by creep and stress relaxation in the soil, [11], [48], [95], [139], [140], [120].

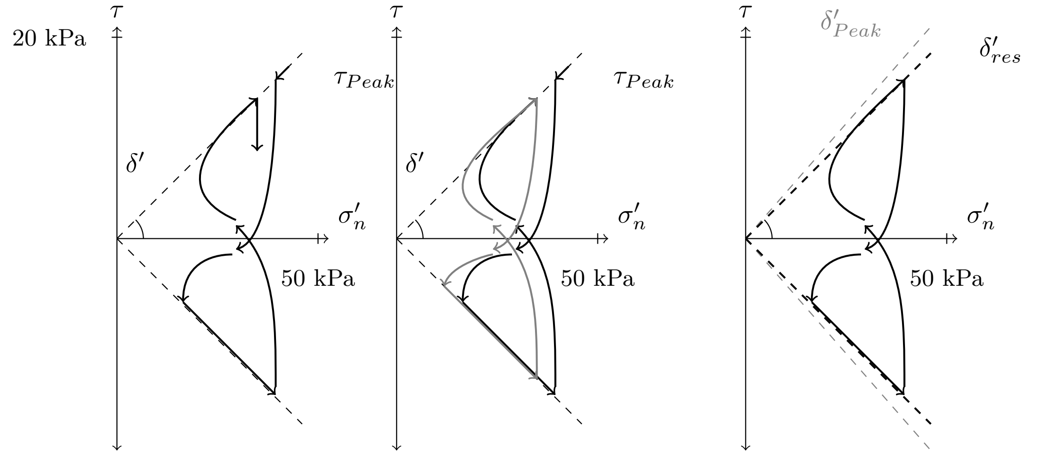

(a) Load cycles in installation stage 2. (b) Change in peak shear/normal stress. (c) Change in interface shear strength δ'.

Figure 2.13: Behaviour of the soil-pile interface during load cycles in idealized soil.

The behaviour of the soil around the pile during the installation is therefore complex, and a combination of laboratory experiments in confined conditions and consequently the experimental tests should be combined to model the whole system, e.g. [34], [124], [148].

2.8.1 Post-installation stage

Measurements of the post-installation stage include axially instrumented piles in the field and in the laboratory, carried out both immediately after installation as well during longer periods, e.g. [11], [141], [148], [231], [256]. Natural soil regains structure after disturbance which is a possible cause for long-term change of observed pile-soil behaviour of impact-driven displacement piles, [11], [48], [47], [82], [95], [139], [140], [228]. Post-installation effects include installation of subsequent piles in a pile group, which makes an assessment of the pile group interaction effect complicated, [24], [46].

2.9 A conceptual framework for installation effects

Experimental model tests are conducted relative to a conceptual model of the prototype. In a simplified model, the soil behaviour is governed by mineral properties, particle size distribution, particle shape, stress level, relative density, soil fabric, stress history and load type. A complete description of the soil is consequently elusive, and practical methods to describe the penetration mechanism contain considerable simplifications, e.g. [25], [82]. The total system response to pile installation constitutes a boundary value problem, in which the displacement- or load controlled deformation mechanism results in a system of stress and strain paths, [1].

The conceptual framework is here adapted from [119], [130], [148]. Current methods of design consist of such a conceptual model in combination with correlation coefficients found in a pile load test database, e.g. [50], [123], [138], [150]. It is essential that the conceptual model is capturing the main mechanisms to establish the reliability of such methods, [178].

2.9.1 Installation behaviour in stage 1

In installation stage 1, the soil is deformed as the pile approaches the soil, resulting in large deformations and stress rotations, [85], [96], [95], [159], [128], [198]. Measurements by embedded stress sensors show increases in the stress components σ'_r, σ'_z and σ'_θ in a cylindrical coordinate system, with decreasing stress magnitude at larger radial distances r from the pile, [119]. Numerical simulations of pile installation show similar types of stress development, [96].

After the initial penetration close to the surface, the soil is displaced in a more confined steady-state material flow, with some similarities to spherical cavity expansion and the strain path method, [187], [244], [243], [252]. The change between the initial kinematic penetration mechanism at the soil surface and the deeper steady state mechanism has been stated to occur at a transition zone, $z_{mode,tr}$, but this is not corroborated by other experimental measurements, [162]. This depth is possibly dependent on the initial void ratio, as well as other parameters in Figure 2.6.

2.10 installation behaviour in stage 2

During installation stage 2, the pile-soil interface behaviour is approximated by Equation 2.8.1. The total horizontal stress at the shaft $\sigma'_{h,tot}$ comprises the horizontal stress at the shaft when the pile is not loaded, $\sigma'_{h,n}$, and the increase in stress $\Delta\sigma'_h$ resulting from a dilating layer at the interface according to Equation 2.8.2.

The cyclic loading at the pile-soil interface results in soil density change, and change in horizontal contact stress, i.e. the friction fatigue effect, [34], [148], [241]. This causes variation in average shaft friction, [104]. The cyclic loadings depends on the number of loads cycles, but field and laboratory measurements have shown that the major part of the friction fatigue effect occurs after a small number of load cycles, [89].

2.10.1 Deformation zones around the pile after installation

The large deformation during installation stage 1 results in large volumetric and shear strains, [34], [159], [119]. After the pile installation, the soil around the pile may approximately be divided in three zones, A, B and C, as shown in Figure 2.14, [130]. These zones experience very different types of deformation, and should therefore be analysed separately.

Zone A is the layer of soil at the interface between the soil and the pile which is primarely sheared during deformation. In stage 1, this soil is located beneath the pile, and constitutes part of the larger stress and strain path envelope, [130]. In sand, this soil layer is dominated

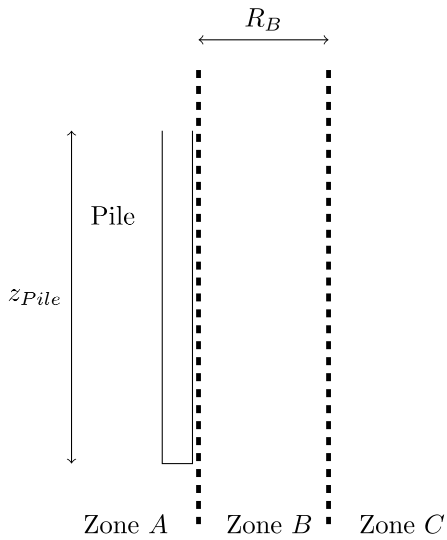

Figure 2.14: Horizontal displacement around the pile: idealized zones, following [130].

by very large shear strains, [103], [119], [148]. Numerical models of pile installation show that the volumetric behaviour of the this Zone depends on the initial relative density of the soil, with compression of the soil in looser samples, and dilation of the soil in denser samples, [159].

Zone B constitutes the soil around the soil annulus which is deformed during the installation, but is not at the interface of the pile. This deformation zone is defined for clay in [130] to establish the extension of deformation during installation, and is useful to define in sand as well. The behaviour of the pile base during loading is also governed by the properties of the soil in Zone B, since the soil beneath and above the pile base is compressed by the installation and consequently has a high stiffness and is also governed by the stress history, [241].

Zone C is the soil far from the pile center, which is not noticeable disturbed during the installation based on deformation measurements, [243], [244], [252]. The behaviour of pile groups which interact are governed by how the stress is redistributed in Zone B and zone C, [82]. The width of this zone defines how large the radial distance of a model show be to avoid boundary effects.

2.10.2 Analysis of stress and strain envelopes in comparison to a normative parameter

The conceptual model of pile-soil interaction is the basis for design. These design methods are based on correlations between a pile load test database and measurements of the soil state, e.g. by cone penetrometer, [119], [130], [148].

For the interface between the soil and the pile, which is located in zone A, the normal stress against the pile is described by Equation 2.8.3.

The effect of friction fatigue gives a reduction of interface normal stress as the pile further advances through the soil. The friction fatigue reduction factor r_{ff} may then be defined, e.g. [183]:

$$r_{ff}(h_y/D_{Pile}) = \frac{\sigma'_{h,h_y/D_{Pile}}}{\sigma'_{h,b}} = f(q_c/p', h_y/D_{Pile}) \tag{2.10.1}$$

where r_{ff} is the friction fatigue reduction factor, $\sigma_{h,h_y/D_{Pile}}$ is the normal horizontal stress at the distance h from the pile base, D_{Pile} is the diameters of the pile, $\sigma'_{h,b}$ is the horizontal normal stress at the pile base.

Deformation $R(z)$ around the pile may then be formulated based on the initial conditions or from the cone resistance:

$$R(r,z) = f(q_c/p', R_d, z) \tag{2.10.2}$$

where R_d is the relative density of the soil, r is the radial length and y is the depth. The soil behaviour is then linked to the cone resistance. This formulation can then be made non-dimensional:

$$\frac{R(r,z)}{D_{Pile}} = f(q_c/p', r/D_{Pile}, z/D_{Pile}) \tag{2.10.3}$$

It is here proposed that the deformation level is mainly defined by what may be called the R_B, or the length of the B-zone, [130]. The layer of soil at the pile-soil interface is assumed to be very small, and consists of some grains and not be dependent of the pile diameter, [148]. The length of the zone B can therefore be described:

$$\frac{R_B}{D_{Pile}} = f(q_c, p', z) \tag{2.10.4}$$

Other possible deformation zones include the main shear zone R_S, and the compaction zone R_C, where the shear strain γ_{yx} and volumetric strain ε_v occur, but these have not previously been analyzed in experimental research.

2.10.3 Stress-strain paths during installation

The behaviour of the soil is represented by many stress paths. Figure 2.15a and Figure 2.15b show conceptual behaviour of the soil during installation. It is consequently not possible to describe the soil behaviour by a single stress-strain curve.

A more detailed analysis has been developed by White, [241] in which the behavior of a specific soil element located adjacent to the pile shaft after installation is followed during the installation. The stress path during installation at specified depths y and radial distance r have also been measured in experimental tests, [128], [127].

Since the soil is displaced during the installation, the soil should be captured in a Langrangian formulation, in which the soil is transported along the displacement. This presents complications for the stress measurements. Horizontal stress measurements normally result in the Eularian type of measurements, i.e. the actual soil is not followed, but the position of the sensor, e.g. [29], [89]. An alternative configuration is an embedment stress transducer system, but the displacement of these sensors are not necessarily the same as the surrounding soil and therefore not a real Lagrangian description, e.g. [85], [119].

Correct Lagrangian stress measurements are possible to conduct with a photoelastic configuration, which requires special soil, [69], [70]. Correct Lagrangian deformation measurements are also possible to carry out with particle image velocimetry (PIV), which is discussed in the next chapter, [238].

2.11 Conclusions

The prototype for the physical model has been specified as a representative sample of rectangular reinforced concrete piles. The parameters governing the behaviour of the soil have been described, and the installation phases discussed, including pre-installation, installation, and post-installation phases. Physical modelling is well suited to study the installation stage, consisting of installation stage 1 and installation stage 2. Experimental measurements and numerical analysis have shown that homogenous elements of soil at different initial position relative to the pile display quite different stress and strain paths. Suitable simplifications are consequently necessary to include in the current modelling approach, since it is not possible to describe the soil response as a homogenous stress and strain path. The large variation in stress path should be taken into account in analysis. Different methods to model the installation stage are described, and physical modelling is found to be a suitable approach.

The aims of the experimental model have been discussed. There are some parts of the current conceptual framework which have not been verified experimentally, and where further experimental research would be helpful. This is specifically the generality and validity of the current methods for different relative densities, the effect of friction fatigue in different relative densities, and the phenomenological description of the components of the horizontal contact stress. The latter governs how scale effects results in different governing mechanisms, and is especially of interest for piles outside the current pile load test database.

The effect of the initial relative density for pile installation effects has been studied in field experiments, e.g. [180]. However, most centrifuge model tests have been conducted in non-homogenous initial relative densities, e.g. [151]. Tests carried out in homogenous samples, e.g. [136], were made in different soil samples, and at different levels of accelerations. There are consequently relatively few model tests, and the results are not conclusive. A larger tests series would therefore be helpful for systematic interpretation.

A larger tests series in different initial relative density is of interest, since the effect of friction fatigue, which alters the average shear stress of the pile, has also been measured at different initial relative densities, [148], [151]. Deformation and stress measurements of friction

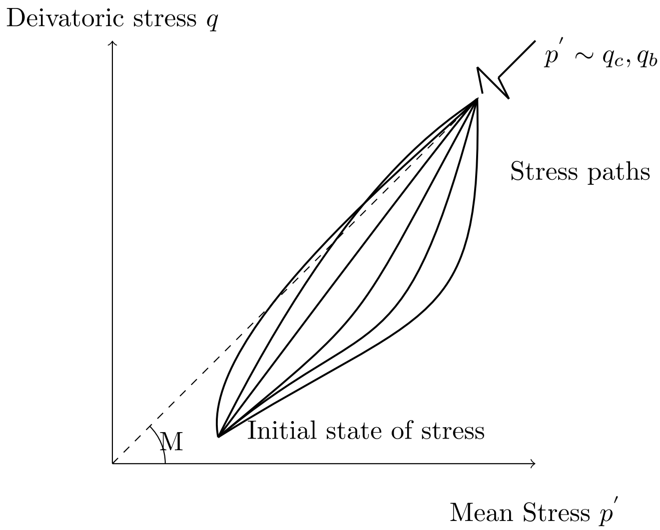

(a) Conceptual figure of variation in stress paths during pile installation, after [241].

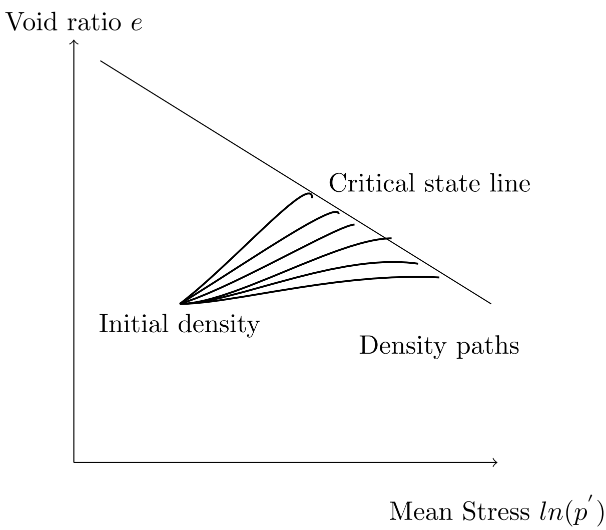

(b) Conceptual figure of variation in density paths during pile installation.

Figure 2.15: Conceptual illustrations of variation in stress and strain path.

fatigue have also only been carried out separately, e.g. [151] and [246].

The components of the horizontal total contact stress $\sigma'_{h,tot}$ have been measured in shear tests and model tests, e.g. [34], [147], and are taken into account in design for large piles, e.g. [150], where the effect of interface dilation is small, [89]. For smaller piles, the dilative component $\Delta\sigma'_h$ can be larger, and is of interest. Especially for computer simulations in which a separate soil-structure interface element is implemented, e.g. [33], [34], a more detailed description of the interface is of interest. A series of tests in different initial relative density is then needed, since the constitutive behaviour of soil depends on the initial relative density.

The deformation zones around the pile have been measured in laboratory tests, [197] and [246]. Normalized measurements have not been systematically presented for different initial relative densities (even though some measurements has been demonstrated, [213]), and the effect of initial relative density has not been measured.

The installation effects also depends on the installation mode, whether the pile is installed in installation cycles or continuously, [151]. The effect of the installation mode is also of interest, especially on the horizontal contact stress after the installation.

The experimental model should consequently be adapted to study these phenomena. In the following chapter, the experimental model is discussed, including the simplification of the prototype compared to the model.

Chapter 3

Experimental methodology

3.1 Introduction

In this chapter the experimental methodology of the physical model tests is presented. First, the aims of the model tests are outlined. Subsequently the relevant empirical and theoretical guidelines for physical model tests in sands are summarized, to assure similarity between the model and the prototype. Appropriate methods of stress and deformation measurements are then discussed. Based on this analysis of experimental possibilities, the model configuration and the test series are finalized, followed by a discussion of the limitations and advantages of the experimental system.

3.2 Aims of the physical model tests

3.2.1 Initial conditions and parameter variation

The soil samples should be modelled at different initial conditions to capture the governing mechanisms, [6], [149]. The current physical model tests are carried out on natural sand with specific material properties presented in the following chapter. State parameters include the mean stress level p' and the relative density R_d. The initial values of these properties are possible to vary in the model tests.

Physical model tests conducted in sand samples with changing levels of relative density with depth include [30], [97], [148], [147], [256]. The non-homogeneity of initial relative density in such tests is a considerable disadvantage for systematic interpretation, since the behaviour of the pile-soil system is a result both of the relative density R_d as well as the mean stress level p', [31], [136].

This effect is exacerbated by the tendency to conduct experimental measurements on small diameter model piles at relatively shallow depths, e.g. [29], [97], [148]. This often results in a stress state p' at corresponding normalized depth L_{Pile}/D_{Pile} which are not comparable to prototype piles.

Physical model tests are possible to carry out at different centrifuge accelerations to scale the model dimensions, e.g. [136], [151], [174]. A disadvantage of these types of tests is that the behaviour of the soil changes with mean stress level p' if the relative density is kept constant, [31]. This can be accounted for by changing the relative density following recommendations for physical modelling in which the state parameter ψ is constant at different stress levels, [6]. A possible disturbance in such tests consists of experimental artifacts in the experimental test set-up, which frequently are a result of the stress conditions and make comparisons of measurements at different acceleration levels cumbersome.

The most practical method to model the soil state is consequently to vary the initial relative density in between the experimental tests.

3.2.2 Modelling the pile-soil system behaviour

The pile-soil behaviour is a result of the development of stress-strain path during installation, described in the previous chapter, [136]. The kinematics and stress evolution during installation stage 1 and 2 are very different. Consequently, the experimental methodology should accommodate different levels of sensitivity to register the whole range of deformation and stress levels.

Experimental aims include an analysis of the penetration response and the subsequent evolution of interface horizontal stress in installation stage 2. This requires combined stress and deformation measurements to capture the stress and density change. It is also suitable to perform a quantification of the mechanism relative to normative parameters such as mean stress level p', relative density R_d, and pile diameter D_{Pile} to aid generalization of the installation effects and comparison to the numerical models, e.g. [96]. The soil surrounding the pile is disturbed during the installation, [130], and the length of the disturbed soil is helpful to define relative to such a parameter, e.g. R_B/D_{Pile} for the length R_B of the disturbed Zone B around the pile, and where D_{Pile} is the pile diameter, [130], [173], [185].

The lateral deformation levels are relatively small in installation stage 2 and the soil-pile kinematic response is dominated by large shear strains at the pile surface, [109], [119], [148], [198]. A variety of horizontal stress distributions have been measured in previous tests, e.g. [148], [187], [231]. Since the shaft friction is governed by the effective horizontal stress $\sigma'_{tot,h}$, experimental measurements of the horizontal normal stress are preferable because of the higher accuracy of such type of sensors, compared to sleeve friction shear measurements in experimental tests, [124], [136].

The possible change in horizontal normal stress as the pile penetrates further into the soil, i.e. friction fatigue, should also be measured, [104], [148]. This physical mechanism is also dependent on the initial relative density, which together with stress level controls the stress and strain paths, and has so far only been studied on soil samples with variation with depth in initial relative density, e.g. [89], [151], [148], [256]. To correctly describe the reduction in shaft friction $R_{ff}(h_y/D_{Pile})$ with distance from the pile tip, h_y/D_{Pile}, measurements

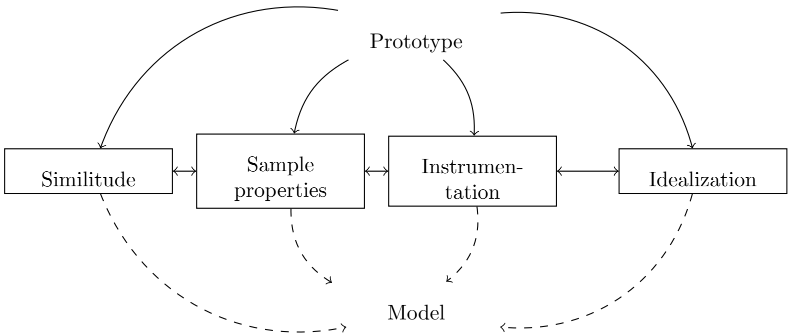

Figure 3.1: Considerations for practical configuration of the model tests which required a compromise between measurement technology and model idealization.

should be carried out at several distances h_y along the pile shaft to capture this specific mechanism, [119].

The fully mobilized horizontal contact stress $\sigma'_{h,tot}$ is exaggerated in small-scale model tests because of significantly increased dilation in the interface shear zone, [34], [85], [83], [88], [136], [148], [147]. The effect of extra horizontal stress $\Delta\sigma'_h$ at the pile-soil interface is accounted for in the current research.

3.3 Experimental approach

Suitable experimental simplification depends on the modelling aims, [250]. It should be pointed out that any experiment is not *objective*, since how and why something is measured is a result of the explicit or implicit assumptions made by the experimentalist, [142]. Figure 3.1 shows the considerations which guide the experimental design, leading to a practical experimental model described at the end of this chapter. The aim of the model is to distill the essential aspects of the prototype to a model through simplification. This is achieved by suitable idealization of the prototype, which must take similitude, sample preparation and instrumentation into account. The aims and configuration of the model should consequently be analyzed in some detail in order to achieve a practical compromise between these often conflicting demands.

3.3.1 Experimental system

A small geotechnical centrifuge system was used to scale the prototype dimensions. The advantage of the centrifuge is that the self-weight of the soil is accurately scaled, [200], [204], while it is possible to prepare soil samples at manageble initial densities, e.g. [85], [136].

This thesis is limited to experimental modelling in the laboratory of displacement pile installation effects in sand. The prototype was described in the previous chapter, and is here simplified to a square 500 mm concrete displacement pile which is installed $10D_{Pile}$ by impact driving (where D_{Pile} is the pile diameter). The prototype should be simplified to achieve a practical experimental model, [217], [222].

The most complicated part of the prototype to replicate is the installation by impact driving, [62], [88], resulting in inconsistency between centrifuge inertial time scale $1/n$ and diffusion time scale $1/n^2$, [222]. A model with dynamic loads also comprise compression wave and shear wave reflections inside the soil sample, [144]. There are consequently relatively few experimental models of structural installation which include dynamic loads, e.g. [5], [38].

Instrumentation of models comprising inertial and consolidation effects is also considerably more complicated, [222]. The instrumentation system is also more prone to disturbances, since such tests require both high data acquisition rate and a large number of pore pressure transducers for accurate pore pressure measurement. The measurement system should therefore include a high performance data acquisition system with a large number of channels, if the inertial and consolidation effects should be modelled.

The experimental tests are consequently carried out in dry sand at a low displacement rate to exclude these effects. It would be possible to separate the inertial and consolidation effects in tests in dry sand, but this was considered to be outside the scope of the current research. Laboratory tests on sand samples show no large influence of strain rate, and these are consequently not taken in account in the test configuration or analysis, [104]. The installation procedure consists of continuous and incremental installation jacks, which corresponds to the installation mechanism of jacked piles, [93]. This model therefore neglects Poisson's ratio effects during propagation of waves in piles, [61].

The limitation of the prototype to a short rectangular pile is also a considerable simplification since displacement piles show large variations in length and diameter, [64], [82]. The experimental model is consequently not valid for other types of piles, especially tubular piles with an inner plug that interacts with the soil, [38], [256]. This simplification is motivated by experimental limitations of laboratory facilities, and results in a relatively straightforward experimental model.

These simplifications result in some differences between the model and the prototype. The prototype installation by impact hammer in saturated soil causes generation and dissipation of excess pore pressure, resulting in changes of effective stresses. These effects are not captured by the model. The inertial effects, such as vibrations, result in stress propagation in the surrounding soil, which has an effect both on the pile itself as well as surrounding piles and structures. The soil response to such load effects is of large interest, but are not captured by the model. The propagation of stress waves are also highly dependent on the specific soil conditions and geometry. It is consequently not suitable to include these in the current model.

3.4 Centrifuge modelling

The rotation of a geotechnical centrifuge creates an artificial centrifugal acceleration which scales the self-weight and the stress gradient of the soil, [200], [204]. The TU Delft centrifuge is a beam centrifuge, in which the soil sample is placed on a platform on the end of the

Factor	$\frac{Dimension_{prototype}}{Dimension_{model}}$
Length	n
Area	n^2
Volume	n^3
Mass	n^3
Stress	1
Strain	1
Displacement	n
Force	n^2

Table 3.1: Relevant scaling factors for drained physical model tests in the geotechnical centrifuge, [88].

centrifuge swing. The scaling factor between the model and the prototype depends on the angular velocity of the centrifuge and the centrifuge arm length, [204], [222]. The magnified acceleration level in the geotechnical centrifuge is frequently described as a multiple n_{cen} of the ratio between the centrifuge acceleration and the earth gravity g:

$$n_{cen} = \frac{R\omega^2}{g} \tag{3.4.1}$$

where R is the centrifuge radius and ω is the angular velocity. A full derivation of the centrifugal acceleration from the angular velocity is given in Appendix B.

The prototype similarity in the centrifuge is described by scale factors between dimensions of the model and prototype. These scale factors are linked to the magnification in acceleration, n_{cen}, and are expressed as a multiple of the gravitational acceleration g. Various catalogues of scaling rules have been established, e.g. [88], [200], [211], [222].

The relatively small model height relative to the centrifuge radius in the current centrifuge results in some variation of the acceleration. This is discussed in Appendix C.

Current physical model tests of pile installation effects were conducted in dry sand. The relevant scaling factors for the current model tests are shown in Table 3.1, [88].

3.5 Similitude

Laws of similarity between the model and the prototype are derived from equilibrium and compatibility equations of the soil at increased acceleration, [88], [222]. Empirical scaling laws are a result of the inherent dualism between the soil grains and the soil mass, [169]. A load in the centrifuge model is distributed among a smaller number of grains compared to the prototype. This results in possible stress concentrations, since a certain number of soil grains are needed to convert the load to a homogenous stress field, [58]. This number is normalized with a certain model dimension D_{Model}, to calculate normalized scaling guidelines in the

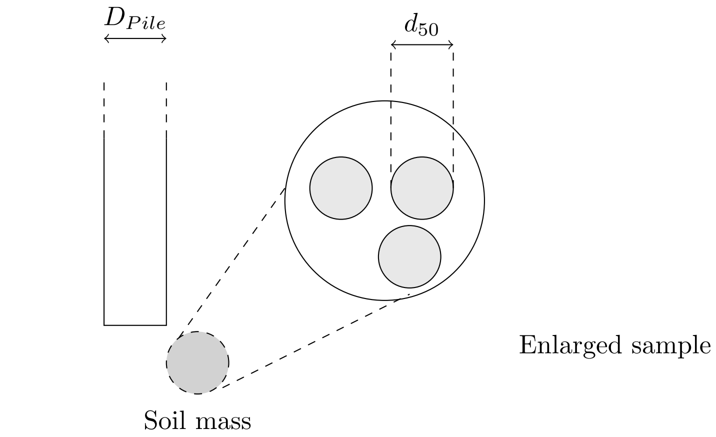

Figure 3.2: The grain-soil mass dualism.

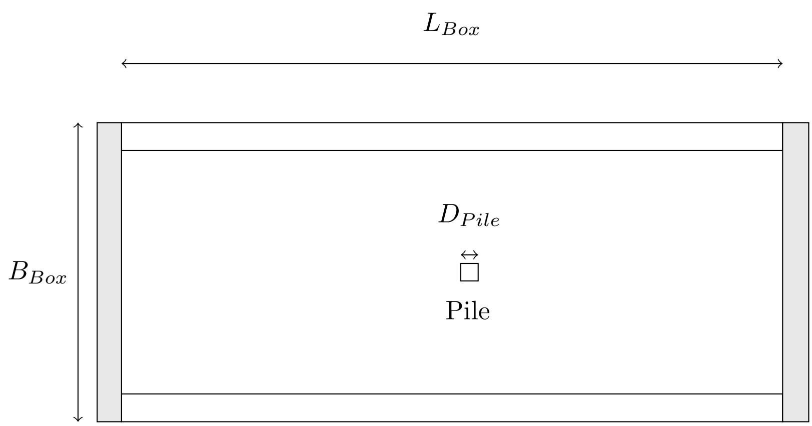

Figure 3.3: Dimensions sample container and model pile.

Dimension	Recommended value
Circular footing	$D_{Footing}/d_{50}$ >35
Strip footing	$D_{Footing}/d_{50}$ >35
Pullout of anchor plate	D_{Pile}/d_{50} >48
Dilation of frictional interface	D_{Pile}/d_{50} >50-100

Table 3.2: Recommended scale value for the pile dimension and mean grain size of the soil, [68], [91], [145], [175] .

Dimension	Recommended value
Distance from boundary	$L_{Boundary}/D_{Pile}$ >10
Diameter of the sample container	$L_{container}/D_{Pile}$ >30

Table 3.3: Recommended scale value for the sample container, [98], [179].

form of D_{Model}/d_{50}, where D_{Model} is the model length, and d_{50} is the mean grain size of the soil, [88].

3.5.1 Empirical scaling laws for the model pile

Table 3.2, shows recommended values of the ratio between the pile diameter and the mean grain size D_{Pile}/d_{50}, shown in Figure 3.2. These recommendations are based on experimental tests on circular footings, [175], strip footings, [91], [145], as well as anchor plates in tension which results in a soil response similar to that of tension piles, [68], [80], [176].

The 10 mm diameter model pile in the current tests results in a D_{Pile}/d_{50}-ratio of 38 with the test sand (described in the following chapter).

3.5.2 Empirical scaling laws for the sample container dimensions

Table 3.3 summarizes recommended scaling laws for the ratio between the length of the box and the pile diameter L_{Box}/D_{Pile}. These recommended values are based on cone penetration tests carried out in the centrifuge, [98], [179].

The equivalent radial distance L_{Box}/D_{Pile} calculated from the rectangular sample container (described in the next chapter) is 12.

3.5.3 Effect of non-scaled dimension of the interface

The size of the interface dilating surface depends on the roughness of the pile surface R_{CLA} and the mean grain size of the soil, d_{50}, [124], [134], and does not scale in scaled physical model tests, [88], [125], [147]. Small scale models consequently display large interface stresses both in the centrifuge or in the calibration chamber, [85], [122]. This should be considered

Dimension	Recommended value
Sensor diameter	L_{Sensor}/d_{50} >12
Stiffness of sensor	$E_{Sensor}/E_{Soilsample} = 1$

Table 3.4: Recommended scale value for the sensor.

when experimental measurements are interpreted, since the confined dilation results in interface stresses dissimilar to the prototype, [88], [148], [147].

3.5.4 Empirical scaling laws for the sensor

The grain-soil mass duality has also an effect on the accuracy of stress sensor measurements, [32], [148]. The scaling rules relating to the sensor are shown in Table 3.4, based on experimental measurements, [92], [206], [220]. Disturbances from low ratios of D_{sensor}/d_{50} include the effect of concentrated load from grains which are very large in comparison to the sensor area, [220], and large grains locked-in during deformation, leading to very large variations in stress concentration, [88], [219].

The stiffness and deformability of the diaphragm also influences the measurements, [133], [177], [220]. Higher sensor stiffness than the soil mass causes over-estimation of the stresses, and a lower stiffness than the soil will cause under-registration of the stresses in the soil mass, [220]. At small strain levels the stiffness of the soil is estimated to be higher, [9], [126].

Arching around the sensor surface likewise changes the stress distribution in the soil at the sensor position. This potentially leads to both over-registration of the stress and lower-registration, depending on the stress distribution, [92], [219]. The normal stress over the sensor area is frequently assumed to be uniformly distributed for sensor analysis, e.g. [52]. This can lead to inaccuracies if the stress distribution is non-homogenous.

3.6 Experimental sample preparation methods

The consistency in the soil sample preparation method depend on target relative density R_d and the mean grain size d_{50} of the soil sample. A practical preparation method for very fine grained sands is slurry mixing, in which the soil is mixed into a slurry, followed by compaction by vibration, e.g. [62]. For soils with a larger mean grain size d_{50}, other preparation possibilities include moist tamping and air pluviation, e.g. [19].

Air pluviation has previously been carried out for calibration chamber tests and centrifuge tests, e.g. [83], [85], [119], [149]. The sample is prepared by pluviating the soil from a predetermined height into the sample container. The height governs the relative density of the soil. A moving sample container is possible to use to increase the accuracy and uniformity of the soil sample, [149].

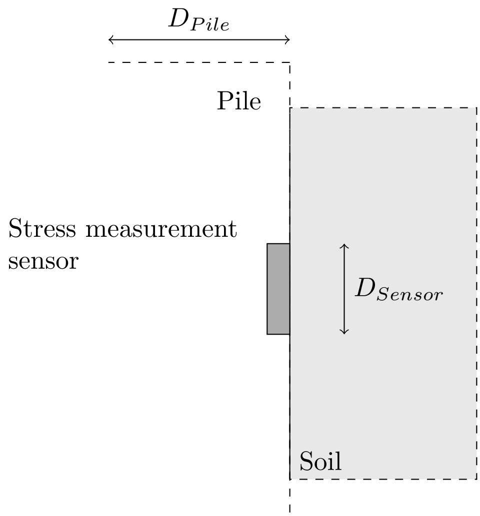

Figure 3.4: Dimensions of the stress measurement sensor.

Since the current experimental tests were carried out in dry soil samples, air pluviation was considered to be the preferred sample preparation method. The sample container was relatively large, and moist tamping was consequently estimated to be relatively time-consuming and potentially resulting in variation of relative density R_d. The possible relative densities resulting from air pluviation were considered to be satisfactory since very loose samples were not modelled. Various possible mechanical set-ups to pluviated the soil into the sample container were assessed, but since the soil sample container was relatively small, the soil was manually sieved into the sample container before densification.

3.7 Design of the measurement system

The measurement system was designed to measure both stresses and deformations in the soil, and will be described in detail in the following two chapters. The design of the measurement system required an extended analysis of possible instrumentation configurations and how these would be suitable for the idealization of the prototype. The resulting measurement system was a compromise between accuracy and space constraints, following Figure 3.1, since the centrifuge model was relatively small.

3.7.1 Measurements of soil stress

A stress measurement system should be accurate and suitable for instrumentation within the small centrifuge model. The possible measurements sensor types comprised sensors located on the pile, or embedment sensors, located in the soil mass, and distributed or local stress measurements.

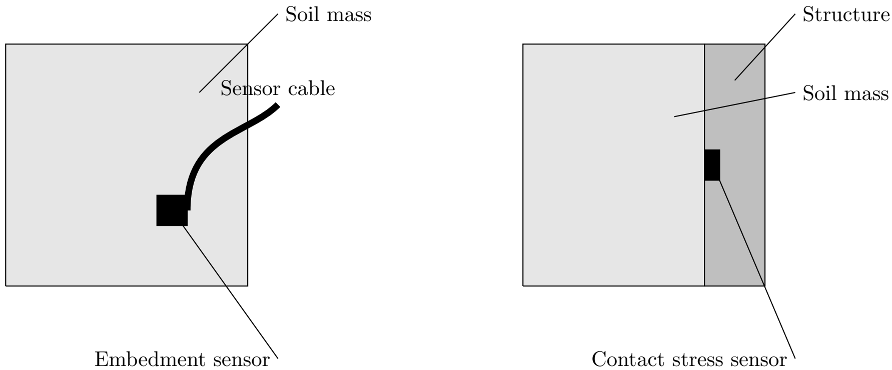

(a) Local stress measurement with soil stress embedment sensor

(b) Local stress measurement with contact soil stress sensor at structure boundary

Figure 3.5: Types of local soil stress measurements

3.7.2 Sensor type

The principle of the embedment stress sensor is shown in Figure 3.5a. The sensor is embedded in the soil mass at a specific location. In contrast, the principle of the contact stress sensor is shown in Figure 3.5b. The sensor measurements are conducted at the surface of a structure.

Contact stress measurements have been carried out at in field conditions in various configurations, [29], [64], [97], [101], [115], [160], [196], [231], [253], [256]. Experimental models have been adapted for the laboratory, e.g. [38], [61], [83], [102], [146]. Embedment soil stress sensor types have been mainly used in the laboratory, [83], [85], [119], [133], [172].

The technology of contact stress measurements is therefore well established, [136]. The alternative embedment stress sensor allows stress measurements within the soil mass, e.g. [119], [172], [224], but has the disadvantage of the interaction between the soil, the sensor, and the wire connections, and possible displacement of the sensors, [133]. The whole embedment stress sensor system should also preferably consist of a relatively large number of sensors to increase the spatial accuracy of the system, [85], [119]. The available space for instrumentation is relatively small inside the centrifuge, and cables to the sensors are also needed in the model. These components do not scale in the centrifuge, and are therefore large in comparison to the model. There is therefore possible interaction between the instrumentation and the soil, [88]. The larger number of output signals from a embedment stress sensor system also results in requirements for high capacity data acquisition system, [119], [222].

Measurements of soil stress on an instrumented model pile are therefore considered more suitable for small scale centrifuge measurements, since they offers the possibility of small instrumentation space and relatively high accuracy. This instrumentation design implies that the stress cannot be measured in installation stage 1, since the soil is then located beneath the pile tip. The stress measurement system should be complemented with deformation

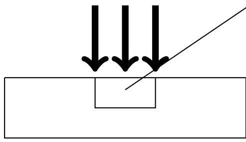

(a) Local stress measurements

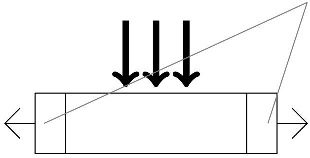

(b) Distributed stress measurements

Figure 3.6: Local and distributed stress measurements

measurements for measuring instrumentation stage 1.

3.7.3 Local and distributed soil stress measurements

A local stress sensor measures the local stress locally at the sensor location, Figure 3.6a. In contrast, distributed stress measurements are correlated from several sensors at different locations, Figure 3.6b. The distributed stress measurement is subsequently inferred from a physical relationship between the sensors, e.g. a stress and strain relationship for an elastic material, e.g. [219].

Shaft friction of piles is frequently measured in distributed measurements by strain gauges mounted in the axial direction of the pile, e.g. [97], [256]. The variation of the external force between the sensors is consequently relatively low between the strain gauges. The average pile shaft friction between two different levels of strain gauges can then be inferred from the difference in axial stress level at the strain gauge levels. Distributed stress measurements are normally conducted by measurements with vibrating wire strain gauges, or electric resistance strain gauges, [107], [231]. The sensors are either mounted on the pile reinforcement bars in the concrete pile, or attached to the surface of a steel pile, e.g. [45], [187]. Various experimental arrangements of distributed soil stress measurement have also been created, such as modular axial strain gauge measurements at large distances and larger number of local measurements in pipe piles, [62], [78].

Distributed measurements of the axial stress distribution in the field are not always accurate, [79], [111], [141], [187]. The large stresses during installation potentially reduces the accuracy of the sensors, [141], and there is also potential strain gauge output shifts, resulting from the installation stress, [78], [187], [256]. Another possible disturbance is the residual load, resulting negative skin friction along part of the pile. The residual stress shifts subsequent measurements if these are normalized with the initial strain gauge output, [36], [111].

The resolution of the distributed shaft friction measurements depends on the spacing of the axial strain gauges. Subtraction of the axial load to calculate the shear between closely positioned strain gauges leads to small differences in comparison to the large base value. The precision of such measurements is relatively low, [256]. Larger strain gauge spacing will increase the electric output precision and resolution of the axial stress measurements, but reduces the spatial resolution of the shear stress measurements, [62], [141]. The axial strain gauge spacing should consequently constitute a compromise between resolution and precision.

Models in the centrifuge are frequently very small and also have a low length to diameter L_{Pile}/D_{Pile} ratio, and instrumentation is consequently cumbersome. Indirect stress measurements with axial strain gauges are therefore considered unsuitable for centrifuge tests if the model pile has a low L_{Pile}/D_{Pile} ratio. The current set-up consists of such as pile, and the measurements system therefore consists of direct stress measurements located at the pile shaft for horizontal contact stress measurements.

3.7.4 Design of the stress sensor for direct stress measurements

The most common mechanical configuration for instrumented model piles is an electric resistance strain gauge configured to a half or a full Wheatstone bridge, [30], [136], [147], [219].

A possible disturbance in all these normal pressure soil stress measurement configurations is the interface between the pile and the sensor, which creates a discontinuous surface at the sensor location, [32], [136]. This discontinuous zone redistributes the loads carried by grains around the stress sensor for very small levels of deformation, [219]. The difference in the roughness of the sensing surface and the rest of the pile could also give a different shear slip mechanism around the sensors, resulting in potential stress redistribution at the location of the sensor.

The stiffness of the sensor governs how stresses are distributed around the sensor location, [220]. The strain is measured by a strain gauge mounted on a flexible diaphragm for a compliant sensor, [92], [113], [206]. Results of measurements with flexible sensors are shown in [129], [168], [172]. To reduce any changes in stress around the sensors, they should have the same stiffness as the soil, and in most cases a rigid sensor with a regulated inner pressure is preferred, [220]. It is not possible to instrument multiple sensors in small scale models, and a preferred solution is a relatively stiff but still deformable membrane, [136]

3.7.5 Adaption of sensor design to the model tests

Based on these considerations, an instrumented model pile with contact stress sensors is a suitable configuration. Restricted space within the centrifuge model makes the embedment sensor system cumbersome to operate, and the low levels of L_{Pile}/D_{Pile} in centrifuge models make axial stress measurements complicated. The sensor should be designed with the same stiffness as the soil and with the same material roughness and geometry relative to the model pile, to prevent potential adverse redistribution of stress.

3.7.6 Measurements of soil deformation

There are many types of configurations for soil optical or thermal soil deformation measurements, [3], [25], [57], [63], [137], [162], [198], [213], [252]. Most of these measurement systems are relatively tedious to install, and consequently do not fit into the centrifuge. The most suitable method is Particle Image Velocimetry (PIV), sometimes called Digital Image Correlation (DIC), [131].

PIV comprises image pair cross correlation between subsections of the image to find incremental displacement of patches (small parts of the total area) of soil with an interpolation algorithm, [131], [237], [238]. The PIV deformation measurement method has been adapted to geotechnical research, [246], and there are many examples of centrifuge models which includes deformation measurements, e.g. [73], [223].

3.7.7 Combination of half-space deformation measurements and 3D stress measurements in the same sample

Measurements of soil deformation with PIV have been carried out in plane strain [73], and half-space configurations, [223]. The half-space configuration consists a semi-symmetrical model in which measurements are carried out at the axis of symmetry, i.e. for one half of the model in half-space, [223]. The advantage of this configuration is the relatively realistic kinematics configurations that are included in the model. Typically, there is space in the remainder of the model for a fully embedded penetration for accurate stress measurements. As a result of the half-space configuration, the deformations can be compared with the stress readings on the structure, since the test was carried out in the same soil sample, even if the conditions where slightly different, [223].

3.7.8 Data processing

The raw image sequence is processed using a PIV algorithm to extract the incremental displacement fields. The program divides the measurement images into smaller interrogation zone, which are correlated with rectangular displacement patches of the same size around the original location, [237]. The interrogation zones are possible to overlap, resulting in an averaged pattern of incremental displacements. Possible sizes of interrogation window are iterated to find a suitable size with regressive reduction in window size, using multi-pass algorithms to minimize integer locking, [237].

3.7.9 Data analysis

The PIV processing results in incremental displacements in-between images. Strain components in two dimensions are possible to calculate from these, [58]. The soil is divided into a grid based on the location of the interrogation windows in the PIV analysis. Shape functions are subsequently used to calculate the strain components in the center of the nodes of the grid which contain the displacement information with an algorithm,[56].

3.8 Description of physical model tests

The experimental procedure of the physical model tests consisted of two tests: (1) deformation measurements in the soil, and (2) contact stress measurements on the pile through a transparent wall during model pile installation in the centrifuge. The layout of the physical model tests in the sample container is shown in Figure 3.7. The deformation measurements were first carried out, with the pile positioned against the Plexiglas window. These measurements were conducted with a non-instrumented pile with a thickness of $0.5D_{Pile}$. The centrifuge was then stopped, and contact stress measurements were then carried out with an instrumented model pile placed in the center of the sample after starting the centrifuge again, shown in Figure 3.7. Both measurement methods followed the test program, which included installation, static pile load test in compression, and a tension test. Continuous and intermittent installation modes were carried out in the tests.

The deformation measurements were carried out with a 5 x 10 mm^2 non-instrumented model pile, which was covered with a plastic layer. The dummy model pile was positioned against the Plexiglas window with the horizontal axis of the actuator. A horizontal aluminum beam mounted on top of the metal frame of the sample container was used to guide the model pile. Care was taken not to remove the lubricant from the sample container window or push soil sample against the lubricated window.

The centrifuge swing lights were then activated, and the camera focus and aperture was adjusted to give a focused image. Both the focus and the aperture were manually controlled on the objective. The camera correction procedures were first carried out with a computer plugged into the in-flight computer and subsequently controlled in the control room. After these procedures were completed, all equipment was controlled and the lights in the centrifuge room switched off and the centrifuge started. The centrifuge was ramped to an acceleration for a specified gravity. At the correct angular velocity, the stability of the mechanical system was assessed. The camera program was then activated and the computer to control the dummy model pile was started. A computer program executed the tests, and afterwards the centrifuge was stopped and the dummy model pile disconnected from the load frame.

The subsequent stress measurements in the centrifuge were carried out in the center of the soil sample, as shown in Figure 3.7. The instrumented model pile was attached to the load frame and the cable from the instrumented model pile was then attached to the data acquisition system. The data acquisition was started with the program *pileheat*, in which the periodic strain gauge measurements were performed, and which is described in detail in the following chapters. The data acquisition of the heat procedures of the instrumented model pile was carried out for at least 0.5 hours before the actual test was started.

Since the centrifuge was restarted, the self-weight of the soil was recycled, resulting in a pre-stressing of the soil, which results in a stress history in the model sample. This possibly changes the initial properties of the soil samples, [151]. However, it was assumed that this effect would be relatively modest, as long as vibrations of the sample were avoided. Measurements of sample height did not show any conclusive volume change between tests.

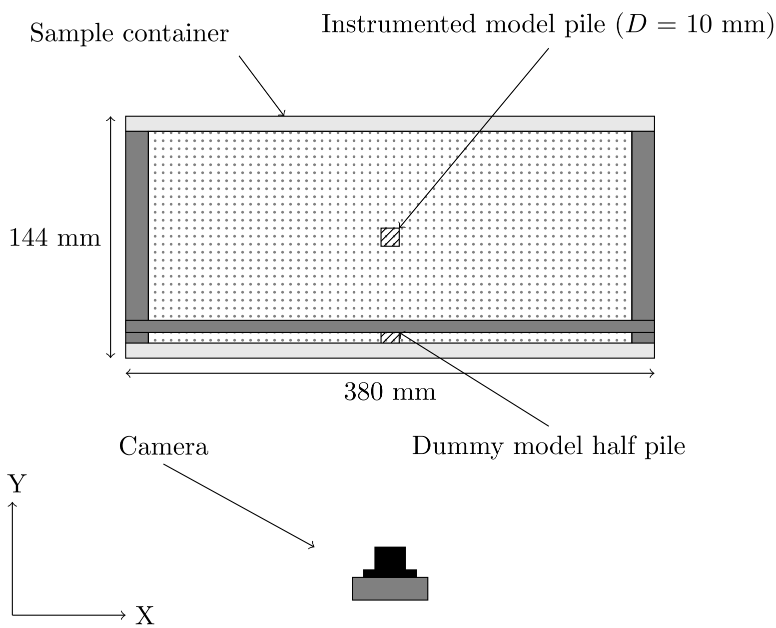

Figure 3.7: Layout of the physical model tests (plane view).

After the centrifuge has been accelerated to the correct angular velocity the test was started. The tests were executed by a computer program. After the measurements had been carried out the centrifuge was stopped and the instrumented model pile was removed from the load frame and dusted of with a wet cloth and paper. The sample container was then transported to the sample preparation room, where the soil was sieved. The sample container was then cleaned with soap and water and dried with paper. It was subsequently air dried for some time before another sample was prepared. The measurements were inspected before the next tests were started.

3.8.1 Test Series

The experimental test series consisted of deformation and stress measurements conducted in loose, medium dense and dense samples. The different installation routines were carried out with the computer programs $Installation - Continuous$ and $Installation - Incremental$. The test series is shown in Table 3.5, where the initial relative density, the type of measurements, and the installation program are shown.

Test type	Initial relative density	Measurement type	Program	Number of tests
$TLDC$	Loose	Deformation	*Continuous*	3
$TLSC$	Loose	Contact stress	*Continuous*	3
$TLDI$	Loose	Deformation	*Incremental*	2
$TLSI$	Loose	Contact stress	*Incremental*	2
$TMDC$	Medium	Deformation	*Continuous*	3
$TMSC$	Medium	Contact stress	*Continuous*	3
$TMDI$	Medium	Deformation	*Incremental*	3
$TMSI$	Medium	Contact stress	*Incremental*	3
$TDDC$	Dense	Deformation	*Continuous*	2
$TDSC$	Dense	Contact stress	*Continuous*	2
$TDDI$	Dense	Deformation	*Incremental*	2
$TDSI$	Dense	Contact stress	*Incremental*	2

Table 3.5: Test series

3.9 Advantages and limitations of the physical model test configuration

3.9.1 Advantages of the physical model test configuration

The aim of the physical model is to capture the effects of initial effective vertical stress level and relative density on pile installation in silica sand. The simplified model allows test execution in consistently prepared samples of various initial relative density.

The physical model is an appropriate idealization of the prototype. Pile installation is modelled by jacking, which simplifies the experimental procedure (avoids scaling issues) and reduces the complexity of instrumentation necessary in the model. The stress wave reflections and the excess pore pressures are therefore not included. Since the model consists of dry sand, it is not necessary to include pore pressure transducers. The dry conditions are also helpful for model execution and sample preparation.

During model testing, the equipment does not need much manual operation, resulting in smooth operating procedures. The low operating cost of the facility allows larger number of tests to be conducted, so that parameter analysis may be carried out, for both deformation and contact stress measurements in the same soil sample.

3.9.2 Limitations of the physical model

The model geometry is somewhat simplified in relation to general piles: the pile is short, and the L_{Pile}/D_{Pile}-ratio is consequently smaller than the prototype piles. On the other hand, displacement piles are frequently not penetrated very far into the the sand layer in layered subs-soils, [64], [82]. This could also influence the stiffness of piles, although prototype piles exhibit large variations depending on the geometry and embedment depth, [148], [181], [256].

Inertial or consolidation effects are not included into the model. This is a suitable simplification given the unattainable instrumentation and boundary control needed to measure these effects reliably, e.g. [62]. The scope of the thesis has therefore been adjusted to the model possibilities.

Chapter 4

Description of the experimental test set-up

4.1 Introduction

Considerable parts of experimental modelling are the build up of a model as well as preparation of a proper sample. The physical model should be reproducible and enough information ought to be provided to repeat the experiment. Hence, in this chapter the experimental test set-up is described. The physical model tests which have been carried out consisted of physical modelling of pile installation in the TU Delft centrifuge. The main parts of the realization of the experiments were the preparation of mechanical and electrical equipment, data acquisition system, camera system and the soil sample. These components of the experimental set-up are described first. Subsequently, the soil sample preparation is described and soil properties are presented from laboratory experiments.

4.2 The TU Delft centrifuge

The physical model tests on pile installation effects were carried out in the TU Delft centrifuge, which is a 1.22 m diameter beam centrifuge. The centrifuge swing and the control beam is shown in Figure 4.1. It consists of a double arm swing system. The swing platform is connected to the centrifuge beam with a hinge. The centrifugal force in the radial direction raises the swing to horizontal position during the test at the used acceleration level ($>20g$). The centrifuge arms consist of rectangular steel beams which are mounted on the central axis with a ball bearing. This is a conventional design for beam centrifuges, which gives an improvement of the original centrifuge system in which the sample was prepared in a vertical position, e.g. [4], [174].

The height of the centrifuge swing is 500 mm, and the length and width result in a base dimension of 450 x 350 mm^2. The swing has four columns and a high strength aluminum base plate. Simultaneous tests may be carried out with samples placed on both swings. If the centrifuge is not balanced by two identical samples, counterweights are placed on the swing

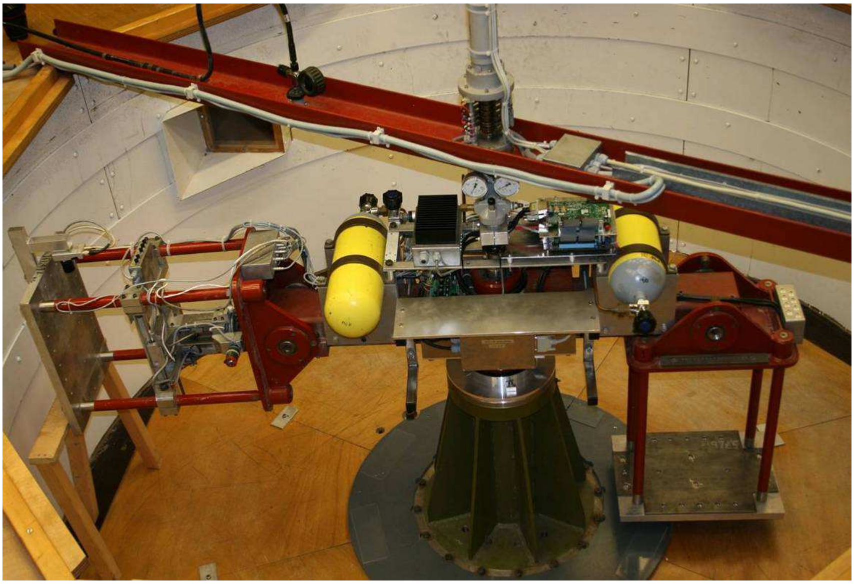

Figure 4.1: The TU Delft centrifuge

opposite to the physical model test. Only one of the swings is used for the current tests. The capacity of the TU Delft centrifuge is presented in Table 4.1. A detailed description of the TU Delft centrifuge can be found in [4].

The laboratory safety precautions are described in Appendix *D*.

4.3 Electrical and communication system

4.3.1 Electrical system

The electrical and communication connections with the centrifuge system at the time of testing are shown in Figure 4.2. The electrical connections are shown in dashed lines. A 12 V DC input voltage is connected to the centrifuge by the slip ring system, shown in Figure, 4.3. The electric supply and data can therefore be maintained during rotation of the centrifuge. This in-flight voltage powers the physical model system and data acquisition system on the centrifuge. The electric voltage is regulated in a small transformation system to suitable voltage for the centrifuge components, seen in Figure 4.2. The actuators are supplied with 12 V DC and 24 V DC, the camera with 24 V DC, the data computer board

Radius	Maximum acceleration	Maximum load at 300g	Maximum capacity	Electrical drive system
1.22 m	300 g	39 kg	120 $g-kN$	13.5 kW

Table 4.1: Details of the TU Delft centrifuge

and data acquisition system and strain gauge amplifiers with 12 V DC and the switching strain gauge supply for the model pile with 6 V DC.

The digital communication system is also shown in solid lines in Figure 4.2. The slip ring system provides a connection between the control room and the centrifuge computer, shown in Figure 4.3. One dedicated connection is used for the VC 5 MP machine vision camera. There is also a wireless connection between the centrifuge and the network. The data acquisition system and the actuator are connected back to the centrifuge computer, for test control and communication.

4.3.2 Centrifuge control software

A dedicated micro-controller regulated control loop controls the centrifuge. This PLC is accessed over a serial port using the program *CUTECOM*. *CUTECOM* sets the PLC of the centrifuge motor.

The centrifuge angular velocity level is measured with a Sharp GP1A50HR photo-interrupter, which is installed between the main support frames of the centrifuge and the rotating centrifuge axis.

The acceleration level at the centrifuge swing is measured by an Analog devices ADXL193 MEMS accelerometer, which is mounted on the bottom plate of one of the swing platform with screws. Before the testing started, the accelerometer was checked at a known angular velocity according to the photo-interrupter, and the acceleration at the location of the accelerometer was calculated. The accelerometer level is measured through the centrifuge data acquisition system to simplify data synchonization.

A National semiconductor LM-60 temperature sensor is connected to the centrifuge to measure the temperature in the room during the tests. The centrifuge tests on pile installation effects were conducted over relatively short test periods, so the temperature was not changing significantly.

The centrifuge facilities are operated from the control room. Standard desktop computers installed in the control room are connected to the centrifuge motor control, the safety cameras, and the physical model test control. The centrifuge control PC is directly connected to the motor control. The computer system for model test control is accessed through the local network via a 32-port switch, which is located in the control room. The safety cameras are also controlled and broadcasted through the network.

4.3.3 Centrifuge actuator control

The experimental model pile is controlled by the load frame, which controls the load rate in the x-axis and y-axis, shown in Figure 4.4a. The vertical load frame consists of an aluminum and stainless steel system, which is translated along a horizontal support frame using a metric spindle. The load frame is a platform for the centrifuge actuators. These actuators move the load frame in the horizontal direction, and a lever attached to the load frame in the

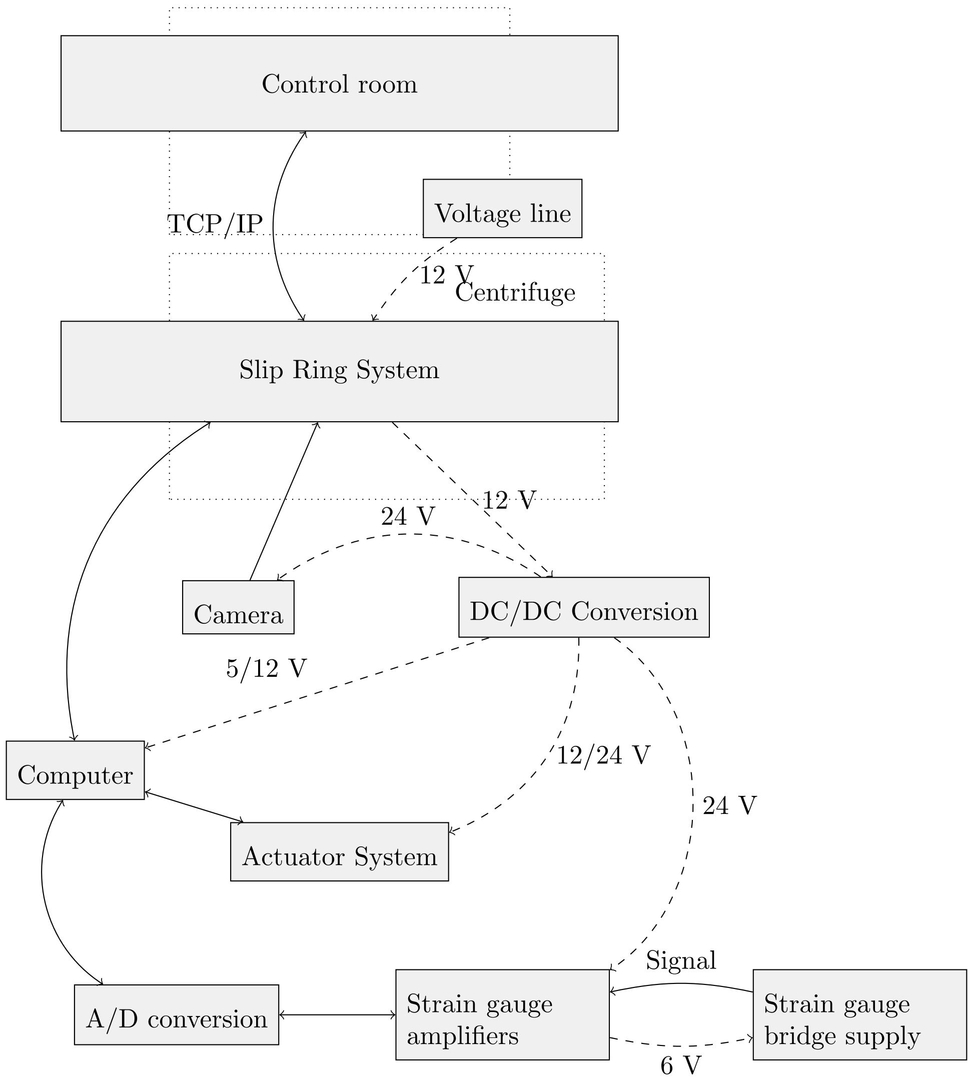

Figure 4.2: Electrical and Communication connections to centrifuge.

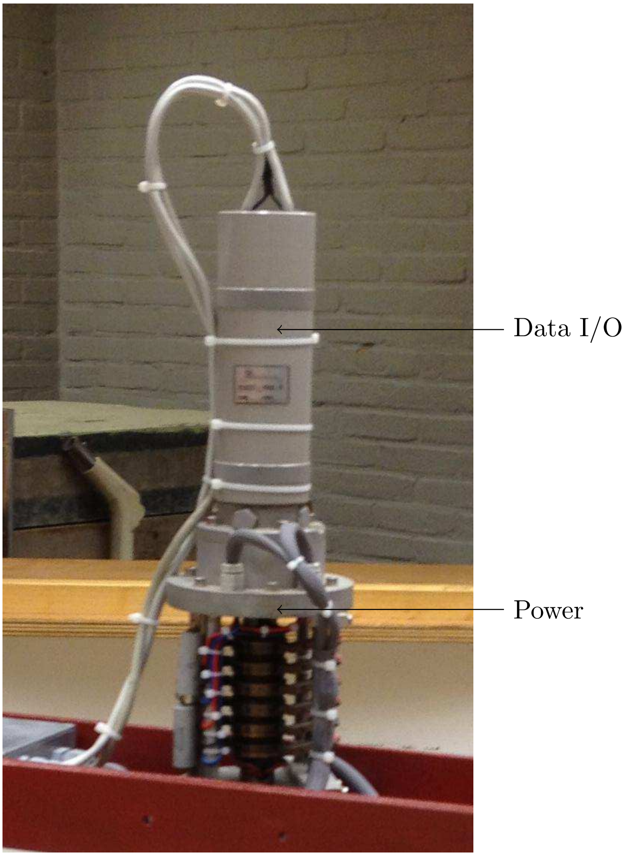

Figure 4.3: Centrifuge slip-ring system.

vertical direction. The instrumented model pile is attached to this lever. The whole system acts as a reaction frame, in which loads applied on the model are resisted by the load frame through its connection to the centrifuge swing.

The horizontal and vertical actuators are powered by electrical motors in combination with gearboxes, which operate in the horizontal and vertical direction. The gearboxes are installed on the motors to give the system a suitable rotating speed and torque. The electric motor systems are shown in Figure 4.4.

The horizontal axis uses Maxon Amax32 GP32A 15 W 24 V DC motor with a GP32A 2ST KL gearbox. This specific motor system gives a 2.25 Nm Torque and a horizontal rate of around 0.5 mm/s. It is connected to the spindle with a series of gears. The horizontal actuator is relatively slow and was not designed for high rates, but mainly positioning.

The vertical axis uses a Maxon RE40GB KL2WE 150 W 12 V DC motor with a GP42C 2ST KL gearbox. The electric motor is installed in a horizontal position and it connected

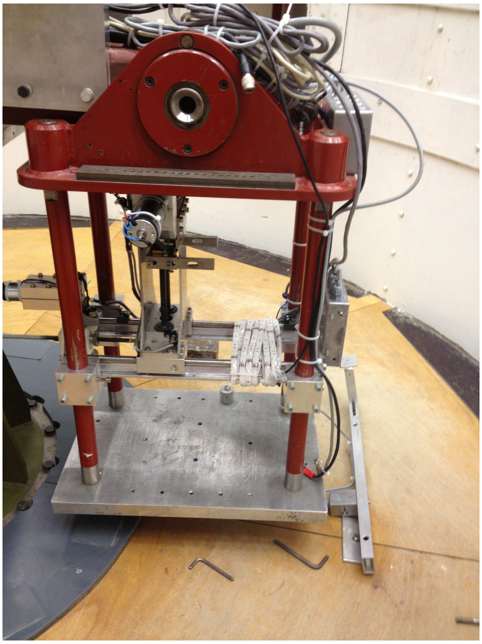

(a) The centrifuge load frame system on y-axis.

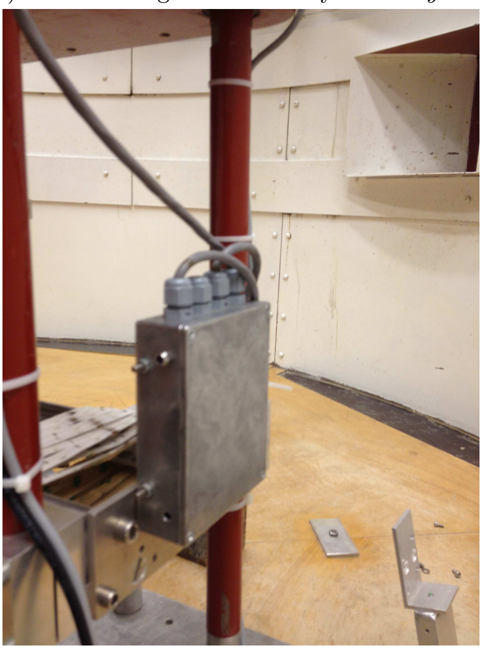

(b) The manual centrifuge actuator control.

Figure 4.4: The load frame actuator system and the manual control box.

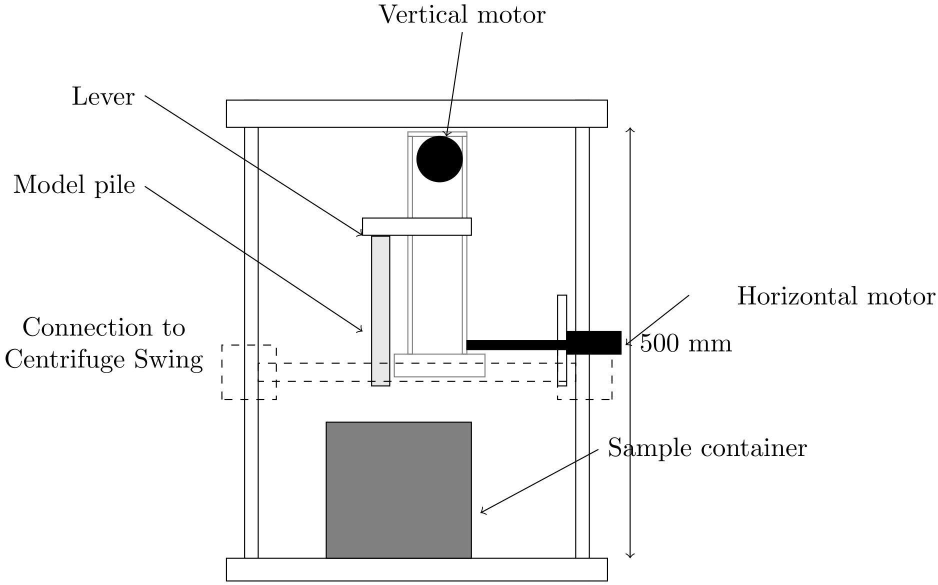

Figure 4.5: Principle sketch of the load frame installed in the centrifuge swing.

to the moving lever by gears and a metric spindle, which converts the torque into a vertical translation. This system gives a 7.5 Nm torque and a maximum vertical rate of around 1 mm/s.

The actuators may be operated either from the control room by control software, or by manual control in the centrifuge room. The manual control consisted of a micro-controller which is installed on the end of the centrifuge swing, shown in Figure 4.4b. The displacement is measured by pulse-meter of the digital mtor, which specifies the vertical location relative the original position. The motor speed during manual operation was set at a low level of around 0.2 mm/s.

Safety switches to stop the electric motors are installed at both ends of the horizontal and vertical axis on which the load frame moved.

The physical model test control is carried out by computer software, which is run on the centrifuge flight computer. The centrifuge computer is an ASUS ITX atom computer board system that is installed on a platform on top of the centrifuge beam. A solid state hard disc is also installed beside the computer.

The computer programs for physical model tests are written in ANSI C. These programs control the actuators and sample data from the sensors, including the accelerometer. The data aquisition of the analog signals uses a National Instruments DAQ card mounted on the centrifuge beam.

The physical model tests were controlled by the programs $Installation - Continuous$ and

Component	$Installation - Continuous$	$Installation - Incremental$
Installation rate (mm/s)	0.25	0.25
Load test rate (mm/s)	0.01	0.01
Pull rate (mm/s)	0.25	0.25
Installation to target depth (100 mm)	x	x
Installation Cycles		x
Removal of pile head load at target depth	x	x
Pile load test to $0.2D$	x	x
Pull test in tension (to $0.5D$)	x	x

Table 4.2: Stages of the installation programs.

$Installation - Incremental$. The content of the programs are shown in Table 4.2.

The $Installation - Continuous$ was programmed to continuously install the model pile, while in the program $Installation - Incremental$ the pile was cyclically installed in predefined installation incremental lengths. The installation increments consisted of displacement controlled penetration at the installation rate to a specific depth of each cyclic interval. The pile head was then unloaded to the initial weight of the pile hanging in the air, which included the self-weight of the pile. The pile was subsequently installed to the target incremental depth with displacement control. The next incremental depth was specified in the beginning of each load step. Piles which exhibited larger rebound lengths would therefore have a larger number of cycles, compared to piles which displayed a smaller rebound. The program measured the number of cycles. The last cycle was stopped at the target installation depth which was specified in the program.

After the target depth was reached, the pile head was unloaded to the initial weight, which included the self-weight of the pile. A static pile load test to a $0.2D$ displacement was then carried out at a 0.01 mm/s installation rate. This static pile load test included loading and unloading of the pile. The pile was subsequently retracted in a pull test in tension at the same rate as during the initial installation. The pull load test was stopped at the initial depth of the pile before installation plus $0.5D$.

4.4 Data acquisition system

Data acquisition in the physical model tests was carried out directly on the centrifuge flight computer through the National instruments PCI bus data acquisition card. A schematic image of the data acquisition system is shown in Figure 4.7. The data acquisition was controlled by the centrifuge computer, an Asus ITX computer board, and stored on an Intel 64GB solid state drive. These were both installed on the instrumentation board located on top of the beam of the centrifuge, shown in Figure 4.6.

The transducers were connected to the amplifiers and the data acquisition system through a switch box located on top of each centrifuge swing. The instrumented model pile was connected directly to the data acquisition system by a cable connected to the pile and secured with tie-wraps on the top of the centrifuge swing, and the rest of the sensors were connected through the box.

Physical model tests consisted of a load controlled or a displacement controlled test program that was controlled by the actuators in the load frame. The control software was run on the centrifuge computer, which was accessed remotely by the network connection through the slip ring system, shown in Figure 4.3 and Figure 4.6. All the sensors were therefore directly accessed on the centrifuge, and the measurements were processed from analog to digital and saved on the centrifuge computer.

Analog measurements were conducted by the sensors through the 16 channel amplifier system that was installed on the centrifuge beam. These channels had a manually switchable 1-10000x amplification system. These measurements were then sampled by the National Instruments PCI-6221 data acquisition board, shown in Figure 4.6, and converted to digital form by the A/D converter in the data acquisition board.

Physical model tests involving load control required digital input values. These were provided by the A/D converted to digital form, after the analog signal had been sampled through the amplifier system, shown in Figure 4.6. The hardware and software components of the physical model control program therefore needed to be coordinated to provide suitable sampling intervals for the program sequence.

At the end of the centrifuge swing a machine vision camera was installed, which was digitally connected to the control room through the slip ring system. The machine vision camera contained a small processor in which image processing took place. The image capture programs therefore run directly on the camera. The images from the camera were sent to a computer in the control room in digital form through the network connection.

4.5 Camera System

The camera system consists of a 80 x 40 x 20 mm^3 Vision Components VC4012nano machine vision camera attached to the centrifuge swing for in-flight image capture, Figure 4.8. The camera is equipped with a Sedeco 8 mm C3M0814 C-mount lens. Network connection to the control room is provided through the slip rings and camera control is carried out through a computer in the control room. The camera is controlled by image software run on the camera computer, which is actively broadcasting video images. These are captured by an external program run on the control room computer.

The camera is equipped with a 1/2.5" CMOS sensor with a 2592 x 1944 pixel^2 resolution. The maximum frame rate is 11.6 FPS, output is generated through a 10/100 TCP/IP Ethernet interface. Data acquisition is controlled through the camera control software which is run on the 3200 MPIS 400 MHz Texas Instrument TMS320C64 processor, and converted into the output digital form with a 1x80 MHz 12 bit A/D conversion. The camera is equipped with 64 MB SDRAM memory.

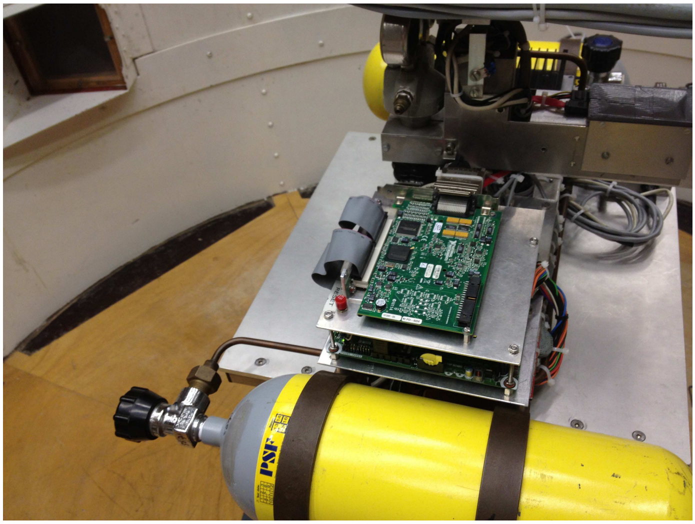

Figure 4.6: Data acquisition board mounted on centrifuge beam

The camera is connected to the 24 V Power supply and the 6-Pin Ethernet connection through cables secured by tie wraps and wrapped around the centrifuge swing column. The camera is mounted on a metal frame which is screwed onto the bottom of the centrifuge swing and equipped with a flexible screw connection that permit vertical adjustment of the camera height, shown in Figure 4.8.

4.6 Data analysis procedures of images

Image processing was carried out on the camera images, with the aim of calculating incremental displacements, displacement paths, and strain fields from the images. The image preprocessing consisted of image preprocessing with the program imageJ, correction of lens distortion, Particle Image Velocimetry (PIV) analysis with the program JPIV. Finally, post processing of the images was carried out with the custom made MATLAB code JPath and JStrain, to calculate the displacement paths and strain fields, based on the displacement increments from the PIV analysis. Figure 4.9 shows a flowchart diplaying the procedures in the image analysis sequence.

4.6.1 Data analysis in imageJ

The images were first pre-processed with the program ImageJ, which is a general image analysis program, [209]. The colour version of the centrifuge camera VC4012nano, which was used in the tests, captures image pixels through a Bayer filter, which creates a 2x2 grid of two green, one red and one blue pixel for recreation of color, [17]. This image pattern was found to influence the PIV analysis, and was removed by a Band pass filter with 2 x 2 pixel minimum size and 39 x 39 pixel maximum object pixel size in imageJ, [209]. The contrast

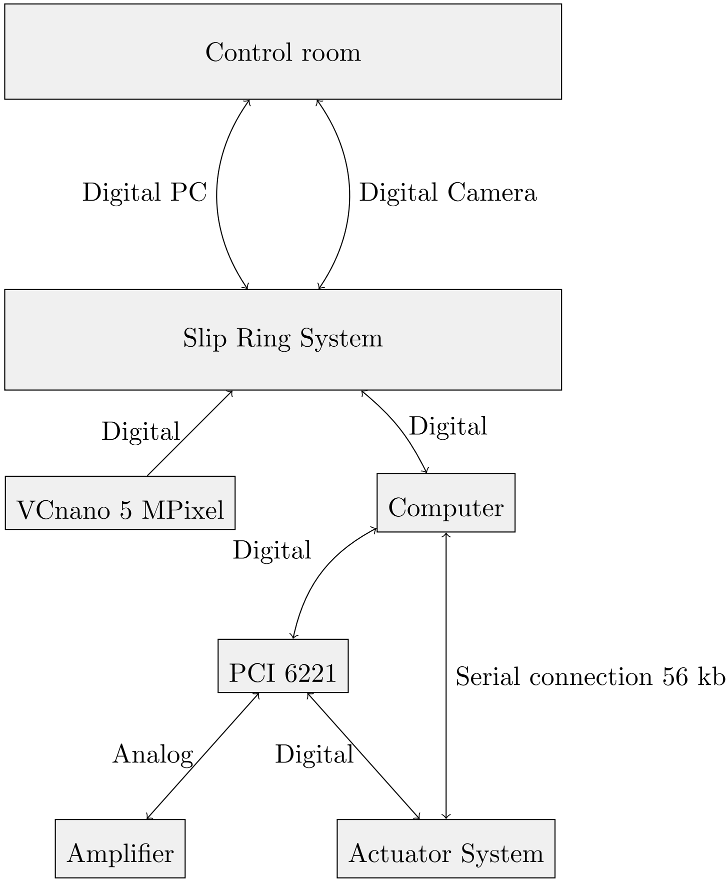

Figure 4.7: Data acquisition system.

is subsequently normalized to the average intensity histogram of the whole series of images, and then partially cropped to the area of interest to reduce processing time in JPIV.

4.6.2 Correction of lens distortion

Lens distortion occurs in most camera objectives and should be corrected to find the correct pixels positions in image analysis, [236]. The most common lens distortion components are radial and tangential distortion, which transforms positions of pixels in the images to new locations as a result of the properties of the lens and camera system. These may be corrected by a computer algorithm, based on a description of the intrinsic lens system, combined extrinsic image data. This extrinsic image data consists of measurements of image positions in comparison to the real positions. This information is obtained by placing control points with known locations on the real object when the images are captured. These locations are then compared with the pixels positions found in the images, [106].

The images are processed in MATLAB with the camera calibration toolbox, created by

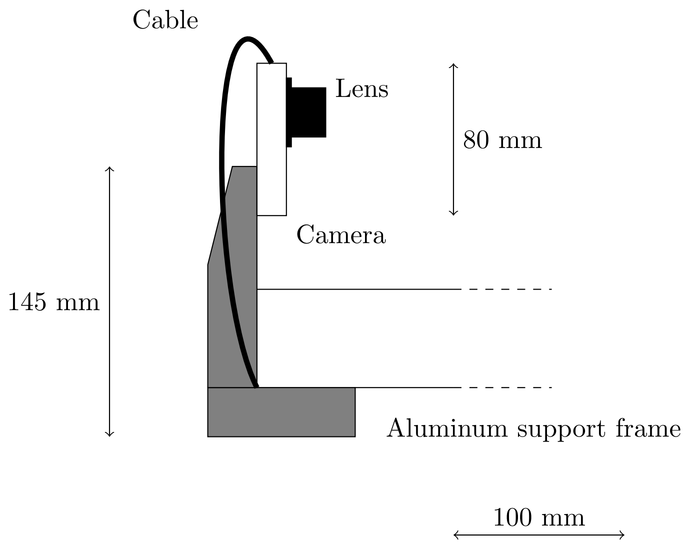

Figure 4.8: Camera connection to centrifuge swing.

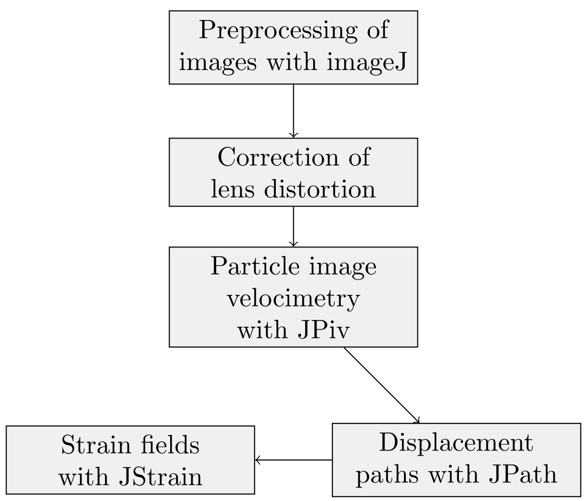

Figure 4.9: Flowchart of components in image analysis.

Heikkila, [105]. The intrinsic components in the program are derived from the C3M0814 lens (8 mm focal length) the size of the CMOS sensor (1/2.5"), in the VC4012nano camera, and the total image size in pixel (2592 x 1944). The extrinsic data are calculated from the image correction points, consisting of twelve 2.5 mm diameter markers had been mounted on the Plexiglas window of the sample container, similar to method in [240]. The markers are black with a white outer circle around the center, with the design specified to simplify image analysis. The marker distances were measured carefully, and used in the extrinsic image information. The distorted marker locations were found by binary image analysis in MATLAB, [161].

The locations of the markers in the image and in the model could then be inserted into the extrinsic system formulation of the camera. The camera distortion coefficients were retrieved using the iterative method contained in the camera calibration toolbox, [106]. These calibration distortion coefficients could then be inverted, to derive the correction coefficients.

The corrected image pixels locations could subsequently be found with the camera calibration toolbox by sub-pixel interpolation of the corrected image to retrieve the updated image pixel positions according to the correction coefficients. The camera correction coefficients were based on the initial distortion analysis of the first series of images. The calibration procedure was therefore not repeated for the whole series of images.

4.6.3 PIV analysis

The PIV analysis was carried out with the program JPIV, [229]. The JPIV procedure consisted of a four passes of PIV analysis with reducing window size, with a 25% overlap between the image windows. The normlized median tests was run between each PIV series to reduce array outliers, [239].

4.6.4 JPath

The displacement paths were calculated with the program JPath, implemented in MATLAB [161], and consisted of analysis of the displacement increments. This program interpolates the displacement increments, and creates displacement paths. These consists of the continuous displacement increments, which are interpolated between the displacement increments of the images.

4.6.5 JStrain

The strain components in the triangular elements could be calculated with the MATLAB code JStrain, [161]. This program calculated the strain components from linear strain triangles.

A detailed description of the image analysis software is outlined in Appendix G. A development of a cross-triangular strain element for calculation of strain components based on the displacement increments is discussed in Appendix H.

d_{50}	d_{60}	d_{10}	C_u	G_s	e_{max}	e_{min}	ϕ_{cs}
0.265	0.277	0.174	1.6	2.6457	0.523	0.823	31

Table 4.3: Soil properties of the test sand.

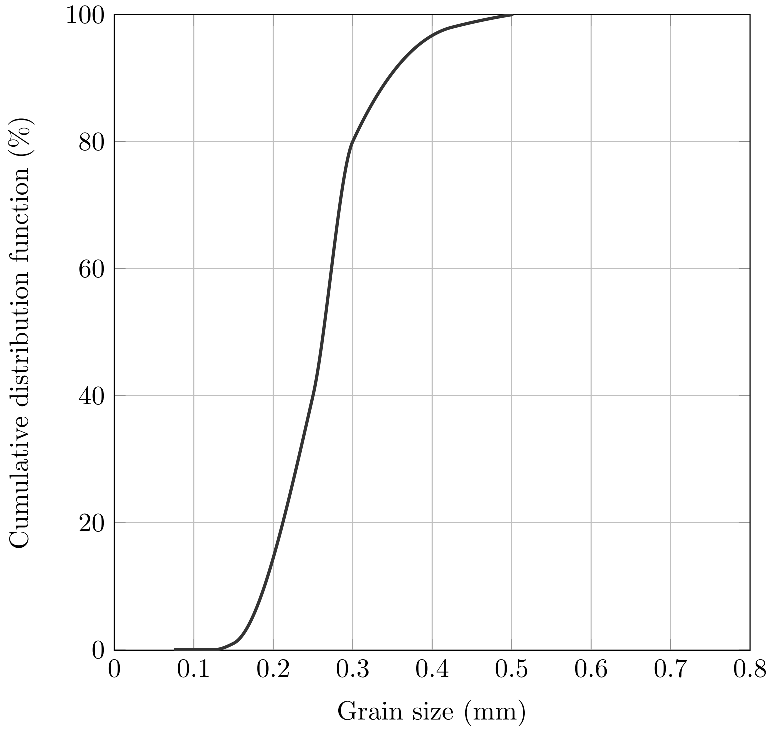

Figure 4.10: Particle size distribution of the test sand.

4.7 Soil properties

The physical model tests were carried out in silica sand samples. The specific properties of sand are known to have a large influence on the soil behaviour, e.g. [19], [31], [136]. The soil properties have been analyzed in the laboratory to provide an accurate description of the soil, and to assist interpretation of the soil relative to the conceptual model of soil behaviour.

Soil properties are presented in Table 4.3. The maximum and minimum void ratio was determined according to the Japanese Geotechnical Society (JGS) procedures, [55]. The specific gravity of the soil was determined with a MagnaChrome Ultrapycnometer. The particle distribution of the soil was determined by a Haver and Boecker Haver EML digital plus sieving machine, and is shown in Figure 4.10. The critical state friction angle was determined from drained triaxial tests in [2].

Figure 4.11: Image of soil in microscope.

4.7.1 Mineral content

Soil grains were studied under the microscope for qualitative analysis of the particulate properties. Figure 4.11 shows a Leica microscope image at 50x magnification including overhead illumination of the grains. The dominant mineral types in the soil assembly are quartz and feldspar. Images of the soil grains at various magnifications are provided in Appendix F.

The grain mineral content was analyzed with X-ray diffraction in a Panalytical Axios Max WD-XRF spectrometer and SuperQ5.0i/Omnian Software. The analysis showed that the sand consisted of 98.832% SiO_2, 0.587% Fe_2O_3 and 0.252% Al_2O_3. The remaining compounds were beneath 0.14% of the grain mineral content. Analysis of the grain mineral content was also carried out with a Bruker D5005 diffractometer and a Huber incident-beam monochromator and Braun PSD detector which confirmed that the major mineral in the soil was quartz (SiO_2).

4.7.2 Grain shape

The shape properties were analyzed from microscope images of the soil, shown in Figure 4.12. The image was analyzed following the procedures described in [43], [156]. The $Particles8Plus$ plugin in ImageJ was used to analyze the particle shapes, [156], [209]. In this program, the roundness R and sphericity S are defined as:

$$R = \frac{4A_c}{\pi L^3_{maximum}} \tag{4.7.1}$$

R	S	ρ
0.624	0.544	0.584

Table 4.4: Grain shape properties of the test sand.

$$S = \frac{R_i}{R_c} \tag{4.7.2}$$

where A_c is the area of the soil grains in the photographs, $L_{maximum}$ is the length of the maximum axis, R_i is the radius of a circle inscribed within the soil grains, and R_c the radius of the circle which is centered at the centre of the mass of the grain and includes the whole grain in the image. In addition, the regularity of the soil grains is defined as:

$$\rho = (R + S)/2 \tag{4.7.3}$$

where R and S are the roundness and the sphericity. This parameter represents the variation from a circular shape in two and three dimensions, [43]. The roundness and sphericity was calculated on 172 particles. The average values are shown in Table 4.4, which also includes the average regularity (ρ). The coefficient of variation $COV_R = \mu_R/\sigma_R$ was 0.15.

The soil shape is categorized as rounded, following the guidelines in [254]. The average aspect ratio was 1.47. The surface roughness of the soil was not analyzed. Based on previous experience with silica sand, an average surface smoothness of comparable silica sand is 0.5 - 0.8, [43]. Formulas for calculation of the maximum and minimum void ratio e_{max} and e_{min} for sands which are moderately uniformly graded have been described by Youd, [156], [254]:

$$e_{max} = 0.554 + \frac{0.154}{R} \tag{4.7.4}$$

$$e_{min} = 0.359 + \frac{0.082}{R} \tag{4.7.5}$$

Where R is the soil grain roundness. The maximum and minimum void ratio e_{max} and e_{min} were calculated with $R = 0.624$, resulting in $e_{max} = 0.801$ and $e_{min} = 0.491$. This resulted in a difference between the computed and measured value using the JGS procedure of 7% for e_{min} and a difference of 3% for e_{max}. The measured maximum and minimum void ratios are therefore in relative agreement with the calculation according to [254]. Another slightly different formula was presented in [203]:

$$e_{max} = 0.615 + \frac{0.107}{R} \tag{4.7.6}$$

$$e_{min} = 0.433 + \frac{0.051}{R} \tag{4.7.7}$$

These formulas results in $e_{max} = 0.786$, and $e_{min} = 0.514$, giving similar predictions for the e_{max} and e_{min} as [254].

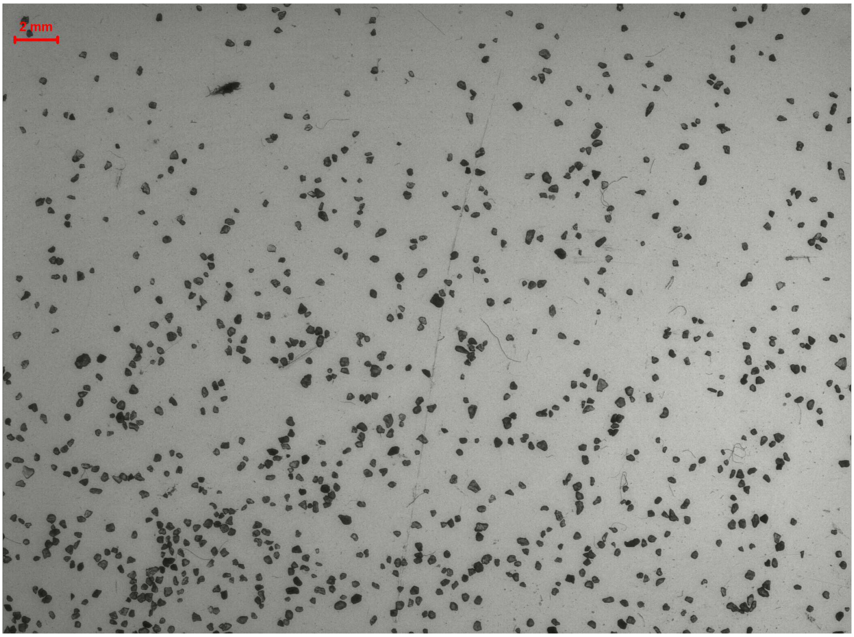

Figure 4.12: Image of test sand grains for analysis of grain shape.

4.8 Sample preparation

One of the aims of the physical model tests was to assess the influence of varying initial relative density. To realize this in the experimental tests, soil sample preparation was carried out at three different initial relative densities. Loose and medium dense soil samples were prepared by pluviation from two different pluviation heights, while the dense soil sample was prepared with a combination of air pluviation and vibration of the strongbox.

4.8.1 Sample container

The soil was prepared in a specially constructed sample container, shown in Figure 4.13. This sample container consisted of a 14 mm aluminum bottom plate, two 14 mm aluminum end plates, and was enclosed with a 12 mm Plexiglas window along the length of the sample container. The internal dimensions of the sample container were 380 x 144 x 150 mm^3. Inside the Plexiglas windows small markers were inserted for correction of image distortion through the lens system. These markers consisted of black circles inside a white circular edge. The edges were marked to improve edge detection and simplify automatic processing of lens correction, [240].

4.8.2 Sample preparation procedure

The sample procedure is shown in a flow chart in Figure 4.16. The sample was prepared at loose, medium dense, and dense initial conditions, shown in Table 4.5. Preparation of the soil sample for physical model tests consisted of a sequence of steps. First the soil sample

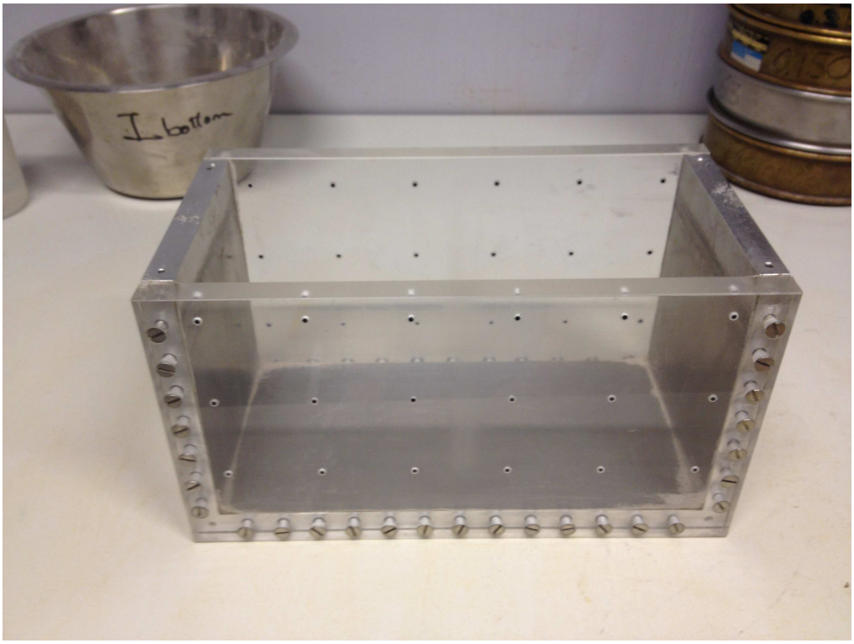

Figure 4.13: Sample container

Sample	Relative density
Loose	0.4
Medium Dense	0.6
Dense	0.8

Table 4.5: Initial relative density of test samples.

container was cleaned, and the Plexiglas windows smeared with Vaseline grease. The container was then placed on a Mettler PM30-K 30 precision scale with ±1 g accuracy [164], and filled with soil by the method of air pluviation. Air pluviation was performed with a small tray which could be moved across the surface of the soil, and which reversed to reach all the boundaries. The pluviation height was measured with a ruler.

After the air pluviation procedure, the volume and the weight of the sample was measured. The relative density of the soil was then calculated based on the specific gravity G_S of the soil and the maximum and minimum void ratio. If the relative density was within the desired range, the soil was carefully manually transported by hand to the centrifuge room. After transport the volume, hence relative density, was subsequently calculated again, based on height measurements at six locations around the soil container. The extra preparation of the dense soil sample consisted of vibration of the specimen.

The sample was pluviated from a small soil vessel situated at a specified pluviation height, shown in Figure 4.14. For the loose soil sample the pluviation height was as small as possible

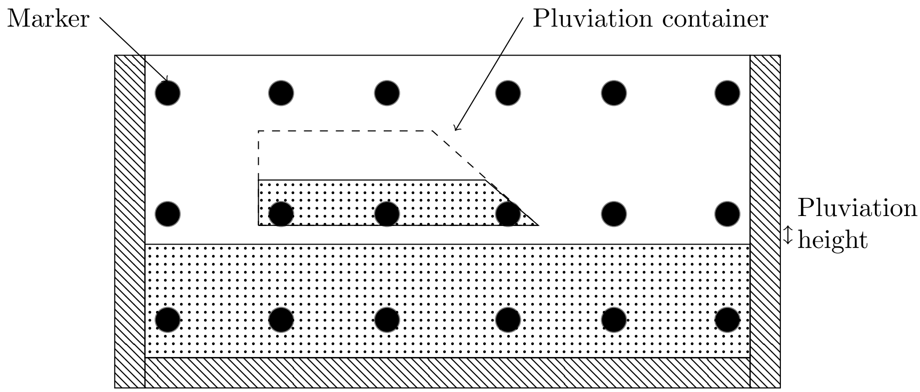

Figure 4.14: Pluviation height in sample container.

without touching the soil surface, approximately 10 mm - 20 mm. For the medium dense soil sample the target pluviation height was 120 mm. The dense soil sample the soil was first pluviated from 120 mm height. It was subsequently compacted in a Haver and Becker EML vibrator for six minutes by harmonic excitation with 2 mm amplitude. The soil container fixed to the vibrator is shown in Figure 4.15.

The sample preparation procedure for the dense soil sample is discussed in Appendix *E* and an analysis of the homogeniety resulting from the preparation method is made.

The experimental test consisted of deformation and stress measurements tests. Possible change in height of the soil sample at different locations in the sample container was carried out to assess the effect of density change. After the centrifuge tests, the sample container was removed from the load frame and transported to the preparation room and weighted. The soil was subsequently re-sieved to remove any larger pieces, and any influence of the experimental tests. After the re-sieving, the soil was mixed with the source sample inside a large sample container. The whole preparation-testing-removing procedure is shown in Figure 4.16.

4.9 Summary

The experimental set-up has been carefully reviewed in order to demonstrate experimental rigour. The experimental set-up was mounted in the TU Delft centrifuge, which included installation for electrical and communication systems. The installation of electric control motors and camera control are controlled by custom-made software. The experiments tests are steered by a computer program that include the pile installation, the pile load test and the extraction test. The image analysis procedure consists of a series of programs that corrects lens distortion, conducts Particle Image Velocimetry (PIV), and interpolates the displacement increments to construct displacement paths. Soil properties include the grain shape and mineral content. The sample preparation procedure consists of a series of steps before and after the test, and is repeated to achieve sample control.

Figure 4.15: Soil sample mounted on vibrator

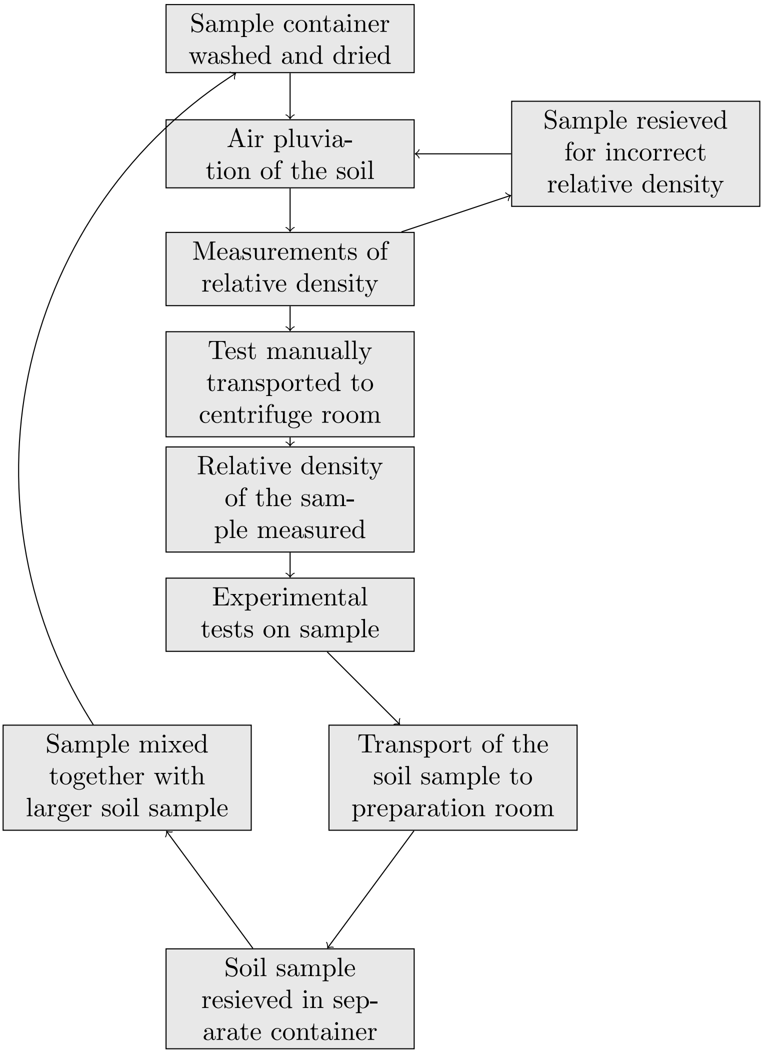

Figure 4.16: Flow-chart of sample preparation procedures.

Chapter 5

Design and realization of an instrumented model pile

5.1 Introduction

Experimental measurements of installation effects comprise measurements of the stress state in the soil adjacent to the pile, both during and after installation. Accurate instrumentation for the measurement of contact stress on the model pile is therefore of great interest to study the installation effects.

Experimental studies of soils show that the mechanical behaviour of soil is governed by the effective stress level σ' as well as the relative density R_d of the soil, [250]. This chapter is limited to the description of stress measurements in soil, carried out on dry sands with relatively high permeability. This implies that total stresses are equal to the effective stresses, and the measurement system therefore measures the total stresses, hence effective stresses, in the soil.

Total stress measurements are known to have relatively low accuracy, both in the field and in the laboratory, [141], [148]. The reason is the large number of factors that influence these measurements, such as the sensor geometry, the structure in the soil, as well as scaling of the model, [136], [219]. Such measurements should be carried out in a properly designed testing program to reduce potential measurements errors.

A systematic and rigorous experimental approach includes both a practical mechanical realization of the measurement system, as well as an analysis of the accuracy, precision and resolution of this system. Accurate calibration of the measurement system in conditions comparable to the experimental setting is therefore helpful to achieve robustness of the measurement system.

In this chapter the mechanical realization of an instrumented model pile is described. The mechanical and electronic configurations of the model pile, as well as the theoretical and practical considerations for the design of such a measurement system are presented and discussed.

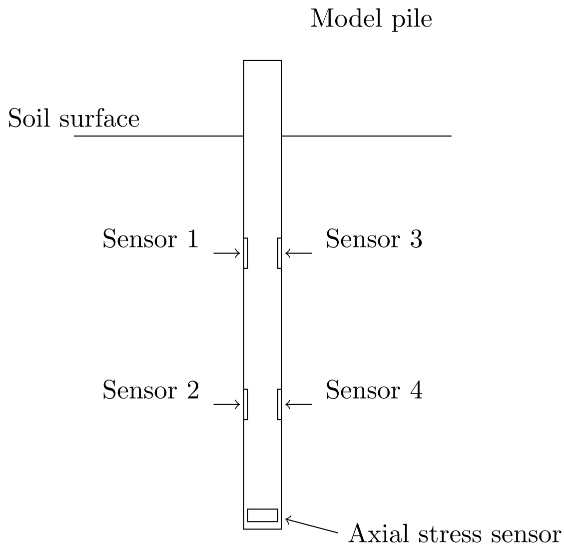

Figure 5.1: Location of the stress sensors on the instrumented model pile. (Dimensions are provided later in the text)

5.2 Considerations for the design of an instrumented model pile

5.2.1 Design of the pile membrane dimensions

The design approach consisted of instrumentation of a model pile to conduct contact stress measurements in the normal direction to the pile surface. The stress sensors comprised membrane strain gauges situated inside the model pile. In the final design, the model pile had a quadratic outer diameter of 10 mm and a length of 125 mm. It was instrumented with four contact stress sensors and an axial stress sensor, shown in Figure 5.1. The contact stress sensors were located at two h_y/D_{Pile} levels, where h_y is the distance from the pile tip in the y-direction, and D_{Pile} is the pile diameter. The h_y/D_{Pile} factor is commonly used in research on piles, e.g. [148], [119]. The sensors were situated at two opposite sides of the model pile.

Typically, a membrane strain gauge consists of a vibrating wire or an electric resistance strain gauge mounted on a flexible diaphragm, e.g. [86], [92], [113]. In this model pile an electric resistance strain gauge half bridge was installed, consisting of two strain gauges and two precision resistors. These were powered by an excitation voltage, V_{ex} of 6 V. The output signal of the strain gauges was measured through the output voltage, V_{output}. During deformation of the diaphragm, or membrane, the output voltage V_{output} of the strain gauge alters, and the stress level is therefore related to this output voltage V_{output} via a calibration factor.

The aim of this specific design was to create a continuous external surface, on which contact stress measurements would be carried out. In previous measurement programs, contact stress sensors were fitted into a hole drilled in the pile body, or in a special earth pressure cell. This discontinuous pile surface potentially results in arching around the sensor surface and redistribution of stress during cyclic loading, e.g. [85], [136], [147]. The risk of arching and stress redistribution around the sensors were considered to be lower for membrane stress sensors. A two-part steel model pile which was connected by epoxy adhesive was therefore designed. The diaphragm or membrane was created by reducing the wall thickness at the sensor location by milling a local cavity on the inside of both pile halves.

The final sensor design comprised 0.3 mm thin membrane for the horizontal normal stress sensors. The half strain gauge bridges were mounted on internal side of these membranes, and both strain gauges were glued on the membrane. The design dimensions of the 8x8 mm^2 membrane were based on estimation of the maximum horizontal stress, [136], [147]. The dimensions of the membrane were then calculated from the design strain level at maximum deformation, chosen from specifications of the strain gauge.

Because of the possible effect of redistribution of axial load into the membranes, the sensors were designed to have a relatively low sensitivity. Other practical solutions show similar strategies, [32], [119], [136]. The specific model design was therefore a compromise between sensor sensitivity and reduction of disturbances from combined loads.

The membrane dimensions were initially calculated from the design strain, based on a simplified analytical solution of a circular clamped plate, [52], [192], [226]. The analytical solution for the membrane strain in the radial direction e_{rr} depends on the thickness h of the membrane, the Poisson's ratio ν_{Pile} ,the elastic modulus of the membrane E and the normal stress σ_n:

$$w = \frac{6\sigma_n(1-v^2)}{32Eh^3}(a^2 - r^2)^2 \tag{5.2.1}$$

$$e_{rr} = \frac{3\sigma_n(1-v^2)}{8Eh^2}(a^2 - 3r^2) \tag{5.2.2}$$

Using eq. 5.2.1 and 5.2.2 the suitable design membrane thickness was estimated to 0.3 mm, which still would allow enough stiffness to protect the sensors from considerable deformation. A numerical model was also set up to analyze the effect of the rectangular shape. The membrane in both these calculations was assumed to be homogeneous, but the fabrication procedures would likely results in some variation of the membrane dimensions resulting from fabrication tolerance levels at the small scale. This possible effect was not evaluated in the design process.

5.2.2 Numerical modelling of the model pile

In the model tests, the instrumented model pile was assumed to be influenced by a combination of loads during the tests, such as axial, torsion and bending loads and the influence of interface shear stress. This behaviour had been observed in similar tests, e.g. [136], [256]. To assess the effects of these combined loads on the accuracy of the model pile, a numerical model was devised, in which the performance of the sensor and the calibration procedure could be analyzed for different load cases.

The model pile was modelled in the finite element analysis program $COMSOL$, [167]. Because of the symmetry of the model pile, one half of the pile was modelled. This simplification was justified, since only horizontal and axial loads were estimated to be present in the model tests. Consequently, the boundaries between the model pile halves were prescribed to have no horizontal or vertical displacements, however, rotations were allowed.

The model was meshed with 10-noded tetrahedral elements with an automatic meshing algorithm, which was refined at the membrane, resulting in around 35000 elements ($\pm$ 2000 elements when different membrane dimensions were studied). The refinement of the mesh was higher in the membrane section of the model pile. The 3D model including the tetrahedral mesh is shown in Figure 5.2. The stainless steel pile material was modelled by an isotropic elastic constitutive model. An elastic modulus $E_{Pile} = 210$ GPa and a Poisson's ratio of $v = 0.28$ were used.

Numerical convergence of the finite element solution was controlled by varying the mesh density in the model, and conducting a series of simulations for the same model, including both horizontal and axial load. The fine mesh was seen to give mesh independent solutions and was used in the model. The simulation time was relatively low, in general less than 0.5 minutes. The simulations of the instrumented model pile were carried out with the finite element $COMSOL$ solver for structural mechanics, [167]. A variety of load cases were modelled.

5.2.3 Simulation of variation in membrane dimensions

The fabrication procedures were assumed to result in some variation in membrane dimensions, caused by limited machine tolerance at the small model scale. A numerical analysis was conducted to analyze this effect, in which the dimensions of the membrane cross-section were varied between 0.27 mm - 0.33 mm. The aim of the simulation was to find upper and lower bounds for how this effect would influence the sensitivity of the sensor. The simulation was carried out with combined horizontal and axial load. Since the model was simulated with isotropic elasticity, it was assumed that these loads could be added by superposition, and an analysis of possible distributions of the combined loads would therefore not be necessary. Torsion and bending loads were not analyzed.

Table 5.1 shows the effect of variation in fabrication dimensions. The membrane cross-section was varied between 0.27 mm - 0.33 mm in the model. A simulation of the model pile response was then conducted. Five different models were simulated, in which the cross-section was 0.27 mm, 0.29 mm, 0.3 mm, 0.31 mm and 0.33 mm. An additional effect changing the result was the new mesh generated on the pile model, since the geometry was altered for each spatial realization of the model. This effect was assumed to be relatively limited, and once convergence was reached for the standard model, the same mesh size was assumed to give convergence in the other models as well.

The simulation was carried out with a simulated horizontal and axial stress. The horizontal stress was assumed to act on all external surfaces of the model pile, and was varied from no stress to a maximum stress of 200 kPa in increments of 25 kPa. The axial stress was simulated to act as a pressure on the pile base. The axial stress was varied to a maximum

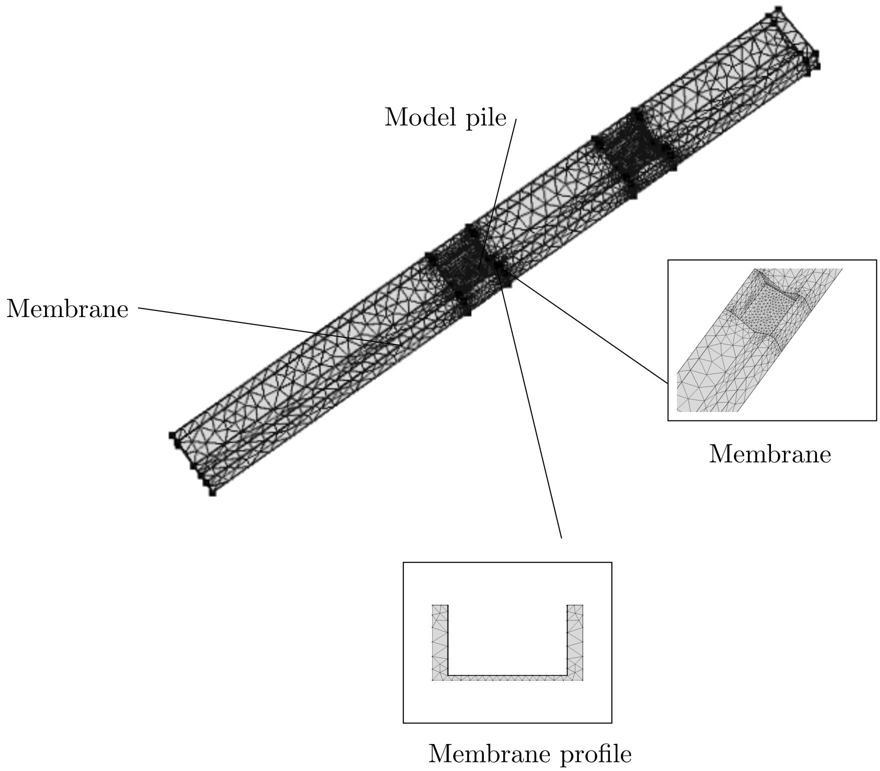

Figure 5.2: Numerical model of one-half of the instrumented model pile.

stress of 18 MPa with a stress increment of 2 MPa.

In all simulations, the strain component ε_{xx}, perpendicular to the pile axis, was sampled from the numerical simulation for later analysis. The strain gauge bridge was mounted in the same direction along the x-axis, and it was therefore of interest to study the additional effect of the axial load in the measurements of the ε_{xx} strain component.

The simulations of the isotropic horizontal stress are shown in Table 5.1. The membrane strain ε_{xx} has for all simulations been normalized with the simulation for the 0.3 mm simulation, $\varepsilon_{xx,30}$, which was the design specification. The divergence from the design could therefore be studied, and it suggests that variation of the normalized strain ratio $\frac{\varepsilon_{xx}}{\varepsilon_{xx,30}}$ is larger for horizontal load than axial load.

Membrane thickness [mm]	horizontal strain ratio $\frac{\varepsilon_{xx,d}}{\varepsilon_{xx,30}}$	axial strain ratio $\frac{\varepsilon_{xx,d}}{\varepsilon_{xx,30}}$
0.27	1.2409	1.0708
0.29	1.0772	1.0236
0.3	1	1
0.31	0.9455	0.9788
0.33	0.8357	0.9363

Table 5.1: Numerical analysis of influence of fabrication precision

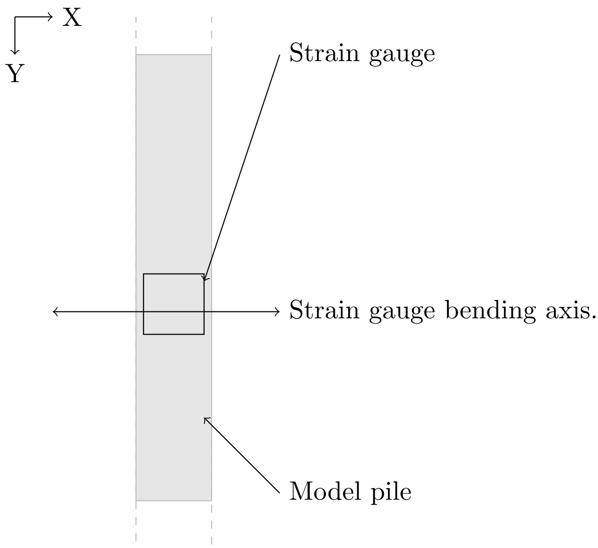

Figure 5.3: Direction of bending for the measurements of the strain gauge.

5.2.4 Simulation of interface shear stress

The membrane stress sensor is configured to measure the strain component perpendicular to the pile axis ε_{xx}, where the y-direction is directed along the pile axis, Figure 5.3. Experimental studies have shown that when the pile capacity is mobilized, a shear stress component will also be present at the soil-pile interface, [136], [148]. This interface shear stress may influence the stress measurements by inducing strain in the membrane. The influence of this effect on the system accuracy was therefore simulated in the numerical model.

The numerical simulation consisted of simulations of horizontal normal and shear stress over the pile surface. The stress was increased to 400 kPa in 50 kPa increments. A frictional shear stress component was added, with the shear stress $\tau = \sigma_n \tan(\delta')$, where δ' is the interface angle, [124]. An initial simulation included a shear component based on an interface friction angle of 25 degrees, which implies a frictional coefficient of around 0.466.

The strain component e_{xx} from the numerical simulation is shown in Figure 5.4, which suggests that the strain levels increases with the shear component present at the interface.

To study the effect of various pile-soil interface angles, a simulation was carried out where this angle was varied between 12 - 32 degrees. The normal stress was kept at 0.1 MPa and 0.4 MPa.

The ratio of the total strain (with the normal and shear stress component) ε_{tot}, and the strain from the normal stress ε_{σ} is used to normalize the effect of the interface angle $\delta_{interface}$. The normalized strain ratio for the two stress levels are shown in Figure 5.5. The simulation was conducted with two different normal stresses, to confirm the elastic behaviour of the structure. It appears that the strain level ε_{tot} is significantly higher when a shear stress component is added to the normal stress component.

Measurements in ring shear devices typically show an interface angle between 12-25 degrees, [124]. Shear box measurements with a similar type of material on the same non-cohesive soil resulted in an interface friction angle $\delta_{interface}$ of 12.9, [60], which may be compared to ring shear tests with a smooth surface, [45], [120]. The excess stress ε_{excess} will therefore be in the range of 10 %. A correction factor for the measurements of horizontal stress of 0.9 should be taken into account to correct the excess stress measurements from shear. This is cumbersome to include in the interpretation of the measurements, since the displacement necessary to mobilize the full shear stress must be taken into account, [218]. The results in potential misestimations of the effect of shear during load cycles. Since this displacement is not known, the measurements are not corrected for the shear load. It is possible to estimate the shear component from the base and pile head load, but due to the variation in shear stress along the pile, it was not possible to calculate a conclusive estimate of the shear stress.

Since the effect of shear stress on the sensor was ignored, the operational normal stress on the sensors will be overestimated at peak horizontal stress. This will have the largest effect on the continuously installed tests and extraction load tests.

5.2.5 Simulation of horizontal stress sensor calibration

The calibration procedure for the horizontal normal stress sensors consisted of a controlled calibration by isotropic stress provided by water pressure. Calibration coefficients would be derived from the calibration measurements. These calibration coefficients would also include the additional strain resulting from isotropic stress at the pile base, $\varepsilon_{xx,Base}$. To estimate the influence of this load, simulations of the calibration were carried out. Simulations of the model pile response for isotropic stress at the pile shaft were compared with simulations of the model pile response for the whole pile, including the pile base. Figure 5.6 shows the numerical simulation. The axial stress contributes extra strain $\varepsilon_{xx,Base}$. The increase is around 3.7 % based on the 0.3 mm membrane cross-section in the numerical model. This additional correction of the calibration measurements were later used to correct the calibration coefficients, as the correction factor $c_{horizontal} = 0.963$.

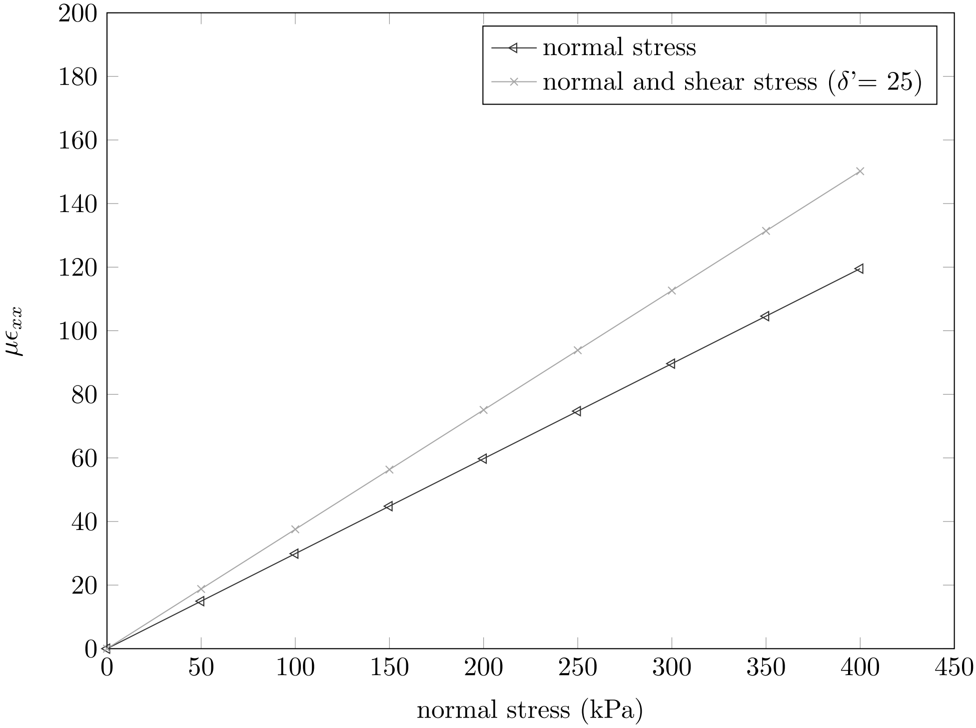

Figure 5.4: Simulation of the influence of combined normal and shear stress.

5.3 Design of the instrumented model pile

The instrumented model pile was realized to conduct measurements of stresses in the physical model. The measurement system consisted of a model pile instrumented with direct soil stress measurement sensors. The aim of the instrumentation was to measure horizontal normal contact stress at two levels of the pile, giving measurements at two different L_{Pile}/D_{Pile}-levels. The instrumented model pile system also comprised an axial stress sensor located at the pile base.

The aim of the mechanical realization of the measurement system were to simplify the model appropriately, while incrementally improve details which may have reduced the accuracy of previous physical models. The instrumented model pile was designed in combination with the rest of the experimental model to reach a broad-based compromise for the practical implementation, i.e. to combine properly scaled physical modelling with relatively accurate measurements in the model.

The specific configuration of the horizontal stress sensors is intended to create a homogenous shear surface at the sensor location. Experimental measurements of interface shear have demonstrated that very small deformations at the interface govern the volumetric behaviour of the soil, and thus the shear stress response of the soil, [34], [218]. Here an alternative design

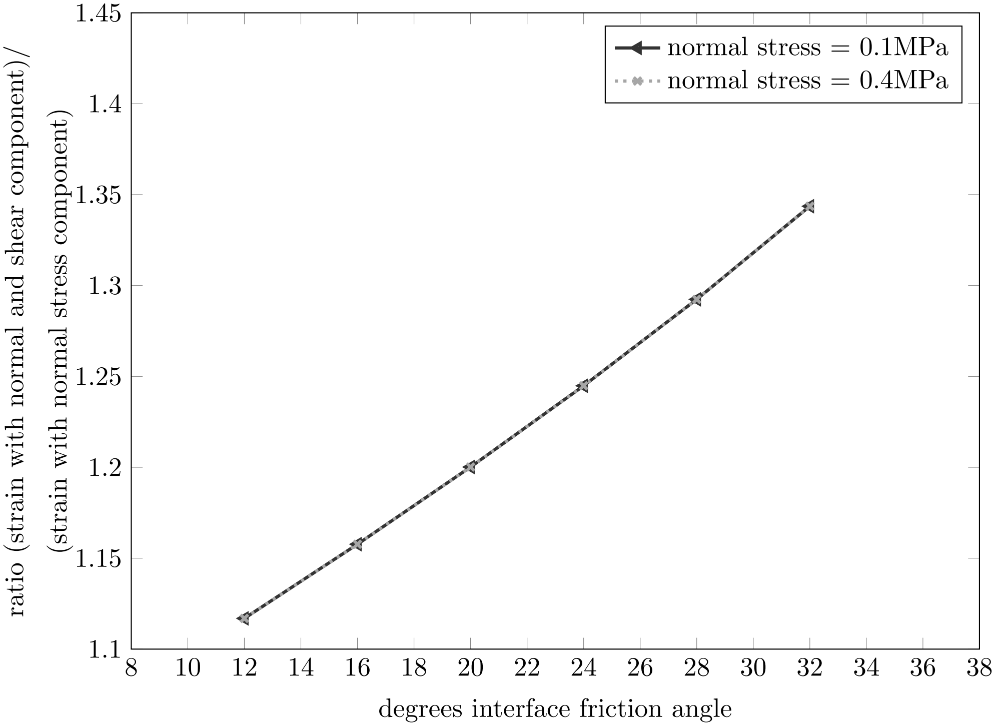

Figure 5.5: Normalized strain ratio $\varepsilon_{tot}/\varepsilon_{\sigma}$.

is used, which results in a slightly deforming continuous shear surface at the sensor location, therefore replicating the prototype more accurately, especially for scaled soil samples, with relatively small numbers of grains next to the sensor.

5.3.1 Mechanical configuration of the instrumented pile

The instrumented model pile consisted of two milled steel 5 x 10 x 125 mm^3 stainless steel rods with an elastic modulus of 210 MPa, and with a Poisson's ratio of 0.28. The longitudinal profile of one half-pile is shown in Figure 5.8. The Figure is shown in the $x - y$ plane, and shows the instrumentation cavity inside the model pile. The fully assembled model pile is shown in Figure 5.10.

The mechanical realization of the instrumented model pile consisted of three differently shaped cross-sections, shown in Figure 5.9. Two separate measurement levels were positioned 25 mm from the pile tip and 70 mm from the pile tip. These measurement levels consisted of thin membranes cut into the pile. The membranes were intended to give a flexible plate, which would deform under the external soil pressure. On these thin plates, strain gauges were mounted so that measurements of the radial strain could be conducted.

The stress sensor membranes measured 8 x 8 mm^2 in the $y - z$ plane and had a design thickness of 0.3 mm in the x-axis, Figure 5.9a. These small membrane dimensions made

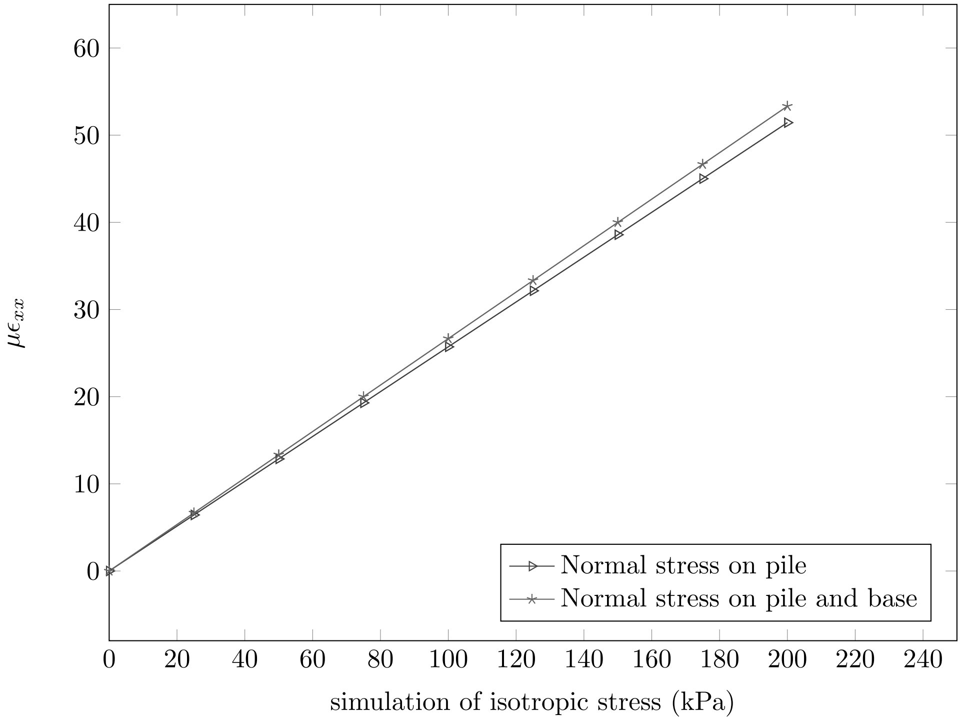

Figure 5.6: Simulation of horizontal stress sensor calibration.

a very accurate cutting depth necessary. The variation of the membrane thickness in the x-plane measured with a micrometer showed that the membrane thickness after manufacturing was 0.29±0.2 mm. Table 5.1 shows that these fabrication tolerances will not have a large effect on the sensor performance, since calibration coefficients were measured for all the membranes and sufficient sensitivity was maintained. A numerical analysis was also conducted to assess the influence of the fabrication accuracy.

Observations showed that there was also a slight increase of the membrane thickness towards the edges of the membrane, which influences the sensitivity of the sensor. This effect was assumed to be present for all membrane dimensions, and mainly influence the clamping of the boundary of the membrane. This disturbance would also be included in the calibration and would therefore not affect the sensor significantly.

The cross-section of the membrane sensor levels is shown at the profile A - A in Figure 5.9a in the $z - y$ plane, 70 mm from the pile tip. The non-instrumented profile of the model pile consisted of solid rectangular 5 x 10 mm^2 section into which a triangular groove was cut, cross-section B - B in Figure 5.9b. In this groove, the electric cables for instrumentation were placed. At the tip, the pile was sealed with a thin plate at a cross-section with a thin edge, C - C in Figure 5.9c.

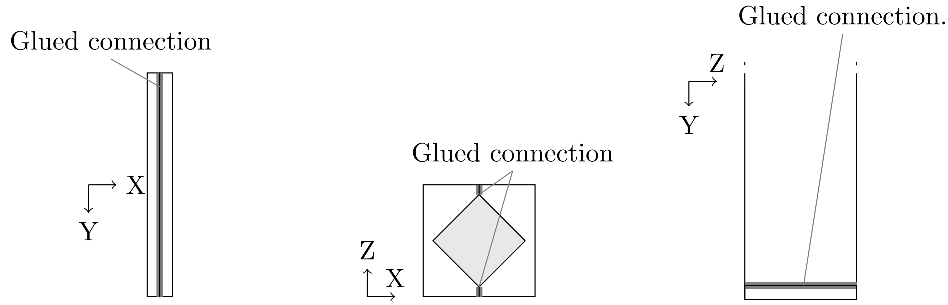

(a) Glued connection between the pile halves.

(b) Glued connection between the pile halves.

(c) Glued connection between pile and tip plate

Figure 5.7: Construction of the glued connections of the instrumented model pile.

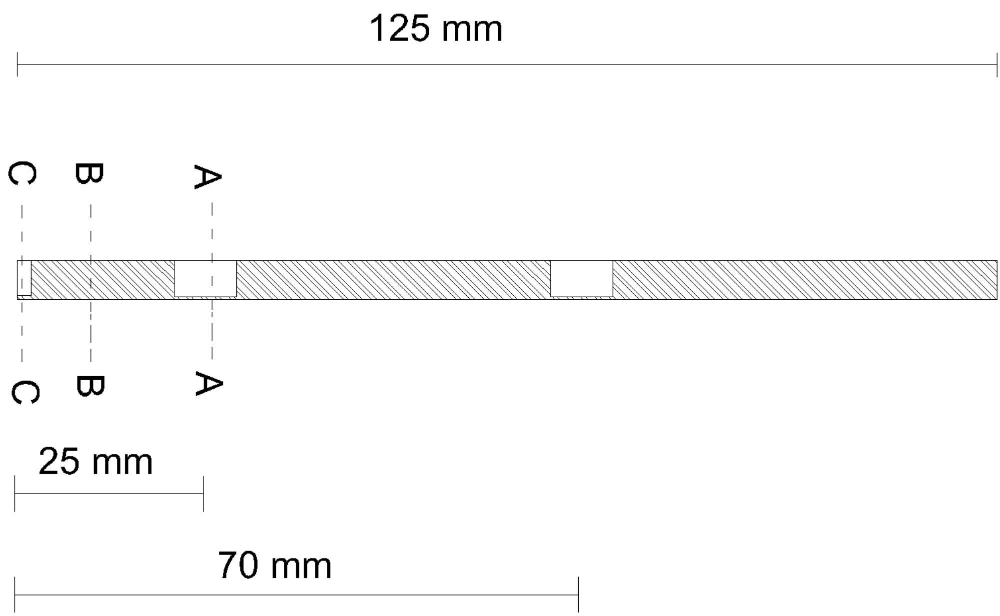

Figure 5.8: One half steel core of the instrumented model pile.

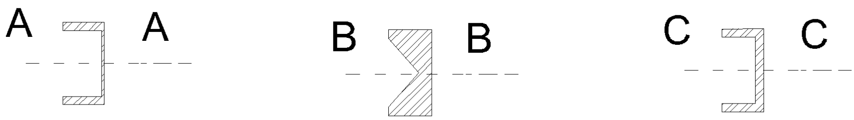

(a) Dimension of the pile at cross-section A.

(b) Dimension of the pile at cross-section B.

(c) Dimension of the pile at cross-section C.

Figure 5.9: Cross-sections of the instrumented model pile.

5.4 Instrumentation of the model pile

5.4.1 Instrumentation system

The pile consisted of four horizontal normal stress sensors and an axial stress sensor instrumented with electric resistance strain gauges. Each of the milled steel bars had two different levels instrumentation levels, and the micrometer measurements showed that the deviation from the intended dimension were similar for the piles halves, i.e. both membranes for each pile halves had the same magnitude. These sensors were instrumented before the model pile halves were enclosed, and the electrical cables were extracted through the pile axis in the groove shown in Figure 5.9c. The intention was to combine the horizontal normal stress measurements on each side of the model pile for one instrumentation level to an average stress reading. The latter reduces the noise level and increases the resolution of the normal stress measurements. The double level horizontal stress measurements were also constructed to measure the effects of friction fatigue on the soil-structure behaviour since the change in normal stress level at the same depth z is measured, [104], [148].

The model pile was instrumented with resistance strain gauges to conduct measurements of the normal stress against the thin membranes. The strain gauge configuration is shown in Figure 5.11. The half strain gauge bridge consisted of two 120 Ω strain gauges and two 120 Ω high precision SMD resistors. The strain gauges were mounted next to each other, perpendicularly to the model pile longitudinal axis. The strain gauge excitation voltage was 6 V, which was supplied by the in-flight amplifier system on the centrifuge. Both the 120 Ω strain gauges were of the type TML FLA 2-11. These had a tolerance of 0.1 %, and a temperature coefficient of 5 ppm/C. The strain gauges were mounted with the TML-CN adhesive on the thin membranes of the model pile. The strain gauge bridge was optimized for an amplification of 1000x in the data acquisition system.

The orientation of the strain measurements relative to the model pile is shown in Figure 5.3. The direction of the strain gauge deformation axis is then perpendicular to the pile longitudinal axis. The strain gauge on the opposite faces of the instrumented model pile

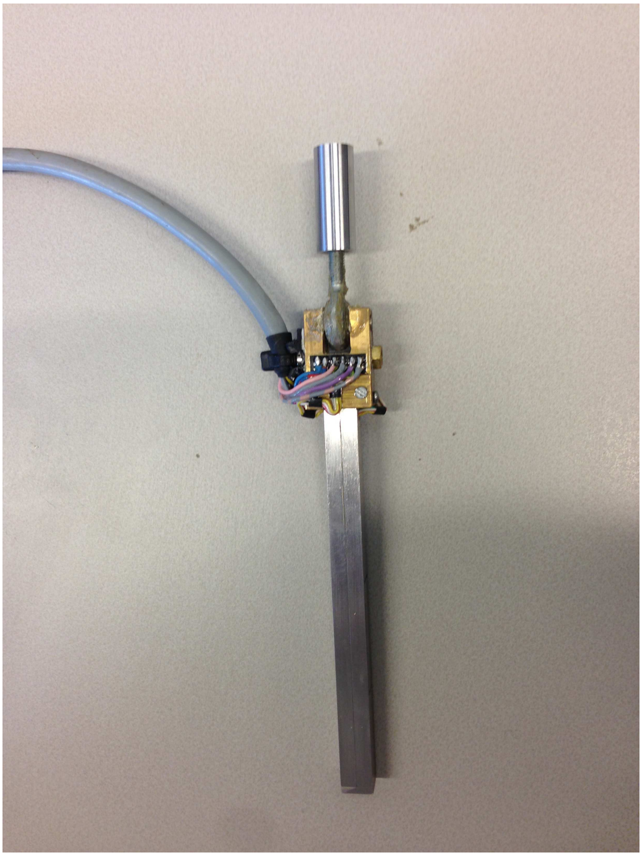

Figure 5.10: Instrumented model pile with cable connection to amplifier system.

had inverse configuration of the bridge voltage, i.e. one face of the model pile gave an increase in the bridge voltage output and the other side a decrease in the bridge voltage output for the same deformation level.

5.4.2 Residual stress during the manufacturing of the instrumented model pile

It is well known that residual stresses in the material will occur after machine process with high contact stresses, [108]. These residual stresses after fabrication of cutting may be a result of the build-up of stresses, which are locked-in the final shape, [35]. During fabrication, the local stress levels at the cut surface have very large magnitude, and could therefore be redistributed in the steel body. This is sometimes also a result of heating and cooling effects, [249].

These residual stresses may influence the stiffness response of the material, and give discontinuous stress-strain curves when residual stresses are released, [249]. This may influence the accuracy of the sensor, [135]. There are practical solutions for reducing the residual stress

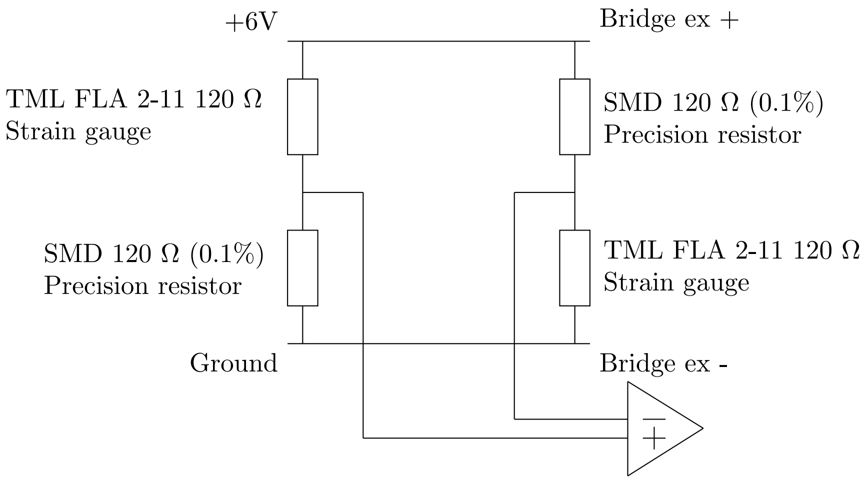

Figure 5.11: Configuration of the strain gauge bridge system.

in steel by cyclic or thermal loads. This process can step-wise release the stress after various levels of loads cycles N, [112]. These residual stress reduction methods were considered relatively cumbersome, and difficult to adapt to the specific geometry of the instrumented model pile. To reduce the effect of residual stress the instrumented model pile was preloaded at a stress level higher than the estimated physical model test loads. The calibration was also carried out up to a relatively high stress level, which was assumed to result in a partial stress release, reducing the residual stress influence at lower stress levels than the calibration stress, [135].

5.4.3 Instrumentation procedures

The strain gauge bridge consisted of a half Wheatstone bridge with one electric resistance strain gauges mounted on each side of an elastic plate, with the resistors completing the bridge placed on another layer in the membrane. This strain gauge configuration is designed to compensate for the axial strain, and only record the bending in the plate. The deformable elastic plate was glued on rollers to the membrane in the half-pile, shown in Figure 5.12a. This minimizes the loading from axial shear strain component. During application of horizontal normal stress at the surface of the pile the deformable plate deforms along with the membrane, whilst reducing the redistribution of axial strain to the strain gauges. The bridge was covered by beeswax after the installation and the cables were extracted through the groove in the pile.

The resulting configuration was found to be least sensitive to additional axial strains from shear on the membrane surface or axial load in the pile wall. However, additional bonding stress from these will still be influencing the measurements on contact stress.

The axial strain gauge for measuring base stress was mounted on the interior pile shaft as close as possible to the tip of the pile, at the pile internal wall with the cross-section shown in Figure 5.9b to minimize any additional shear resistance in the base load measurements.

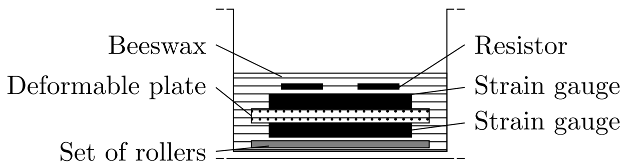

(a) Configuration of the strain gauge mounted on the membrane.

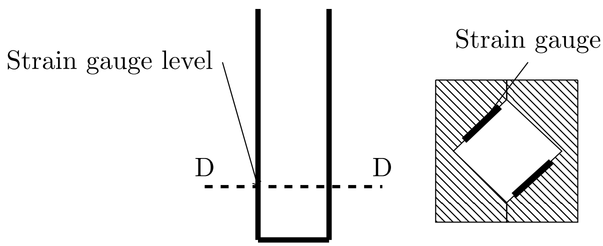

(b) Location of strain gauges for axial measurements.

Figure 5.12: Configuration of the horizontal normal stress and axial stress strain gauges mounted on the instrumented model pile.

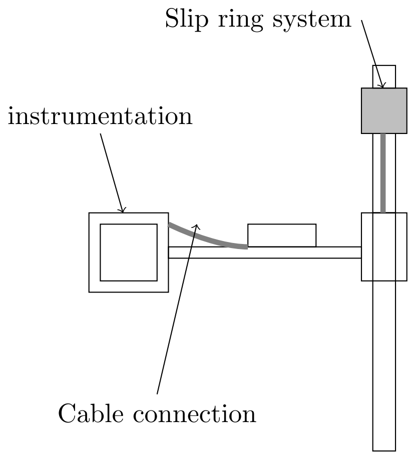

Figure 5.13: Cable connection from the instrumented model pile to ampifiers.

The axial strain gauges were fixed on the pile surface with epoxy adhesive, Figure 5.12b. The strain gauge bridge consisted of two strain gauges that were attached to the opposite interior faces of the pile. This specific configuration reduced the influence of bending on the measurements. The strain gauge cables, which consisted of excitation voltage V_{ex} and the output voltage, V_{output} for each sensor location, were guided through the center of the pile to the amplifiers. The axial strain gauge bridge was covered with plastic coating before the pile was enclosed.

After instrumentation the two pile halves were glued together with epoxy adhesive. The adhesive was placed on the 1 mm wide surface of the steel rods which was located at each side of the groove which was cut in the pile, shown in Figure 5 b. The glued connection which enclosed the instrumented model pile is shown in Figure 3. The glued connections are shown in Figure 5.7a and in Figure 5.7b. At the pile tip a 10x10 mm^2 plate was placed at the pile body with glue at opening of the steel rods at cross-section C - C in Figure 5 c. The plate had a 8x8 mm^2 extrusion on which glue was placed to enclose the model pile. The glued connection is shown in Figure 3 c. The extra pieces of glue at the pile surface were sanded down, to ensure that the surface would be relatively homogenous. The stiffness of the adhesive used to enclose the model pile was approximately the same as the stainless steel, therefore reducing effects of stress redistribution in the model pile.

The instrumented model pile was connected to the 16 channel bridge amplifier and then to the National Instruments PCI-6221 data acquisition system, which was mounted on the centrifuge beam for in-flight measurements. The strain gauge connections were bundled together, and connected to a small terminal board which was attached to the pile cap.

5.5 Switched strain gauge supply

The initial calibration of the instrumented model pile showed that heat effects influenced the accuracy of the measurements. The relatively large current in each strain gauge resulting from the low resistance strain gauges heated the model pile, hence altering the measurements. This was resolved by implementing an alternating excitation voltage V_{ex} in combination with triggered acquisition. It was found that still a specified heating time before centrifuge testing was needed to assure a stable strain gauge temperature.

5.5.1 Switched strain gauge excitation voltage

In order to reduce the heating of the membrane, the strain gauge voltage supply was reconfigured to have a switched activation time. The system consisted of an electric switch and a timer that provided a 6 V excitation voltage V_{ex} to the instrumented model pile. The duty cycle was 9% at 1.3 Hz frequency. During active periods, the strain gauge would heat up, and during passive periods, the heat could dissipate. The principle is shown in Figure 5.14. In Figure 5.14a, the strain gauge supply voltage is activated and stopped with a predefined active period. In Figure 5.14b, the strain gauge temperature alternately increases and decreases, when the voltage is activated. It was assumed that the temperature would stabilize after a specified time, and that the heat effect would subsequently not influence the accuracy of the measurements.

The electric circuit consisted of a Diodes Inc ZXMP6A17G electronic switch, connected to a National Semiconductor LM555 timer. These two components were configured to switch the excitation voltage V_{ex} from the amplifiers. The switch gave a rectangular wave as input to the switched voltage supply for the strain gauge bridge, as shown in Figure I.1. The full configuration of the A-stable multi-vibrator is shown in Appendix *I*.

Figure 5.16 shows the heat reduction for one of the horizontal strain gauge sensors. The measurements for all the sensors are shown in Appendix *I*. The Figure shows the temperature effects when the pile is heated, and displays the reduction in temperature disturbance for the instrumented model pile when the alternate voltage supply system in activated. The reduced temperature disturbance was more than tenfold.

5.6 Calibration Procedure

The instrumented model pile was calibrated using two separate calibration devices. The reason for this calibration arrangement was the relatively different load conditions, in which load of different magnitude had to be calibrated on the model pile. The horizontal normal stress and the axial stress sensors could therefore not be calibrated simultaneously.

The calibration loads consisted of isotropic stress, followed by a moment-free axial load. The horizontal normal stress sensor calibration was consequently carried out with a calibration vessel, which is shown Figure 5.17. The axial calibration was carried out with a lever system, shown in Figure 5.17.

5.6.1 Horizontal stress sensor calibration procedure

The horizontal membrane strain gauges were calibrated in a metal calibration vessel, Figure 5.17. For proper calibration of the membrane sensors it is not possible to have pressure inside the model pile, hence this special vessel was constructed to seal the pile and retain it in

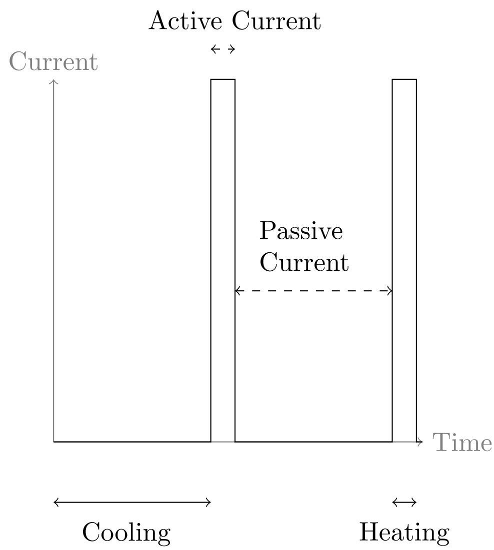

(a) Alternate current supply for the model pile

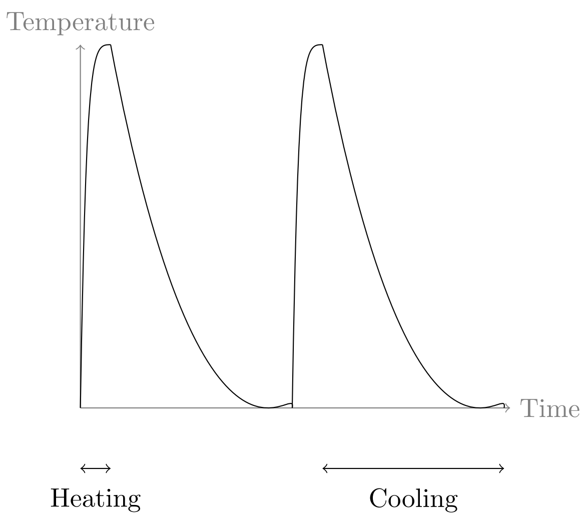

(b) temperature control

Figure 5.14: Heat stabilizing mechanisms with alternate voltage

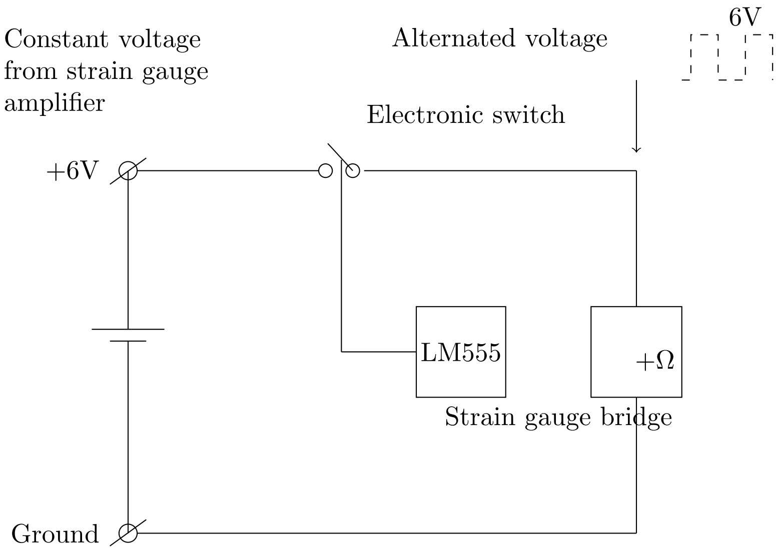

Figure 5.15: Circuit showing the LM555 timer in the strain gauge system.

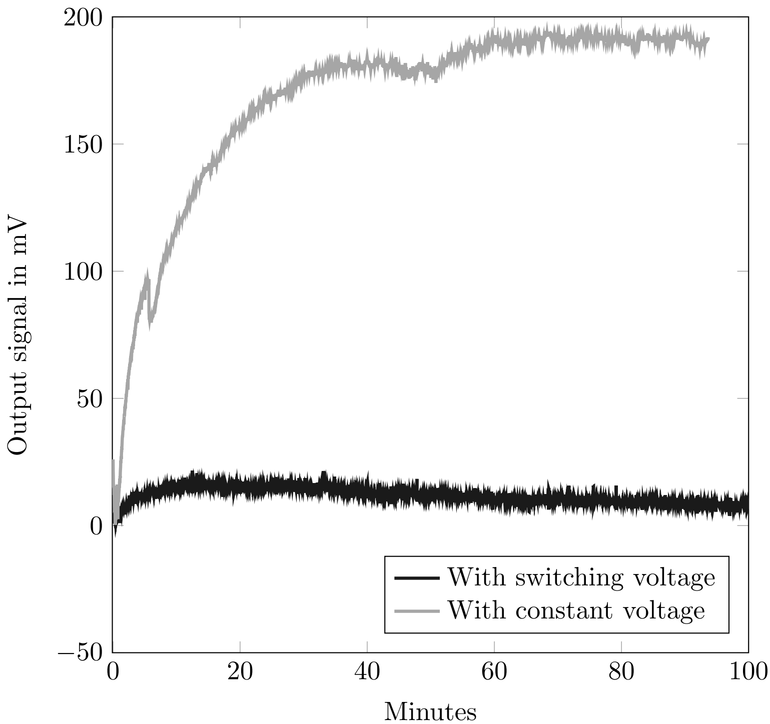

Figure 5.16: Strain gauge output voltage V_{hor}^{tot} with and without alternate voltage supply.

the calibration vessel. Calibration measurements of the horizontal normal stress sensors and the axial stress sensors were carried out in the device. These measurements were compared to the analytical and numerical calculations of the membrane strain level. Before calibration the pile and acquisition system were warmed up to their equilibrium with ambient temperature.

The calibration vessel consisted of a cylindrical steel container and a double-plate aluminum top seal. During calibration the pressure inside the vessel was increased from no load in increments of 25 kPa up to a maximum of 200 kPa, which simulated the real pressure in the physical model. A large difference between the vessel and the model tests conditions was that the water does not mobilize shear stress. The difference may influence the accuracy of the calibration procedure, and influence the hysteresis behaviour of the sensors, since an additional deformation of the membrane is mobilized by the shear stress when the pile is pushed into the soil, [220].

The water pressured calibration vessel was controlled by a GDS GD Standard Pressure Controller. To assure the accuracy of the water pressure measurements, separate water pressure measurements were conducted using Druck PDCR-8 pore pressure meters. These were installed through holes which were drilled in the calibration vessel and sealed with Teflon Tape, Figure J.1. Measurements were made at a data acquisition rate of 1 Hz for about 30 seconds at each pressure level. Before calibration the model pile and the acquisition system were warmed up to their equilibrium ambient temperature. The pressure in the calibration vessel was measured before the start of the calibration. The instrumented model pile was calibrated four times in the calibration vessel.

5.6.2 Axial stress sensor calibration procedure

A lever system was used for calibration of the axial stress sensor. The calibration system consisted of a balanced lever system placed in the centrifuge load frame. In the 1:5 lever system, the instrumented model pile was mounted in the load frame to achieve a balanced counter weight. The calibration load was subsequently provided by the step-wise loading with 0.5 kg steel weights on the other end of the lever, while holding the lever system horizontal. A steel hinge was installed in a drilled hole on the metal lever to achieve a moment-free connection between the model pile and the lever.

The temperature control system was included in the calibration procedure. The output measurement was monitored, and when no significant change was recorded, the calibration procedures started.

The calibration consisted of a load sequence in which the instrumented model pile was axially loaded in 1 kg increments up to 10 kg. The load was incrementally increased and reduced to capture the hysteresis in the sensor, as shown in Figure 5.21. This calibration load represented the calibration axial pressure of in total 5 MPa in 500 kPa increments. The calibration procedure was repeated four times. Between the calibration cycles the instrumented model pile was repositioned to reduce the systematic measurements of bending during loading. The new position would result in a different bending mode. The effect of bending loads in the pile would therefore result in variation in the measurements, reducing the possibility of including systematic loading effects caused by the calibration procedure.

The base load of the model pile further governed by an extra area which mobilized by an estimated row of grains, with an estimated length of $2d_{50}$ along each side of the pile base, as well as the shear stress measured by the axial stress sensor, which is located around 10 mm from the pile base. A correction factor c_a to adjust these effects is derived and discussed in Appendix K.

5.7 Calibration results

The calibration measurements are represented by the maximum and minimum bounds of measurements in the calibration series. The full calibration measurements are presented in Appendix J and Appendix L. Appendix J presents the measurements in the calibration vessel. Appendix L presents the measurements in the axial compression system.

For physical model test interpretation, the calibration coefficients $k_{h,v}$ and $k_{a,v}$ with unit [kPa/mV] (horizontal and axial sensors in the vessel), $k_{h,l}$ with unit [mV/MPa], $k_{a,l}$ with unit [MPa/mV] (horizontal and axial sensors in the lever) of these measurements have been calculated based on the calibration data. Calibration coefficients for both loading and unloading have been calculated.

The calibration measurements were calculated by fitting to a curve $y = kx$. During combined normal and axial loading, the load effect on the horizontal normal stress and axial sensors consists of two components:

$$V_{output,hor}^{tot} = V_{output,hor}^{normal} + V_{output,hor}^{axial} \tag{5.7.1}$$

where $V_{output,hor}^{tot}$ is the total strain gauge output signal, $V_{output,hor}^{normal}$ is the strain gauge output signal resulting from normal stress, and $V_{output,hor}^{axial}$ is the strain gauge output signal resulting from axial load in the pile.

The axial sensor output signal is solely a result of the axial output voltage:

$$V_{output,axial}^{tot} = V_{output,axial}^{axial} \tag{5.7.2}$$

During calibration of the instrumented model pile in the vessel, the axial load increases the strain gauge output level. The corrected horizontal normal stress correlation coefficient is found by subtracting this axial component from the measurements:

$$k_{h,v}^{cor} = R_{axial} k_{h,v}^{tot} \tag{5.7.3}$$

where $k_{h,v}^{tot}$ is the calibration coefficient calculated from the calibration in the pressure vessel, and R_{axial} is the axial load calibration coefficient reduction factors from the numerical simulation.

The horizontal normal stress is then calculated by multiplying the strain gauge output voltage resulting from normal stress, $V_{output,hor}^{normal}$, with the corrected calibration coefficient $k_{h,v}^{cor}$:

$$\sigma_h = k_{h,v}^{cor} V_{output,hor}^{normal} \sigma_h = k_{h,v}^{cor} (V_{output,hor}^{tot} - V_{output,hor}^{axial}) \tag{5.7.4}$$

where $V_{output,hor}^{tot}$ is measured from the strain gauge output signal, and $V_{output,hor}^{axial}$ is calculated from the axial stress near the pile base, σ_{axial}, with the calibration coefficient $k_{h,a}$ in the unit [mV/MPa]:

$$V_{output,hor}^{axial} = k_{h,a} \sigma_{axial} \tag{5.7.5}$$

The axial stress is calculated with the axial calibration coefficient:

$$\sigma_{axial} = k_{a,l} V_{output,axial}^{tot} \tag{5.7.6}$$

The effective normal and axial stress σ_h and σ_{axial} a therefore possible to calculate from the model test measurements of V_{axial}^{tot} and V_{hor}^{tot}.

5.7.1 Calibration of the horizontal sensor system

During calibration, the output levels of the strain gauges were measured through the data acquisition system. The measurements, which were conducted with the alternate voltage supply system, were post-processed with the trigger software. The calibration principle is shown in Figure 5.17. After each completed load cycle the pile was removed from the calibration vessel. The mechanical set-up was checked and the pressure seal reinstalled before the next calibration was started. Four series of calibration in the calibration vessel were carried out.

A full calibration cycle for Sensor 1 is shown in Figure 5.19a. At each pressure increment a small jump in pressure is recorded because of the response from the GDS pressure controller and the calibration vessel, which displayed some minor leaks during calibration. Some hysteresis is observed during the load cycle of the horizontal sensor system. Separate calibration coefficients for loading and unloading were therefore calculated for the interpretation of the physical model tests.

The loading and unloading responses were analyzed separately. The maximum and minimum bounds from the loading of the pile in the four calibration tests are plotted in Figure 5.20. The Figure shows the range for all four horizontal contact stress sensors during loading of the pile. The maximum and minimum bounds of the calibration measurements for the unloading of the instrumented model pile from the maximum isotropic stress are similar, and are shown in detail in Appendix J.

Sensor nr	Cal. 1	Cal. 2	Cal. 3	Cal. 4	Average cal.
sensor 1	1.515	1.581	1.627	1.570	1.573
sensor 2	1.155	1.145	1.186	1.180	1.166
sensor 3	0.9402	0.9474	0.9401	0.9430	0.9427
sensor 4	1.433	1.444	1.438	1.425	1.435
axial	14.16	21.00	21.34	17.21	18.43

Table 5.2: Calibration coefficients from the calibration vessel stress calibration for incremental stress increase.

Sensor nr	Cal. 1	Cal. 2	Cal. 3	Cal. 4	Average cal.
sensor 1	1.594	1.588	1.603	1.604	1.597
sensor 2	1.180	1.227	1.186	1.180	1.193
sensor 3	0.9294	0.9440	0.9412	0.9548	0.9423
sensor 4	1.425	1.458	1.447	1.440	1.442
axial	26.99	21.95	22.96	23.44	23.83

Table 5.3: Calibration coefficients from the calibration vessel stress calibration for incremental stress decrease.

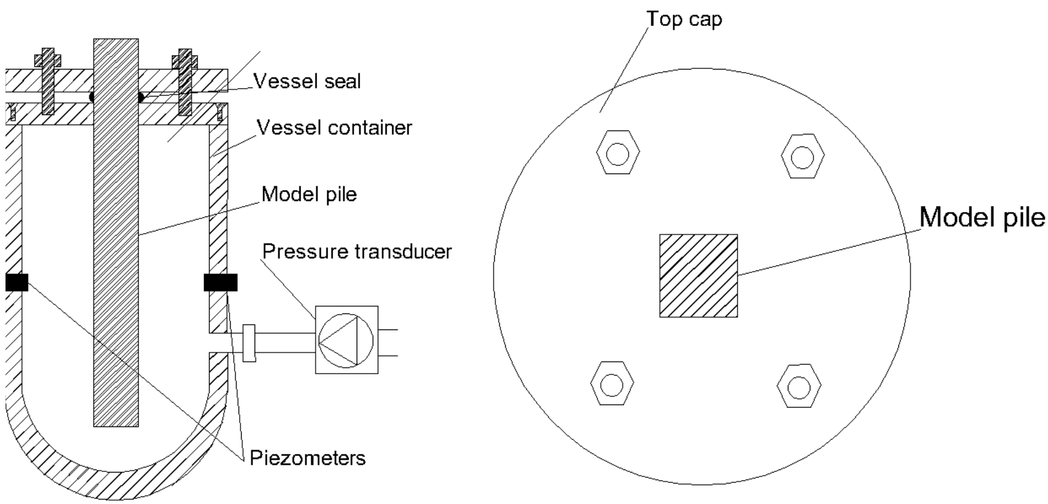

Figure 5.17: Vessel for calibration of the horizontal membrane strain gauges.

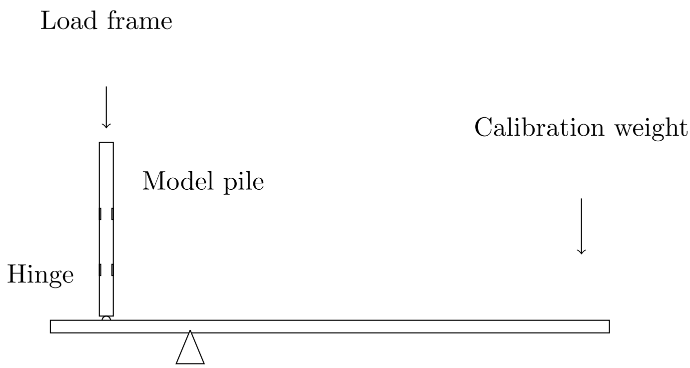

Figure 5.18: Calibration of model pile with lever.

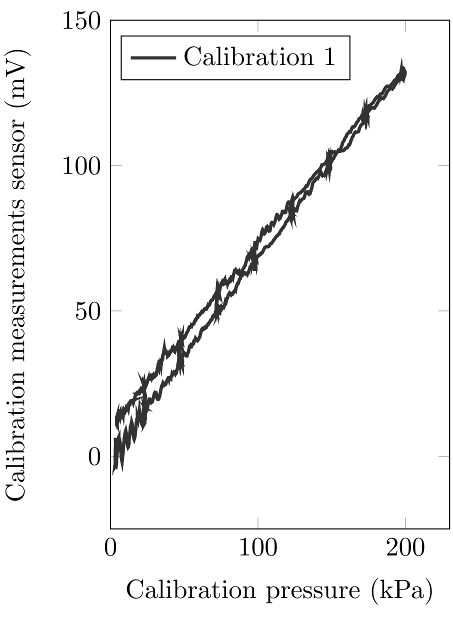

(a) Sensor calibration.

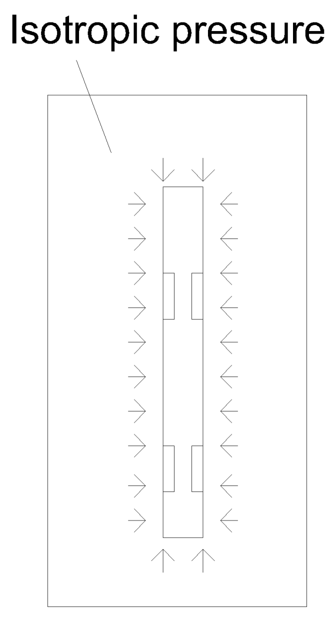

(b) Diagram of the horizontal calibration.

Figure 5.19: Calibration of the model pile in the horizontal calibration system.

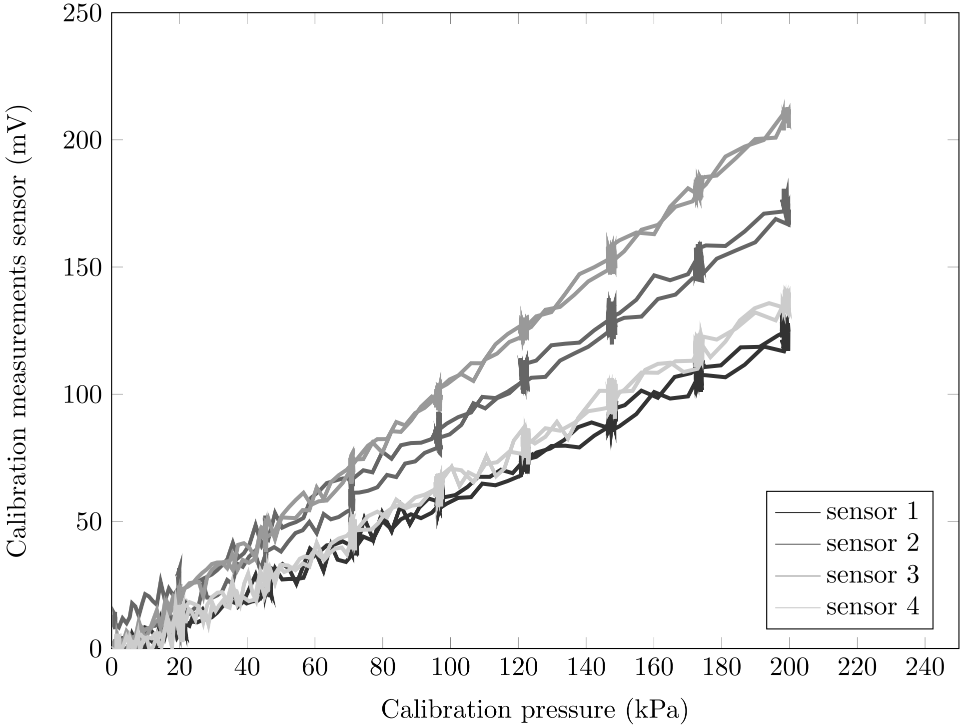

Figure 5.20: Bounds of calibration horizontal normal stress measurements in loading in the calibration vessel.

5.7.2 Calibration in the lever system

The instrumented model pile was subsequently calibrated in the axial compression lever system. The calibration procedure was carried out in the centrifuge room and the instrumented model pile was connected to the data acquisition system including heat reduction system. The principle of the calibration is shown in Figure 5.21b where the pile is subjected to the axial compression. Since the calibration was conducted in the surrounding air, the temperature effect was assumed to have a larger influence in comparison to the calibration vessel system. Care was therefore taken to assure that the temperature was stable. Because the axial load was assumed to influence the horizontal stress sensors in addition to the axial stress sensor, measurements were carried out for all sensors in the pile.

A load cycle during calibration for the horizontal stress sensor 1 is shown in Figure 5.21a. The calibration consisted of four such load cycles, in which the axial stress at the pile base was loaded to a maximum level of 5 MPa with an increment of 0.25 MPa. The calibration procedure was repeated four times to assure repeatability and reduce the influence of inclined load of the pile.

The maximum and minimum bounds of the axial sensor during loading are shown in Figure 5.22. The maximum and minimum bounds for the axial sensor during unloading are similar, and are shown in detail in Appendix *L*. Because of the instability during the load increments when the lever was manually supported, only the average measurement at the calibration loads are shown in the Figures as diamonds.

The bounds for the calibration measurements for the horizontal stress sensors during loading are shown in Figure 5.23a. The measurements show some significant axial load influence on the horizontal stress sensors. The variation in this influence is relatively large for the separate sensors. The upper and lower bounds for the calibration measurements of the horizontal stress sensors during unloading of the pile are shown in Figure 5.23b. There is some variation between the loading and unloading with an increased variation in unloading of the instrumented model pile.

Sensor nr	Cal. 1	Cal. 2	Cal. 3	Cal. 4	Average Cal.
sensor 1	7.197	6.708	6.645	6.544	6.774
sensor 2	13.62	13.92	13.50	13.19	13.56
sensor 3	0.1081	0.3052	0.5727	0.5883	0.3935
sensor 4	1.400	1.031	1.439	1.608	1.370
axial	0.01872	0.01839	0.01847	0.01830	0.01847

Table 5.4: Calibration coefficients from the axial stress calibration for incremental stress increase.

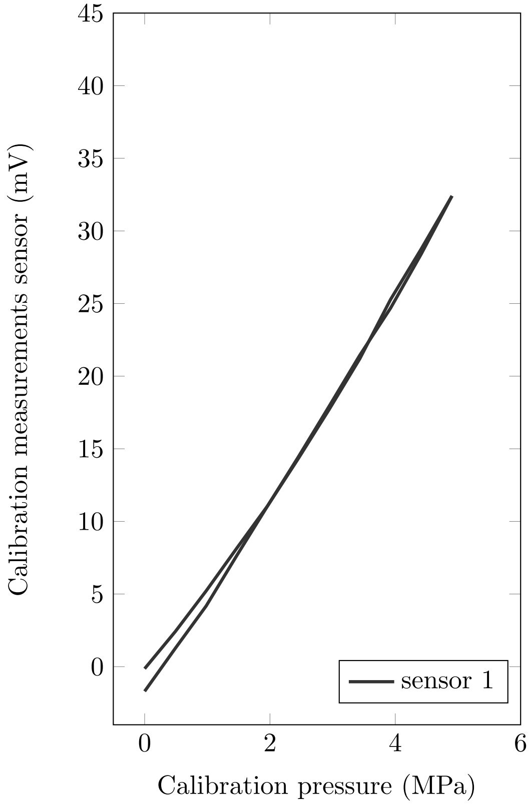

(a) Load cycle during axial sensor calibration

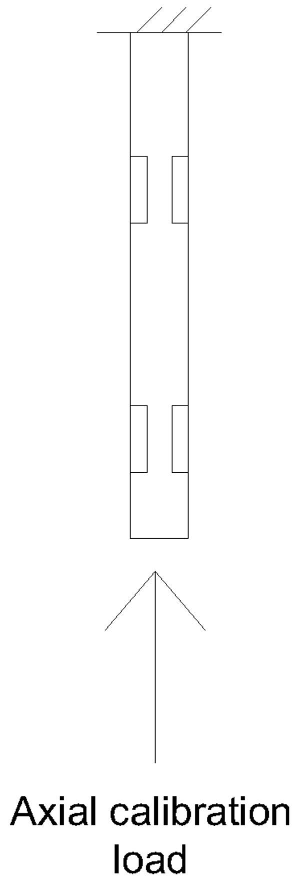

(b) Diagram of the axial calibration.

Figure 5.21: Calibration of the instrumented model pile in axial compression

Sensor nr	Cal. 1	Cal. 2	Cal. 3	Cal. 4	Average Cal.
sensor 1	7.924	7.320	6.998	6.81	7.264
sensor 2	13.49	13.04	12.06	11.86	12.61
sensor 3	-0.7106	0.3861	0.6843	0.8284	0.2970
sensor 4	0.9709	1.514	2.049	2.213	1.687
axial	0.01874	0.01844	0.01861	0.01841	0.01855

Table 5.5: Calibration coefficients from the axial stress calibration for incremental stress decrease.

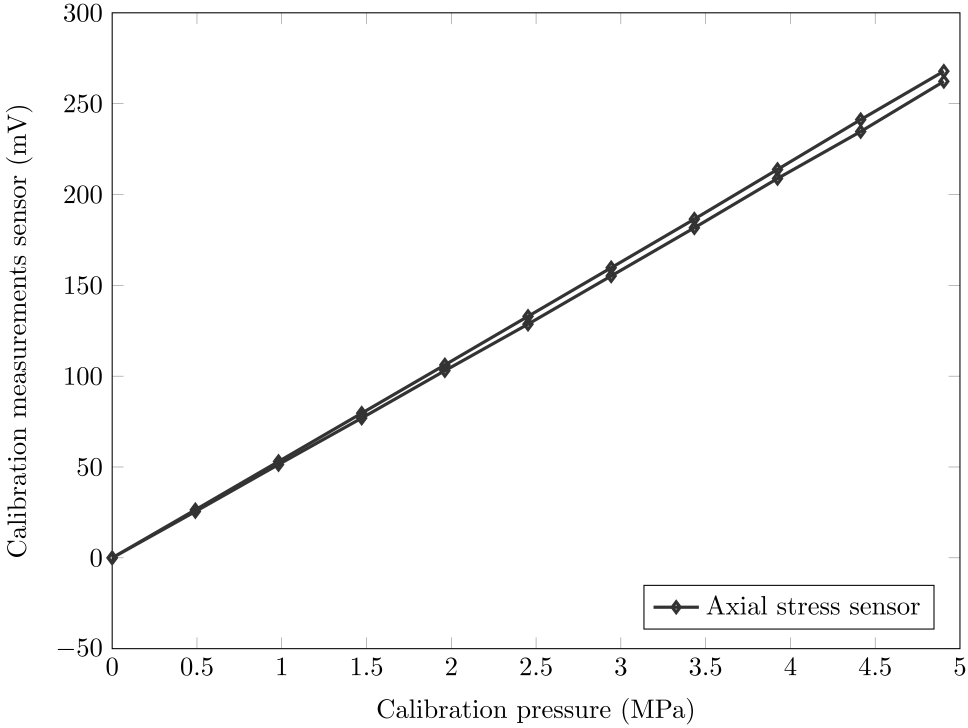

Figure 5.22: Bounds of calibration axial stress sensor measurements in loading in the lever system.

5.8 Conclusions

An instrumented model pile for measurements of horizontal contact stress in the geotechnical centrifuge was realized. The model configuration includes small-scale sensors, and calibration equipment which was specially made for the particular apparatus. The model pile design was analyzed in a numerical model to assess the effect of shear stress, axial loading and calibration. The small scale of the model pile resulted in significant oscillations in strain gauge output signal, possibly as a result of thermal expansion of the strain gauge membranes. A switched voltage supply and accompanying software was implemented to alleviate this effect. Calibration of the model pile showed good sensor performance.

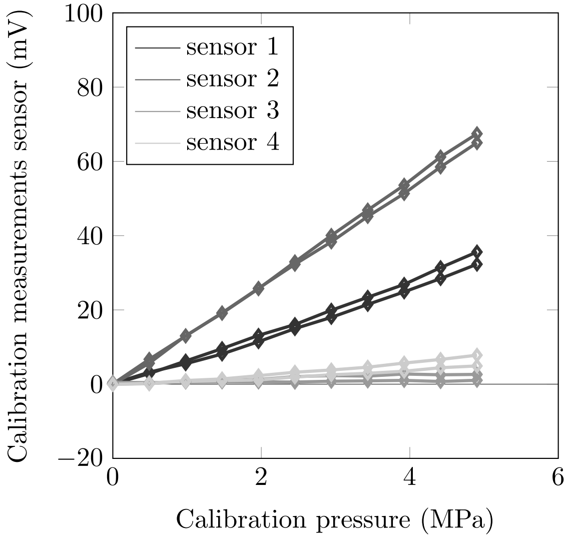

(a) Ranges of horizontal stress sensor calibration measurements during incremental stress increase.

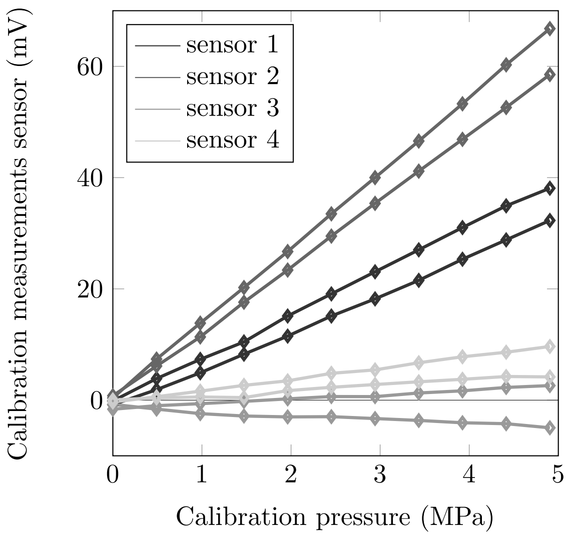

(b) Ranges of horizontal stress sensor calibration measurements during incremental stress decrease.

Figure 5.23: Calibration results: range of measurements

Chapter 6

Measurements

6.1 Stress measurements

6.1.1 Measurements of pile head load during continuous and incremental installation

The pile head load, base load and the total shaft friction are presented here to assess the behaviour of the whole model pile. The pile head load, base load, and total shaft resistance were measured and normalized with the pile area, A_{Pile}. The unit of the measurements were consequently force per area, which was convenient for the interpretation since these were converted into the same dimension. It was consequently possible to compare how these quantities evolves during the test.

The total penetration z/D is relatively small compared to prototype piles. The shaft friction measurements are consequently potentially influenced by the stress distribution close to the soil surface, e.g. surface heave. This potential disturbance was not possible to quantify.

The pile head load has been corrected for the self-weight of the model pile (measured at $1-g$ with a Mettler PM30-K 30 precision scale with ± 1 g accuracy [164]), and adjusted for the magnified average acceleration at $50-g$. During installation, the location of the pile in the centrifuge in the radial direction will change, and also the self-weight of the pile. This was not corrected for in the measurements, because the difference in relative radius is less than 10% before and after installation, and the difference from the mean acceleration is consequently even smaller. As a proportion of the total pile head load the inaccuracy of the self-weight of the pile is therefore small.

Figure 6.1 shows the principle for measurement of pile head load and pile base load. The pile base load was multiplied with the correction factor c_a, as explained in Appendix K. The total shaft friction per area was then calculated from the difference between the pile head and base load.

Figures 6.2, 6.3 and 6.4 show measurements of the pile head load, the pile base resistance, and the total shaft friction in the loose, medium dense, and dense soil sample. These mea-

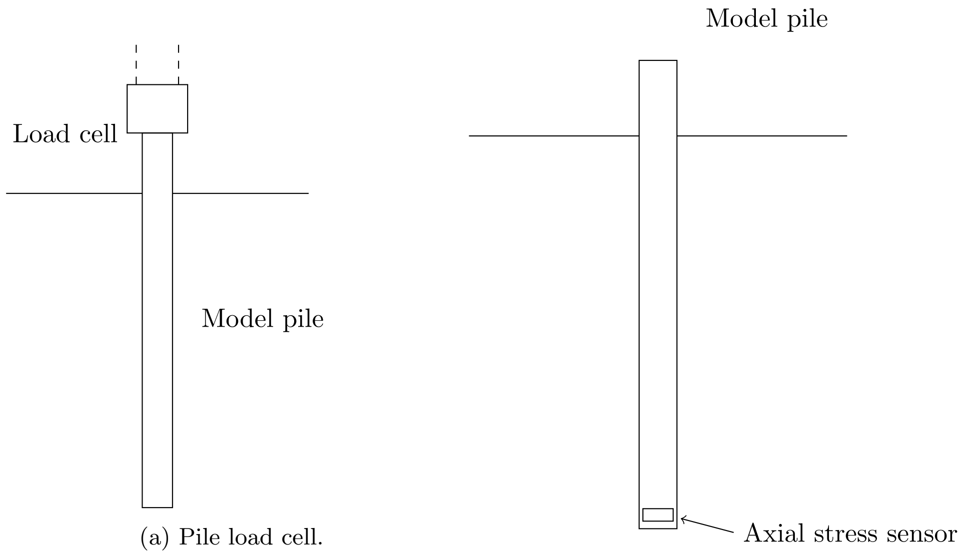

(a) Pile load cell.

(b) Pile base sensor.

Figure 6.1: Measurements of pile head load and pile base resistance.

surements are expressed in terms of force per unit area. Both the average and the range of the measurements are shown in Figures 6.2, 6.3 and 6.4. The range consists of the total range of the measurements at the same initial conditions and installation mode, shown in Table 3.5.

The measurements of pile head load in Figures 6.2, 6.3, and 6.4 show relatively good reproducibility of the experimental tests. The dense soil sample displays some variation in relative density with depth ($R_d = f(z)$) as a result of the sample preparation procedure, as seen by the change in pile base load in Figure 6.4, compared with e.g. [49]. This is further discussed in Appendix E.

The type of overall response during continuous installation corresponds to the behaviour observed in several other laboratory tests of silica sands in different experimental variations, e.g. [53], [136], [151]. The pile head load in Figures 6.2a, 6.3a, and 6.4a increases gradually with penetration. The effect of the soil grain shape has been shown to have a large effect on the soil behaviour in experiments, e.g. [203], but has not been analyzed in these tests since only one soil type was used. The soil sample was prepared from a large soil container and was consequently fresh for each test which means that any possible change in soil properties would not affect the subsequent model tests.

The stress level was correctly scaled in the model tests, and did not display the type of behaviour observed in samples tested at a low stress level or at a higher constant stress level (in the calibration chamber), which also levels off to a more steady state behaviour after the initial installation, e.g. [197]. The difference between the loose and the medium dense sample is not very large in Figures 6.2a, 6.3a, and 6.4a, which suggests further densification of the loose soil sample as a result of the vibrations experienced during startup of the model (this effect was not possible to observe in the deformation measurements (since the gravitational acceleration resulted in an elastic deformation of the beam which carried the camera), and is therefore not corroborated by experimental evidence).

The measurements of incremental installation in Figures 6.5, 6.6 and 6.7 display a similar behaviour to continuous installation at full mobilization of each load cycles. During the load reversal, i.e. when then pile is unloaded and subsequently loaded, the pile head load decreases rapidly, and both the unloading and reloading stage show a large load-deformation stiffness that is higher than the penetration resistance stiffness for the continuously installed model.

The incremental installation behaviour has been modelled in some previous model tests, e.g. [38], [151] and [197]. The load cycles result in step-wise two way loading of the model, [128]. In between the load cycles, the horizontal stress is lowered to the non-loaded level, and the shaft friction is only carrying the self-weight of the model pile, similar to the prototype during impact driving, [82]. In the prototype, the dynamic load in saturated soil results in inertial and consolidation effects, but these are not included in the model, [47].

The incremental installation behaviour in Figures 6.5, 6.6 and 6.7 is different from that observed in the field, [151]. The friction fatigue effect will be discussed later in the text, but the response of the small model pile is dominated by the end-bearing, and not by the shaft friction. The effect of friction fatigue is consequently relatively small in comparison to standard types of piles which have a higher L_{Pile}/D_{Pile}, [89], [150], [241].

The pile base load in Figures 6.2b, 6.3b, and 6.4b is similar to that observed in other model tests, [151]. The behaviour in the field is more cumbersome to overview, since most tests have been carried out with slender piles with large L/D-ration, that more resemble the cone penetration tests, and consequently display a similar behaviour, e.g. [49], [89], [148], and also depends on the installation method.

The total shaft friction in Figures 6.2c, 6.3c, and 6.4c is shown to constitute a relatively small part of the total pile head load, but seems to increase steadily in the model tests. The effect of friction fatigue is discussed later in the test for the incremental installation mode.

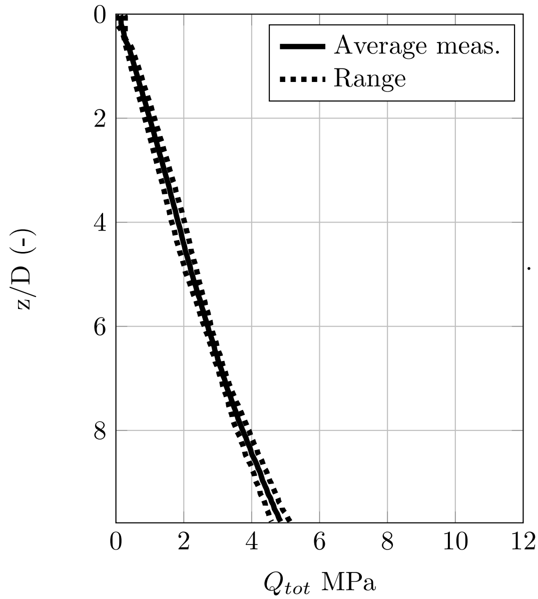

(a) Pile head load per area.

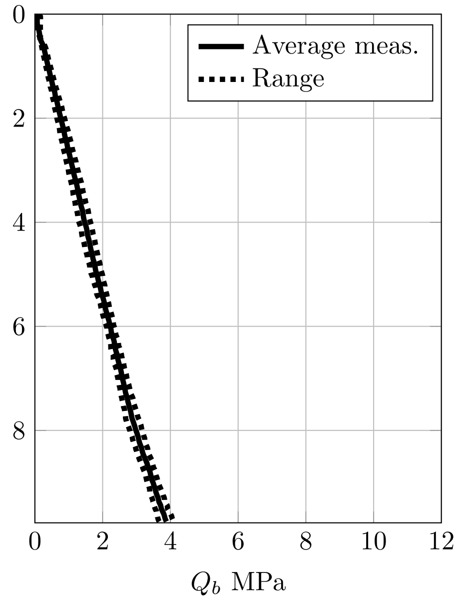

(b) Pile base resistance.

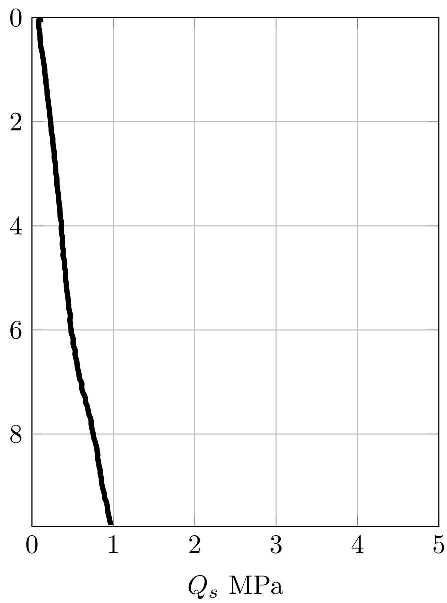

(c) Total shaft resistance.

Figure 6.2: Measurements of pile head load, base resistance, and total shaft friction per area in the loose soil sample during continuous installation.

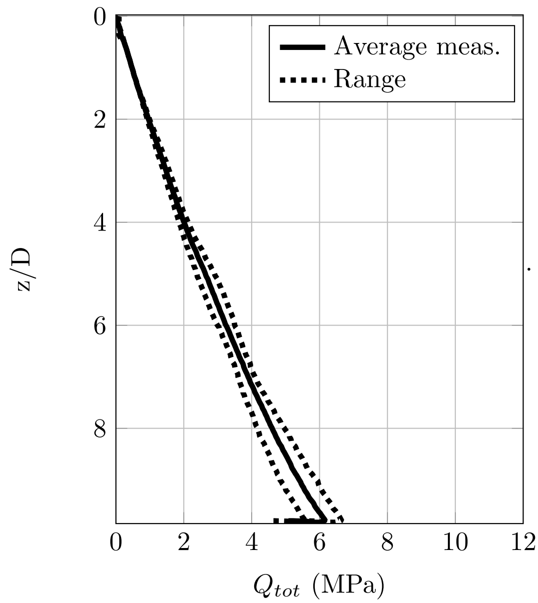

(a) Pile head load per area.

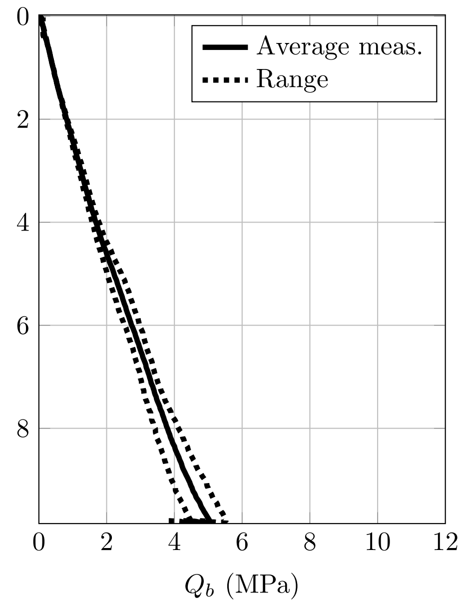

(b) Pile base resistance.

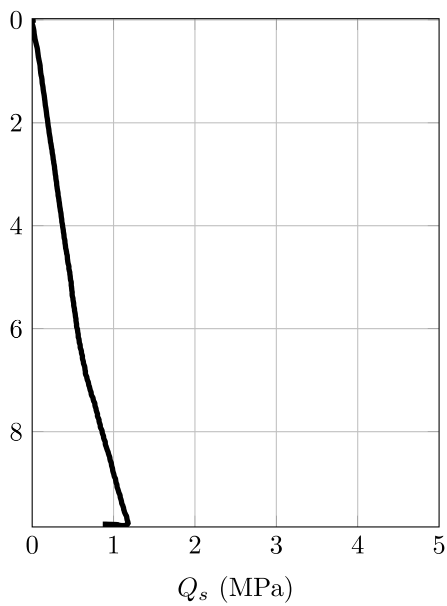

(c) Total shaft friction.

Figure 6.3: Measurements of pile head load, pile base resistance, and total shaft friction in the medium dense soil sample during continuous installation.

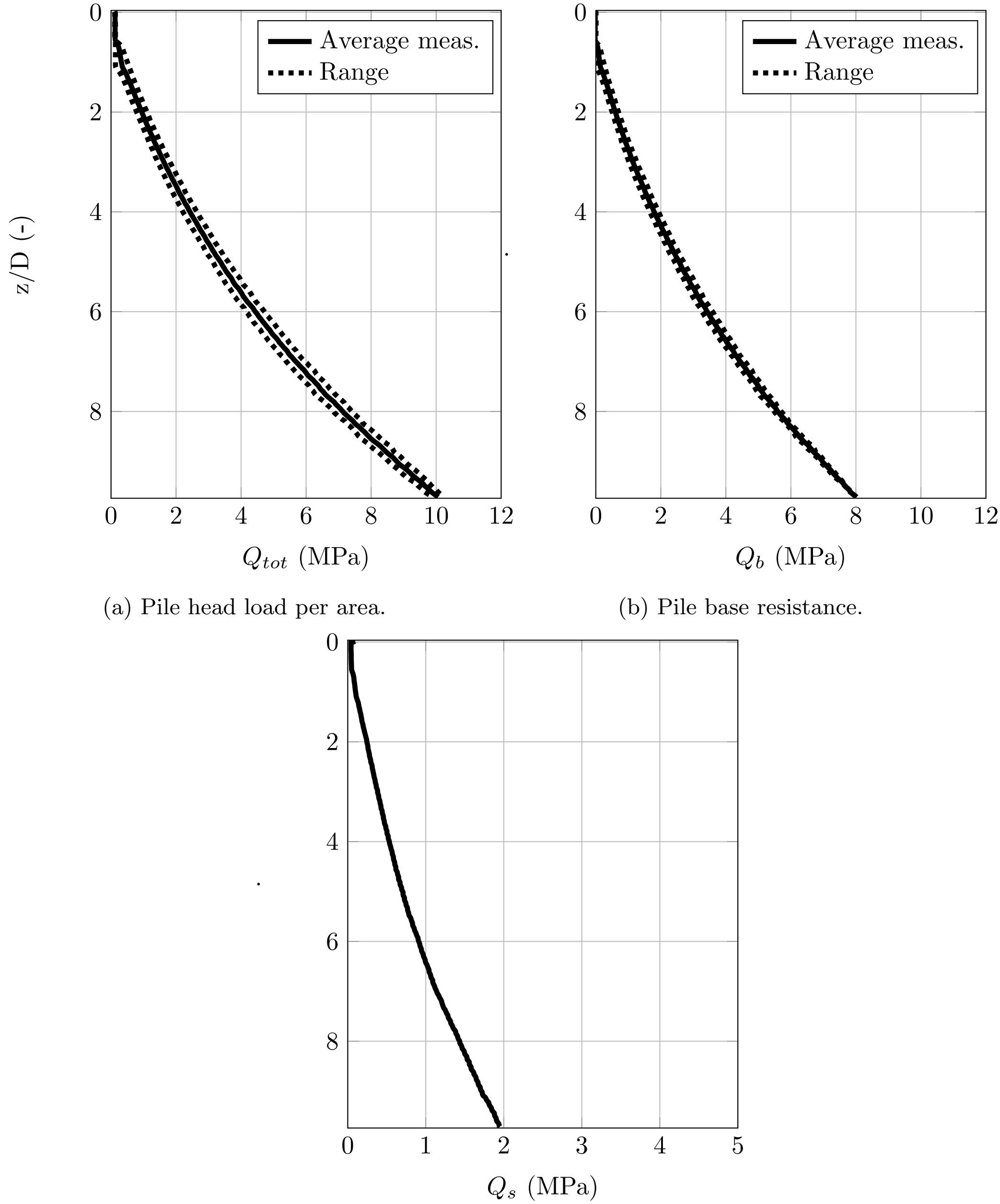

(a) Pile head load per area.

(b) Pile base resistance.

(c) Total shaft friction.

Figure 6.4: Measurements of pile head load, pile base resistance, and total shaft friction in the dense soil sample during continuous installation.

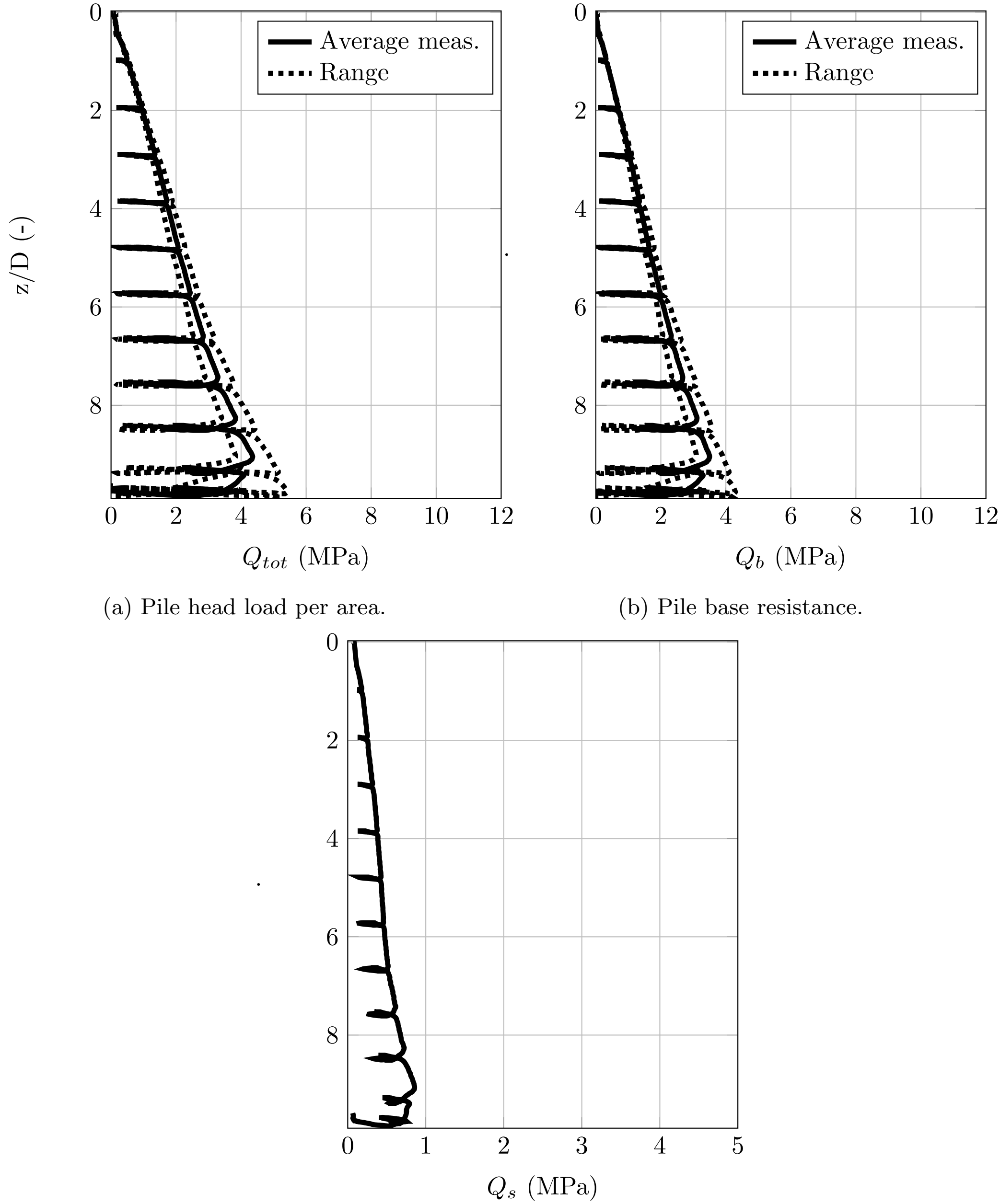

(a) Pile head load per area.

(b) Pile base resistance.

(c) Total shaft fricton.

Figure 6.5: Measurements of pile head load, pile base resistance, and total shaft fricton per area in the loose soil sample during incremental installation.

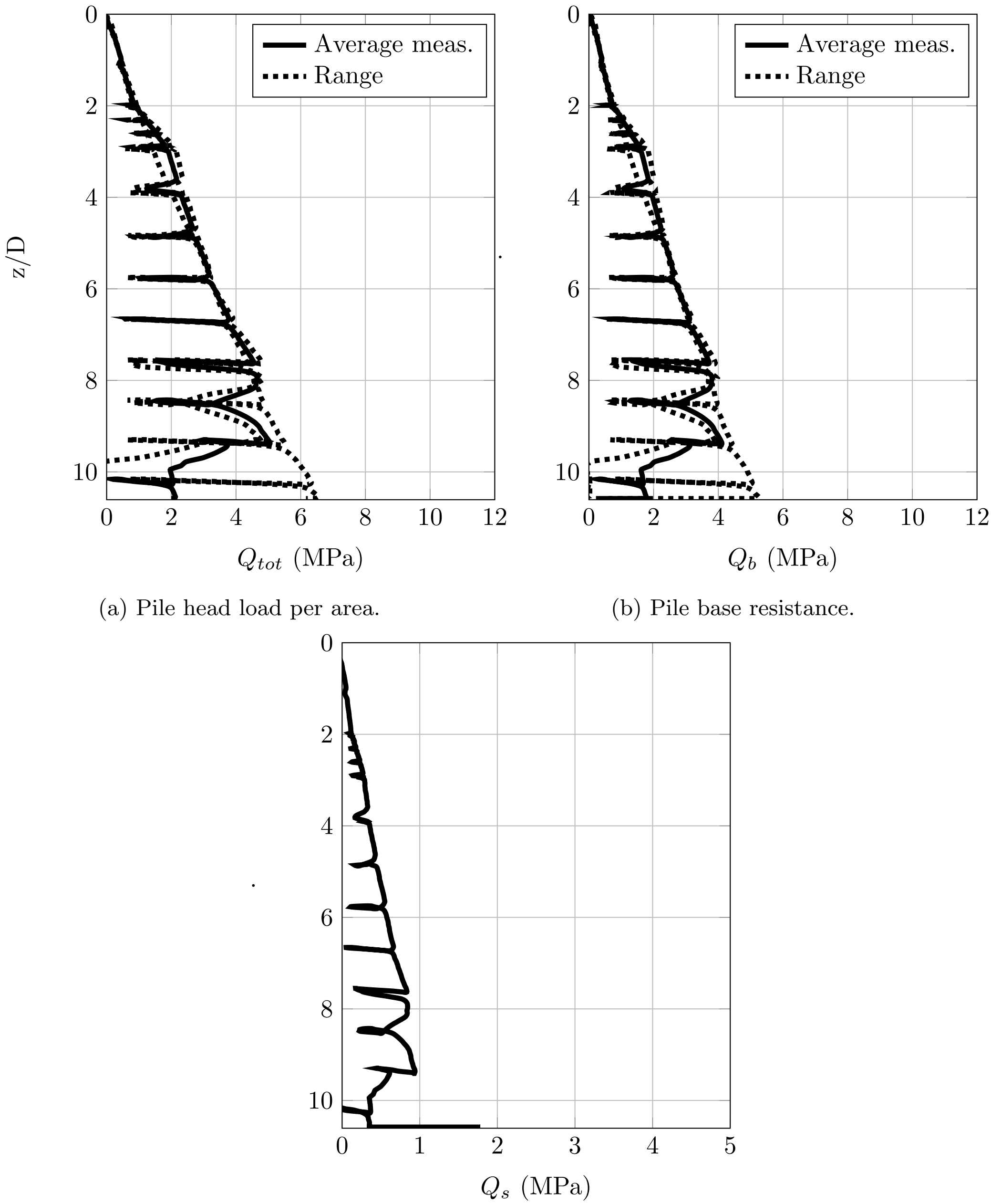

(a) Pile head load per area.

(b) Pile base resistance.

(c) Total shaft friction.

Figure 6.6: Measurements of pile head load, pile base resistance, and total shaft friction per area in the medium dense soil sample during incremental installation.

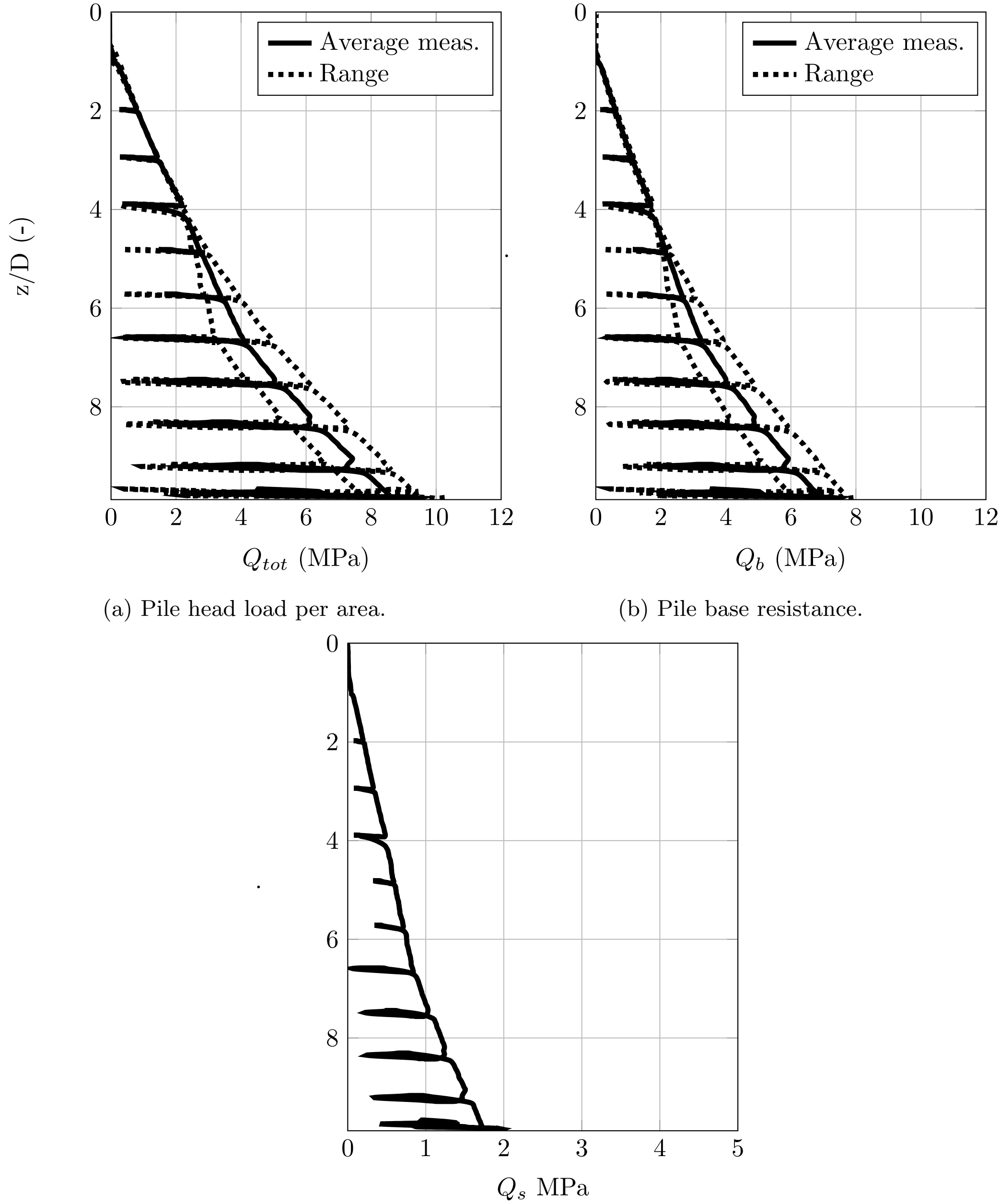

(a) Pile head load per area.

(b) Pile base resistance.

(c) Total shaft friction.

Figure 6.7: Measurements of pile head load, pile base resistance, and total shaft friction per area in the dense soil sample during incremental installation.

6.1.2 Measurements of total horizontal contact stress $\sigma'_{h,tot}$ during continuous and incremental installation

Figures 6.9, 6.10 and 6.11 show measurements of the horizontal contact stress at instrumentation levels 1 and 2, (Figure 6.8). The measurements show the mean value of the two or three test (according to Table 3.5) in the solid line, and the range of measurements in dotted lines. The full set of measurements are given in Appendix M and N.

The measurements in Figures 6.9, 6.10 and 6.11 again agree relatively well with the behaviour seen in other tests, e.g. [53], [136], [151]. The total horizontal stress is seen to be governed by the change of the effective vertical stress, which results in a steady increase of the total horizontal stress during installation. This is in contrast with measurements in the calibration chamber, e.g. [83], [128], [127], in which the total horizontal stress reaches a maximum value at the constant vertical effective stress.

The horizontal stress in Figures 6.9, 6.10 and 6.11 is also observed to be governed by the initial relative density. This agrees with the assumptions frequently made in design, e.g. [82], [141], [163]. In such types of analysis, the shaft friction is linked to the initial relative density of the soil through the frictional properties of the soil, [31]. This seems to be a reasonable assumption for the continuously installation piles in Figures 6.9, 6.10 and 6.11.

These measurements do not show evidence of friction fatigue. The reason is believed to be the relatively large ratio of dilational stress ($\Delta\sigma'_h$) relatively to the total horizontal stress ($\sigma_{h,tot} = \sigma_{h,n} + \Delta\sigma'_h$, where $\sigma_{h,n}$ is the stationary stress) for the small scale pile. Later in the text the effect of scaling on the horizontal stress is discussed in more detail.

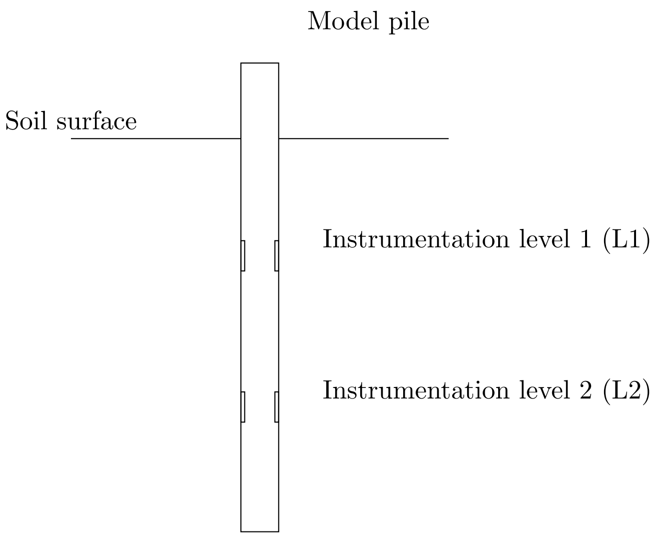

Figure 6.8: Instrumentation level 1 and 2 on the instrumented model pile.

Figures 6.12, 6.13 and 6.14 show measurements of the the total horizontal contact stress for

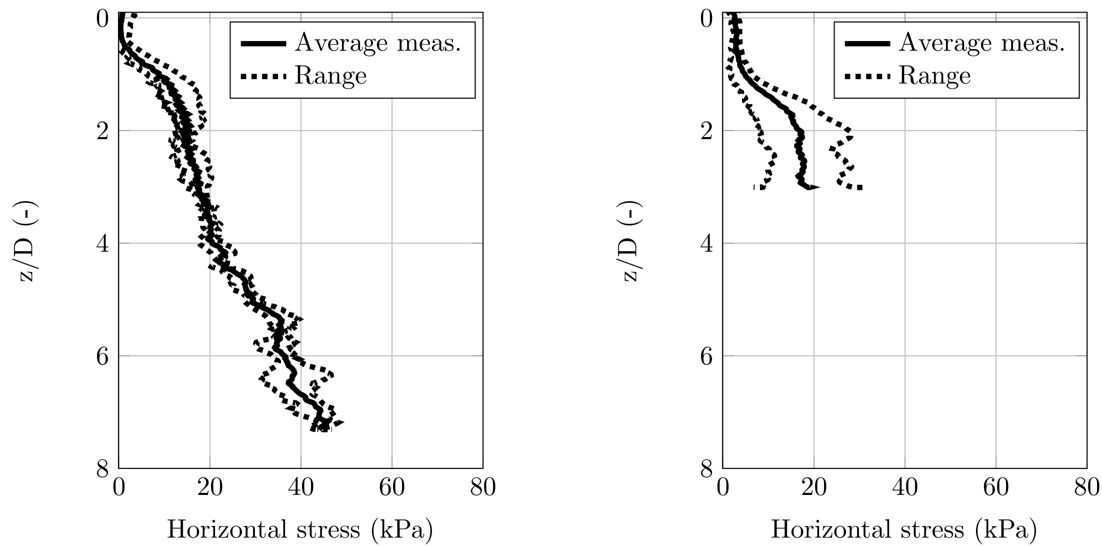

(a) Instrument level L2.

(b) Instrument level L1.

Figure 6.9: Range of measurements of total horizontal stress $\sigma'_{h,tot}$ in the loose soil sample for instrument level L1 and L2 during continuous installation.

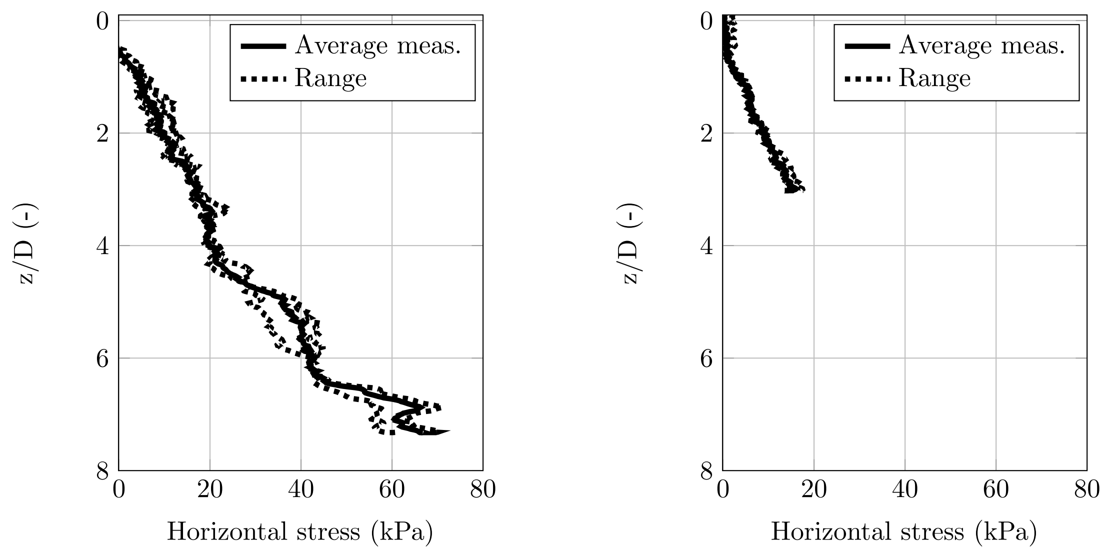

(a) Instrument level L2.

(b) Instrument level L1.

Figure 6.10: Range of measurements of total horizontal stress $\sigma'_{h,tot}$ in the medium dense soil sample for instrument level L1 and L2 during continuous installation.

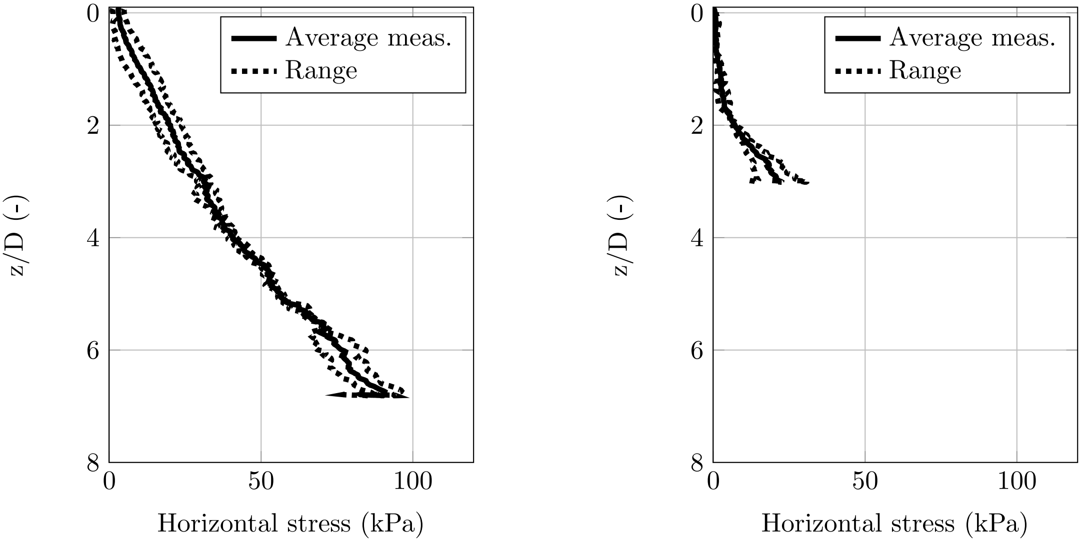

(a) Instrument level L2.

(b) Instrument level L1.

Figure 6.11: Range of measurements of total horizontal stress $\sigma'_{h,tot}$ in dense soil sample for instrument level L1 and L2 during continuous installation.

instrumentation level 1 and 2 for incremental installation in loose, medium dense and dense soil samples.

These measurements of the incremental installation mode change between loading and unloading in cycles. The difference in stress mobilization is probably caused by the load cycles during installation, in which the stress is initially increased during loading and subsequently decreased during unloading. The total horizontal stress is mobilized at each load cycle, and increases for rest to the peak value in the same way as for the pile head load. The cyclically installed behaviour of the total horizontal stress was also measured in [151]. It was observed that the effect of the load cycles was larger for the non-loaded horizontal stress than for the total horizontal stress.

Figures 6.12, 6.13 and 6.14 also show that the load cycles result in shear loading at the pile-soil interface during the installation, which is similar to field measurements and laboratory measurements, [83], [148], [151]. This is later discussed in relation to the friction fatigue effect.

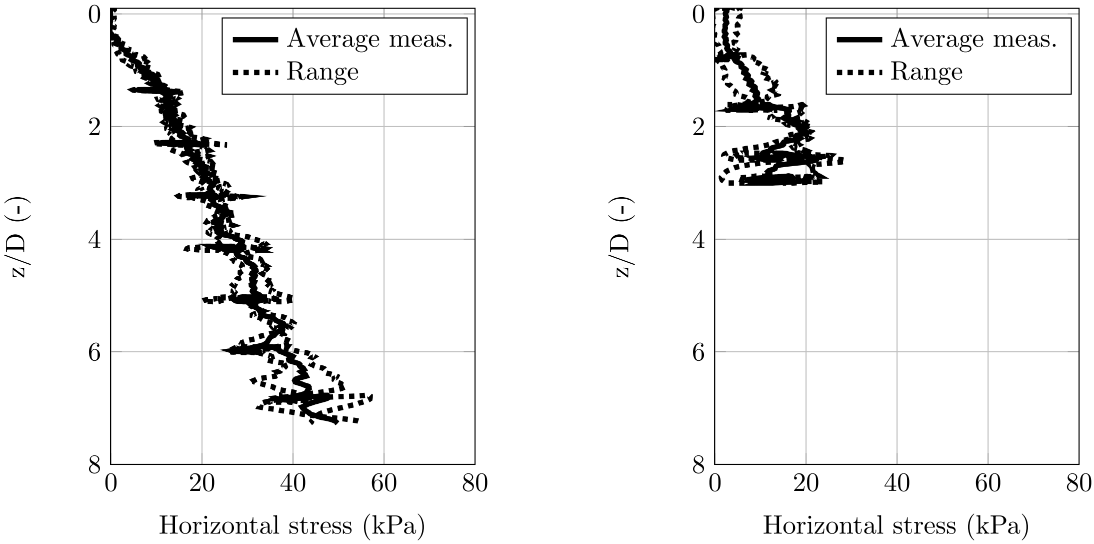

(a) Instrument level L2.

(b) Instrument level L1.

Figure 6.12: Range of measurements of total horizontal stress $\sigma'_{h,tot}$ in loose soil sample for instrument level L1 and L2 during incremental installation.

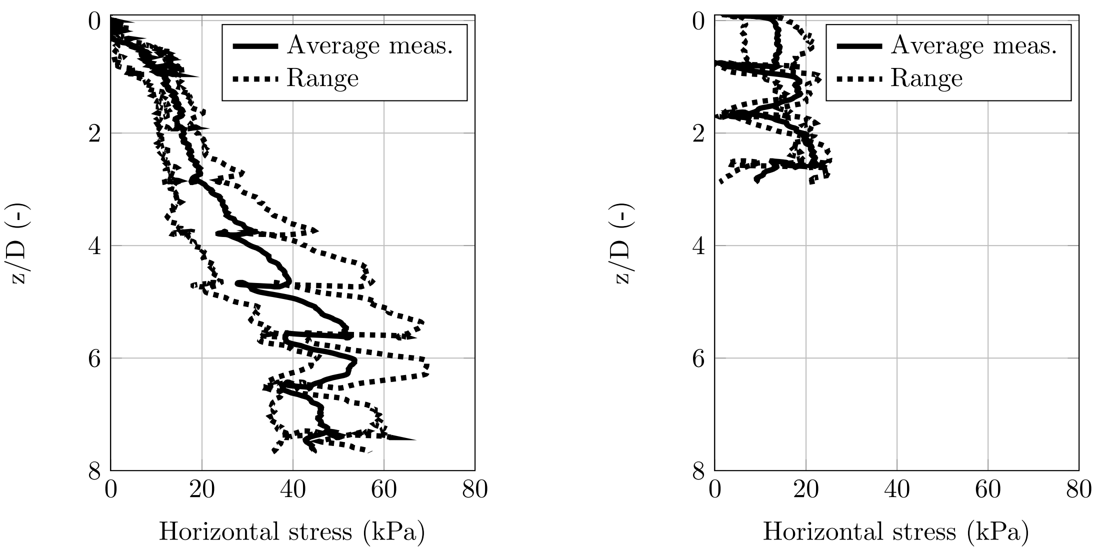

(a) Instrument level L2.

(b) Instrument level L1.

Figure 6.13: Range of measurements of total horizontal stress $\sigma'_{h,tot}$ in the medium dense soil sample for instrument level L1 and L2 during incremental installation.

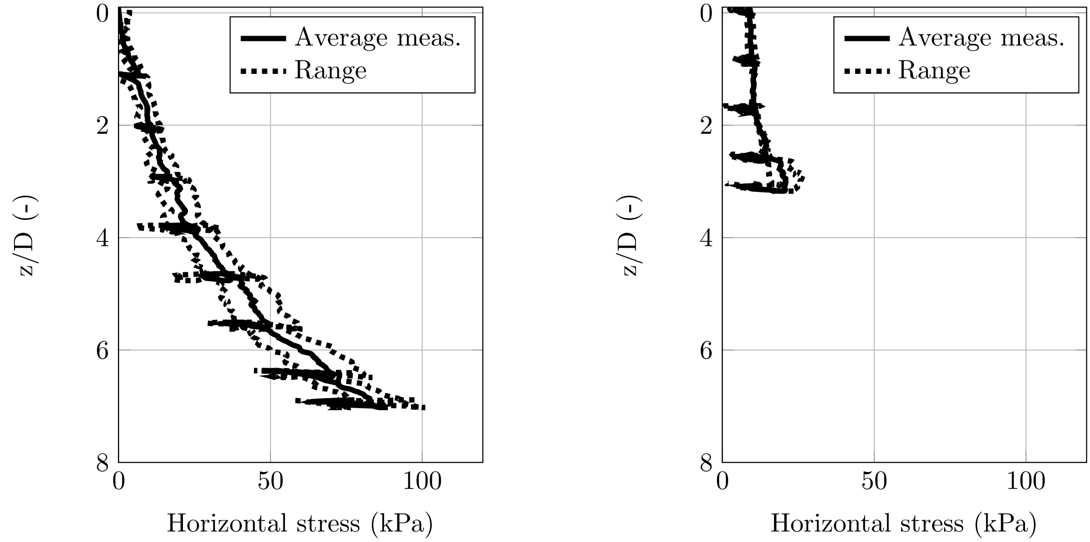

(a) Instrument level L2. (b) Instrument level L1.

Figure 6.14: Range of measurements of total horizontal stress $\sigma'_{h,tot}$ in the dense soil sample for instrument level L1 and L2 during incremental installation.

6.1.3 Measurements of horizontal contact stress normalized to base resistance

Figures 6.15a, 6.15b and 6.15c show the total horizontal contact stress $\sigma'_{h,tot}$ normalized with the pile base resistance, σ_b in the soil sample at the same depth y (hence σ_b is not taken at the same time t as the $\sigma'_{h,tot}$, but when the horizontal stress sensor has reached the same depth y).

The measurements during the initial phase probably suggests that the total horizontal contact stress measurements are less accurate when the stress level is low, since the measurement value is a small part of the total range of the sensor.

The steady level (at the pile tip position, with no friction fatigue included) of the total horizontal contact stress $\sigma'_{h,tot}$ normalized with the pile base resistance, σ_b is assumed in many empirical design methods, e.g. [40], [50], [64] for the horizontal stress.

It is also interesting to compare the model and prototype through the skin friction on a CPT. The expected value for the skin friction ($\tau_f = \tan(\delta)\sigma'_h$) at the tip of the pile is around 1% for sands, [49]. This results in a horizontal stress of around 2%-2.5% for normal frictional surfaces. The measured value of 1.5% is therefore low compared with field measurements by the CPT, e.g. in [256]. The possible reason is probably that the measuremnent is conducted at around $2.5D$ from the pile tip with some change in stress distribution which is similar to what was measured in [128].

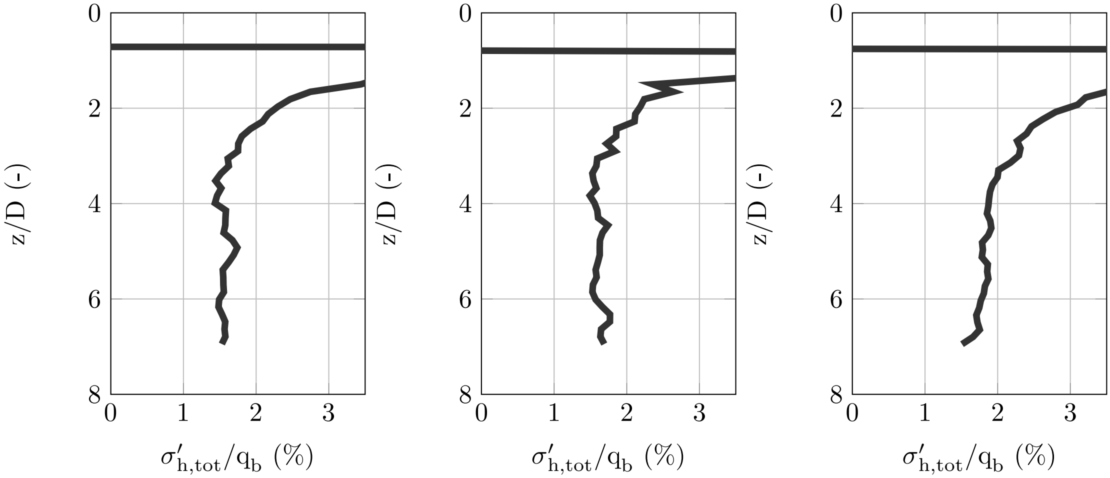

(a) $\sigma'_{h,tot}\sigma_b$ in the loose soil sample.

(b) $\sigma'_{h,tot}\sigma_b$ in the medium dense sample.

(c) $\sigma'_{h,tot}\sigma_b$ in the dense soil sample.

Figure 6.15: Normalized measurements of horizontal contact stress, $\sigma'_{h,tot}\sigma_b$.

6.1.4 Measurements of non-loaded horizontal contact stress $\sigma'_{h,n}$

The non-loaded horizontal contact stress $\sigma'_{h,n}$ consists of the horizontal stress level when the pile head is unloaded during incremental installation, following the methodology in [89], [148], [151]. This is not necessarily the lowest horizontal contact stress at the specific depth during the load cycle, as some changes occur when the pile is loaded again (probably as a result of stress rotations, [62]). But for a more formal definition it is measured at the location y when the pile head reaches its minimum load during an installation cycle.

The measurements were interpolated and subsequently plotted in Figures 6.16, 6.17 and 6.18. These measurements show the range of measurements of non-loaded horizontal contact stress $\sigma'_{h,n}$ in loose, medium dense, and dense soil samples during incremental installation procedure for the instrumentation level 1 and 2 of the model according to Figure 6.8.

The non-loaded horizontal contact stress $\sigma'_{h,n}$ in Figure 6.16, 6.17 and 6.18 is generally at least 10-20% lower than the total horizontal contact stress $\sigma'_{h,tot}$ (at full mobilization for incremental installation in Figures 6.12, 6.13 and 6.14). This is probably caused by the mobilization of horizontal stress during loading, in which the volumetric behaviour of the soil has a large effect on the pile-soil interaction, [34], [89], [151]. This effect will be discussed later in the text.

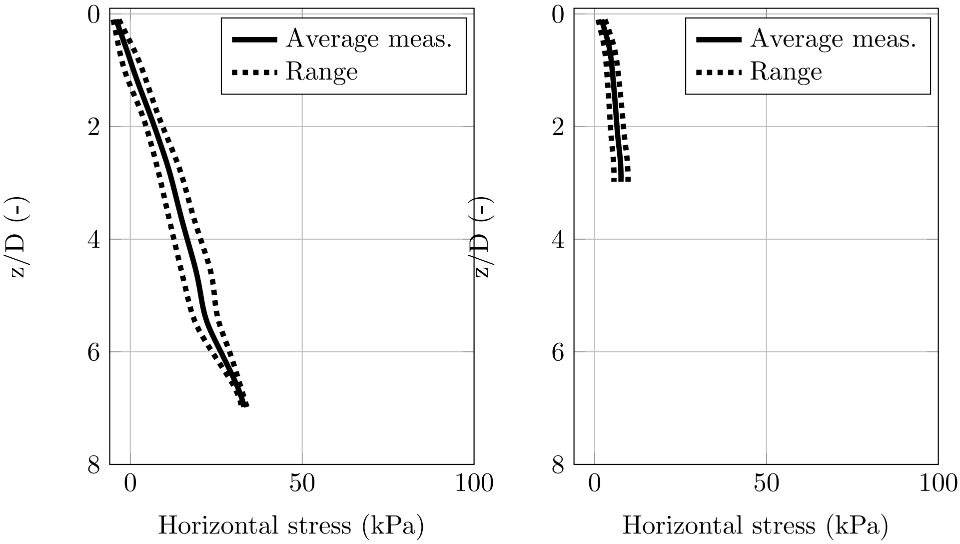

(a) Instrument level L2.

(b) Instrument level L1.

Figure 6.16: Range of measurements of non-loaded horizontal stress $\sigma'_{h,n}$ in the loose soil sample.

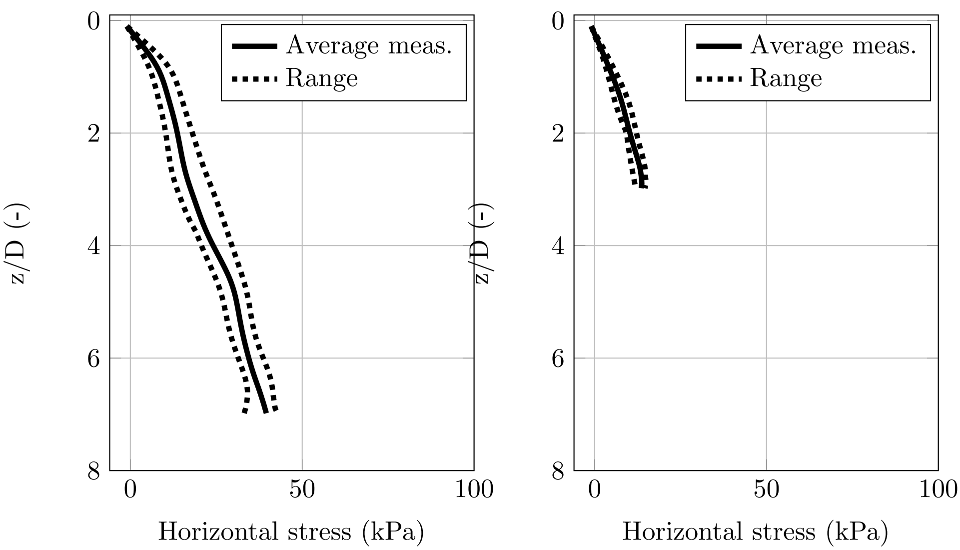

(a) Instrument level L2.

(b) Instrument level L1.

Figure 6.17: Range of measurements of non-loaded horizontal stress $\sigma'_{h,n}$ in the medium dense soil sample

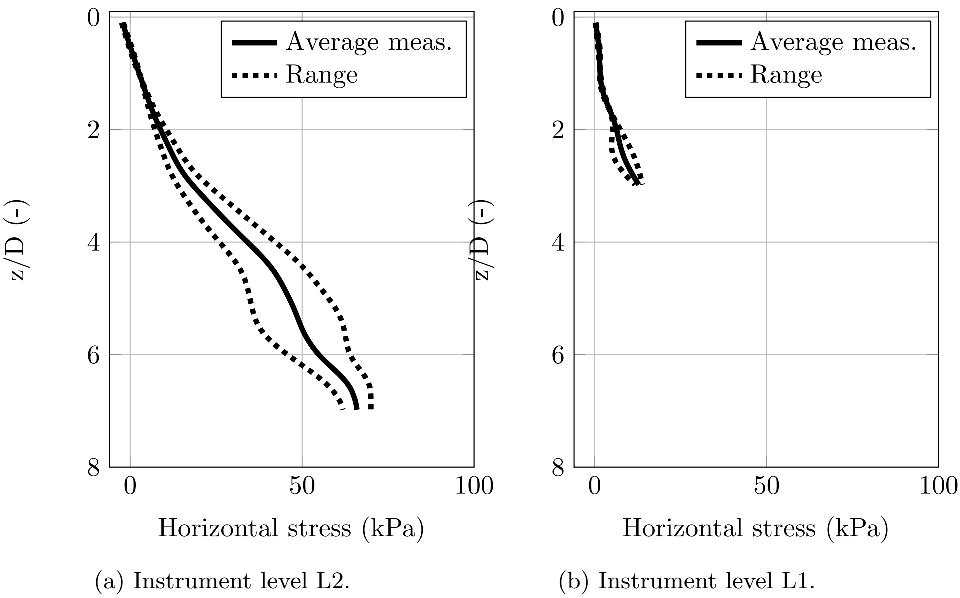

Figure 6.18: Range of measurements of non-loaded horizontal stress $\sigma'_{h,n}$ in the dense soil sample.

6.1.5 Stress components

Here the empirical methods to analyze the stress increase resulting from dilation (dilational stress) in [34], [125] and [148], is applied to the measurements to predict the effect of dilation. The presentation of the composition of the horizontal stress consists of total horizontal stress measurements from continuous installation $\sigma'_{h,tot}$, and non-loaded horizontal stress from incremental installation $\sigma'_{h,n}$, as well as the dilational stress component $\Delta\sigma'_h$ from continuous installation (which did not include the load cycles and was easier to calculate than the incremental measurements). The principle of the stress components is that the non-loaded horizontal contact stress $\sigma'_{h,n}$ and dilation are added together at each depth y, as shown in Figure 6.19. The principle of the measurements are shown in Figure 6.20 for a medium dense soil sample with the Baldi correlation for the shear modulus for the dilational horizontal stress.

The dilational component is calculated from the standard expression for axisymmetric cavity expansion around a circular pile, which is expanded to a rectangular pile shape in the same form, [34], [89], [148]:

$$\Delta\sigma'_h = \frac{4G}{D_{Pile}}\Delta h \tag{6.1.1}$$

This is obviously a simplified expression, since e.g. stress rotation, absolute horizontal stress, and stress distribution around the play may also govern the evolution of dilation, [62], [148], [218].

Correlation	Δh
Baldi ([12])	0.005 mm
Duncan-Chang ([75])	0.005 mm
Janbu ([117])	0.005 mm

Table 6.1: Parameters in correlation of $\Delta\sigma'_h$.

where the initial shear modulus G_{in} was calculated from three different empirical correlations by Baldi et al (B in Figure 6.21), Duncan and Chang (D in Figure 6.21), and Janbu (J in Figure 6.21), [12], [75], [117], according to Table 6.1. The shear modulus G is not constant according to the correlations, and is therefore not described in Table 6.1. A detailed description of the correlations for the shear modulus G_{in} is discussed in Appendix Q. The shear modulus was then multiplied with 0.4 to represent the shear modulus at large deformations, [151]. The size of the dilational expansion Δh was then found by fitting Equation (6.1.1) to the Δh which gave a good fit for the sum of the components $\sigma'_{h,n} + \Delta\sigma'_h$ and $\sigma'_{h,tot}$. This resulted in $\Delta h = 0.005$ mm, which is much smaller than the recommended values in [125] and [150] (around 25% of the recommended value). The model pile is significantly smoother than the prototype pile, which partly accounts for the lower interface friction. Figure 6.21a, Figure 6.21b, and Figure 6.21c show the components of the total horizontal effective stress $\sigma'_{h,tot}$. Measurements conducted on model piles show that the shear modulus could be an even smaller fraction of G_{in} [147], which means that the whole term $G\Delta h$ here represents the correlation of dilational expansion. Since two coefficients are subsequently needed to calculate the dilational horizontal stress, possible combinations of the two parameters have not been explored in the measurements. The effect of the relatively large shear zone in comparison to the prototype possibly has also a large effect on the estimated size of the Δh, since the same effect was estimated in scaled tests, [147]. The differences between the model and the prototype are consequently partly possible to explain by the effect of scaling, [53].

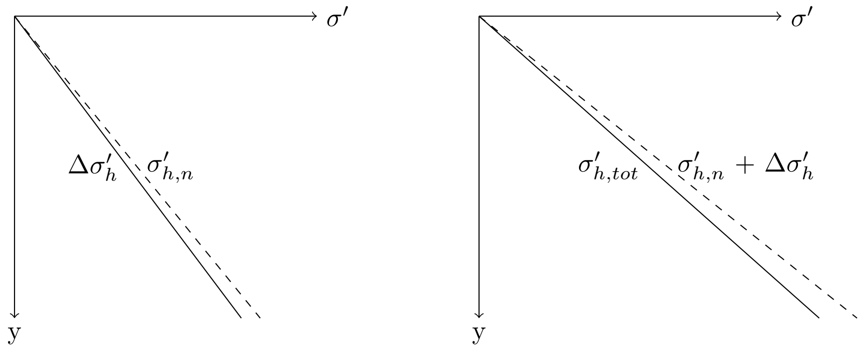

(a) $\sigma'_{h,n}$ and $\Delta\sigma'_h$.

(b) $\sigma'_{h,n} + \Delta\sigma'_h$ compared to $\sigma'_{h,tot}$.

Figure 6.19: Explanation of the components of horizontal total stress $\sigma'_{h,tot}$.

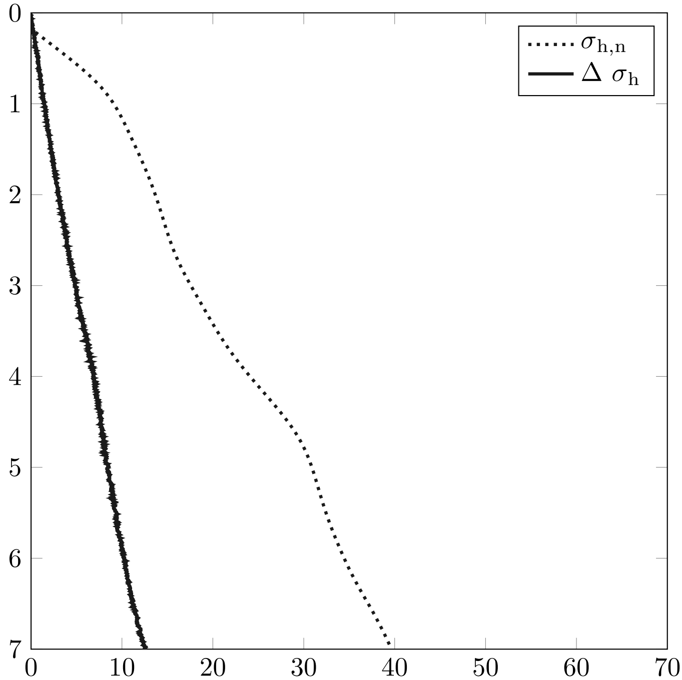

Figure 6.20: Dilational horizontal stress $\Delta\sigma'_h$ and non-loaded horizontal stress $\sigma'_{h,n}$ for a medium dense soil sample.

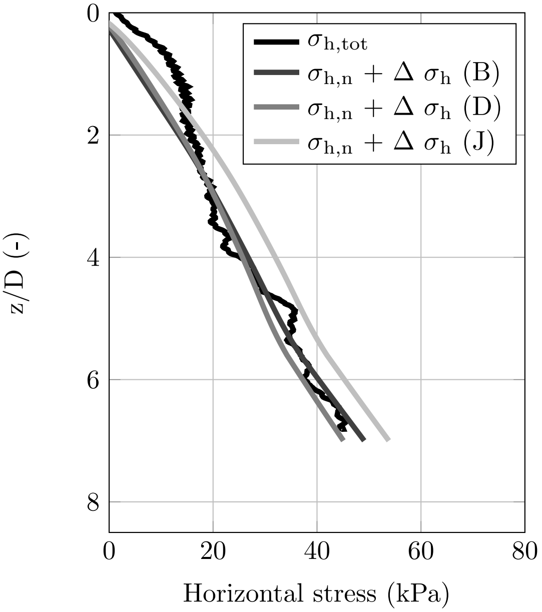

(a) The loose soil sample.

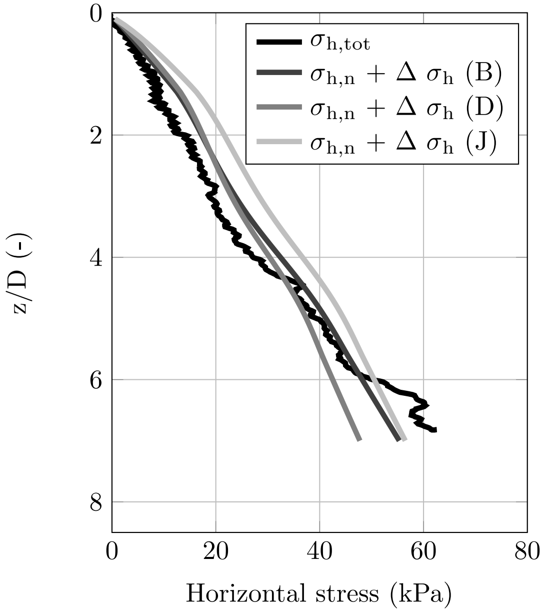

(b) The medium dense soil sample.

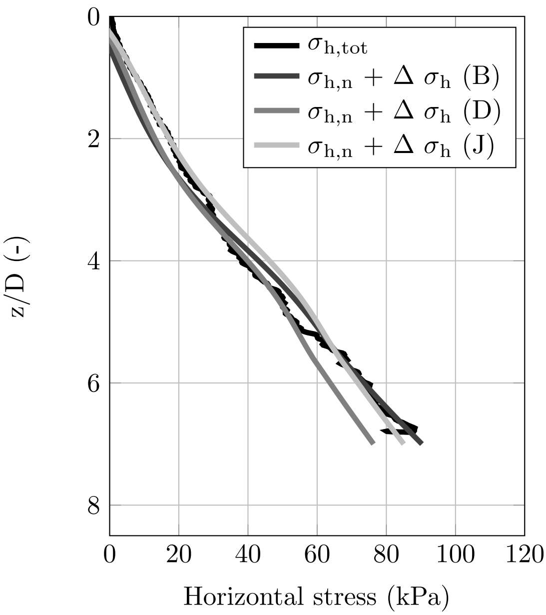

(c) The dense soil sample.

Figure 6.21: Stress component during installation

6.1.6 Measurements of friction fatigue

The friction fatigue effect was studied by the measurements of the non-loaded horizontal contact stress, $\sigma'_{h,n}$. This approach to measure friction fatigue is the most common in the laboratory and the field, e.g. [89], [151], [148]. Figures 6.22a, 6.22b and 6.22c show the mean measurements of the non-loaded horizontal contact stress $\sigma'_{h,n}$ at instrumentation level 1 and 2 in the loose, medium dense, and the dense soil sample.

The non-mobilized horizontal contact stress $\sigma'_{h,n}$ at instrument level $L2$ is multiplied by a linear friction fatigue factor R_{ff} (which is a linear correction factor) to find the $\sigma'_{h,n}$ at the other instrument level $L1$ after the effect of friction fatigue, [241]. The friction fatigue factor R_{ff} for the soil samples are shown in Table 6.22.

The measurements are comparable to field and laboratory experiments in [89], [151], [148]. It appears that the friction fatigue effect scales relatively well in different initial relative densities, which means that the relative effect is similar. This is also confirmed in field observations in [148], where the friction fatigue factor R_{ff} did not show a large variation even though the horizontal stress level changed. This means that the current CPT based design methods which take friction fatigue into account (e.g. [123], [138] and [150]) seem to be conceptually correct at different initial relative densities, which is an advantage.

Soil sample	R_{ff}
Loose (R_d = 40 %)	0.4-0.8
Medium dense (R_d = 60 %)	0.6-0.9
Dense (R_d = 80 %)	0.5-0.9

Table 6.2: The friction fatigue factor for the soil samples.

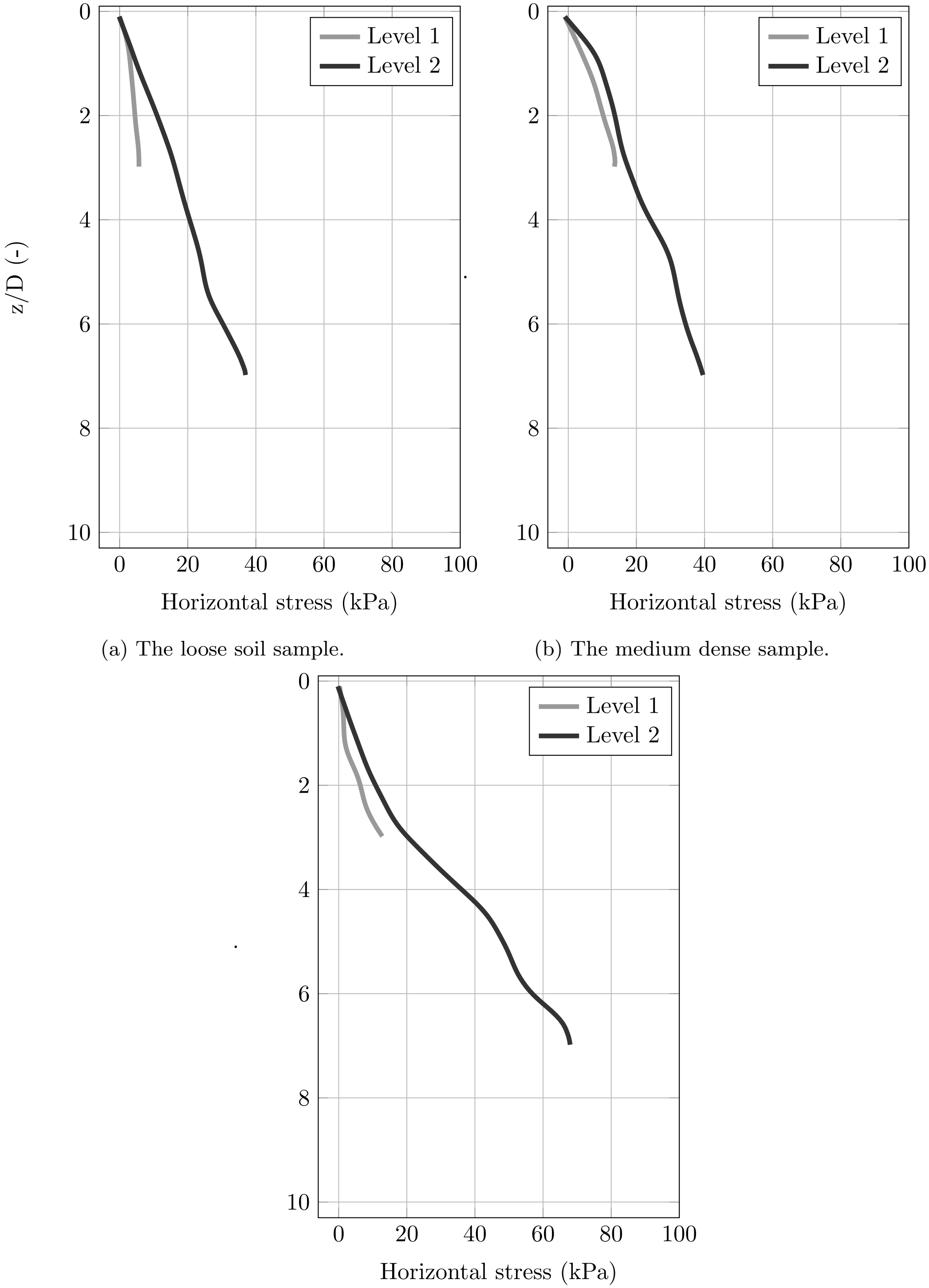

(a) The loose soil sample.

(b) The medium dense sample.

(c) The dense soil sample.

Figure 6.22: Measurements of non-loaded horizontal contact stress $\sigma'_{h,n}$.

6.1.7 Normalized measurement of pile head load and pile base load: continuous and incremental installation

The pile head load was measured both during continuous and incremental installation. Figures 6.23a, 6.23b and 6.23c show the pile head load during incremental installation normalized with the pile head load during continuous installation in similar initial conditions.

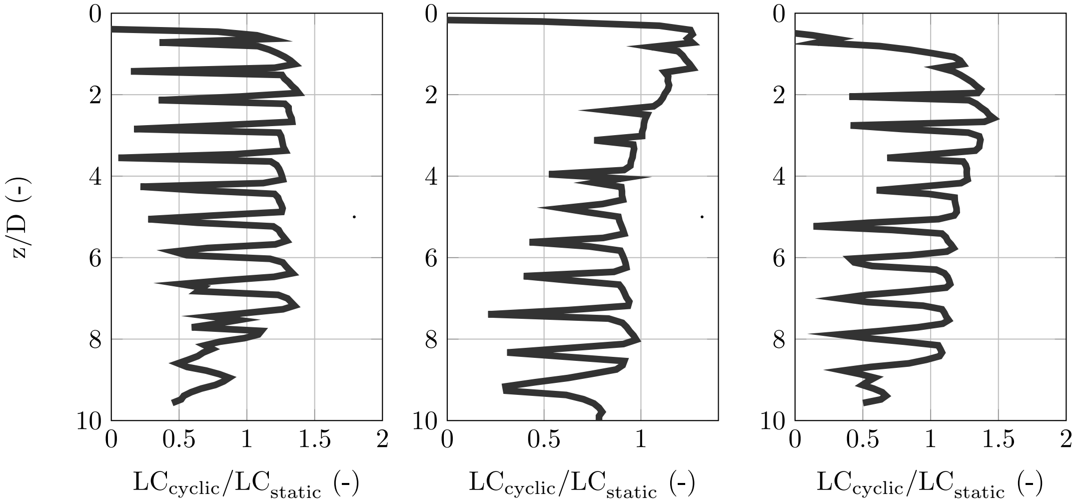

(a) The loose soil sample. (b) The medium dense sample. (c) The dense soil sample.

Figure 6.23: Pile head load during incremental installation, normalized with pile head load during continuous installation.

Figures 6.24a, 6.24b and 6.24c show the total pile base stress $\sigma_{b,incr}$ during incremental installation normalized with the pile base load per area during continuous installation $\sigma_{b,incr}$, in loose, medium dense, and the dense soil sample. Similar measurements were carried out in [151], but a comparable normalization was not carried out.

The ratio over 1 in the loose and dense tests probably results from the densification of the soil sample in between the tests, but this has not been possible to confirm through measurements of the sample height in between the tests.

The measurements suggest some effect of friction fatigue effect (e.g. loss of shaft resistance) is more pronounced in the incrementally installed model tests, since the base load in not influenced by the load cycles, while there is some effect of the load cycles in the pile head load measurements. There are several factors which obscures a clear conclusion, such as the low ratio in the beginning of the tests (resulting a lower accuracy, since the measurements represent a smaller part of the total range), and possible densification in the denser soil test as a result of the loading and unloading and could depend on the pile slenderness ratio L_{Pile}/D_{Pile} and the boundary conditions.

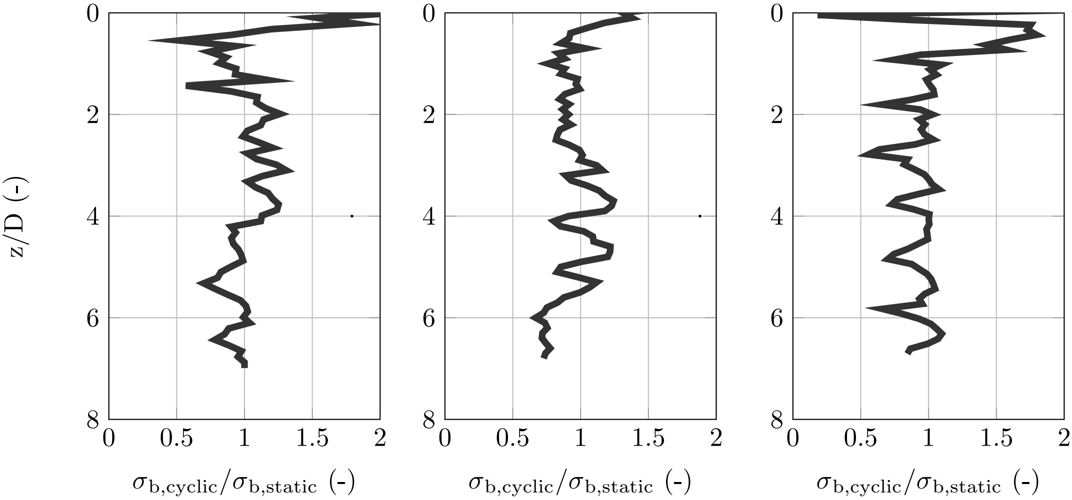

(a) The loose soil sample. (b) The medium dense sample. (c) The dense soil sample.

Figure 6.24: Normalized measurements of incremental and continuous pile base load, $\sigma_{b,incr}/\sigma_{b,cont}$.

6.1.8 Measurements of pile head load during static pile load tests

The model pile was unloaded after installation. Subsequently a displacement controlled static pile load test to $0.2D$ (at 0.01 mm/s displacement) was carried out.

Figures 6.25a, 6.25b and 6.25c show the mean measurements of pile head load during a static pile load test in the loose, medium dense and dense soil sample after both the continuous and the incremental installation method.

The full range of measurements are presented in Appendix *P*.

Figures 6.25a and 6.25b show that there is not a large difference between the maximum capacity of the loose soil sample and the medium dense soil sample for the $0.2D$ displacement. There could be a result of the densification of the soil during installation, [82]. The pile are also relatively short with a large diameter, which means that the end-bearing capacity dominates the total shaft capacity of the pile, [173]. The densification of the loose soil sample is consequently sufficient to give a a relatively high base capacity in comparison with the loose soil sample, [125].

Relatively similar tests have been carried out in the laboratory, e.g. [38], [154], [153] but not necessarily for the wider range of initial relative densities shown here. Some tests, e.g. [38] have also been conducted in saturated soil, which seems to have less risk of compacting during cyclic load because of the damping of the water. The loose soil sample tested in the current test series could also be somewhat compacted after the installation of the model pile.

The dense soil sample in Figure 6.25c exhibits a more step-wise behaviour which seems to suggest that it interacts with the load frame. This effect is also present in the medium dense soil sample in Figure 6.25b. The load frame is consequently not stiff enough for the maximum load. This complicated to analyse before hand because of the relatively complicated geometry and load distribution of the load frame.

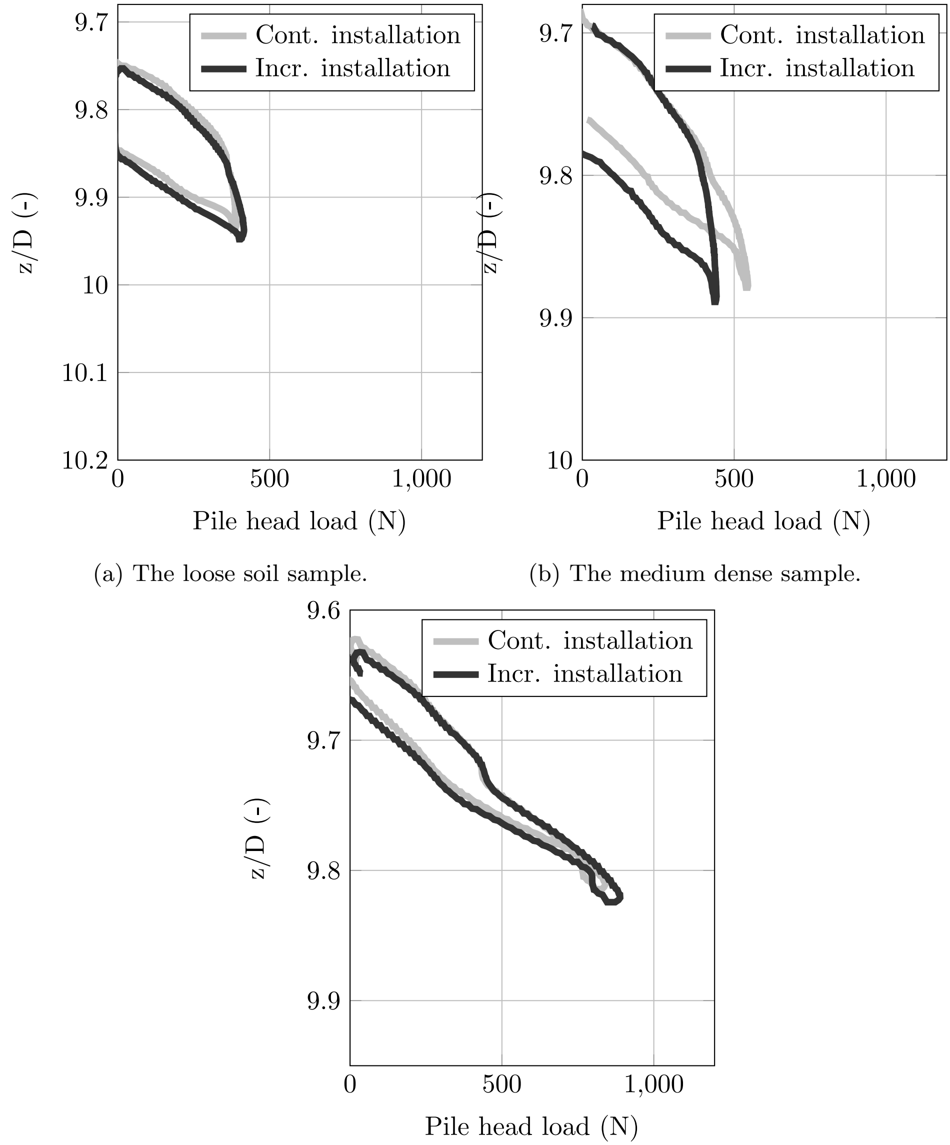

(a) The loose soil sample.

(b) The medium dense sample.

(c) The dense soil sample.

Figure 6.25: Pile head load measurements during static pile load test for continuous and incremental installation.

6.1.9 Measurements of total stress $\sigma'_{h,tot}$ during extraction test after continuous installation

After the static pile load test, an extraction test in tension was carried out. Figures 6.26, 6.27 and 6.28 show the measurements of total horizontal contact stress $\sigma'_{h,tot}$ at instrumentation level $L2$ in extraction tests after continuous installation in loose, medium dense, and dense soil sample.

The measurements in Figures 6.26, 6.27 and 6.28 show a maximum mobilized horizontal stress during loading that is around 50-60% of that measured during installation. This results in an lower ratio between compression and tension loading than was is normally adapted in most design models, e.g. [40], [50], [64].

Static pile load tests in tension have previously been carried out both in the laboratory and in the field, e.g. [47], [148], [151] and [256]. The current extraction test include the initial tension force, but also the post peak behaviour. Previous types of measurements have shown less softening after peak resistance, e.g. [47], [148] and [256]. Such tests have shown a quite large quantitative difference between different initial relative densities, but have not delved deeply into the qualitative behaviour, which is present in the current tests.

Figures 6.26, 6.27 and 6.28 show a relatively large difference between the loose and medium dense soil sample and the dense soil sample during pile extraction. The dense soil sample in Figure 6.28 shows a smaller peak value and a slower decline of horizontal contact stress. Since the loose and medium dense sample exhibit a different behaviour, this seems to be a result of the installation effects. The extraction tests probably also includes stress rotation after installation, which also seems to depend on the installation effects, [62].

The measurements in Figures 6.26, 6.27 and 6.28 show that the maximum horizontal stress $\sigma'_{h,tot}$ in tension is lower than in compression, by an estimated factor 0.6-0.7 at $h/D = 2.5$. This provides further evidence that piles in compression have a higher horizontal normal stress and consequently shaft friction than the same piles in tension. Explanation for this behaviour ranges from stress rotations to the Poisson's ratio effect, but are not possible to explain by the measurements, [62], [148], [147].

The full measurements of the extraction tests in tension are shown in Appendix P.

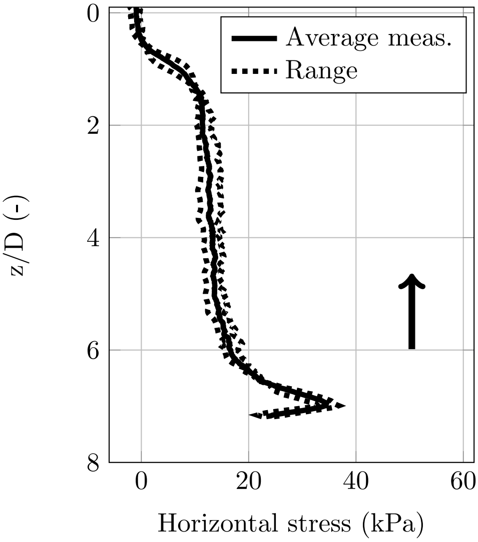

(a) The loose soil sample: instrument level L2.

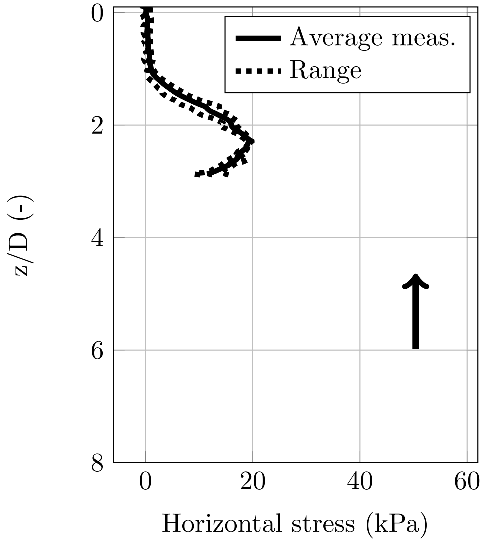

(b) The loose soil sample: instrument level L1.

Figure 6.26: Total horizontal stress $\sigma_{h,tot}$ in the initial loose soil sample during extraction test.

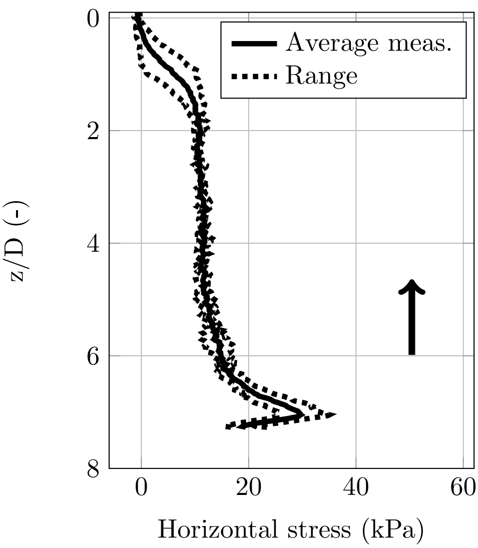

(a) The medium dense soil sample: instrument level L2.

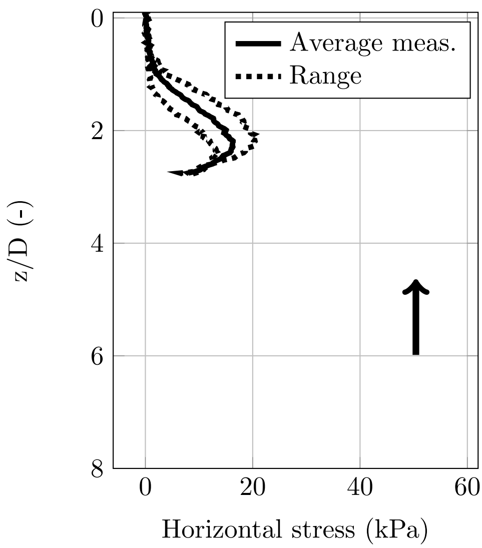

(b) The medium dense soil sample: instrument level L1.

Figure 6.27: Total horizontal stress $\sigma_{h,tot}$ in the initial medium dense soil sample during extraction test.

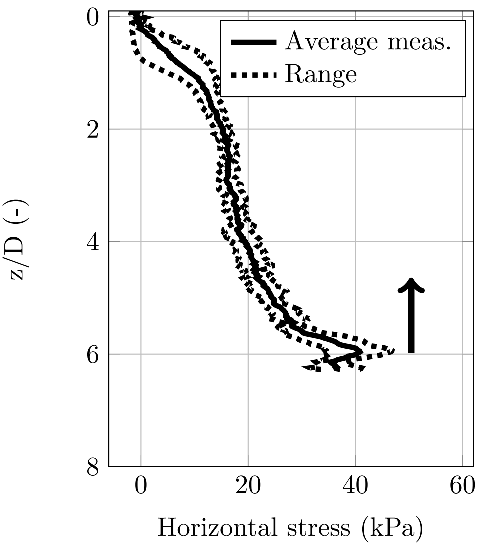

(a) The dense soil sample: instrument level L2.

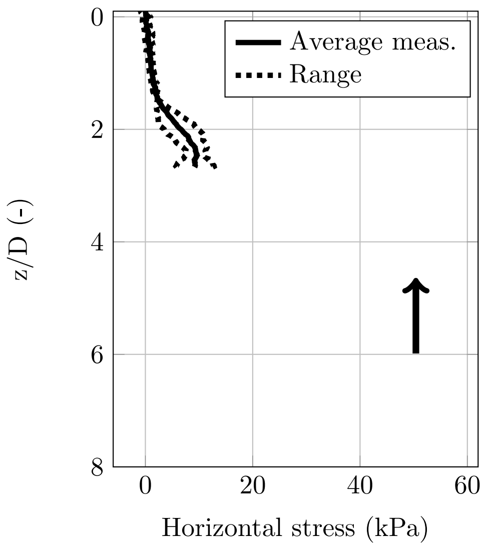

(b) The dense soil sample: instrument level L1.

Figure 6.28: Total horizontal stress $\sigma_{h,tot}$ in the initial dense soil sample during extraction test.

6.1.10 Measurements of total stress $\sigma'_{h,tot}$ during extraction test after the incremental installation procedure

Figures 6.29, 6.30 and 6.31 show the measurements of the total horizontal contact stress $\sigma'_{h,tot}$ during the extraction test after incremental installation in a loose, medium dense, and dense soil sample.

The measurements of extraction tests after incremental installation are relatively similar to those after continuous installation. The maximum horizontal stress is around 50-60% of the installation stress in Figures 6.29, 6.30 and 6.31. The pile has experienced at least one load cycle during the static pile load test, which previously has been shown to give a large effect of friction fatigue, [89]. The effect of dilation could also be relatively large during tensile loading, [34], [147], [151], and could have a large effect on the measurements.

The full measurements are shown in Appendix P.

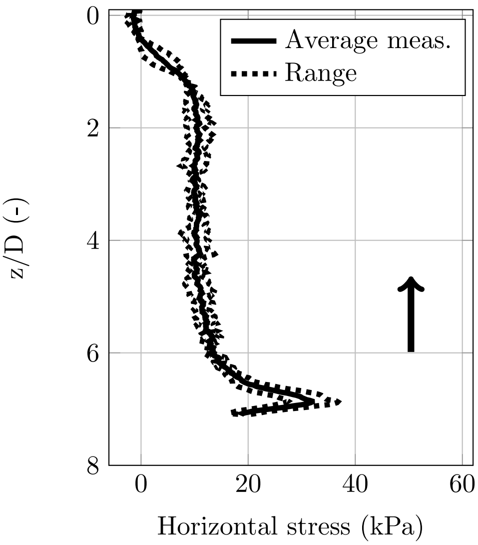

(a) The loose soil sample: instrument level L2.

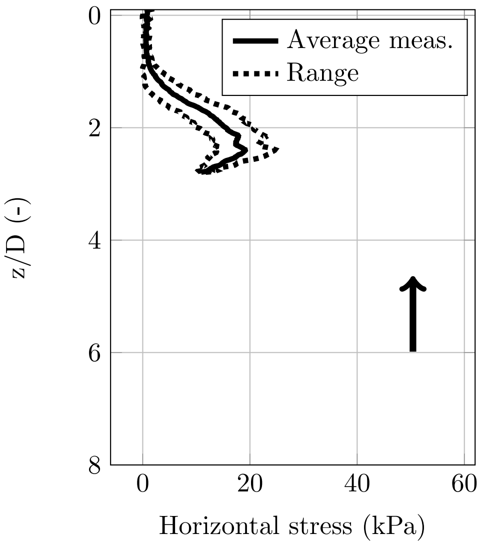

(b) The loose soil sample: instrument level L1.

Figure 6.29: Total horizontal stress $\sigma_{h,tot}$ in the initial loose soil sample during extraction test.

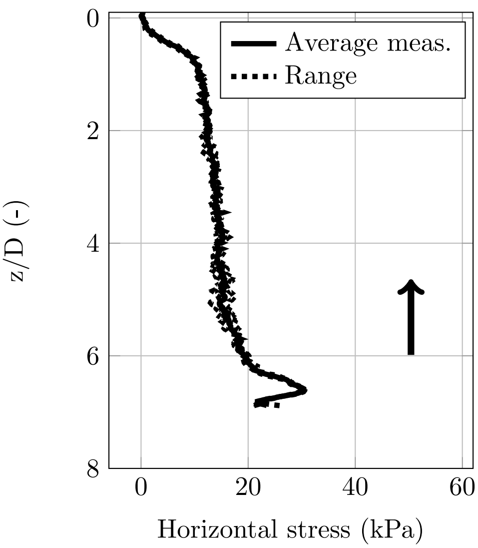

(a) The medium dense soil sample: instrument level L2.

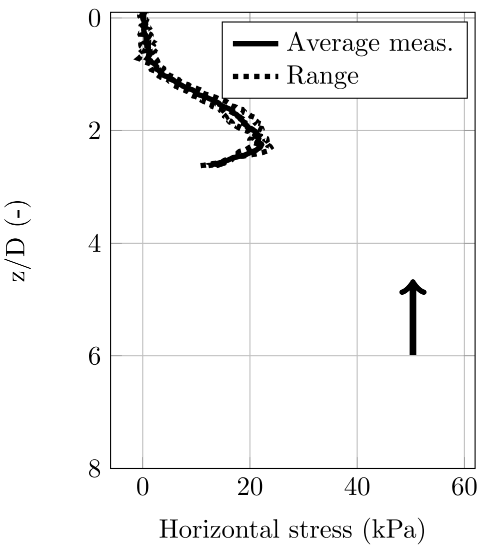

(b) The medium dense soil sample: instrument level L1.

Figure 6.30: Total horizontal stress $\sigma_{h,tot}$ in the initial medium dense soil sample during extraction test.

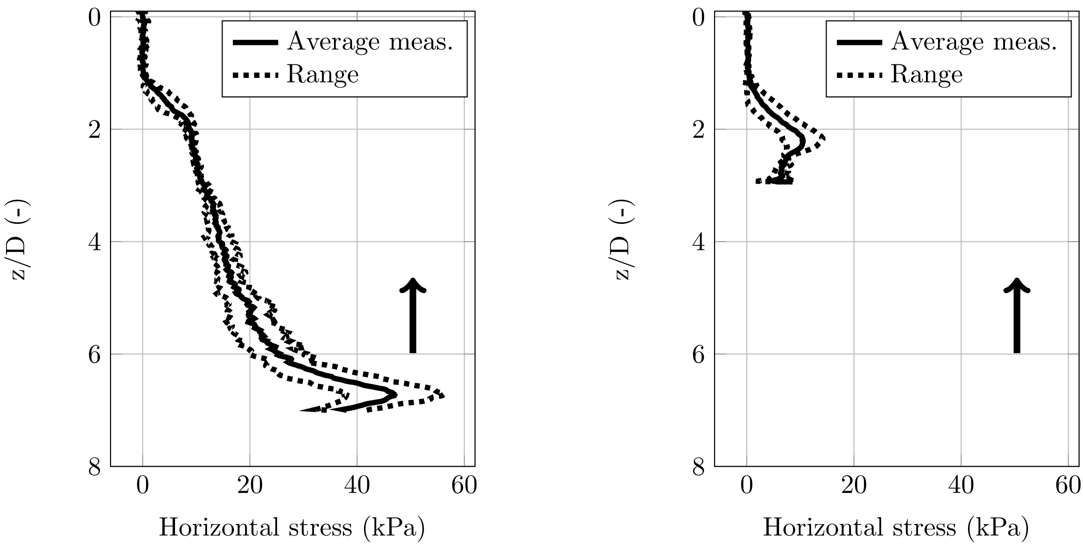

(a) The dense soil sample: instrument level L2.

(b) The dense soil sample: instrument level L1.

Figure 6.31: Total horizontal stress $\sigma_{h,tot}$ in the initial dense soil sample during extraction test.

6.2 Measurements of deformations

6.2.1 Displacement contours after installation

The deformation measurements are now presented through calculations of displacements paths and strain fields. The displacement paths of were calculated following the procedure presented in Appendix *G*.

Figures 6.32a, 6.32b and 6.32c show the displacement contours after installation, which represents the boundary between Zone *B* and Zone *C* according to [130], where there are no displacements (except for small stray displacement cross-section, which were filtered through the normalized median test in JPIV, [229]). The heavy dark line represents the boundary where there are no displacements.

The displacement contours in Figures 6.32a, 6.32b and 6.32c are related to the influence zone in [190], but the measurements exclusively concerns displacements. The actual field of influence (stress as well as strain) by the analysis discussed in [190] is probably larger, as a result of the stiffness of the soil at small strain, which results in relatively small deformations, [10], [147], [214]. This is also related to the effect of installation of subsequent piles, which probably will change the installation effect of the original pile, measured in [45]. These influence zones indicate where the soil is displaced during installation. The measurements implies that a model of a pile should at least include the boundaries of no displacements. These measurements also suggest that the soil sample container should be wider.

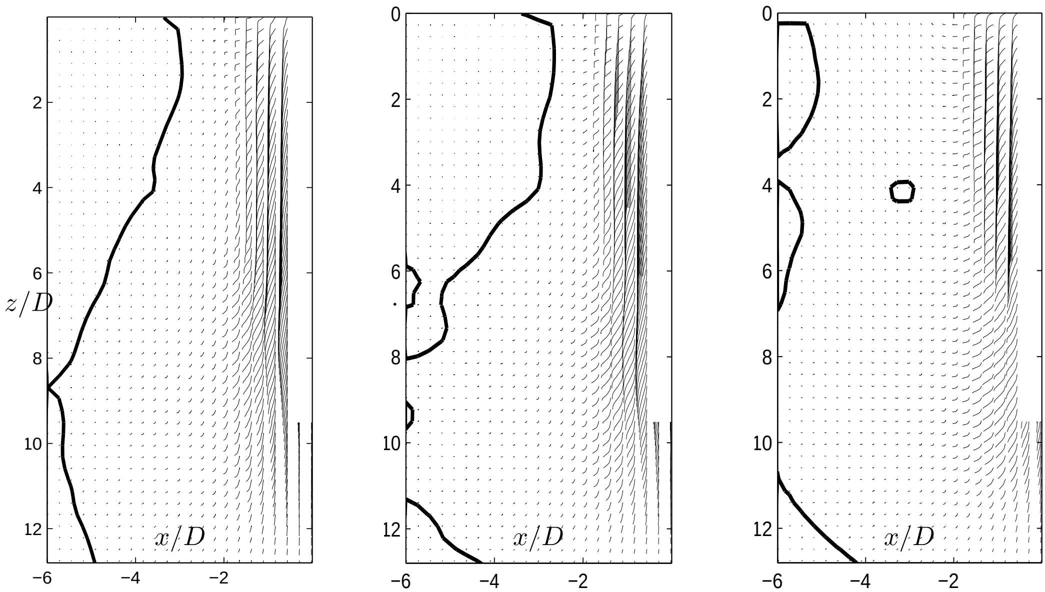

(a) The loose soil sample. (b) Medium dense sample. (c) The dense soil sample.

Figure 6.32: Boundary of discernible displacement contours for loose, medium dense, and dense soil sample.

6.2.2 Measurements of displacement paths

The displacement paths were calculated from the displacement increments following the procedure discussed in Appendix G. Figure 6.33 shows the displacement paths for the medium dense soil sample. The part of the soil that is displaced by the pile is here shown underneath the pile contour. The displacement path at these locations ewre disturbed by the large deformation, and therefore showed much noise. A similar presentation of displacement paths is shown in [243].

Some cross-sections of horizontal and vertical displacement path were calculated and plotted separately to aid interpretation of the displacement during and after installation. This consisted of a line of displacement paths that had the same initial $x/D-$position (vertical) or $y/D-$position (horizontal). The set of vertical cross-sections are analyzed first. Figure 6.34 shows the location after the full installation (before the static pile load test) of the vertical cross-section which were initially located at three locations A, B, and C, at distances $1x/D$, $1.7x/D$ and $3.9x/D$ from the model pile, in the continuous installation sample for loose, medium dense, and dense soil sample in Table 3.5.

Figures 6.35a, 6.35b and Figure 6.35c show the displacement paths at location A, at $1x/D$ initial location. Figures 6.36a, 6.36b and 6.36c show the displacement paths at location B,

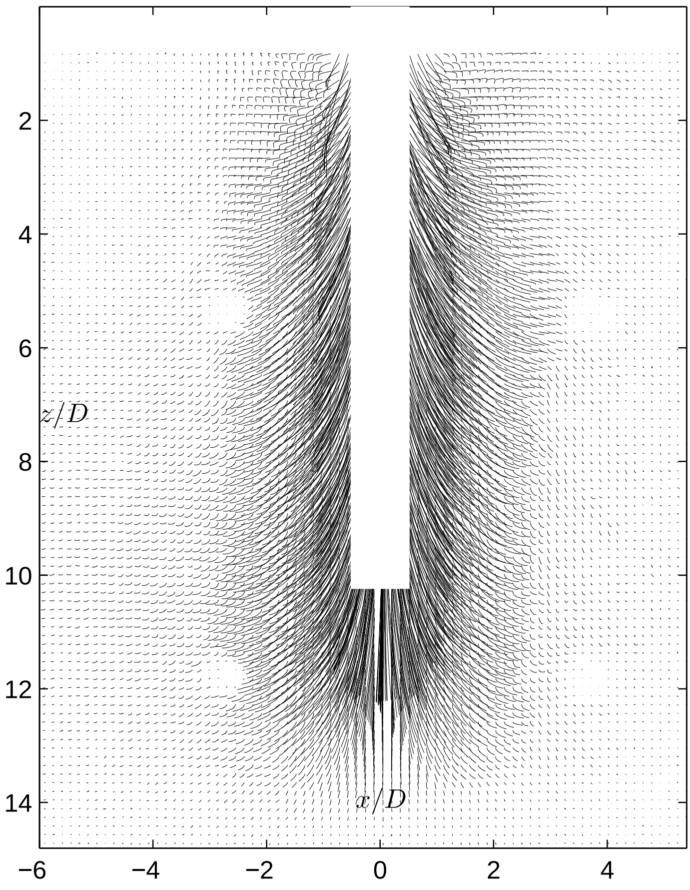

Figure 6.33: Measurements of displacement paths for the medium dense soil sample.

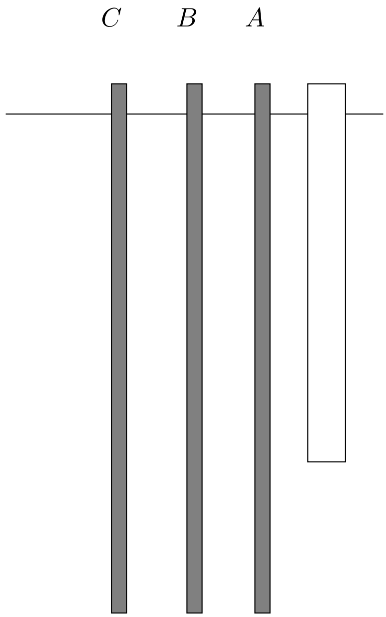

Figure 6.34: The displacement paths with the same initial position x/D calculated and presented and vertical displacement arrays.

at $1.7x/D$ initial location. Figures 6.37a, 6.37b and 6.37c show the displacement paths at location C, at $3.9x/D$ initial location.

The vertical cross-section of displacement show a pattern corresponding to that of [197], [215], [243] with displacements extended from the pile during installation, with lower displacements further from the pile. There seems to be a relatively large effect of initial density, with more heaving vertical displacement for the dense soil sample in Figures 6.35c, 6.36c and 6.37c.

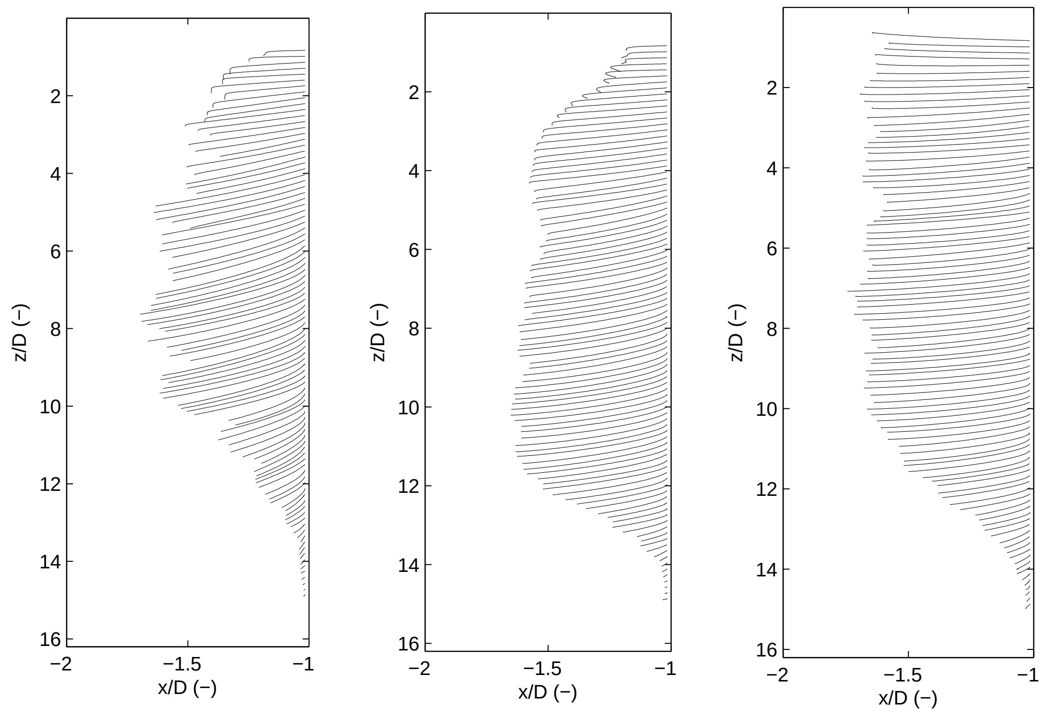

(a) The loose soil sample.

(b) The medium dense sample.

(c) The dense soil sample.

Figure 6.35: Vertical array of displacement paths at location A.

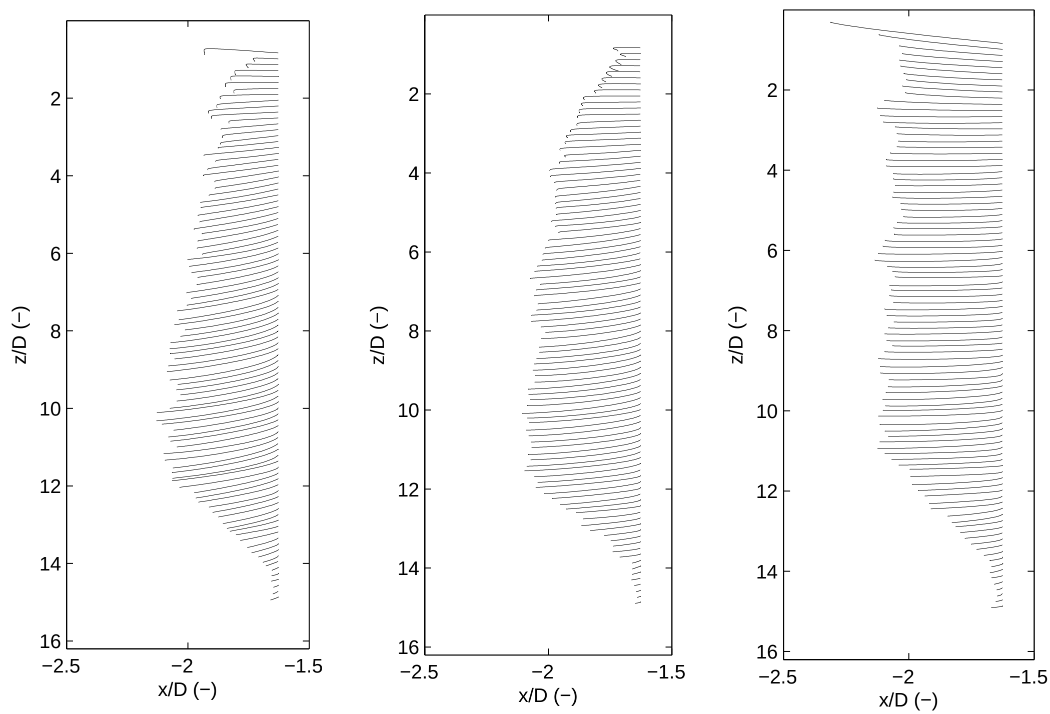

(a) The loose soil sample.

(b) The medium dense sample.

(c) The dense soil sample.

Figure 6.36: Vertical array of displacement paths at location B.

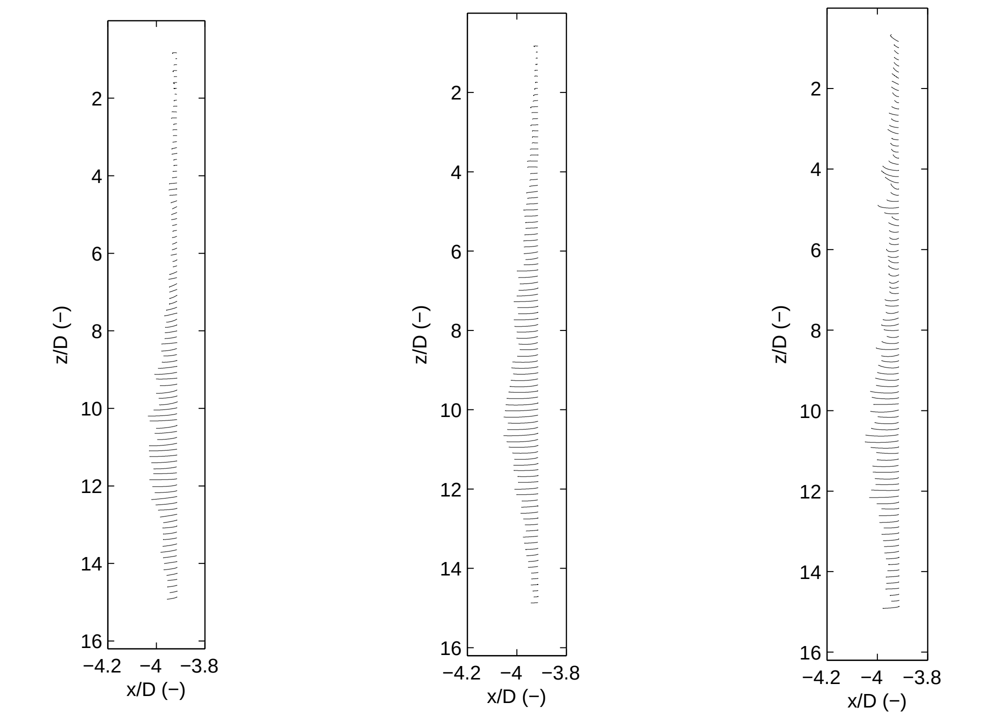

(a) The loose soil sample.

(b) The medium dense sample.

(c) The dense soil sample.

Figure 6.37: Vertical array of displacement paths at location C.

6.2.3 Analysis of an initially horizontal cross-section of displacement paths

Horizontal displacement cross-sections with the same initial position y/D were calculated from the displacement increments to assess the displacements paths after the full installation (before the static pile load test) on the first continuous installation tests in Table 3.5. The position of the horizontal arrays are shown in Figure 6.38.

Figure 6.39, Figure 6.40, and Figure 6.41 show the displacements at an initially horizontal array at location $A = 2.4x/D$, $B = 6.2x/D$ and $C = 8.2x/D$, following conceptually from Figure 6.38. The Figure size has been adjusted to the displacement paths in the dense soil sample.

The horizontal cross-section of displacement paths are relatively similar to the behaviour measured in [197], [215] and [241]. The displacements are smaller further from the pile, and there is a clear effect of the initial relative density. The soil deformations results in more of a compaction response in the loose soil sample, while the dense sample is more characterized by shear strain, similar to that discussed in [243].

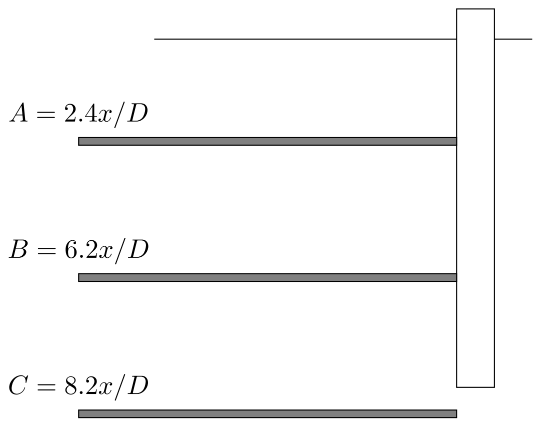

Figure 6.38: The displacement paths with the same initial position y calculated and presented and vertical horizontal arrays.

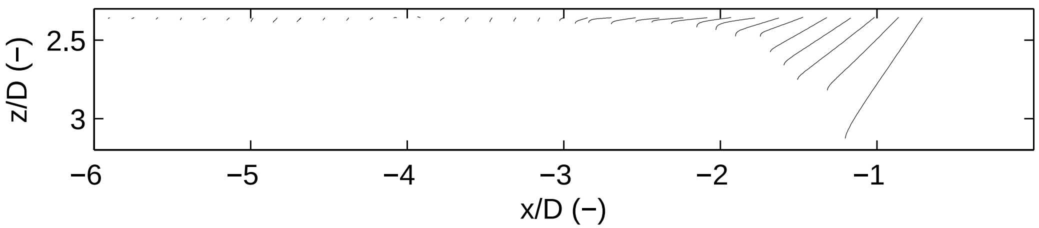

(a) The loose soil sample.

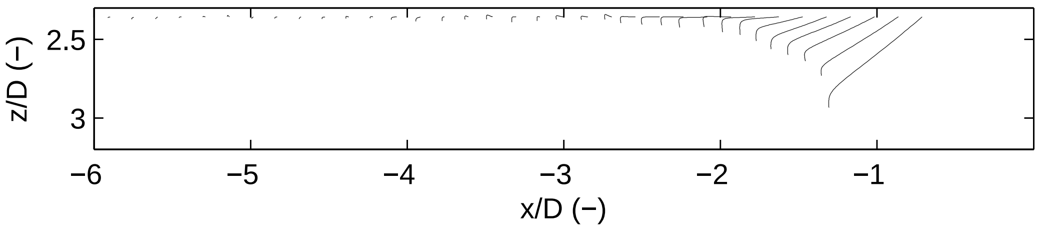

(b) The medium dense soil sample.

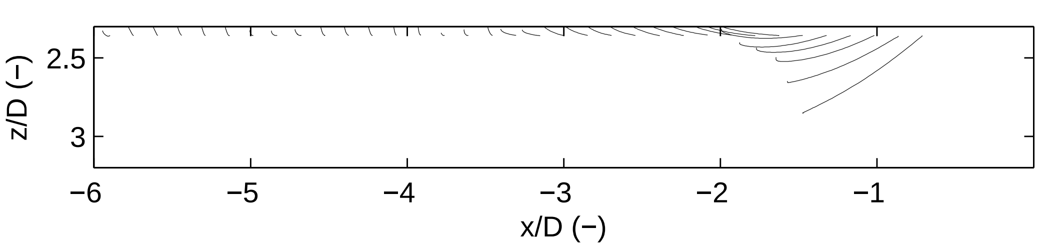

(c) The dense soil sample.

Figure 6.39: Horizontal array of displacement paths at location A for the dense soil sample.

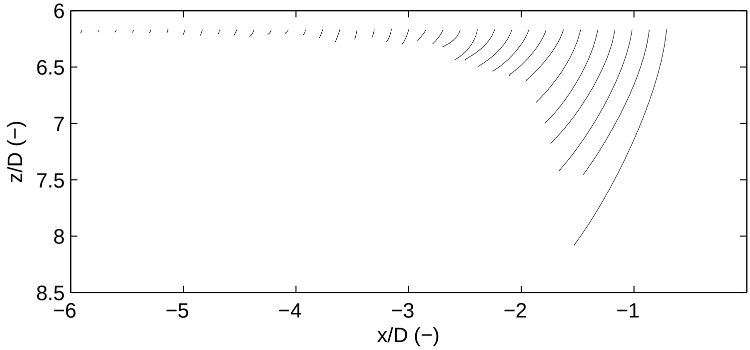

(a) The loose soil sample.

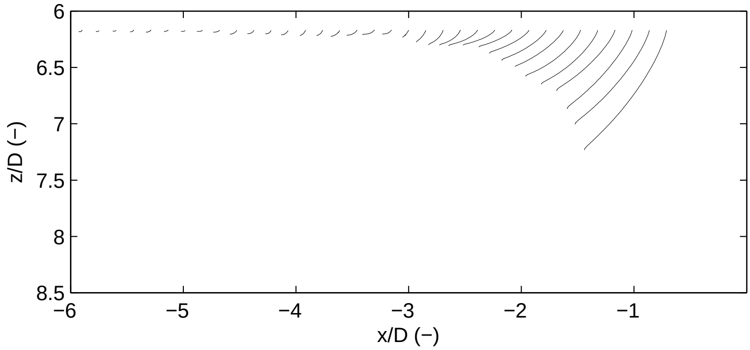

(b) The medium dense soil sample.

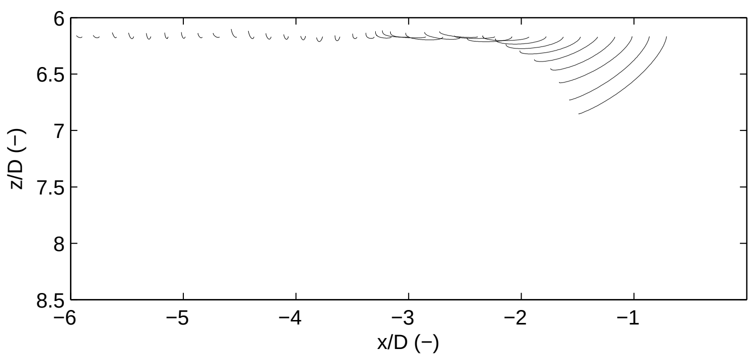

(c) The dense soil sample.

Figure 6.40: Horizontal array of displacement paths at location B for the dense soil sample.

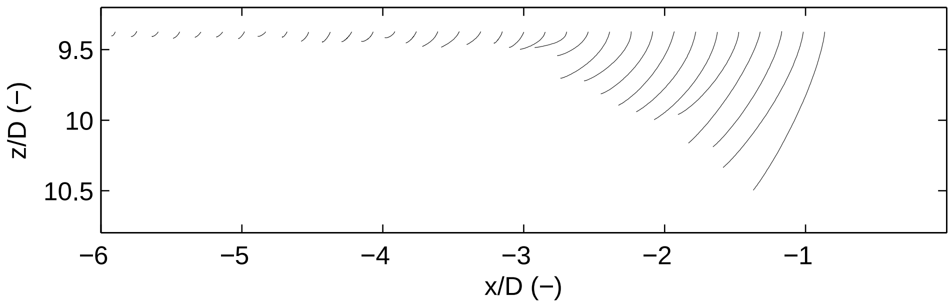

(a) The loose soil sample.

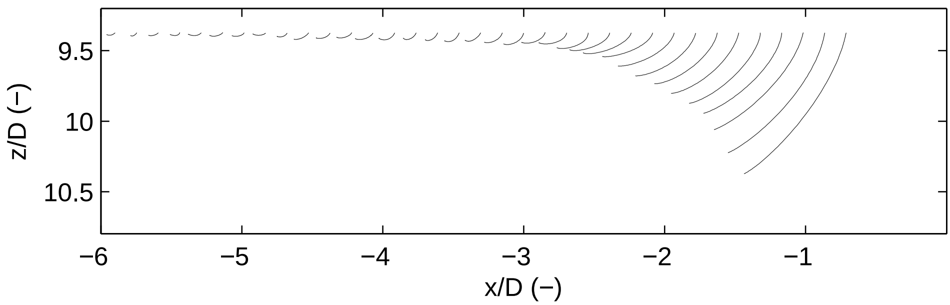

(b) The medium dense soil sample.

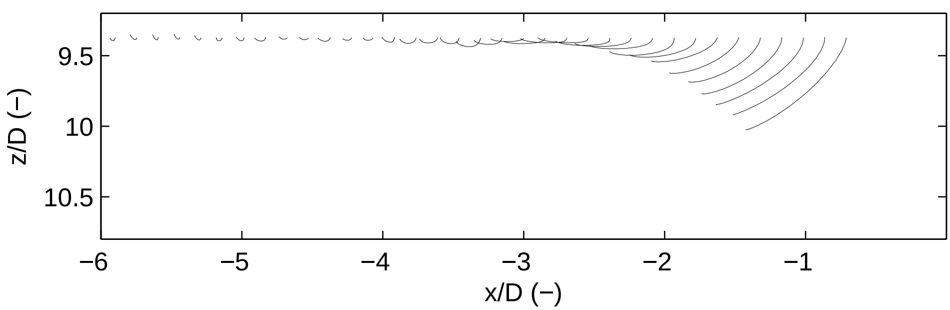

(c) The dense soil sample.

Figure 6.41: Horizontal array of displacement paths at location B for the dense soil sample.

6.2.4 Horizontal displacements during incremental installation procedure

The effect of friction fatigue was studied by measuring the displacement paths during installation stage 2, [246]. Figure 6.42 shows the part of the soil which was studied. The deformation measurement procedure discussed in Appendix G was implemented to calculate the horizontal displacement.

Figures 6.43a, 6.43b and 6.43c show the horizontal displacement in installation stage 2 in the loose, medium dense, and the dense soil sample. The measurements were made during the complete installation stage 2 at the initial depth of $1.75D$ to the full installation depth. The measurements were made in the first incremental installation model tests, i.e. $T-L-D-I-1$, $T-M-D-I-1$ and $T-D-D-I-1$ in Table 3.5.

Comparable measurements were conducted in [243], but for one relative density for different types of sand. The measurements in the current research are relatively similar, with very small horizontal displacements towards the pile. Research has shown that these very small displacement result in large stress changes at the interface, [34]. The measurements therefore seem to show that the friction fatigue effect is relatively similar in various relative densities. This has previously not been discussed in detail, e.g. [241], although measurements have been carried out in different initial relative densities, e.g. [89], [148], [256], which indicated such behaviour.

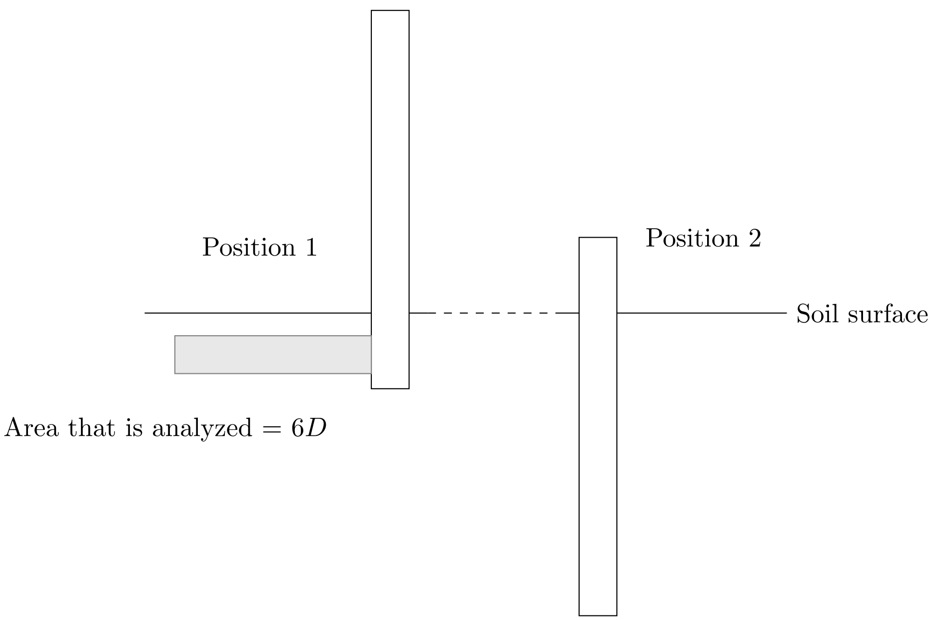

Figure 6.42: Area that is analyzed during PIV.

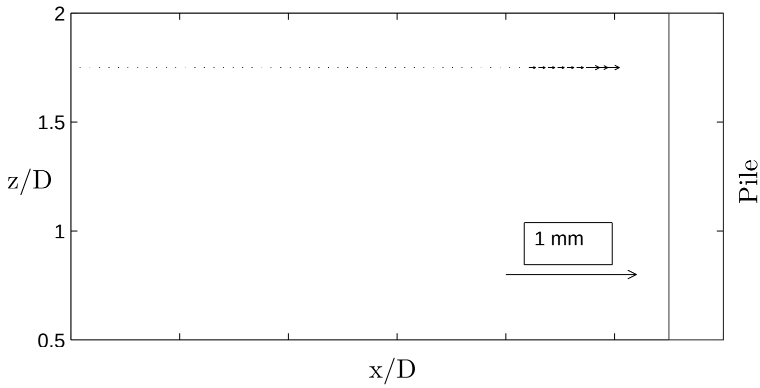

(a) The loose soil sample.

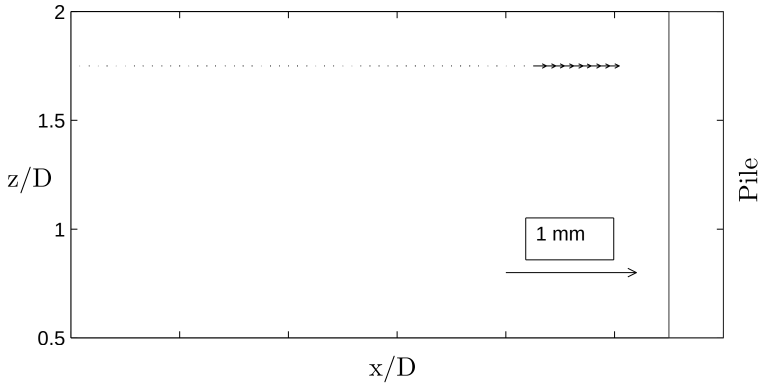

(b) The medium dense soil sample.

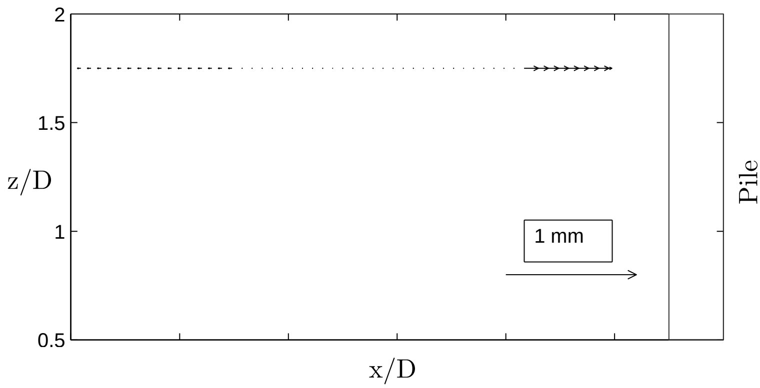

(c) The dense soil sample.

Figure 6.43: Horizontal displacement during the installation stage 2.

6.2.5 Measurements of strain

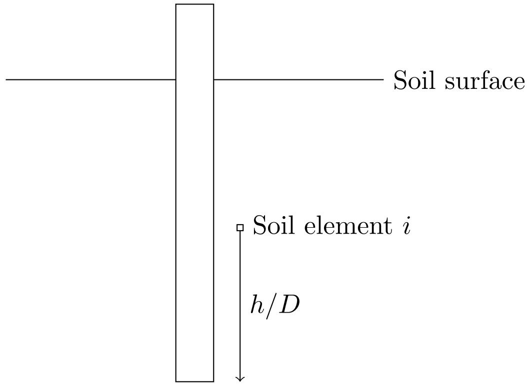

Figure 6.44: Definition of h/D in the measurements for soil element i.

A cross-section of the strain was derived from the displacements using the calculation procedure described in Appendix H. The ε_{xx}-, ε_{yy}-, γ_{yx}-, and ε_{vv}- strains were calculated from the displacement measurements in a Lagrangian framework, in which the location of the strain component moved along with the displacement paths during deformation.

The evolving strain level was plotted for different values of the respective normalized ratio h/D from the model pile, as defined in [128]. The normalized ratio h/D is defined in Figure 6.44 for an arbitrary soil element i.

Three different depth were studied, $z/D = 4$, $z/D = 8$, and $z/D = 12$. Figures 6.45, 6.46, 6.47 show these strain components at these locations, but for different levels of h/D.

These Figures show the strain change similar to that observed in [85], [128], [127]. There are relatively large strain changes as the pile approaches, and subsequently primarily close to the pile after the pile tip has passed. The increase in strain is seen in Figure 6.47, in which the soil is gradually deforming.

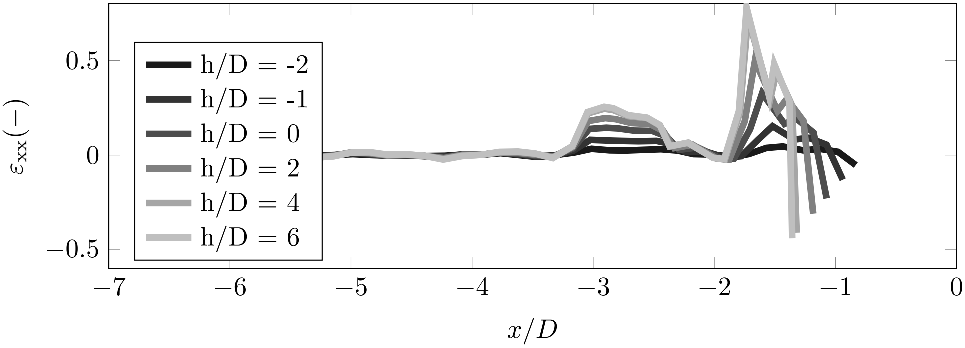

(a) Strain component ε_{xx}.

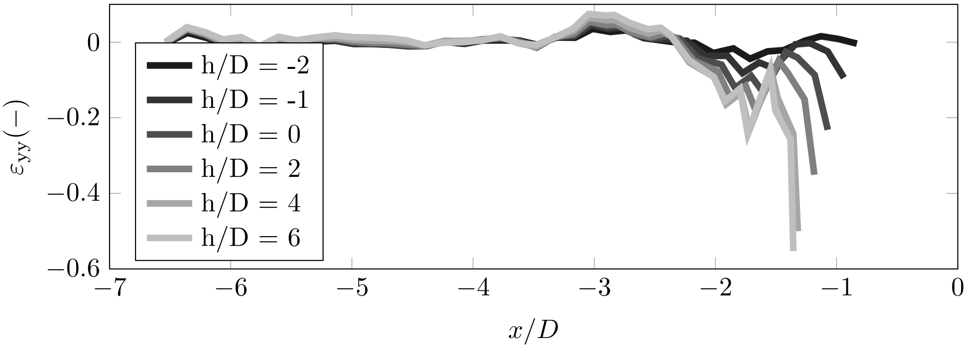

(b) Strain component ε_{yy}.

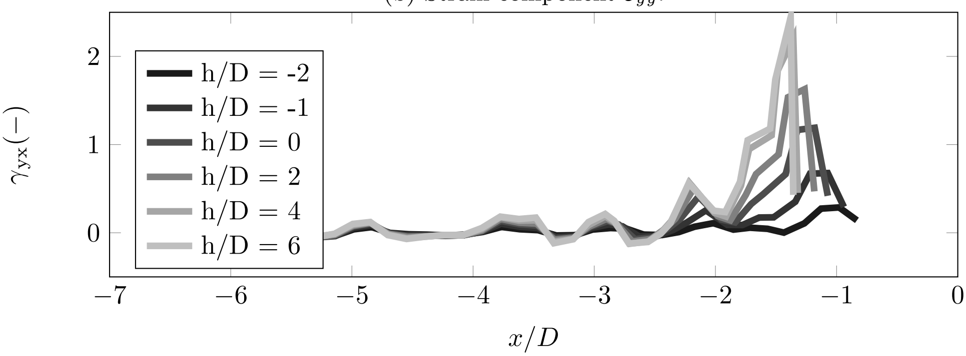

(c) Strain component ε_{yx}.

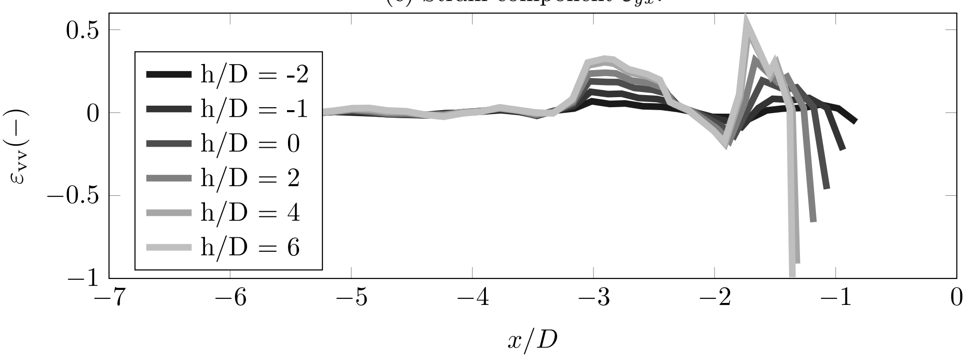

(d) Strain component ε_{vv}.

Figure 6.45: Strain componenents at location $z/D = 4$.

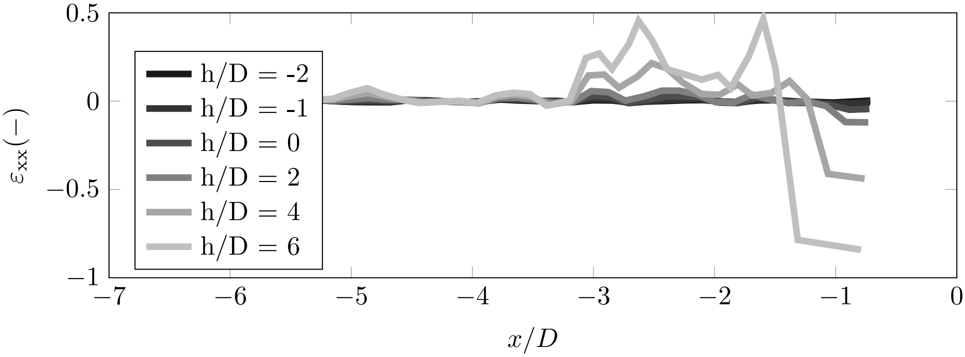

(a) Strain component ε_{xx}.

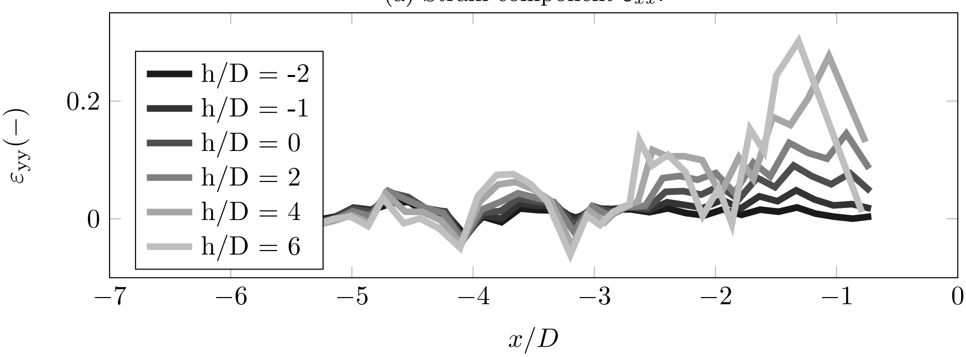

(b) Strain component ε_{yy}.

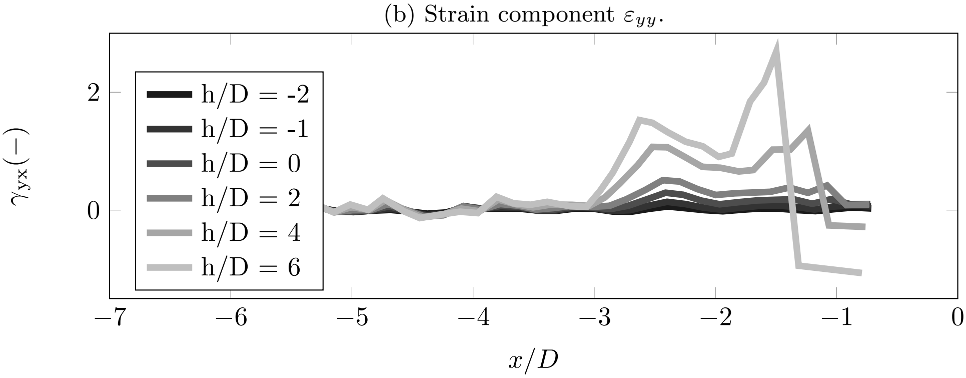

(c) Strain component ε_{yx}.

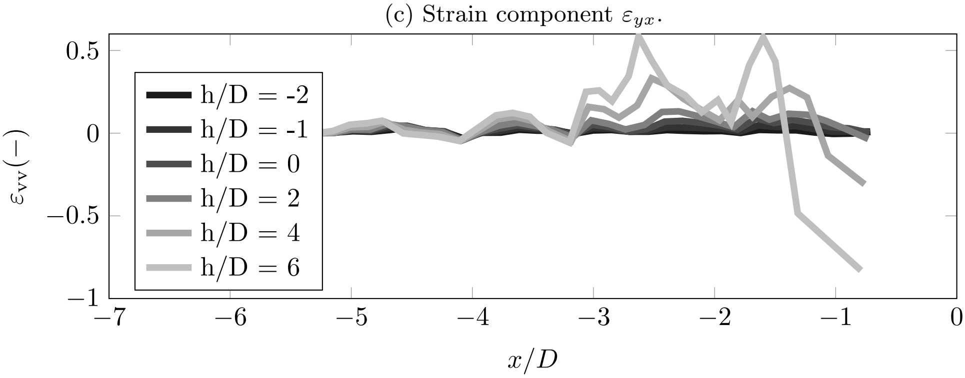

(d) ε_{vv}.

Figure 6.46: Strain componenents at location $z/D = 8$.

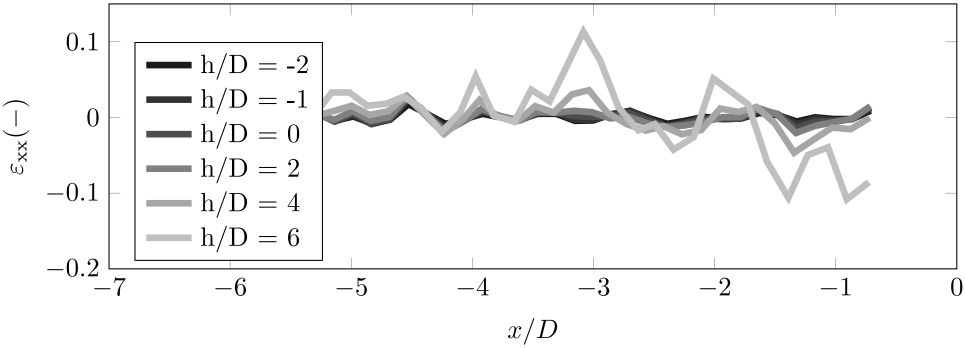

(a) Strain component ε_{xx}.

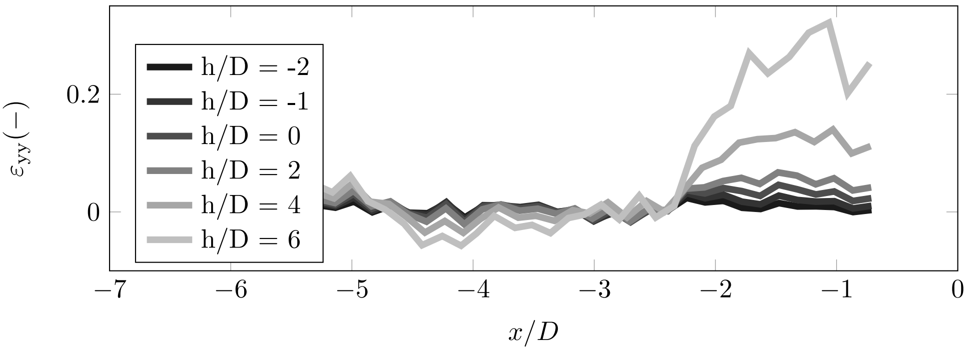

(b) Strain component ε_{yy}.

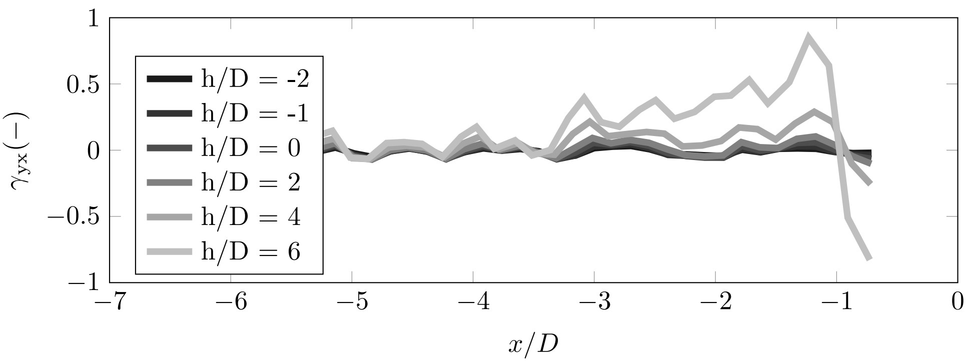

(c) Strain component ε_{yx}.

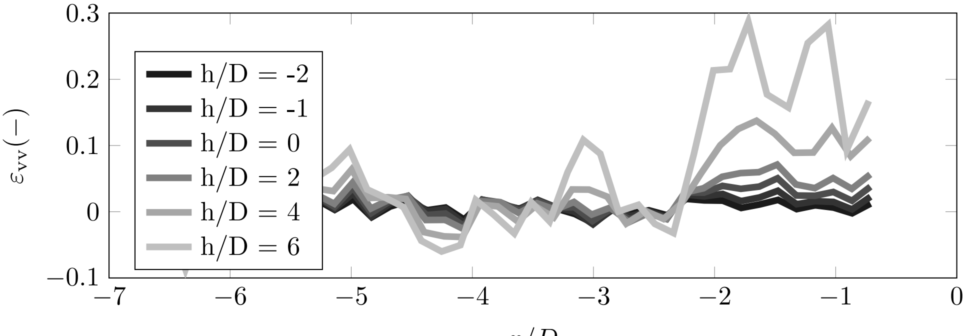

(d) Strain component ε_{vv}.

Figure 6.47: Volumetric and shear strain components at location $z/D = 12$.

6.3 Combination of stress and incremental strain measurements

The stress and strain measurements were combined by plotting the detrended $\sigma'_{h,tot}(t)$ and the incremental strain component $\Delta\varepsilon_{ij}(t)$ as a function of installation time, i.e. $\sigma'_{h,tot}(z/D,t)$ and $\varepsilon_{ij}(z/D,t)$ in the same plot for the complete installation procedure, following the sensor. The analysis was carried out for the incrementally installed model pile, and the cyclic loads were consequently included in the analysis.

The incremental strain components have been sampled from a horizontal cross-section which follows the location z/D of the sensor at the time t, shown in Figure 6.48. The location $z_{sensor}(t)/D$ as is consequently always located at the stress sensor, so that the $\sigma'_{h,tot}(z/D,t)$ is matched with the $z_{sensor}(t)/D$ in the measurements.

The total horizontal stress $\sigma'_{h,tot}(z/D,t)$ was measured at the time t, as shown in Figure 6.49a. It was then fitted to a straight line, and the detrended stress level $\sigma'_{h,tot}(z/D,t)$ was plotted.

The location x/D (which is between x/D = -1 and x/D = -6) is signified by the colour of the line, which is black at x/D = -6 and is changed to a lighter grey close to the pile, as shown in Figure 6.49b. The pile starts at $x/D = -0.5$. The part of the strain measurements within $0.5D$ to the pile are not analyzed because of the large distortions of the triangular elements, which result in very large strain levels.

Figures 6.50 and 6.51 show detrended measurements of $\sigma'_{h,tot}(z/D,t)$ and γ_{yx} and ε_{vv}. The aim of the detrended strain-stress measurements was to analyse the effect of stress changes on the strain levels. It appears from the measurements that increase in the detrended stress results in significantly more shear strain in Figure 6.50. This also suggests that the shearing mechanisms depends on the initial relative density.

The strain measurements seemingly contradict the measurements of horizontal displacement, in which the soil seems to be compressing close to the pile, which is similar to the behaviour observed in [243]. It appears that the strain paths in installation stage 1 are very different, and the volumetric behaviour of the soil with different initial relative density are therefore different. This results in a behaviour observed in numerical simulations, in which the loose soil sample contracts, and the denser soil samples dilate, [76].

Strain development during installation is shown in Appendix R, based on the strain calculation method discussed in Appendix S. The stress-strain behaviour with the normal stress level (not detrended) are shown in Appendix T.

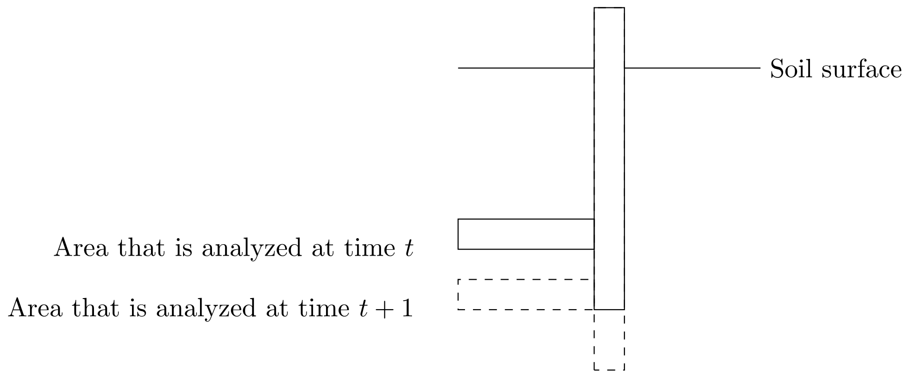

Figure 6.48: Idealized illustration of moving sampling of strain: Calculation at time t and $t+1$.

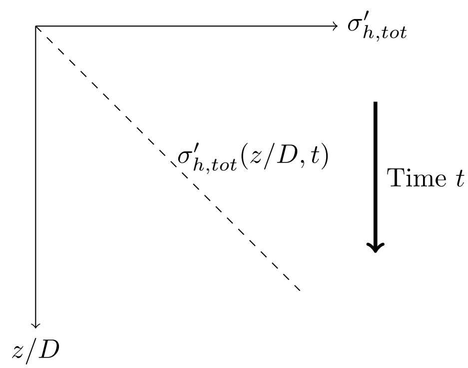

(a) Measurements of $\sigma'_{h,tot}(z/D,t)$ at time t.

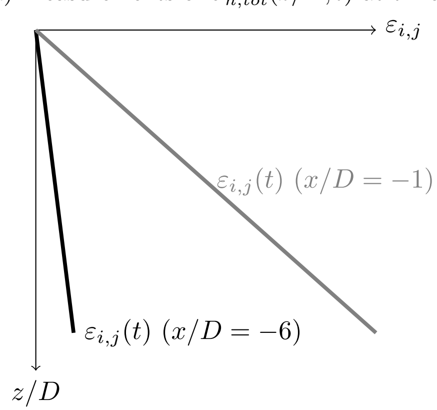

(b) Measurements of strain at varying x/D from the pile center.

Figure 6.49: Idealized principle for measurement of stress and strain at time t.

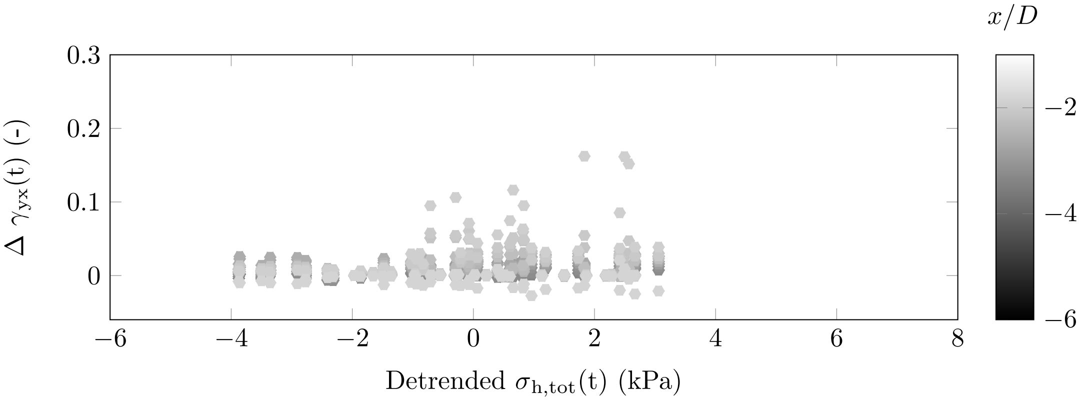

(a) The loose soil sample.

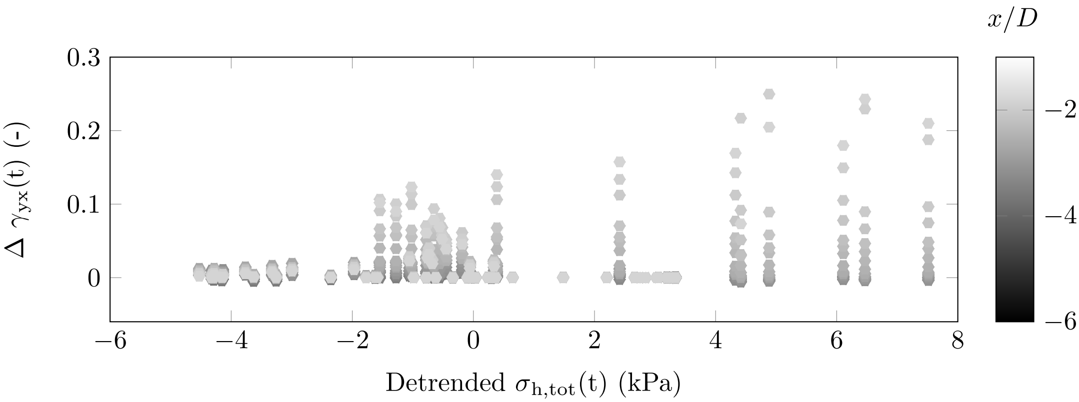

(b) The medium dense sample.

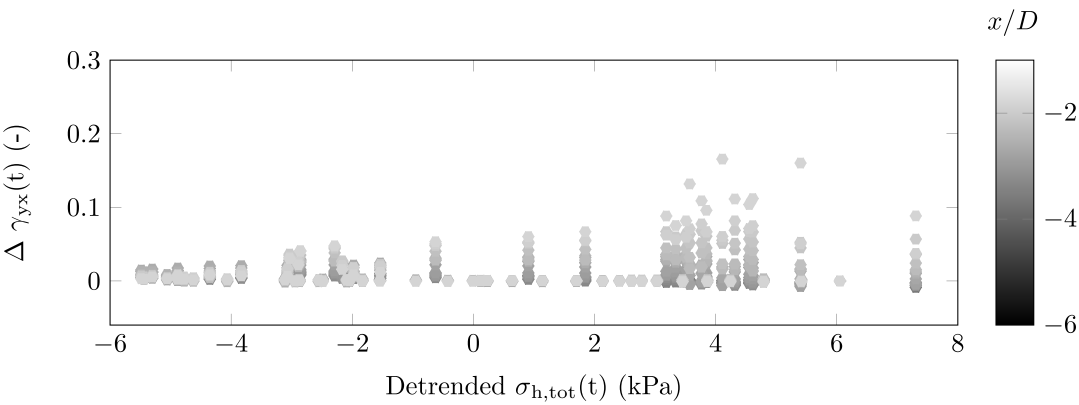

(c) The dense soil sample.

Figure 6.50: Detrended measurements of stress-strain path.

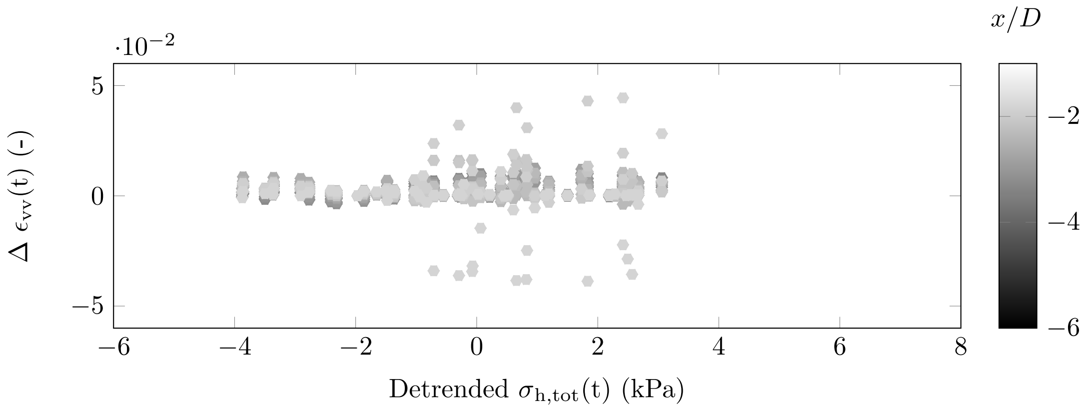

(a) The loose soil sample.

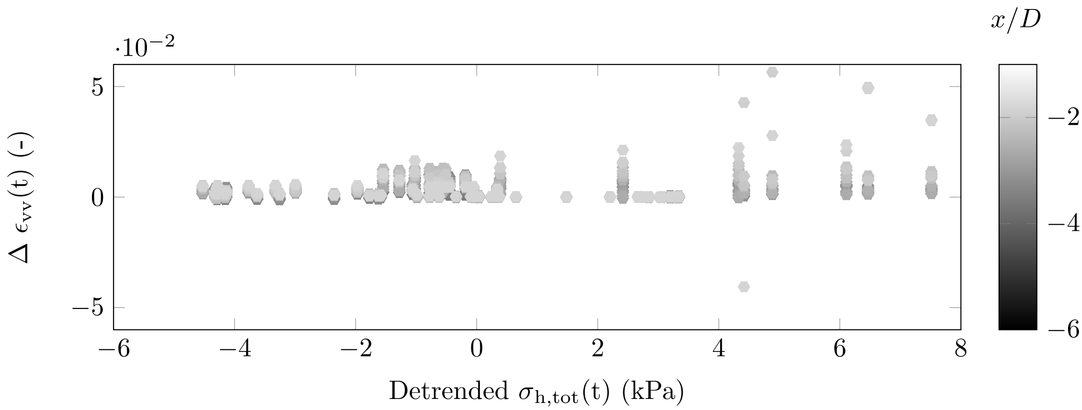

(b) The medium dense sample.

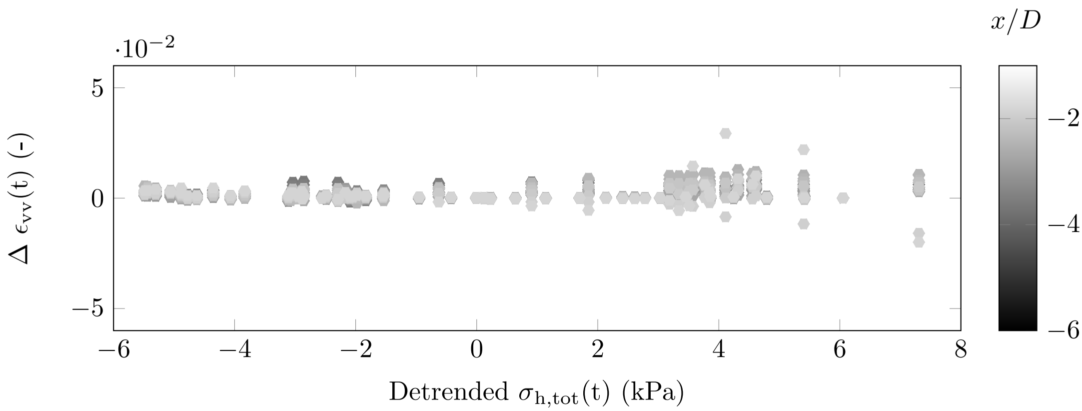

(c) The dense soil sample.

Figure 6.51: Detrended measurements of stress-strain path.

6.4 Summary

The experimental tests consisted of stress and deformation measurements. The stress measurements contained pile head load, pile tip and horizontal contact stress measurements. These were analysed in order to show the effect of relative density and installation method. The influence of cyclic loads on the distribution of the horizontal stress was investigated in some detail. The resulting stress distribution around the pile was displayed in the pile extraction tests, in which the initial relative density was seen to have a large effect of the load-deformation response. On the other hand, the pile load tests showed that the pile (with a small L/D-ratio and thus dominated by the pile base) had a relatively similar load-deformation response for small loads.

The deformation measurements studied the deformation behaviour of the soil during installation. The effect of relative density was studied, as well the influence of cyclic loads. Small horizontal deformations, possibly resulting from friction fatigue, were measured. The displacement paths were studied (in horizontal and vertical arrays) to assess the displacement pattern for soils of different initial relative density. The incremental stress change was estimated at the location of the stress sensor.

Chapter 7

Interpretation and discussion

The model tests were designed to study the effect of initial relative density, installation mode (including the load cycles), the effect of friction fatigue, the components of the horizontal stress, as well as the deformation behaviour during pile installation in sand. The aim was also to both characterize and quantify the installation effects for the model pile at different initial conditions and installation modes.

The soil samples were prepared at 40%±5%, 60%±7% and 80%±4% relative density. These are representative for normal soil conditions, since the very loose soil conditions outside the sample conditions rarely appear in soils subjected to piling, [82].

The effect of initial relative density is observed both in the continuous and incremental installation mode. The pile head load measurements during continuous installation mode (Figures 6.2, 6.3 and 6.4) display a steady increase with initial relative density of around 30%-80% for the medium dense and the dense soil sample respectively. Similar behaviour is observed for the pile base load and the total shaft friction. This has also been observed in a series of previous field and laboratory experiments, e.g. [53], [89], [148]. The same pattern is observed in numerical simulations, e.g. [96].

The trend in the horizontal stress measurements during continuous installation in Figures 6.9, 6.10 and 6.11 display a stress response that is comparable to the pile head load, shown in Figures 6.9, 6.10 and 6.11. Comparable measurements have been conducted in silica sand in the field and in the laboratory, [89], [127], [151]. The horizontal contact stress in these measurements increases with installation depth, and do not seem to reach a limiting value to the stress level in the experiment (which is significantly different than longer prototype piles). This is also observed in the current measurements. The incrementally installed model tests seems to show a similar behaviour in Figure 6.12, 6.13 and 6.14.

It is also possible to analyze the effect of initial relative density on the ratio of the horizontal normal stress and the pile base $\sigma'_{h,tot}/\sigma_b$ in Figure 6.15. The small ratios in the beginning of the installation are followed by a more stable ratio at around 1.5% at the end of the installation. This is similar for all initial relative densities. Since the shaft friction is governed by Coulomb friction, [124], this confirms the recommendation to calculate shaft friction as a ratio of the cone resistance, which is followed in most CPT-based design methods, e.g. [40], [50], [64]. This also explains why the CPT based methods are giving more accurate results in various initial relative densities compared to more traditional methods of design, [41].

The effect of the installation mode is possible to distinguish from the pile head load measurements (Figures 6.5, 6.6 and 6.7). These show a maximum pile head load during the load cycles which are comparable to the maximum pile head load at the same depth z/D during continuous installation, represented both by the base resistance and shaft friction. For a clearer analysis of the installation mode, the pile head load during incremental installation mode is normalized with the pile head load during continuous installation in Figure 6.23. The loose and dense soil samples in Figure 6.23a and 6.23c show a relatively small, but declining ratio of the maximum pile head load during installation. The corresponding plot of the pile base load, Figure 6.24, does not present the same behaviour, but rather a steady ratio. Is is consequently mainly the shaft friction which is influenced by the load cycles. The pile head load measurements in Figures 6.25a, 6.25b and 6.25c suggest that the stiffness of the load frame has a significant effect mainly in the dense sample. The trend of the pile head load in Figure 6.25c shows that this effect is not present during initial reloading and final unloading in each cycle, but rather at full mobilization during each loading cycle. The interaction between the model and the load frame stiffness is consequently not present during most of the load cycle, and only when a one-way cycle is performed at full mobilization. This type of load cycles have previously been observed to have a smaller effect on the volumetric response, [151].

This supports the conjecture that the installation mode governs the changes in shaft friction. This is related to the friction fatigue phenomena, which is studied in Figure 6.22, in which the non-loaded horizontal stress is displayed, following e.g. [148]. Instrumentation level 1 experiences at non-loaded horizontal stress which is around 40%-60% of the observed at instrument level 2. This corroborates other studies, e.g. [104], [89], [151]. The friction fatigue effect is observed in all initial relative densities and was shown in Figure 6.23 to have an effect on $\sigma'_{h,tot}$ as well.

The friction fatigue phenomena explains why the assumption about the constant ratio of pile base load and shaft friction probably is too simplified to given an accurate description of the shaft friction, [104], [148], [241]. Since the distribution of horizontal stress after installation has a large effect on subsequent load-deformation analysis, this makes analysis of piles cumbersome, e.g. [111]. This is especially the case for comparison of piles in tension and compression, in which the stress rotations play a big role, [62]. The measurements showed that the maximum horizontal stress in tension is around 50%-70% of that in compression. This could be influenced by the experimental set-up, because of the pile load test and load cycle before extraction. The ratio α is consequently relatively low. The results of the model tests thereby contribute to the more nuanced description of the stress distribution of piles, in which the installation effects are an important component as a result of the stress history and cyclic shear loading during installation, [34], [241], [243].

The shaft interaction mechanism is complex, since the frictional interface consists of a relatively small number of grains (around 10-20), which is intensively sheared, [34]. This soil layer does consequently not constitute a continuum, since the number of grains is too small to result in a homogenous stress distribution, [58]. The translational and rotational resistance of the grain interface govern the behaviour during shear, [74]. Relatively small normal displacements (from soil compaction or expansion against the pile) result in significant normal stress changes, [34]. Laboratory measurements of different soils have shown that changes in the loading direction have a significant effect on the stiffness of the soil, [214]. Similarly, load cycles result in volumetric changes in the soil (such as gradual compaction), [218]. It is here proposed that the cyclic shearing mechanism results in large changes in stiffness in each cycle as well as gradual volumetric change of the soil, which reduces the horizontal stress at the soil-pile interface, which was found in the measurements through PIV. The changes in stiffness are also confirmed by other model pile experiments, [147].

The measurements of horizontal displacements also show the mechanism of friction fatigue in Figure 6.43. The displacement increment plots during installation stage 2 present displacements towards the pile, which suggests compaction of the soil, simular to observations of cyclic loading in numerical simulations of vibration, [159]. This leads to decreasing horizontal stress, as suggested by [243]. There are very few measurements of this phenomena, and it is not known how much the measurements depend on the current testing conditions. The displacements in Figure 6.43 are also very small, however both theory and experiments show that such very small displacements have a large effect on the equivalent radial stress distribution around the pile, [34], [147], [151].

The measurements of the strain components show that the stress-strain behaviour depends on the initial relative density, shown in Figure 6.45-6.47. The total stress response during installation seems to be rather uniform and scales relatively well with initial relative density, even though the mechanisms are different, as shown by the normalized measurements in Figure 6.15. The post-installation response, as shown in the extraction tests in Figure 6.26-6.31 is different and depends on the initial relatively density. Such qualitatively different behaviour is not discussed in detail in descriptions of the friction fatigue and installation effects but governs the pile-soil behaviour for layers with large variation in initial relative density, [241].

The components of horizontal stress have been analyzed by adding the non-loaded horizontal stress σ'_n and the dilational stress $\Delta\sigma'_h$, the principle shown in Figure 6.1. The measurements in Figure 6.21 show that the same constant dilational interface size Δh results in a suitable fit with the total horizontal stress $\sigma'_{h,tot}$. This effect has been discussed in other types of tests, e.g. [34], [89], [151], and is here studied for several initial relative densities, which suggests that the standard formulation for the stress components during full stress mobilization (in e.g. [148]) is relatively accurate. The specific formulation of the shear modulus G and the interface size Δh is more difficult to evaluate, since other laboratory measurements have shown the mobilized shear modulus G to be a rather small fraction of the maximum shear modulus G_{max}, [147]. The three different correlations for the shear modulus G gave similar results, but with a low value of the dilational interface Δh. A combined value of $G\Delta h$ may be a suitable method to evaluate the dilational stress component.

The effect of the post-installation response for the pile in tension is observed in the extraction load tests in Figures 6.26, 6.27 and 6.28 for the continuously installation model tests. In these tests the pile passes through an already sheared zone of the soil, in contrast to

[34], [147], [218], where the soil sample was prepared before shearing. In the current model the installation effects are already included. The initial response for the loose soil in Figure 6.26 is relatively brittle, with a peak value and thereafter a residual stress during extraction. The medium dense and dense soil samples in Figure 6.27 and 6.28 suggests a more gradual softening behaviour, which is more clear for the dense soil sample. Tension load tests were carried out in field and laboratory measurements in [47], [148], [151], [147], but not in a uniform initial relative density after installation, and the total effect was measured. Here the density effect is clearly identified, and seems to give a large effect on the load-deformation response. It is also possible that the scale effect during dilation is dominant, but this effect is inherent in these tests, but this should also be considered, [147].

The extraction tests after incremental installation are shown in Figures 6.29, 6.30 and 6.31. The load-deformation response is similar to that of the continuously installed piles. This means that the load cycle during the static pile load tests could have a large effect of the interface behaviour of the pile, since the friction fatigue mechanism has been observed to develop in a small number of load cycles, [89]. The dense soil samples after continuous and incremental installation both display a more gradual change in stress compared to that of the loose and medium dense soil sample. The peak stress for the loose soil sample appears after around $1D$, which suggests that relatively large displacements are needed for softening. A response which includes less softening is displayed in field pile load tests in tensions, [47]. Since the scaling of the models governs the interface behaviour, this deformation response is not necessarily similar to the prototype case, which explains part of the difference of the load-deformation response, [151].

The deformation behaviour of the soil is complex, as seen in Figures 6.35, 6.36 and 6.37 for a vertical cross-section, and Figures 6.39, 6.40 and 6.41 for a horizontal cross section. Analysis of the soil response through a limited part of the soil close to the pile in [34], [148] and [241] is a clear simplification which may not accurately represent the whole soil-structure interaction. The far-field behaviour of the soil is more similar to numerical simulations in [159], in which the volumetric compaction of the soil at around $1D$ from the pile has a large effekt on the stress distribution at the pile shaft. There is some difference between the initial relative densities, with larger horizontal displacements in both the horizontal vertical cross-sections in the medium dense and dense soil. This is partly similar to the deformations from different soil types in [243]. The shape of the displacement paths also suggests more vertical rebound for the denser soil samples, which probably has an effect on the stress distribution and the post-installation response in Figure 6.26-6.31.

The contour plots in Figure 6.32 shows displacements for at least $4D$ from the pile, with larger horizontal displacements for the dense soil sample.

Stress and incremental strain measurements were also calculated in Figure 6.50 and 6.51 for the detrended stress measurements. These Figures are plotted with the $\sigma'_{h,tot}$ on the abscissa and the strain component on the ordinate. The medium dense and dense soil samples display a more expansive volumetric behaviour close to the model pile, which suggests dilative mechanical behaviour closer to the pile shaft during installation.

This stress-strain behaviour is also discussed in [76], resulting in a volumetric compaction of loose soil, and volumetric expansion of the denser soil. The observed response could partly explain the difference between the pile-soil interaction at different initial relative densities. The shearing mechanism during the cyclic installation cycles is governed by the volumetric response of the soil upon shear loading, [241]. This is similar to the response seen in deformation measurements in Constant Normal Stiffness (CNS) tests, [65]. The loose soil sample therefore has a lower horizontal stress, since the soil can compact, and the denser soil sample have higher horizontal stress which results from the dilation. These conclusions are partly supported by the experimental evidence, but more experimental research is needed to fully verify these conjectures.

Finally, the experimental measurements have consequently resulted in a more detailed characterization of displacement pile installation effects which is briefly presented: The pile installation has been separated in between installation stage 1 and 2. During installation stage 1, an arbitrary element of homogenous soil is located beneath the pile tip. This soil element is displaced as the pile is installed through the ground. The displacement behaviour depends on the initial relative density. Installation stage 2 starts when the pile reaches the soil element. The stress level changes as a result of the cyclic loads during incremental installation. The load cycles result in a reduction of the horizontal contact stress, and therefore lower shaft capacity. After installation, the distribution of horizontal stress has been observed to follow an exponential curve with the highest stress located at the pile tip. The measurements also show that the stress-strain behaviour in installation stage 2 depends on initial relative density. This short description of the installation effects will be discussed in further detail in the following chapter.

Chapter 8

Conclusions and recommendations

8.1 Conclusions

This thesis introduces the design and realization of a Ng physical model test to investigate installation effects of a displacement pile in dry sand. This includes a novel miniature model pile capable of measuring horizontal contact stresses at mobilization and at rest and axial loads and a centrifuge setup which facilitates an in-flight camera system. The latter allows to measure the deformations in the soil behind a transparent window.

The experimental configuration in the current research results in a novel physical model which allows both contact stress and full field deformation measurements during pile installation. The aim of the experimental research is to clarify and improve the current conceptual framework by experimental model tests.

The experimental approach is based on a careful study of modelling considerations related to the similitude of the model as well as instrumentation technology. The current physical model is a compromise between model simplicity and retaining the governing mechanisms of the prototype in the model. Relevant scaling laws and recommendations for the model were mostly fulfilled, resulting in an adequate description of the installation procedure.

An instrumented model pile was realized to conduct contact stress measurements. The pile was equipped with novel membrane stress sensors and an axial stress sensor. Sensor instability resulting from possible heat generation was solved by installing an alternating strain gauge bridge supply. The sensitivity of the model pile is relatively low, which is a result of the membrane mechanical configuration. This is a compromise between model robustness and reliability. The fabrication tolerance was relatively low compared to the very thin membrane, which would impair a more sensitive realization of the instrumented model.

An experimental model was designed for the TU Delft centrifuge. The model sample container was equipped with markers, allowing lens correction in the deformation image processing. The physical model was computer-controlled through the centrifuge control mechanism, and data communication was realized through a slip-ring system.

Displacement pile installation effects were modelled in the centrifuge with two different installation modes: continuous installation and incremental installation with unloading. The experimental tests were carried out in initial loose, medium dense and dense soil samples (40%±5%, 60%±7% and 80%±4% relative density) and repeated to assure repeatability of the experimental model. Full field deformation measurements and horizontal contact stress measurements from sensors located on the pile were conducted and processed with custom-made software to calculate the strain components from displacement increments. The experimental procedure consisted of installation, a static load tests, and an extraction test.

The research aim was to provide a more complete characterization and quantification of the displacement pile installation effects. The description includes quantification of the stress and deformation behaviour of the model pile, as well as an improved characterization of the installation. The experimental tests were conceived to study the effect of initial relative density and installation mode (continuous and incremental installation) in particular.

Pile head load, axial stress and horizontal contact stress measurements show a clear dependence on the initial relative density. The variation in measurement output between samples prepared at the same initial relative density was relatively small. The normalized measurements showed that the normalized horizontal stress $\sigma'_{h,tot}/\sigma_b$ reaches a relatively stable level of around 1.5% in the installation stage 2, for all the initial relative densities.

The total horizontal normal stress $\sigma'_{h,tot}$ has been confirmed to consist of the non-loaded horizontal stress $\sigma'_{h,tot}$, and the dilational stress $\Delta\sigma'_h$. This has not previously been explicitly carried out in experimental measurements by stress component separation, but has still guided model configuration, and was therefore studied in detail. The measurements showed that the standard expression for the dilational stress as a function of the shear modulus G, the volumetric change Δh, and the pile diameter D_{Pile} results in relatively accurate prediction of the total stress $\sigma'_{h,tot}$ if the shear modulus is calculated by standard types of correlations for the shear modulus, e.g. [12]. There is still large uncertainty about the evolution of shear modulus during increasing shear strain, e.g. [147], and several other mechanism contribute to the behaviour of the interface response, e.g. stress rotations, [62].

Measurements of horizontal contact stress for the non-loaded pile $\sigma'_{h,n}$ for the instrumentation levels L1 and L2 consistently show the effect of friction fatigue at between 40%-60% level of the horizontal stress at the upper level, compared to the lower instrumentation level for all tests. The friction fatigue effect is compared to the exponential declines presented in the advanced pile design models, and show distribution of horizontal stress similar to the empirical method distributions. The absolute levels of horizontal stress were lower than the prototype piles, e.g. [41].

Deformation measurements showed that the horizontal deformation during installation stage 2 consists of small deformations towards the pile, which results in the friction fatigue mechanism. The compaction of the soil was observed in the loose and medium dense soil sample, but large deformations were not found in the dense soil sample. However, for the first time some evidence has been shown to confirm the friction fatigue mechanism both for stress and deformation measurements. The horizontal displacements occur after the soil has passed the pile tip, resulting in a different stress regime, in which dense soil may initially expand becuase of the lower confining stress, and eventually compact because of cyclic loading.

The stress distribution in the soil after installation was governing the load-deformation response during the pile extraction tests. In these the pile was pulled from the soil, thereby only including shaft friction. Possible reasons between the difference in shaft friction in tension and compression are the Poisson's ratio effects and the distribution of stress, as well as stress rotations and stress reversal after loading. The measurements show a ratio α between horizontal stress in tension and compression to be around 50%-60%, which is larger difference than e.g. [148]. It is possible that the distance to the pile tip could have an effect on the horizontal stress, since the L/D-ratio distance to the sensor is smaller than in other models, e.g. [32]. The design models also incorporate the same type of behaviour in different initial relative densities with only the magnitude of the shaft friction being dependent on the relative density. This homogenous deformation mechanism was not observed in the measurements. The loose and medium dense soils samples instead displayed a somewhat more brittle behaviour than the dense soil sample after maximum horizontal stress level. The tension tests show that the stress field around the pile seems to be preserved in the dense, and to some extent also in the medium dense soil sample, when the pile is extracted from the soil. The stress history thereby results in a higher shaft friction at the lower part of the pile, which is correlated to the effective vertical stress σ'_v.

The horizontal stress measurements are conducted on a relatively low level of the sensitivity range of the sensor (25%). The large deformations during installation results in very large strains. The calculation mesh grid during installation is consequently distorted, resulting in some inaccurate strain levels.

The experimental research therefore gives novel information about the displacement pile installation effects. The conceptual model which guides the modern pile design methods is shown to be relatively correct concerning the effect of relative density, friction fatigue, and the conceptual description of the components of the total horizontal contact stress $\sigma'_{h,tot}$. But the measurements show that the response in tension have different behaviour for the different initial relative densities, which brittle behaviour for the loose soil sample, possibly resulting from the difference in volumetric strain change during installation. This implies that the reliability of the pile at different relative densities is different, since the brittle behaviour results in more risk of collapse in comparison to a ductile behaviour, in which stress distribution is possible. Consequently, the current conceptual model does not correctly differentiate between the reliability of piles in tension for different initial relative densities. Statistical methods for description of the reliability of the structure are consequently not appropriate for different initial relative densities of the soil. The magnitude of this effect is not known, and it may not be of large significance.

8.2 Recommendations

Installation effects govern the post-installation load-deformation behaviour of displacement piles. These should be taken into account in analysis of piles and pile groups. Methods of analysis include numerical and the modern CPT-based design methods.

The strain computational method could be improved by including a remeshing technique, in which the strain would be calculated from a well-configured triangle that is constructed by interpolation of the displacement increments to a suitable triangular shape in each step. This was considered to be outside the scope of the thesis because of numerical complications during interpolation, but could lead to improved stability of the strain calculations.

Further research into the long-term behaviour of piles is also recommended. Field measurements have shown large changes in load capacity after installation, resulting from possible creep and stress relaxation. This time-dependent effect was not included in the model but could be modelled in the future.

Laboratory, field and numerical experiments on the behaviour of multiple piles during installation would be helpful to comprehend the effect of installation effects in pile groups. Relatively few such field tests of this phenomena have been carried out. A combination of field tests and laboratory tests, coupled with extensive parameters tests by numerical simulation is hence recommended.

Numerical simulations of displacement pile installation offers the possibility to model the complete stress-strain response. The experimental model showed the intricate behaviour of the soil, especially the large variation in stress and strain paths during the installation. Because of the large deformations during installation, special numerical frameworks, such as the material point method that could model large deformations, are recommended.

The inertial and consolidation effects were not included in the experimental model. This is especially of interest for tubular or pipe piles, in which the Poisson's ratio effect is large during stress wave propagation, and also for the analysis of structure close to a pile installed by impact driving. Further research into such effects would be beneficial.

The effect of cyclic loading on the horizontal normal stress may be included into routine numerical simulation by a macro interface element with a stress-strain response. These types of interface analysis are now mainly included in advanced models for shallow foundations.

It is also recommended that a full analysis of the grain properties is conducted before and after installation in an experimental model. This would give the possibility of analysing the effect of the shape and mineral content on the behaviour of the soil.

Bibliography

[1] D. W. Airey and D. M. Wood. An evaluation of direct simple shear tests on clay. *Géotechnique*, 37(1):25–35, 1987.

[2] E. A. Alderlieste. Experimental modelling of lateral loads on large diameter mono-pile foundations in sand. *TU Delft*, 2010.

[3] H. G. B. Allersma. On line measurement of soil deformation in centrifuge tests by image processing. In *Proc. Int. Conf. on Experimental Mechanics, Copenhagen*, pages 1739–1748, 1990.

[4] H. G. B. Allersma. The university of Delft geotechnical centrifuge. In *Proc. Int. Conf. Centrifuge*, volume 94, pages 47–52, 1994.

[5] H. G. B. Allersma, J. R. Hogervorst, and M. Pimoulle. Centrifuge modeling of suction pile installation in layered soil by percussion method. In *OMAE Conf*, pages 87–93, 2001.

[6] A. Altaee and B. H. Fellenius. Physical modeling in sand. *Canadian Geotechnical Journal*, 31(3):420–431, 1994.

[7] K. H. Andersen. Bearing capacity under cyclic loading-offshore, along the coast, and on land. the 21st Bjerrum Lecture presented in Oslo, 23 November 2007 . *Canadian Geotechnical Journal*, 46(5):513–535, 2009.

[8] A. Andresen, T. Berre, A. Kleven, and T. Lunne. Procedures used to obtain soil parameters for foundation engineering in the North sea. *Marine Georesources & Geotechnology*, 3(3):201–266, 1979.

[9] J. H. Atkinson. Non-linear soil stiffness in routine design. *Géotechnique*, 50(5):487–508, 2000.

[10] J. H. Atkinson. Non-linear soil stiffness in routine design. *Géotechnique*, 50(5):487–508, 2000.

[11] G. Axelsson. A conceptual model of pile set-up for driven piles in non-cohesive soil. *Geotechnical Special Publication*, 1:64–79, 2002.

[12] G. Baldi, R. Bellotti, E. Cris, N. Ghionna, M. Jamiolkowski, et al. Stiffness of sands from CPT, SPT and DMT-a critical review. In *Penetration testing in the UK, Geotechnology Conference, 1988, Birmingham, United Kingdom*, 1989.

[13] M. M. Baligh. Strain path method. *Journal of Geotechnical Engineering*, 111(9):1108–1136, 1985.

[14] P. Banerjee and R. Butterfield. *Boundary element methods in engineering science*, volume 17. McGraw-Hill London, 1981.

[15] S. Bardenhagen, J. Brackbill, and D. Sulsky. The material-point method for granular materials. *Computer methods in applied mechanics and engineering*, 187(3):529–541, 2000.

[16] P. Barentsen. Short description of a field testing method with cone-shaped sounding apparatus. In *Proceedings of the 1st International Conference on Soil Mechanics and Foundations Engineering*, pages 6–10, 1936.

[17] B. E. Bayer. Color imaging array, July 20 1976. US Patent 3,971,065.

[18] K. Been, J. H. A. Crooks, D. E. Becker, and M. G. Jefferies. The cone penetration test in sands: part i, state parameter interpretation. *Géotechnique*, 36(2):239–249, 1986.

[19] K. Been and M. G. Jefferies. A state parameter for sands. *Géotechnique*, 35(2):99–112, 1985.

[20] K. Been, M. G. Jefferies, J. H. A. Crooks, and L. Rothenburg. The cone penetration test in sands: part ii, general inference of state. *Géotechnique*, 37(3):285–299, 1987.

[21] K. Been, M. G. Jefferies, and J. Hachey. The critical state of sands. *Géotechnique*, 41(3):365–381, 1991.

[22] K. Been, M. G. Jefferies, J. A. Sladen, J. Krahn, and R. D. Hollander. Discussion: A state parameter for sands. *Géotechnique*, 36(1), 1986.

[23] L. Bendel. Comparison between the penetration-curve of sounding needle before and after the placing into position of a pile. In *Proc. II Internat. Conf. Soil Mech. and Found, engng*, volume 4, 1948.

[24] L. Bendel. Movements of a driven-in pile, when new piles are being driven. In *Proc. II Internat. Conf. Soil Mech. and Found, engng*, volume 4, 1948.

[25] V. Berezantzev. Load bearing capacity and deformation of piled foundations. *Proc. 5th ICSMFE, Paris, 1961*, 2:11–12, 1961.

[26] P. Berg, R. de Borst, and H. Huetink. An eulerean finite element model for penetration in layered soil. *International journal for numerical and analytical methods in geomechanics*, 20(12):865–886, 1996.

[27] L. Bjerrum. Engineering geology of norwegian normally-consolidated marine clays as related to settlements of buildings. *Géotechnique*, 17(2):83–118, 1967.

[28] L. Bjerrum, I. Johannessen, and O. Eide. Reduction of negative skin friction on steel piles to rock. In *Soil Mech & Fdn Eng Conf Proc Mexico*, 1963.

[29] J. Bogard and H. Matlock. In-situ pile segment model experiments at Empire, Louisiana. In *Offshore Technology Conference*, 1990.

[30] J. Bogard, H. Matlock, J. Audibert, and S. Bamford. Three years' experience with model pile segment tool tests. In *Offshore Technology Conference*, 1985.

[31] M. D. Bolton. The strength and dilatancy of sands. *Géotechnique*, 36(1):65–78, 1986.

[32] A. J. Bond, R. J. Jardine, and J. C. P. Dalton. Design and performance of the Imperial college instrumented pile. *ASTM geotechnical testing journal*, 14(4):413–424, 1991.

[33] M. Boulon. Basic features of soil structure interface behaviour. *Computers and Geotechnics*, 7(1):115–131, 1989.

[34] M. Boulon and P. Foray. Physical and numerical simulation of lateral shaft friction along offshore piles in sand. In *Proceeding., 3rd International Conference on Numerical Methods in Offshore piling, Nantes*, pages 127–148, 1986.

[35] W. Bouzid Saı, N. Ben Salah, and J. L. Lebrun. Influence of machining by finishing milling on surface characteristics. *International Journal of Machine Tools and Manufacture*, 41(3):443–450, 2001.

[36] J.-L. Briaud and L. M. Tucker. Piles in sand: a method including residual stresses. *Journal of Geotechnical Engineering*, 110(11):1666–1680, 1984.

[37] W. Broere and A. F. van Tol. Modelling the bearing capacity of displacement piles in sand. *Proceedings of the ICE-Geotechnical Engineering*, 159(3):195–206, 2006.

[38] D. Bruno and M. F. Randolph. Dynamic and static load testing of model piles driven into dense sand. *Journal of geotechnical and geoenvironmental engineering*, 125(11):988–998, 1999.

[39] J. B. Burland. On the compressibility and shear strength of natural clays. *Géotechnique*, 40(3):329–378, 1990.

[40] M. Bustamante and L. Gianeselli. Pile bearing capacity prediction by means of static penetrometer CPT. In *Proceedings of the 2nd European Symposium on Penetration Testing*, volume 2, pages 493–500, 1982.

[41] G. Cai, S. Liu, L. Tong, and G. Du. Assessment of direct CPT and CPTu methods for predicting the ultimate bearing capacity of single piles. *Engineering Geology*, 104(3):211–222, 2009.

[42] A. Casagrande. The structure of clay and its importance in foundation engineering. *Boston Society Civil Engineers Journal*, 1932.

[43] G.-C. Cho, J. Dodds, and J. C. Santamarina. Particle shape effects on packing density, stiffness, and strength: natural and crushed sands. *Journal of Geotechnical and Geoenvironmental Engineering*, 132(5):591–602, 2006.

[44] M. Chong. Density changes of sand on cone penetration resistance. In *Proceedings of the first international symposium on penetration testing ISOPT*, volume 1, pages 707–714, 1988.

[45] F. Chow. *Investigations into the behaviour of displacement piles for offshore foundations.* PhD thesis, Imperial College London (University of London), 1996.

[46] F. C. Chow. Field measurements of stress interactions between displacement piles in sand. In *Ground Engineering*, volume 33. Elsevier, 1996.

[47] F. C. Chow, R. J. Jardine, F. Brucy, and J. F. Nauroy. Effects of time on capacity of pipe piles in dense marine sand. *Journal of Geotechnical and Geoenvironmental Engineering*, 124(3):254–264, 1998.

[48] F. C. Chow, R. J. Jardine, J. F. Nauroy, and F. Brucy. Time-related increases in the shaft capacities of driven piles in sand. *Géotechnique*, 47(2), 1997.

[49] H. P. Christoffersen and T. Lunne. Interpretation of cone penetrometer data for offshore sands. In *Offshore Technology Conference*, 1983.

[50] C. J. F. Clausen, P. M. Aas, and K. Karlsrud. Bearing capacity of driven piles in sand, the NGI approach. In *Proceedings of Proceedings of International Symposium. on Frontiers in Offshore Geotechnics, Perth*, pages 574–580, 2005.

[51] M. R. Coop and J. H. Atkinson. The mechanics of cemented carbonate sands. *Géotechnique*, 43(1):53–67, 1993.

[52] R. Correia, J. Li, S. Staines, E. Chehura, S. W. James, J. Kutner, P. Dewhurst, P. Ferreira, and R. P. Tatam. Fibre bragg grating based effective soil pressure sensor for geotechnical applications. In *Proc. of SPIE Vol*, volume 7503, pages 75030F–1, 2009.

[53] W. H. Craig. Installation studies for model piles. *Publication of: Balkema (AA)*, 1985.

[54] W. H. Craig and K. Chua. Deep penetration of spud-can foundations on sand and clay. *Géotechnique*, 40(4):541–556, 1990.

[55] M. Cubrinovski and K. Ishihara. Maximum and minimum void ratio characteristics of sands. *Soils and foundations*, 42(6):65–78, 2002.

[56] P. A. Cundall and R. D. Hart. Numerical modelling of discontinua. *Engineering computations*, 9(2):101–113, 1992.

[57] J. L. Davidson and A. Boghrat. Displacements and strains around probes in sand. In *Geotechnical Practice in Offshore Engineering*, pages 181–202. ASCE, 1983.

[58] R. O. Davis and A. P. S. Selvadurai. *Elasticity and Geomechanics*. Cambridge University Press, 1996.

[59] R. O. Davis and A. P. S. Selvadurai. *Plasticity and geomechanics*. Cambridge: Cambridge University Press, 2002.

[60] T. De Blaeij, A. van Tol, J. Dijkstra, and H. Everts. On the modelling of installation effects on laterally cyclic loaded monopiles. 2013.

[61] A. De Nicola and M. Randolph. The plugging behaviour of driven and jacked piles in sand. *Géotechnique*, 47(4):841–856, 1997.

[62] A. De Nicola and M. F. Randolph. Tensile and compressive shaft capacity of piles in sand. *Journal of geotechnical engineering*, 119(12):1952–1973, 1993.

[63] C. J. De Pater and J. D. Nieuwenhuis. Method for measuring the deformations of a sand surface. *Géotechnique*, 36(4):581–585, 1986.

[64] J. De Ruiter and F. L. Beringen. Pile foundations for large North sea structures. *Marine Georesources & Geotechnology*, 3(3):267–314, 1979.

[65] J. T. Dejong, M. F. Randolph, and D. J. White. Interface load transfer degradation during cyclic loading: a microscale investigation. *Soils and foundations*, 43(4):81–93, 2003.

[66] C. Desai, E. Drumm, and M. Zaman. Cyclic testing and modeling of interfaces. *Journal of Geotechnical Engineering*, 111(6):793–815, 1985.

[67] R. Descartes. *Descartes: Meditations on first philosophy: With selections from the objections and replies*. Jan de Maire, 1634.

[68] E. A. Dickin and C. F. Leung. Centrifugal model tests on vertical anchor plates. *Journal of Geotechnical Engineering*, 109(12):1503–1525, 1983.

[69] J. Dijkstra. *On the Modelling of Pile Installation*. PhD thesis, Technische Hogeschool Delft, 2009.

[70] J. Dijkstra and W. Broere. New method of full-field stress analysis and measurement using photoelasticity. *Geotechnical Testing Journal*, 33(6):1, 2010.

[71] J. Dijkstra, W. Broere, and O. M. Heeres. Numerical simulation of pile installation. *Computers and Geotechnics*, 38(5):612–622, 2011.

[72] J. Dijkstra, W. Broere, and A. F. Van Tol. Numerical investigation into stress and strain development around a displacement pile in sand. In *Proceedings of the sixth European Conference on Numerical Methods in Geotechnical Engineering*, pages 595–600, 2006.

[73] H. R. C. Dingle, D. J. White, and C. Gaudin. Mechanisms of pipe embedment and lateral breakout on soft clay. *Canadian Geotechnical Journal*, 45(5):636–652, 2008.

[74] A. Drescher and G. De Josselin de Jong. Photoelastic verification of a mechanical model for the flow of a granular material. *Journal of the Mechanics and Physics of Solids*, 20(5):337–340, 1972.

[75] J. M. Duncan and C.-Y. Chang. Nonlinear analysis of stress and strain in soils. *Journal of the Soil Mechanics and Foundations Division*, 96(5):1629–1653, 1970.

[76] H. K. Engin. *Modelling pile installation effects: a numerical approach*. PhD thesis, Technische Hogeschool Delft.

[77] A. Eslami and B. H. Fellenius. Pile capacity by direct CPT and CPTu methods applied to 102 case histories. *Canadian Geotechnical Journal*, 34(6):886–904, 1997.

[78] B. H. Fellenius. Down-drag on piles in clay due to negative skin friction. *Canadian Geotechnical Journal*, 9(4):323–337, 1972.

[79] B. H. Fellenius. From strain measurements to load in an instrumented pile. *Geotechnical news - Vancouver*, 19(1):35–38, 2001.

[80] V. Fioravante. On the shaft friction modelling of non-displacement piles in sand. *Soils and foundations*, 42(2):23–33, 2002.

[81] W. G. K. Fleming. A new method for signle pile settlement prediction and analysis. *Géotechnique*, 42(3):411–425, 1992.

[82] W. G. K. Fleming, A. J. Weltman, M. F. Randolph, and W. K. Elson. *Piling engineering.* Taylor & Francis, 2008.

[83] P. Foray, L. Balachowski, and J.-L. Colliat. Bearing capacity of model piles driven into dense overconsolidated sands. *Canadian Geotechnical Journal*, 35(2):374–385, 1998.

[84] P. Foray, L. Balachowski, and G. Rault. Scale effect in shaft friction due to the localisation of deformations. In *International conference Centrifuge 98*, pages 211–216, 1998.

[85] P. Foray and J. F. Nauroy. Bearing capacity of driven model piles in dense sands from calibration chamber tests. In *Offshore Technology Conference*, 1993.

[86] R. French. Membrane strain gauge, Oct. 11 1966. US Patent 3,278,881.

[87] A. Gajo and D. Muir Wood. Severn–trent sand: a kinematic-hardening constitutive model: the q–p formulation. *Géotechnique*, 49(5):595–614, 1999.

[88] J. Garnier, C. Gaudin, S. M. Springman, P. J. Culligan, D. J. Goodings, D. Konig, B. L. Kutter, R. Phillips, M. F. Randolph, and L. Thorel. Catalogue of scaling laws and similitude questions in geotechnical centrifuge modelling. *International Journal of Physical Modelling in Geotechnics*, 7(3):1–23, 2007.

[89] K. G. Gavin and B. C. O Kelly. Effect of friction fatigue on pile capacity in dense sand. *Journal of geotechnical and geoenvironmental engineering*, 133(1):63–71, 2007.

[90] G. W. Gee and D. Or. Particle-size analysis. *Methods of soil analysis. Part 1*, 4:255–293, 2002.

[91] M. C. Gemperline and H. Ko. *Centrifugal model tests for ultimate bearing capacity of footings on steep slopes in cohesionless soils.* 1985.

[92] P. Gieb. Membrane-type strain gauge, Oct. 19 1965. US Patent 3,213,400.

[93] Giken-Ltd. *Tubular sheet pile Press-in method.* Giken-Seisakusho, 2012.

[94] G. G. Goble and F. Rausche. Pile driveability predictions by CAPWAP. In *Proceedings Conference on Numerical Methods in Offshore Piling*, 1979.

[95] J. Grabe, P. Busch, and T. Hamann. On the set-up of piles. In *ASME 2014 33rd International Conference on Ocean, Offshore and Arctic Engineering*, pages V003T10A027–V003T10A027. American Society of Mechanical Engineers, 2014.

[96] J. Grabe, T. Pucker, and T. Hamann. Numerical simulation of pile installation processes in dry and saturated granular soil. In *8th European Conference on Numerical methods in Geotechnical Engineering*, 2014.

[97] O. S. Gregersen, G. Aas, and E. Dibiagio. Load tests on friction piles in loose sand. In *Proc.eigth Int. Conf. on Soil Mech. Found. Engng, Moscow*. Elsevier, 1973.

[98] M. W. Gui and M. D. Bolton. Geometry and scale effects in CPT and pile design. In *Proceeding of the 1st International Conference of Site Characterization. Atlanta:[sn]*, volume 1, pages 063–1, 1998.

[99] R. C. Gupta. Finite strain analysis for deep cone penetration. *Journal of Geotechnical Engineering*, 117(10):1610–1630, 1991.

[100] S. Gupta and W. E. Larson. A model for predicting packing density of soils using particle-size distribution. *Soil Science Society of America Journal*, 43(4):758–764, 1979.

[101] T. M. Gurtowski and M.-J. Wu. Compression load tests on concrete piles in alluvium. In *Analysis and Design of Pile Foundations*, pages 138–153. ASCE, 1984.

[102] T. H. Hanna and R. H. S. Tan. The behavior of long piles under compressive loads in sand. *Canadian Geotechnical Journal*, 10(3):311–340, 1973.

[103] E. P. Heerema. Predicting pile driveability: Heather as an illustration of the friction fatigue theory. In *SPE European Petroleum Conference*, 1978.

[104] E. P. Heerema. Relationships between wall friction, displacement velocity and horizontal stress in clay and in sand, for pile driveability analysis. *Ground engineering*, 12(1), 1979.

[105] J. Heikkila. Geometric camera calibration using circular control points. *Pattern Analysis and Machine Intelligence*, 22(10):1066–1077, 2000.

[106] J. Heikkila and O. Silven. A four-step camera calibration procedure with implicit image correction. In *Computer Vision and Pattern Recognition, 1997. Proceedings., 1997 IEEE Computer Society Conference on*, pages 1106–1112. IEEE, 1997.

[107] S. Helfrich, E. Wiltsie, W. Cox, and K. A. Shafie. Pile load tests in dense sand: planning, instrumentation, and results. In *Offshore Technology Conference*, 1985.

[108] E. K. Henriksen. Residual stresses in machined surfaces. ASME, 1948.

[109] T. Y. K. Ho, R. J. Jardine, and N. Anh-Minh. Large-displacement interface shear between steel and granular media. *Géotechnique*, 61(3):221–234, 2010.

[110] B. A. Hofmann, D. C. Sego, and P. K. Robertson. In situ ground freezing to obtain undisturbed samples of loose sand. *Journal of geotechnical and geoenvironmental engineering*, 126(11):979–989, 2000.

[111] D. Holloway, G. Clough, and A. Vesic. The effects of residual driving stresses on pile performance under axial loads. In *Offshore Technology Conference*, 1978.

[112] H. Holzapfel, V. Schulze, O. Vöhringer, and E. Macherauch. Residual stress relaxation in an AISI 4140 steel due to quasistatic and cyclic loading at higher temperatures. *Materials Science and Engineering: A*, 248(1):9–18, 1998.

[113] P. Huet. Electromechanical transducer, Jan. 20 1970. US Patent 3,491,324.

[114] C. B. Hunt et al. Geology of soils: Their evolution, classification and uses. *Geology of Soils: Their Evolution, Classification and Uses.*, 1972.

[115] A. H. Hunter and M. T. Davisson. Measurements of pile load transfer. 1969.

[116] M. J. Hvorslev. *Uber die Festigkeitseigenschaften gestorter bindiger Boden.* Danmarks Naturvidensk Samfund, 1937.

[117] N. Janbu. Soil compressibility as determined by oedometer and triaxial tests. In *European Conference on Soil Mechanics and Foundation Engineering*, volume 1, pages 19–25, 1963.

[118] R. Jardine, J. Standing, Health, and L. U. K. Safety Executive. Pile load testing performed for hse cyclic loading study at dunkirk, france volume 1. *OFFSHORE TECHNOLOGY REPORT-HEALTH AND SAFETY EXECUTIVE OTO*, 2000.

[119] R. Jardine, B. Zhu, P. Foray, and Z. Yang. Interpretation of stress measurements made around closed-ended displacement piles in sand. 2012.

[120] R. J. Jardine. Bishop lecture. 2014.

[121] R. J. Jardine and F. C. Chow. *New design methods for offshore piles.* Marine Technology Directorate, 1996.

[122] R. J. Jardine and F. C. Chow. Some recent developments in offshore pile design. *Offshore site investigation and geotechnics, Confronting New Challenges and Sharing Knowledge*, 2007.

[123] R. J. Jardine, F. C. Chow, R. Overy, and J. Standing. *ICP design methods for driven piles in sands and clays.* Thomas Telford London, 2005.

[124] R. J. Jardine, B. M. Lehane, and S. J. Everton. Friction coefficients for piles in sands and silts. In *Offshore Site Investigation and Foundation Behaviour*, pages 661–677. Springer, 1993.

[125] R. J. Jardine, R. F. Overy, and F. C. Chow. Axial capacity of offshore piles in dense North sea sands. *Journal of geotechnical and geoenvironmental engineering*, 124(2):171–178, 1998.

[126] R. J. Jardine, D. M. Potts, A. B. Fourie, and J. B. Burland. Studies of the influence of non-linear stress–strain characteristics in soil–structure interaction. *Géotechnique*, 36(3):377–396, 1986.

[127] R. J. Jardine, B. T. Zhu, P. Foray, and Z. X. Yang. Interpretation of stress measurements made around closed-ended displacement piles in sand. 2013.

[128] R. J. Jardine, B. T. Zhu, P. Foray, and Z. X. Yang. Measurement of stresses around closed-ended displacement piles in sand. *Géotechnique*, 63(1):1–17, 2013.

[129] C. E. Johnson, R. D. Girsso, T. A. Nichols, and A. C. Bailey. Shear measurement for agricultural soil: A review. *Trans. ASAE*, 30(4):935–938, 1987.

[130] K. Karlsrud and F. Nadim. Axial capacity of offshore piles in clay. In *Offshore Technology Conference*, 1990.

[131] R. D. Keane and R. J. Adrian. Theory of cross-correlation analysis of piv images. *Applied scientific research*, 49(3):191–215, 1992.

[132] R. King, W. Hooydonk, H. Kolk, and D. Windle. Geotechnical investigations of calcareous soils on the North west shelf, australia. In *Offshore Technology Conference*, 1980.

[133] J. Kirby. Soil stress measurement: Part i. transducer in a uniform stress field. *Journal of Agricultural Engineering Research*, 72(2):151 – 160, 1999.

[134] H. Kishida and M. Uesugi. Tests of the interface between sand and steel in the simple shear apparatus. *Géotechnique*, 37(1):45–52, 1987.

[135] F. Klocke and T. Krieg. Coated tools for metal cutting–features and applications. *CIRP Annals-Manufacturing Technology*, 48(2):515–525, 1999.

[136] E. U. Klotz and M. R. Coop. An investigation of the effect of soil state on the capacity of driven piles in sands. *Géotechnique*, 51(9):733–751, 2001.

[137] T. Kobayashi and R. Fukagawa. Characterization of deformation process of CPT using x-ray tv imaging technique. *Deformation Characteristics of Geomaterials/Comportement Des Sols Et Des Roches Tendres*, page 43, 2010.

[138] H. Kolk, A. Baaijens, and M. Senders. Design criteria for pipe piles in silica sands. In *Proc., 1st Int. Symp. on Frontiers in Offshore Geotechnics*, pages 711–716. Balkema Perth, Australia, 2005.

[139] F. König and J. Grabe. Time dependant increase of the bearing capacity of displacement piles. piling and deep foundations. In *Conference Proceedings, DFI EFFC, Amsterdam*, pages 709–717, 2006.

[140] F. König, J. Grabe, J. Francke, and J. Woldt. Load bearing behaviour of an existing pile foundation and its changes with time. In *INternational Conference on Reuse of Foundations for Urban Sites, UK*, pages 199–211, 2006.

[141] L. M. Kraft Jr. Performance of axially loaded pipe piles in sand. *Journal of Geotechnical Engineering*, 117(2):272–296, 1991.

[142] T. S. Kuhn. The function of measurement in modern physical science. *Isis*, 52(2):161–193, 1961.

[143] T. S. Kuhn. The structure of scientific revolutions. 1962.

[144] B. L. Kutter. Recent advances in centrifuge modeling of seismic shaking. In *Proc., 3rd Int. Conf. on Recent Advances in Geotechnical Earthquake Engineering and Soil Dynamics*, volume 2, pages 927–942. Univ. of Missouri Rolla, MO, 1995.

[145] B. L. Kutter, A. Abghari, and J. A. Cheney. Strength parameters for bearing capacity of sand. *Journal of geotechnical engineering*, 114(4):491–498, 1988.

[146] Y.-J. Lee and R. H. Bassett. Influence zones for 2D pile–soil-tunnelling interaction based on model test and numerical analysis. *Tunnelling and underground space technology*, 22(3):325–342, 2007.

[147] B. M. Lehane, C. Gaudin, and J. A. Schneider. Scale effects on tension capacity for rough piles buried in dense sand. *Géotechnique*, 55(10):709–720, 2005.

[148] B. M. Lehane, R. J. Jardine, A. J. Bond, and R. Frank. Mechanisms of shaft friction in sand from instrumented pile tests. *Journal of Geotechnical Engineering*, 119(1):19–35, 1993.

[149] B. M. Lehane, J. A. Schneider, J. K. Lim, and G. Mortara. Shaft friction from instrumented displacement piles in an uncemented calcareous sand. *Journal of Geotechnical and Geoenvironmental Engineering*, 138(11):1357–1368, 2012.

[150] B. M. Lehane, J. A. Schneider, and X. Xu. The UWA-05 method for prediction of axial capacity of driven piles in sand. In *Proc., 1st Int. Symp. on Frontiers in Offshore Geotechnics*, pages 683–689. Balkema Perth, Australia, 2005.

[151] B. M. Lehane and D. J. White. Lateral stress changes and shaft friction for model displacement piles in sand. *Canadian geotechnical journal*, 42(4):1039–1052, 2005.

[152] S. Leroueil and P. R. Vaughan. The general and congruent effects of structure in natural soils and weak rocks. *Géotechnique*, 40(3):467–488, 1990.

[153] Z. Li, M. D. Bolton, and S. K. Haigh. Cyclic axial behaviour of piles and pile groups in sand. *Canadian Geotechnical Journal*, 49(9):1074–1087, 2012.

[154] Z. Li, S. K. Haigh, and M. D. Bolton. Effect of previous cyclic axial loads on pile groups. *International Journal of Physical Modelling in Geotechnics*, 12(1):15–23, 2012.

[155] M. L. Lings. Predicting the shaft resistance of driven pre-formed piles in sand. *Proceedings of the ICE-Geotechnical Engineering*, 125(2):71–84, 1997.

[156] Q. B. Liu and B. M. Lehane. The influence of particle shape on the (centrifuge) cone penetration test (CPT) end resistance in uniformly graded granular soils.

[157] D. S. Liyanapathirana, A. J. Deeks, and M. F. Randolph. Numerical modelling of large deformations associated with driving of open-ended piles. *International journal for numerical and analytical methods in geomechanics*, 24(14):1079–1101, 2000.

[158] T. Lunne, P. Robertson, and J. Powell. CPT in geotechnical practice. *Blackie Academic and Professional*, 1997.

[159] K. Mahutka, F. König, and J. Grabe. Numerical modelling of pile jacking, driving and vibratory driving. *Numerical modelling of construction processes in geotechnical engineering for urban environment. Taylor & Francis, London*, pages 235–246, 2006.

[160] C. I. Mansur and R. I. Kaufman. Pile tests, low-sill structure, old river, Louisiana. *Transactions of the American Society of Civil Engineers*, 123(1):715–743, 1958.

[161] Matlab. The mathworks, guide, matlab users. *Inc., Natick, MA*, 5, 1998.

[162] A. Mayer and R. L'Herminier. Le pouvoir portant des pieux en milieu coherent. In *Comp. Rend. du Troisieme Congress International des Sols et des Travaux de Fondation, VIII*, volume 2, pages 5–8, 1953.

[163] G. G. Mayerhof. Bearing capacity and settlem of pile foundations. *Journal of Geotechnical and Geoenvironmental Engineering*, 102(ASCE 11962), 1976.

[164] Mettler. Operating instructions for high capacity pm scales. 2008.

[165] N. Mikasa and N. Takada. Significance of centrifuge model tests in soil mechanics. In *Proc.eigth Int. Conf. on Soil Mech. Found. Engng, Moscow*, volume 12, page 98. Elsevier, 1975.

[166] R. D. Mindlin. Force at a point in the interior of a semi-infinite solid. *Journal of Applied Physics*, 7:195–202, 1936.

[167] G. C. M. Modeling. Comsol version 3.5 a. *COMSOL AB*, 2008, 1998.

[168] M. Molenda, M. Montross, and J. Horabik. Performance of earth pressure cell as grain pressure transducer in a model silo. *International agrophysics*, 21(1):73, 2007.

[169] D. Muir Wood. The magic of sands-the 20th Bjerrum lecture. *Canadian Geotechnical Journal*, 44(11):1329–1350, 2007.

[170] D. Muir Wood and K. Maeda. Changing grading of soil: effect on critical states. *Acta Geotechnica*, 3(1):3–14, 2008.

[171] Q. I. Ni, C. C. Hird, and I. Guymer. Physical modelling of pile penetration in clay using transparent soil and particle image velocimetry. *Géotechnique*, 60(2):121–132, 2010.

[172] T. A. Nichols, A. C. Bailey, C. E. Johnson, and R. D. Grisso. A stress state transducer for soil. *Trans. ASAE*, 30(5):1237–1241, 1987.

[173] C. Olsson and G. Holm. *Pålgrundläggning*. Svensk byggtjänst, 1993.

[174] N. K. Ovesen. Centrifugal testing applied to bearing capacity problems of footings on sand. *Géotechnique*, 25(2):394–401, 1975.

[175] N. K. Ovesen. The use of physical models in design: The scaling law relationship. In *Proc., 7th European Conf. on Soil Mechanics and Foundation Engineering*, volume 4, pages 318–323. British Geotechnical Society London, 1979.

[176] N. K. Ovesen. Centrifuge tests of the uplift capacity of anchors. In *Proceedings of the 10th International Conference on Soil Mechanics and Foundation Engineering, Stockholm*, volume 1, pages 717–722, 1981.

[177] K. R. Peattie and R. Sparrow. The fundamental action of earth pressure cells. *Journal of the Mechanics and Physics of Solids*, 2(3):141–155, 1954.

[178] J. Pelletier, J. Murff, and A. Young. Historical development and assessment of the current API design methods for axially loaded pipes. In *Offshore Technology Conference*, 1993.

[179] R. Phillips and A. J. Valsangkar. Experimental investigation of factors affecting penetration resistance in granular soils in centrifuge modelling. *Cambridge University, Engineering Department,(Technical Report) CUED/D-Soils*, 1987.

[180] G. Plantema and C. Nolet. Influence of pile driving on the sounding resistance in a deep sand layer. In *Proc. 4th Int. Conf. Soil Mech*, volume 2, pages 52–55, 1957.

[181] H. G. Poulos. Analysis of residual stress effects in piles. *Journal of geotechnical engineering*, 113(3):216–229, 1987.

[182] H. G. Poulos. Pile behaviour: theory and application. *Géotechnique*, 39(3):365–415, 1989.

[183] H. G. Poulos. Effect of pile driving on adjacent piles in clay. *Canadian geotechnical journal*, 31(6):856–867, 1994.

[184] H. G. Poulos and E. H. Davis. *Pile foundation analysis and design*. Wiley, 1980.

[185] H. G. Poulos and M. F. Randolph. Pile group analysis: a study of two methods. *Journal of Geotechnical Engineering*, 109(3):355–372, 1983.

[186] T. Pucker and J. Grabe. Numerical simulation of the installation process of full displacement piles. *Computers and Geotechnics*, 45:93–106, 2012.

[187] M. F. Randolph, J. Dolwin, and R. Beck. Design of driven piles in sand. *Géotechnique*, 44(3):427–448, 1994.

[188] M. F. Randolph and A. R. House. The complementary roles of physical and computational modelling. *International Journal of Physical Modelling in Geotechnics*, 1(1):1–8, 2001.

[189] M. F. Randolph, M. O'Neill, D. Stewart, and C. Erbrich. Performance of suction anchors in fine-grained calcareous soils. In *Offshore Technology Conference*, 1998.

[190] M. F. Randolph and C. P. Wroth. Analysis of deformation of vertically loaded piles. *Journal of the Geotechnical Engineering Division*, 104(12):1465–1488, 1978.

[191] M. F. Randolph and C. P. Wroth. An analysis of the vertical deformation of pile groups. *Géotechnique*, 29(4):423–439, 1979.

[192] J. N. Reddy. *Theory and analysis of elastic plates and shells*. CRC, 2006.

[193] O. Reul and M. F. Randolph. Design strategies for piled rafts subjected to nonuniform vertical loading. *Journal of geotechnical and geoenvironmental engineering*, 130(1):1–13, 2003.

[194] O. Reynolds. On the dilatancy of media composed of rigid particles in contact. *Philos. Mag. Ser. 5*, 50, 1885.

[195] O. Reynolds. Experiments showing dilatancy, a property of granular material, possibly connected with gravitation. In *Proc. Royal Institution of Great Britain, Read*, volume 12, 1886.

[196] R. D. Rieke and J. C. Crowser. Interpretation of pile load test considering residual stresses. *Journal of geotechnical engineering*, 113(4):320–334, 1987.

[197] E. I. Robinsky and C. F. Morrison. Sand displacement and compaction around model friction piles. *Canadian Geotechnical Journal*, 1(2):81–93, 1964.

[198] E. I. Robinsky, W. L. Sagar, and C. F. Morrison. Effect of shape and volume on the capacity of model piles in sand. *Canadian Geotechnical Journal*, 1(4):189–204, 1964.

[199] K. M. Rollins, K. T. Peterson, and T. J. Weaver. Lateral load behavior of full-scale pile group in clay. *Journal of geotechnical and geoenvironmental engineering*, 124(6):468–478, 1998.

[200] K. H. Roscoe. Soils and model tests. *The Journal of Strain Analysis for Engineering Design*, 3(1):57–64, 1968.

[201] K. H. Roscoe. The influence of strains in soil mechanics. *Géotechnique*, 20(2):129–170, 1970.

[202] K. H. Roscoe, A. N. Schofield, and C. P. Wroth. On the yielding of soils. *Géotechnique*, 8(1):22–53, 1958.

[203] P. C. Rouse, R. J. Fannin, and D. A. Shuttle. Influence of roundness on the void ratio and strength of uniform sand. *Géotechnique*, 58(3):227–231, 2008.

[204] P. Rowe. The relevance of soil fabric to site investigation practice. *Géotechnique*, 22, 1972.

[205] P. W. Rowe. The stress-dilatancy relation for static equilibrium of an assembly of particles in contact. *Proceedings of the Royal Society of London. Series A. Mathematical and Physical Sciences*, 269(1339):500–527, 1962.

[206] R. Rusinek, M. Molenda, and J. Horabik. Performance of membrane pressure transducers in granular materials of various particle sizes. *Powder Technology*, 190(3):410–414, 2009.

[207] J. H. Schmertmann. Effects of in-situ lateral stress on friction-cone penetrometer data in sands. In *Proc., Fugro Sondeer Symp*, pages 37–39, 1972.

[208] J. H. Schmertmann. Guidelines for cone penetration test (performance and design). Technical report, 1978.

[209] C. A. Schneider, W. S. Rasband, and K. W. Eliceiri. Nih image to imagej: 25 years of image analysis. *Nat Methods*, 9(7):671–675, 2012.

[210] J. A. Schneider, D. J. White, and B. M. Lehane. Shaft friction of piles driven in siliceous, calcareous and micaceous sands. *Offshore site investigation and Geotechnics, Confronting New Challenges and Sharing Knowledge*, 2007.

[211] A. N. Schofield. Cambridge geotechnical centrifuge operations. *Géotechnique*, 30(3):227–268, 1980.

[212] A. N. Schofield and C. P. Wroth. Critical state soil mechanics. 1968.

[213] E. W. Shublaq. Soil disturbance due to installation of model piles and pile groups. *Soils and foundations*, 32(4):17–26, 1992.

[214] B. Simpson. Thirty-second rankine lecture: Retaining structures: displacement and design. *Géotechnique*, 42:539–539, 1992.

[215] J. Steenfelt, M. Randolph, and C. Wroth. *Model tests on instrumented piles jacked into clay.* Cambridge University Engineering Department, 1981.

[216] R. Stevens. The effect of grain shape on pile capacity in sand. In *Offshore Technology Conference*, 2012.

[217] H. G. Stuit. Sand in the geotechnical centrifuge, 1995.

[218] J. T. Tabucanon, D. W. Airey, and H. G. Poulos. Pile skin friction in sands from constant normal stiffness tests. *ASTM geotechnical testing journal*, 18(3):350–364, 1995.

[219] M. Talesnick. The effect of compliance and grain size on the outcome of soil pressure measurements in granular soils. *Research, Development, and Practice in Structural Engineering and Construction, ASEA-SEC-1, Perth*, 2012.

[220] M. Talesnick. Measuring soil pressure within a soil mass. *Canadian Geotechnical Journal*, 12, 2013.

[221] K. G. Taylor, R. L. Gawthorpe, C. D. Curtis, J. D. Marshall, and D. N. Awwiller. Carbonate cementation in a sequence-stratigraphic framework: Upper cretaceous sandstones, book cliffs, utah-colorado. *Journal of Sedimentary Research*, 70(2):360–372, 2000.

[222] R. N. Taylor. Centrifuges in modeling: principles and scale effects. *Geotechnical centrifuge technology*, pages 19–33, 1995.

[223] K. L. Teh, M. J. Cassidy, C. F. Leung, Y. K. Chow, M. F. Randolph, and C. K. Quah. Revealing the bearing capacity mechanisms of a penetrating spudcan through sand overlying clay. *Géotechnique*, 58(10):793–804, 2008.

[224] H. S. Thomas and W. H. Ward. The design, construction and performance of a vibrating-wire earth pressure cell. *Géotechnique*, 19(1), 1969.

[225] G. W. L. Thompson and R. J. Jardine. The applicability of the new Imperial college pile design method to calcareous' sands. In *Offshore Site Investigation and Foundation Behaviour'New Frontiers: Proceedings of an International Conference*, 1998.

[226] S. Timoshenko, S. Woinowsky-Krieger, and S. Woinowsky. *Theory of plates and shells*, volume 2. McGraw-hill New York, 1959.

[227] F. E. Toolan and D. A. Fox. Geotechnical planning of piled foundations for offshore platforms. In *ICE Proceedings*, volume 62, pages 221–244. Thomas Telford, 1977.

[228] P. R. Vaughan. Assumption, prediction and reality in geotechnical engineering. *Géotechnique*, 44(4):573–609, 1994.

[229] P. Vennemann. Jpiv: Introduction and how-to guide. 2009.

[230] P. A. Vermeer. *Formulation and analysis of sand deformation problems*. PhD thesis, Technische Hogeschool Delft, 1980.

[231] A. S. Vesic. Tests on instrumented piles, ogeechee river site. *Journal of Soil Mechanics & Foundations Div*, 1970.

[232] A. S. Vesic. Expansion of cavities in infinite soil mass. *Journal of Soil Mechanics & Foundations Div*, 98(sm3), 1972.

[233] Vitruvius. *The ten books on architecture*. Echo Library, 2008.

[234] P. von Wolffersdorff. A hypoplastic relation for granular materials with a predefined limit state surface. *Mechanics of Cohesive-frictional Materials*, 1(3):251–271, 1996.

[235] D. Warrington. *Vulcanhammer Guide to Pile Driving Equipment*. Vulcan-Hammer, West Palm Beach, Florida, 2008.

[236] J. Weng, T. S. Huang, and N. Ahuja. Motion and structure from line correspondences; closed-form solution, uniqueness, and optimization. *Pattern Analysis and Machine Intelligence*, 14(3):318–336, 1992.

[237] J. Westerweel. Digital particle image velocimetry. *Delft University*, pages 17–18, 1993.

[238] J. Westerweel. Fundamentals of digital particle image velocimetry. *Measurement Science and Technology*, 8(12):1379, 1997.

[239] J. Westerweel and F. Scarano. Universal outlier detection for piv data. *Experiments in Fluids*, 39(6):1096–1100, 2005.

[240] D. White, W. Take, and M. Bolton. Measuring soil deformation in geotechnical models using digital images and piv analysis. In *10th International Conference on Computer Methods and Advances in Geomechanics, Tucson, Arizona*, pages 997–1002, 2001.

[241] D. J. White. A general framework for shaft resistance on displacement piles in sand. In *Proceedings of the 1st International Symposium on Frontiers in Offshore Geotechnics, ISFOG 2005*, pages 697–704. Taylor and Francis, 2005.

[242] D. J. White. Contributions to géotechnique 1948–2008: Physical modelling. *Géotechnique*, 58(5):413–421, 2008.

[243] D. J. White and M. D. Bolton. Displacement and strain paths during plane-strain model pile installation in sand. *Géotechnique*, 54(6):375–397, 2004.

[244] D. J. White and M. D. Bolton. Displacement and strain paths during plane-strain model pile installation in sand. *Géotechnique*, 54(6):375–397, 2004.

[245] D. J. White and B. M. Lehane. Friction fatigue on displacement piles in sand. *Géotechnique*, 54(10):645–658, 2004.

[246] D. J. White, W. A. Take, and M. D. Bolton. Soil deformation measurement using particle image velocimetry (piv) and photogrammetry. *Géotechnique*, 53(7):619–632, 2003.

[247] T. Wichtmann, A. Niemunis, and T. Triantafyllidis. Strain accumulation in sand due to cyclic loading: drained triaxial tests. *Soil Dynamics and Earthquake Engineering*, 25(12):967–979, 2005.

[248] T. Wichtmann, A. Niemunis, and T. Triantafyllidis. On the determination of a set of material constants for a high-cycle accumulation model for non-cohesive soils. *International journal for numerical and analytical methods in geomechanics*, 34(4):409–440, 2010.

[249] P. J. Withers and H. K. Bhadeshia. Residual stress. part 2–nature and origins. *Materials Science and Technology*, 17(4):366–375, 2001.

[250] D. M. Wood. *Soil behaviour and critical state soil mechanics.* Cambridge University Press, 1991.

[251] Z. X. Yang, R. J. Jardine, B. T. Zhu, P. Foray, and C. H. C. Tsuha. Sand grain crushing and interface shearing during displacement pile installation in sand. *Géotechnique*, 60(6):469–482, 2010.

[252] N. Yasufuku and A. F. L. Hyde. Pile end-bearing capacity in crushable sands. *Géotechnique*, 45(4):663–676, 1995.

[253] T.-L. Yen, H. Lin, C.-T. Chin, and R. Wang. Interpretation of instrumented driven steel pipe piles. In *Foundation engineering: Current principles and practices*, pages 1293–1308. ASCE, New York, 1989.

[254] T. Youd. Factors controlling maximum and minimum densities of sands. *Evaluation of relative density and its role in geotechnical projects involving cohesionless soils*, (523):98, 1973.

[255] O. C. Zienkiewicz and R. L. Taylor. *The finite element method*, volume 3. McGraw-hill London, 1977.

[256] H. Zuidberg and P. Vergobbi. Euripides, load tests on large driven piles in dense silica sands. In *Offshore Technology Conference*, 1996.

Appendix A

Definition of R_{CLA}

A.1 Roughness of surface R_{CLA}

R_{CLA} is an expression of the roughness of a surface. It is a simplification of the complicated pattern of peaks and troughs of the surface, but is considered to contain sufficient information, [82], [124], [188].

R_{CLA} is defined as the average center-line height of the asperities on the surface of a structure, [124]. The height y_i of the peak-to-trough i along the surface is shown in Figure A.1.

The roughness of the average peak-to-trough i is the mean value of the n peaks:

$$R_{CLA} = \sum_{i}^{n} y_i \tag{A.1.1}$$

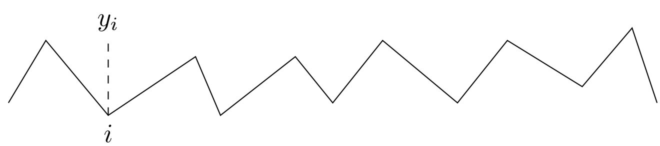

Figure A.1: Definition of Peak-to-trough height y_i for the peak i.

Appendix B

Derivation of centripetal acceleration

B.1 Acceleration of the centrifuge

In this appendix the centrifugal acceleration in the centrifuge $(R(\omega)^2)$ is derived to give a fuller description of the centrifuge system. More detailed descriptions are found in other texts, e.g. [217], [222].

The position of the centrifuge swing relative to the centrifuge axis is here described by the coordinates x and y, seen in the rotating plane of the centrifuge in FigureB.1. In this Figure the axis of the centrifuge is located at the origin of the coordinate system. The angle of rotation around the centrifuge is here ω and the radius R. The coordinates x and y are described in circular coordinates as:

$$x = r\cos\theta \tag{B.1.1}$$

$$y = r\sin\theta \tag{B.1.2}$$

The velocity of the centrifuge swing is found by derivation:

$$\frac{dx}{dt} = cos\theta\frac{dR}{dt} - R\sin\theta)\frac{d\theta}{dt} \tag{B.1.3}$$

$$\frac{dx}{dt} = sin\theta\frac{dR}{dt} + R\cos\theta\frac{d\theta}{dt} \tag{B.1.4}$$

The acceleration is found by further derivation:

$$\frac{d^2x}{dt^2} = cos\theta\frac{d^2R}{dt^2} - 2\sin\theta\frac{dR}{dt}\frac{d\theta}{dt} - R\cos\theta\left(\frac{d\theta}{dt}\right)^2 - R\sin\theta\frac{d^2\theta}{dt^2} \tag{B.1.5}$$

$$\frac{d^2y}{dt^2} = sin\theta\frac{d^2R}{dt^2} + 2\cos\theta\frac{dR}{dt}\frac{d\theta}{dt} - R\sin\theta\left(\frac{d\theta}{dt}\right)^2 + R\cos\theta\frac{d^2\theta}{dt^2} \tag{B.1.6}$$

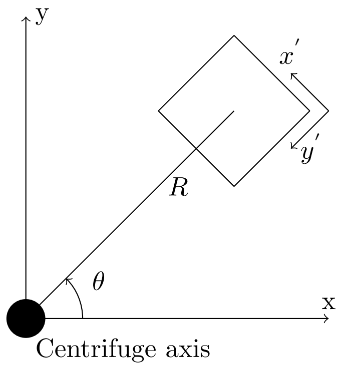

Figure B.1: Soil sample and the centrifuge in the different coordinate systems

These expression describe the acceleration in the original coordinates x and y. The acceleration in the soil sample is shown in Figure B.1. This acceleration is described in polar coordinates r and θ through a coordinate transformation:

$$\begin{pmatrix} x' \\ y' \end{pmatrix} = \begin{pmatrix} -\sin\theta & \cos\theta \\ -\cos\theta & -\sin\theta \end{pmatrix} \begin{pmatrix} x \\ y \end{pmatrix} \tag{B.1.7}$$

The velocity and acceleration is derived from the transformation:

$$\begin{pmatrix} \frac{dx'}{dt} \\ \frac{dy'}{dt} \end{pmatrix} = \begin{pmatrix} -\sin\theta & \cos\theta \\ -\cos\theta & -\sin\theta \end{pmatrix} \begin{pmatrix} \frac{dx}{dt} \\ \frac{dy}{dt} \end{pmatrix} \tag{B.1.8}$$

$$\begin{pmatrix} \frac{d^2x'}{dt^2} \\ \frac{d^2y'}{dt^2} \end{pmatrix} = \begin{pmatrix} -\sin\theta & \cos\theta \\ -\cos\theta & -\sin\theta \end{pmatrix} \begin{pmatrix} \frac{d^2x}{dt^2} \\ \frac{d^2y}{dt^2} \end{pmatrix} \tag{B.1.9}$$

If the transformed coordinates x and y are placed into the expression for the acceleration, the acceleration in the soil sample is described as:

$$\begin{aligned} \frac{d^2x'}{dt^2} = & -\sin\theta\left(\cos\theta\frac{d^2R}{dt^2} - 2\sin\theta\frac{dR}{dt}\frac{d\theta}{dt} - R\cos\theta\left(\frac{d\theta}{dt}\right)^2 - R\sin\theta\frac{d^2\theta}{dt^2}\right) \\ & +\cos\theta\left(\sin\theta\frac{d^2R}{dt^2} + 2\cos\theta\frac{dR}{dt}\frac{d\theta}{dt} - R\sin\theta\left(\frac{d\theta}{dt}\right)^2 + R\cos\theta\frac{d^2\theta}{dt^2}\right) \end{aligned} \tag{B.1.10}$$

$$\begin{aligned} \frac{d^2y'}{dt^2} = & -\cos\theta\left(\cos\theta\frac{d^2R}{dt^2} - 2\sin\theta\frac{dR}{dt}\frac{d\theta}{dt} - R\cos\theta\left(\frac{d\theta}{dt}\right)^2 - R\sin\theta\frac{d^2\theta}{dt^2}\right) \\ & -\sin\theta\left(\sin\theta\frac{d^2R}{dt^2} + 2\cos\theta\frac{dR}{dt}\frac{d\theta}{dt} - R\sin\theta\left(\frac{d\theta}{dt}\right)^2 + R\cos\theta\frac{d^2\theta}{dt^2}\right) \end{aligned} \tag{B.1.11}$$

The acceleration in the x and y coordinates are then:

$$\frac{d^2x^{'}}{dt^2} = 2\frac{d\theta}{dt}\frac{dR}{dt} + R\frac{d^2\theta}{dt^2} \tag{B.1.12}$$

$$\frac{d^2y^{'}}{dt^2} = -\frac{d^2R}{dt^2} + R\left(\frac{d\theta}{dt}\right)^2 \tag{B.1.13}$$

The centrifugal acceleration is then:

$$R\left(\frac{d\theta}{dt}\right)^2 = R\left(\omega\right)^2 \tag{B.1.14}$$

Appendix C

Variation of stress gradient in the centrifuge

C.1 Effect of centrifuge and swing length

Since the radius is not constant along the depth y in the centrifuge, the accelerated gravity will diplay a variation in the y-axis. The effects of the varying acceleration are discussed in some detail in [204], [211], [222]. The difference in the gravitational level at the top and bottom of the sample should be less than 10 per cent for properly scaled samples, [204], [222].

In this appendix the difference between the gravity a at specified depth y in the prototype and the model is derived to clarify the limitations of the centrifuge model.

The radial acceleration at a distance r and with a angular velocity ω is:

$$g(z) = r\omega^2 \tag{C.1.1}$$

In the standard centrifuge model tests the prototype gravity is specified in the middle of the soil sample. In a centrifuge with a centrifuge arm length R_{arm} and a model height L_{model}, the gravity $g_{prototype}$ in the middle of the sample at the depth $L_{model}/2$ is consequently:

$$g_{prototype} = r\omega^2 = (R_{arm} + L_{model}/2)\omega^2 \tag{C.1.2}$$

For the centrifuge model, the gravity level g_{model} is a function of the radius to the center of the centrifuge axis:

$$g_{model}(y_{model}) = r\omega^2 = (R_{arm} + y_{model})\omega^2 \tag{C.1.3}$$

where

$$y_{model} \leq L_{model} \tag{C.1.4}$$

The ratio between the accelerated gravity at the model sale g_{model} and the gravity at the prototype scale $g_{prototype}$ is:

$$\frac{g_{model}}{g_{prototype}} = \frac{(R_{arm} + y_{model})\omega^2)}{(R_{arm} + L_{model}/2)/\omega^2} = \frac{R_{arm} + y_{model}}{R_{arm} + L_{model}/2} \tag{C.1.5}$$

It is more convenient to transform the centrifuge arm length R_{arm} to the centrifuge radius R_{cen}, so that:

$$R_{cen} = R_{arm} + L_{model} \tag{C.1.6}$$

The ratio $g_{model}/g_{prototype}$ is then:

$$\frac{g_{model}}{g_{prototype}} = \frac{(R_{cen} + y_{model} - L_{model})}{R - L_{model}/2} = \frac{(R_{cen}/L_{model} + y_{model}/L_{model} - 1)}{R_{cen}/L_{model} - 1/2} \tag{C.1.7}$$

where R_{cen}/L_{model} is the ratio between centrifuge ratio and the length of the model, and y/L_{model} is the normalized depth in the model. Figure C.1 shows the ratio $g_{model}/g_{prototype}$ for different values of R_{cen}/L_{model}.

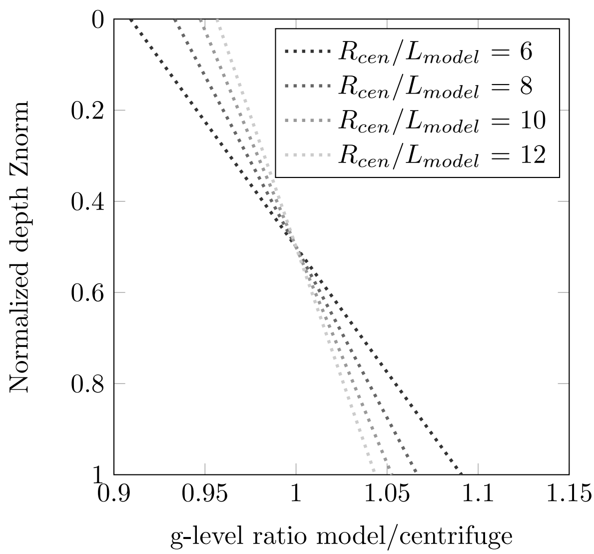

Figure C.1: The variation of the gravity in the sample with R_{cen}/L_{model}.

The centrifuge length R_{cen} in the small TU Deft centrifuge is 1.22 m, as described in Chapter 4. For a model length of 0.148 m, the ratio R_{cen}/L_{model} is around 8. Figure C.1 shows that the variation in acceleration consequently is less than 7%.

Appendix D

Laboratory safety precautions

Safety precautions during centrifuge testing were considered essential to perform experimental research in the TU Delft laboratory. The test procedures and safety precautions are therefore briefly described.

The test procedure consisted of preparation of equipment, sample preparation and test execution. Before each step considerations were made about the safety of the procedure and possible precautions. Possible casus of risk were identified for each step and the personnel involved were informed before any activities commenced. The TU Delft safety procedures were followed before the testing started. These consisted of consultation with the responsible persons of the laboratory through the TU Delft safety form.

The equipment preparation involved installation of electromechanical equipment in the centrifuge and operation of the centrifuge itself. Many pieces of mechanical and electrical equipment were installed in the centrifuge or other facilities. The possible risks were injuries resulting from sharp edges and heavy tools and electrical shocks from cables and circuits in the centrifuge data acquisition system. The latter risk was estimated to be more important since the tools and equipment were of relatively low weight. The power supply to the centrifuge motor was connected with a secure cable and presented only a minor risk. Before any electrical equipment such as cables or amplifiers on the data acquisition system was adjusted the power supply to the centrifuge was switched off and care was taken not to plug in the cable before any modification was completed.

The sample preparation consisted of a series of procedures to fill the sample container with soil of specified relative density. This step was assessed not to present mush risks since the sample container weight was low, around 12 kg. A Haver and Broeker EML vibration was used for the preparation of the dense soil sample but the vibration was prepared at low amplitude and the sample container was secured.

Execution of the centrifuge test presented the highest risks of the test procedures. The centrifuge was always run by at least two persons to control the safety of the test. The test was started after the soil sample was placed in the centrifuge swing. The counterweight in the other centrifuge swing was controlled to make sure that the centrifuge was in balance.

All cable and mechanical connection of the centrifuge swing were controlled before the test started. The area around the centrifuge was controlled to make sure that no equipment was in the vicinity of the centrifuge. The centrifuge was started by a small start controller which was activated with a key. After the centrifuge started rotating a low angular velocity the centrifuge pit was surveyed again and the centrifuge room was evacuated. The door was locked and controlled. A rotating light was activated outside the centrifuge room when the motor was started. This light was controlled before the test started. The centrifuge velocity was then increased to the target angular velocity and the centrifuge test was started. During the test the control software Cutecom was observed to control the stability of the centrifuge. During long tests the temperature in the centrifuge room was also control to reduce the risk of overheating an possible influence on measurements. After the test the centrifuge was slowed down to the minimum velocity of the motor. The centrifuge room was then entered and the electric motor was manually turned off.

Appendix E

Preparation of the dense soil sample

The loose and medium dense soil samples were prepared by air pluviation of the soil, following standard procedures, e.g. [85], [88], [136]. The air pluviation method was tried out for the dense sample preparation but it was found to be relatively cumbersome to prepare a homogenous soil sample because of the boundary effects. This boundary effect caused a development of heterogeneous soil around the edges of the sample container. When the soil was released into the small soil container with some movement along the boundaries it was bouncing further into the sample strongbox and creating small formation of soil which resembled small sand dunes at the edges of the sample container. It was estimated that this preparation method would result in variation of relative density in the soil sample and between sample preparations since it was quite complicated to carry out the pluviation in a consistent way, and an alternative sample preparation method was therefore considered.

In the alternative preparation method the air pluviation of the soil from a lower height was combined with vibration of the soil to homogenize the soil sample. The dense soil sample was prepared by air pluviation as specified for the medium dense soil sample, followed by vibration of the soil sample in a Haver and Boecker HAVER EML digital plus sieving machine. The strongbox containing the sample was strapped to the vibrating pad in the sieving machine with the two plastic screws at the top of the machine, shown in Figure E.1. It was then vibrated at constant mode with 0.2 mm amplitude for five minutes. It was subsequently released form the machine and the soil surface was slightly adjusted to remove small peaks of soil. The sample was moved by hand to the centrifuge room and the height of the soil sample was measured at six locations and averaged for the calculation of the initial void ratio of the sample. The sample was then installed in the swing before flight.

This preparation method which was a combination of air pluviation and vibration was assumed to result in relatively homogenous soil samples. Possible disturbances during the vibration phase may come from non-homogenous soil vibration and soil flow. To assess the influence of these factors particle image Velocimetry (PIV) measurements were carried out on the soil sample during preparation in the vibrating machine. A camera with a specified

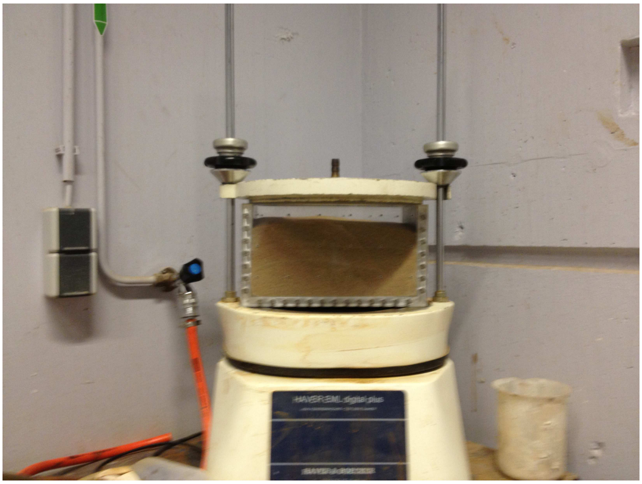

Figure E.1: Set-up of dense soil sample prepared with vibration.

lens was placed in front of the vibrating machine. The sample container was illuminated with a lamp and an image sequence of the vibration movement was captured by the camera. The image sequence was processed with program imageJ in which a band pass filter with 2 pixel size objects were filtered to reduce the locking effect during the PIV analysis, [209]. The images were processed in the JPIV with a 64 x 64 pixel interrogation window, 32 x 32 pixel search window and 18 x 18 array spacing (resulting in some PIV overlap), [229].

Several different time-steps between the images were made to find a relatively suitable interval for analysis with moderate velocity of the soil. The JPIV array images were further processed with a filter to reduce array disturbances, [239]. The arrays from the PIV analysis on the surface of the image are shown in Figure E.2.

Figure E.2 shows that the soil is not homogenously vibrated in the soil sample container. The vibration motion of the sieving machine results in a flow of the soil from the top of the sample into the bottom of the sample. The other side of the sample container as not observed so conclusions about the complete behaviour of the soil in the sample container may not be made. If the soil flows for a certain amount of time in the vibration machine all the soil in the sample should have passed through a flow cycle and should have at a reduction in relative density. This conclusion was made considering measurements of the sample volume after vibration. In these measurements it was concluded that soil compaction representing a relative density of around 80 percent is reached relatively soon after vibration is started. The extra vibration time was added to increase the reliability of the preparation method and to rigorously prepare the soil sample.

The sample preparation method for the dense soil sample may therefore result in some variation in soil properties but it is here assumed that these variations are relatively small and are concentrated to the lower part of the sample. The alternative preparation method would presumably result in large variation of relative density and also some variation in between different soil samples prepared with the same method.

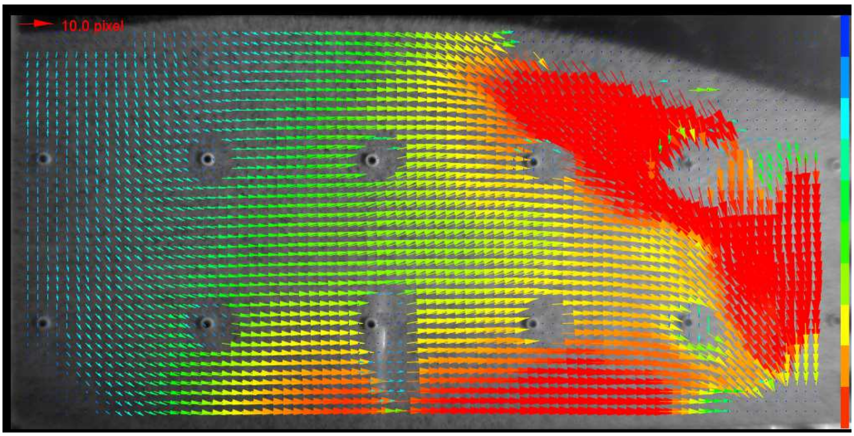

Figure E.2: PIV analysis of soil displacements during sample preparation.

Appendix F

Properties of the experiment soil

Here some further information is given about the soil sample based on highly magnified images of the soil grains. Figure F.1 shows the soil magnified at 50x. The soil consists mainly of quartz and feldspar grains.

Figure F.3 shows an increased magnification of the grains in which the shape of the grains may be observed. Most grains are relatively rounded, but some quartz grains have higher angularity. The illumination of the soil grains, which may reflect light on the grains, seems to show that several of the grains are almost transparent. The grain sizes are relatively uniform.

In Figure F.3 the surface roughness of the soil grains may be observed at 100x magnification, with a very smooth feldspar grain and quartz grains which have a higher roughness. The quartz grains in Figure F.3 display some variation in surface roughness and analysis of a small amount of grains may lead to conclusions that are not representations of the whole soil mass. Some of the grains with higher roughness are also relatively angular which may be a result of the depositional history of the soil.

In Figure F.4 the 200x magnification of feldspar and quartz grains is shown. The feldspar grain has a very smooth surface and the discontinuities of the mineral structure with in the grain may be seen. The quartz grains are relatively homogenous with the exception of the rough and angular grain.

Figure F.1: Magnified image of the soil grains (50x).

Figure F.2: Magnified image of the soil grains (100x).

Figure F.3: Magnified image of the soil grains (200x).

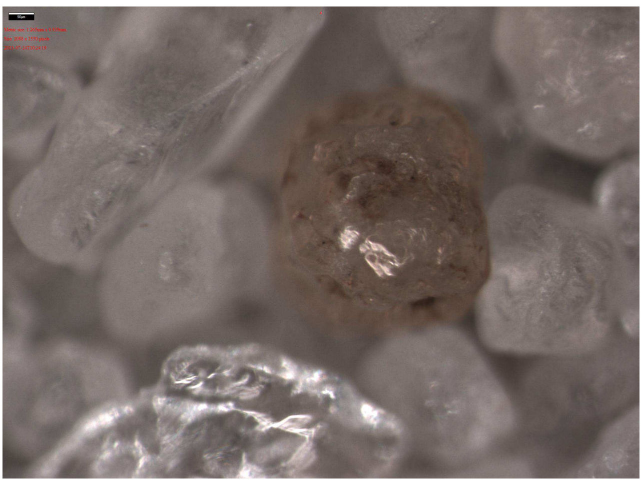

Figure F.4: Magnified image of the soil grains.

Appendix G

Calculation of strain from displacement increments

The strain components ε_{xx}, ε_{yy}, ε_{yx} and ε_{vv} are calculated from the displacement incremenets. In this appendix a more detailed description of the calculation procedure is given.

G.1 Displacement increments from JPIV

The displacement increments are retrieved from the deformation images by the program JPIV, [229]. Figure G.1 shows an image for deformation analysis. The displacement increments are shown in Figure G.2.

The displacement increments are retrieved with a four-step PIV cross-calculation schedule, shown in Table G.1, [229].

G.2 Calculation of displacement paths in JPATH

The displacement paths were calculated with the program JPATH which was implemented in MATLAB, [161]. The program contained a subroutine that interpolated the displacement increments with the 2D MATLAB subroutine interp2, [161]. The displacement paths were subsequently created by creating array containing the displacement increments connected at the end points of each increments. The displacement paths contained all the connecting displacement increments, and are shown in Figure G.3.

Figure G.1: Image for deformation analysis.

Component	Step 1	Step 2	Step 3	Step 4
Interrogation window width	125	64	64	32
Interrogation window height	125	64	64	32
Search domain width	64	64	18	18
Search domain height	64	64	18	18
Horizontal array spacing	125	64	32	32
Vertical array spacing	125	64	32	32

Table G.1: Description of cross-correlation interrogation of deformation image.

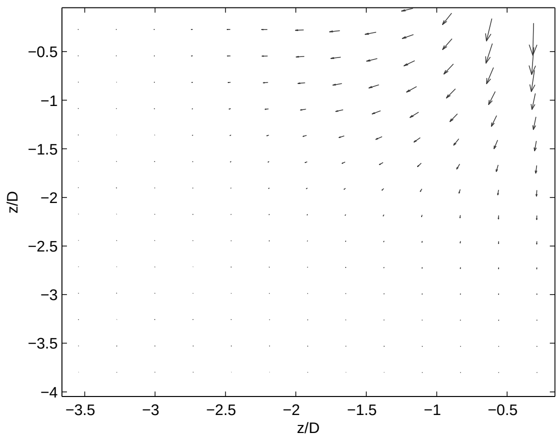

Figure G.2: Displacement increments from JPIV

G.3 Calculation of strain components with the program JSTRAIN

The strain components of the displacement path were calculated with the program JSTRAIN, implemented in MATLAB, [161]. A constant strain triangle grid was connected with the original positions of the displacements paths, shown in Figure G.4. The positions were stored in an array, and the strain of the elements in the grid were calculated for the same initial triangles. Alternative formulations for the strain calculation are discussed in the following Appendix.

The strain components were calculated by polar decomposition of the strain into the rotation and stretch tensors, [58]. The engineering shear strain was calculated by adding the shear strain components ($\gamma_{yx} = \varepsilon_{xy} + \varepsilon_{yx}$). The horizontal strain for initial installation in loose soil sample is shown in Figure G.5, including the deformed mesh after the initial penetration and deformation of the soil sample, showing some deformed elements of the initial triangular mesh from Figure G.4.

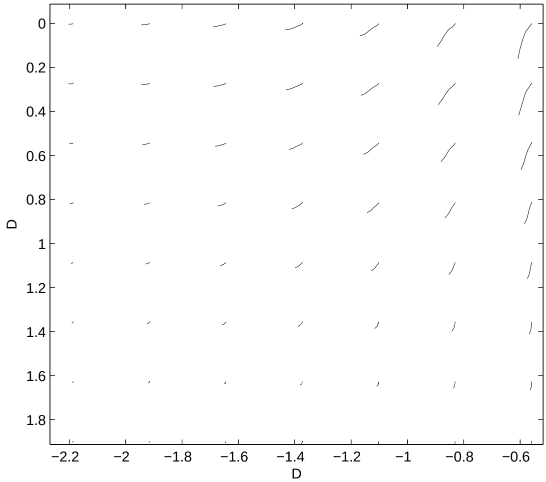

Figure G.3: Displacement paths calculated from the displacement increments in the program JPATH.

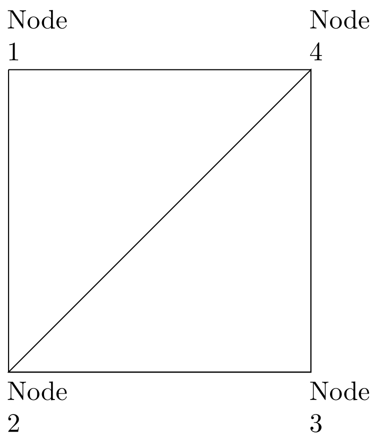

Figure G.4: Constant strain triangles from initial positions of the displacement paths.

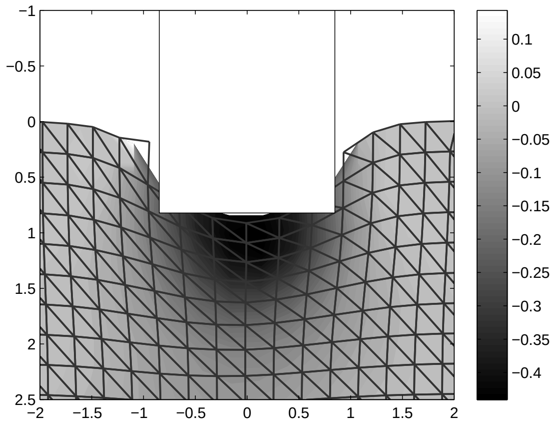

Figure G.5: Strain component ε_{xx} and deformed mesh after initial installation in the loose soil sample.

Appendix H

Calculation of strain components by cross-triangular formulation

H.1 Oscillations in the constant strain triangle

The calculation of strain by the constant strain triangle resulted in relatively large oscillations of the strain levels. The reason is believed to be measurement disturbances, which distort the constant strain triangles, thereby resulting in erroneous strain levels from the noise in the data.

An alternative solution was to use a combination of constant strain triangles in in cross-triangular formulation to reduce the noise in the measurements. This idea resulted from discussion with Ivo Herle, and his advice is greatly appreciated.

H.2 Cross-triangular formulation A

Cross-triangular formulation A was constructed from an arbitrary node i, j from the JPIV mesh. This node is surrounded by corner nodes, as shown in Figure H.1.

In formulation A, these nodes form triangles extending from the node i, j, as shown in Figure H.2.

During calculation of the strain components, the strain components $\varepsilon_{i,j}$ are calculated for all triangles, and the mean value is assumed to represent the strain level at node i, j.

H.3 Cross-triangular formulation B

In the cross-triangular formulation B, larger triangles with corners at nodes $i+1, j+1$, $i+1, j-1$, $i-1, j-1$ and $i-1, j+1$ are formed.

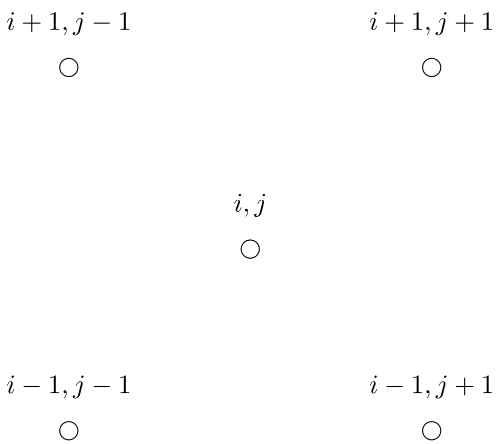

Figure H.1: Nodes around i, j forming the cross-triangular formulation.

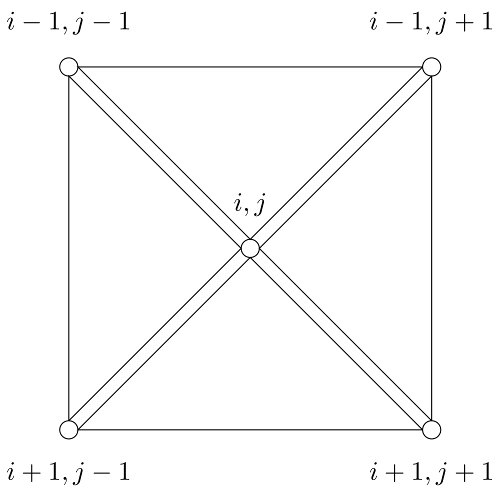

Figure H.2: Nodes around i, j forming the cross-triangular formulation A.

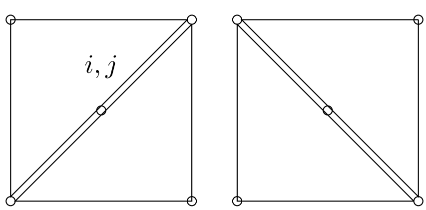

Figure H.3: Nodes around i, j forming the cross-triangular formulation B.

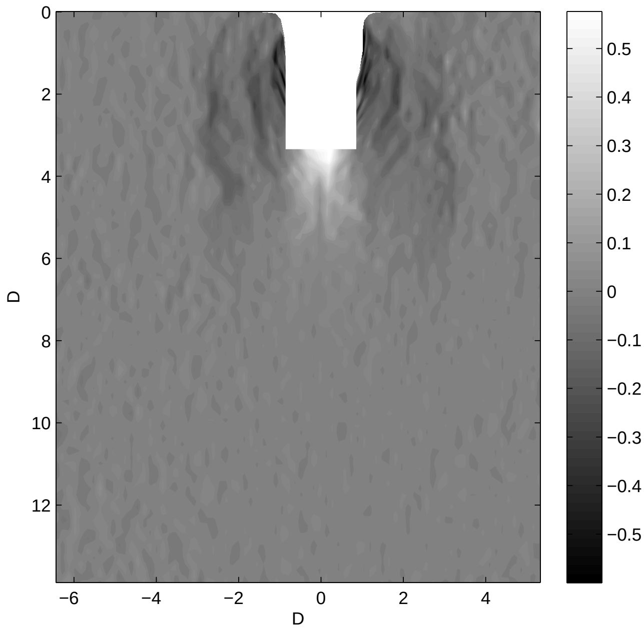

Figure H.4: The strain component ε_{xx} calculated with the constant strain triangle.

Similar to method A, the strain components $\varepsilon_{i,j}$ are calculated for all triangles, and the mean value is assumed to represent the strain level at node i, j.

H.4 Strain calculation with constant strain triangle, method A and B

The strain component ε_{xx} was calculated for the medium dense soil sample for some initial installation. The measurements was processed by the method discussed in the previous Appendix.

The strain component ε_{xx} was then calculated with the constant strain triangle, and cross-triangular formulation A and B presented in the current Appendix.

Figure H.4 shows ε_{xx} calculated with the constant strain triangle, Figure H.5 shows ε_{xx} calculated with the cross-triangular formulation A, and Figure H.6 shows ε_{xx} calculated with the cross-triangular formulation B.

The measurements were thought to show that the cross-triangular formulation B gives more stability in the measurements, while still not filtering out all the information. The strain measurements are consequently calculated by the cross-triangular formulation B here.

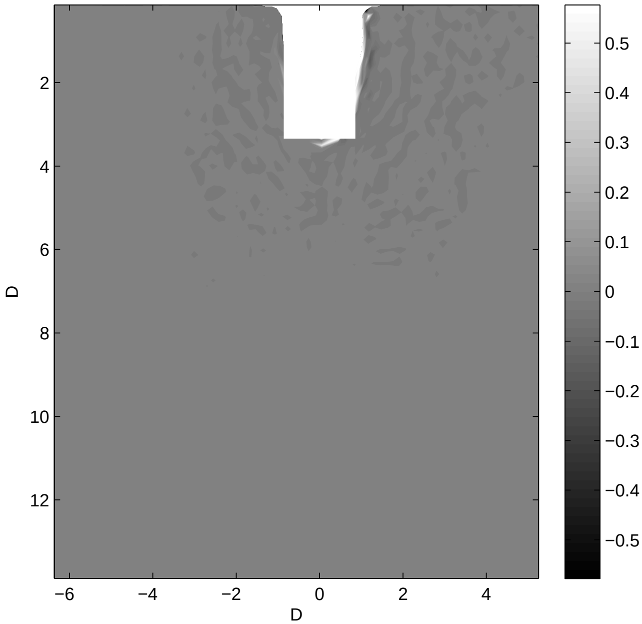

Figure H.5: The strain component ε_{xx} calculated with the cross-triangular formulation A.

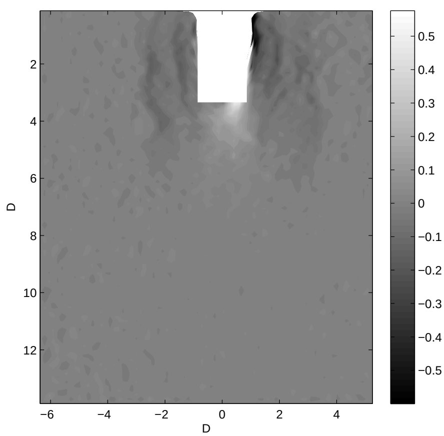

Figure H.6: The strain component ε_{xx} calculated with the cross-triangular formulation B.

Appendix I

Reduction of temperature disturbances in the model pile

A temperature regulation system was devised to reduce the heating effect on the strain gauge bridges. In this appendix the configuration of this system is described in detail and measurements of heat reduction are shown.

I.1 Configuration of heat reduction circuit

The layout of the heat reduction circuit and its connection to the measurement devices is shown in Figure I.1. The temperature reduction system is place between the strain gauge bridges and the data acquisition system. The data acquisition system provides the strain gauges with an excitation voltage, V_{ex}, which consists of 6 V Direct Current to each sensor in the measurement system.

The temperature reduction system consists of a National Semiconductor LM555 and a Diodes Inc ZXMP6A17G electronic switch. The timer is manually adjusted to provide a specified time interval in which the $6V$ excitation voltage is active. The switch is subsequently switched on and off in periods to supply the strain gauge system with an alternate current supply.

The layout of the National Semiconductor LM555 timer connected to the switch is shown in Figure I.2. The time period has been specified to 1.3 s.

I.2 Strain gauge bridge measurements with temperature control

Figure I.3 - I.6 shows the reduction in strain gauge output voltage with the temperature reduction system. There are also disturbances when the heat is increasing, which creates a discontinuous deformation of the membrane.

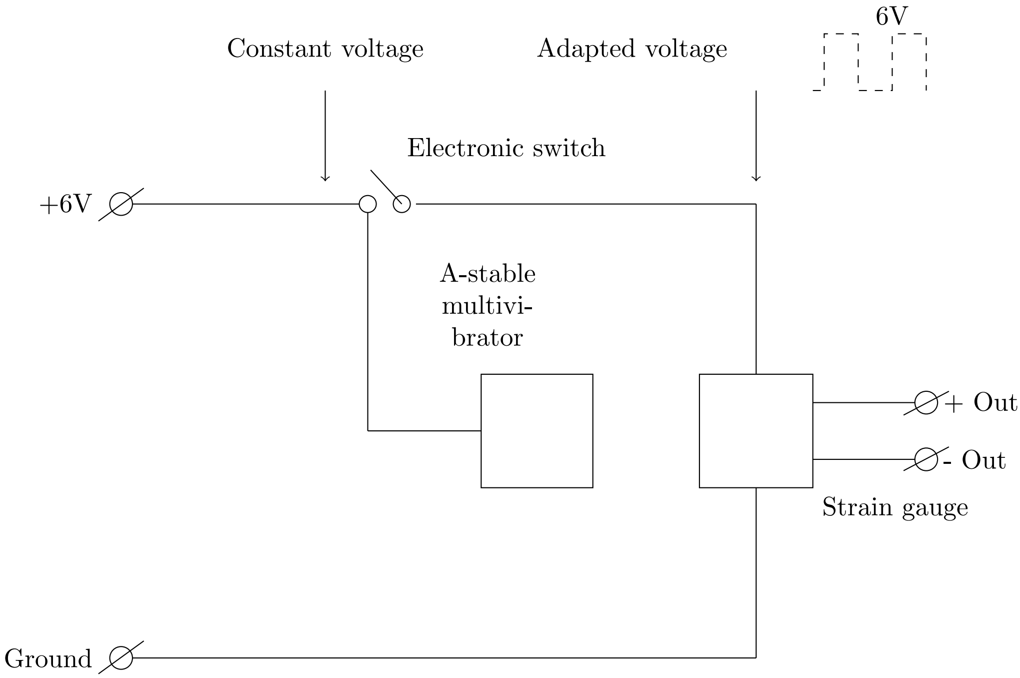

Figure I.1: Circuit showing the A-stable multivibrator in the strain gauge system.

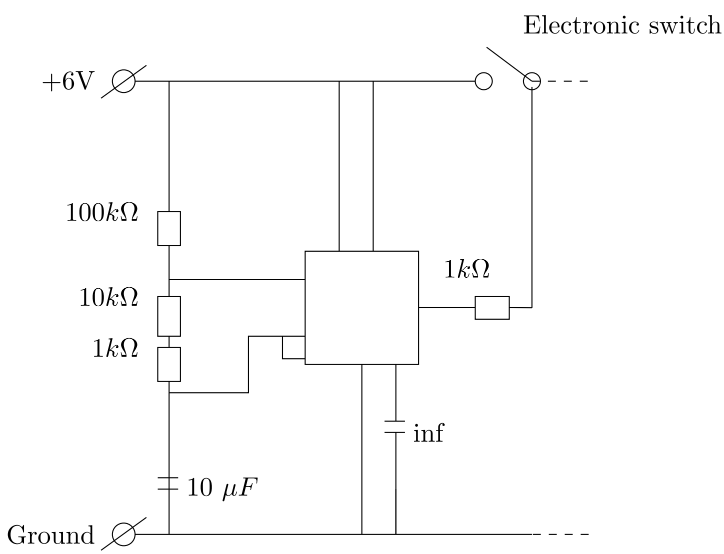

Figure I.2: Circuit showing the A-stable multivibrator in the strain gauge system.

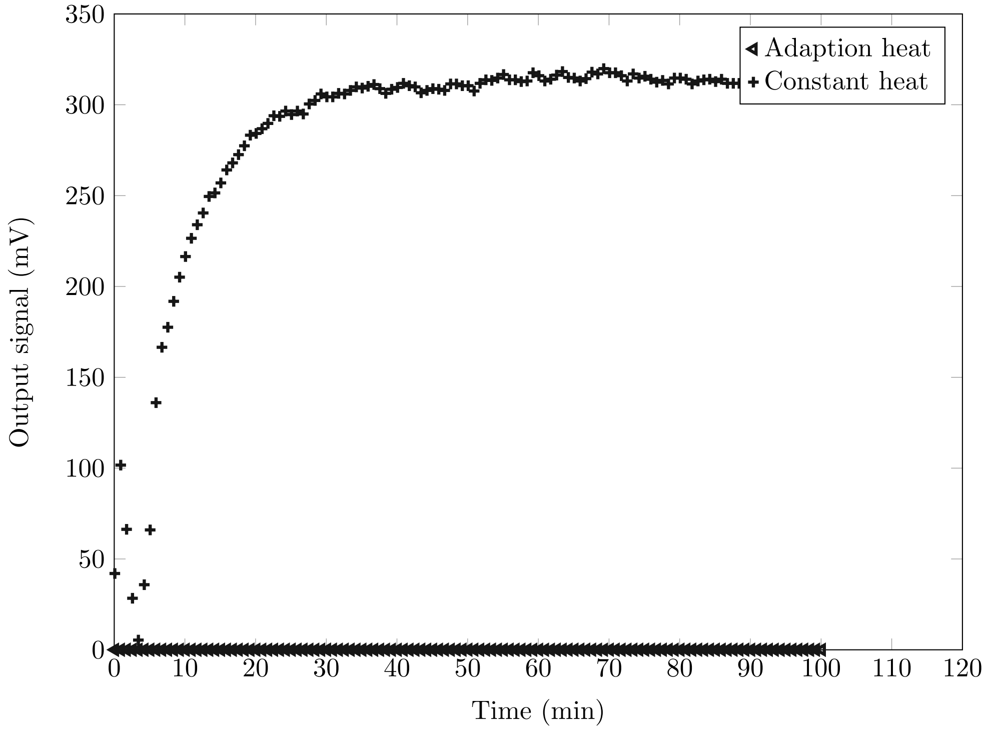

Figure I.3: Horizontal sensor 1

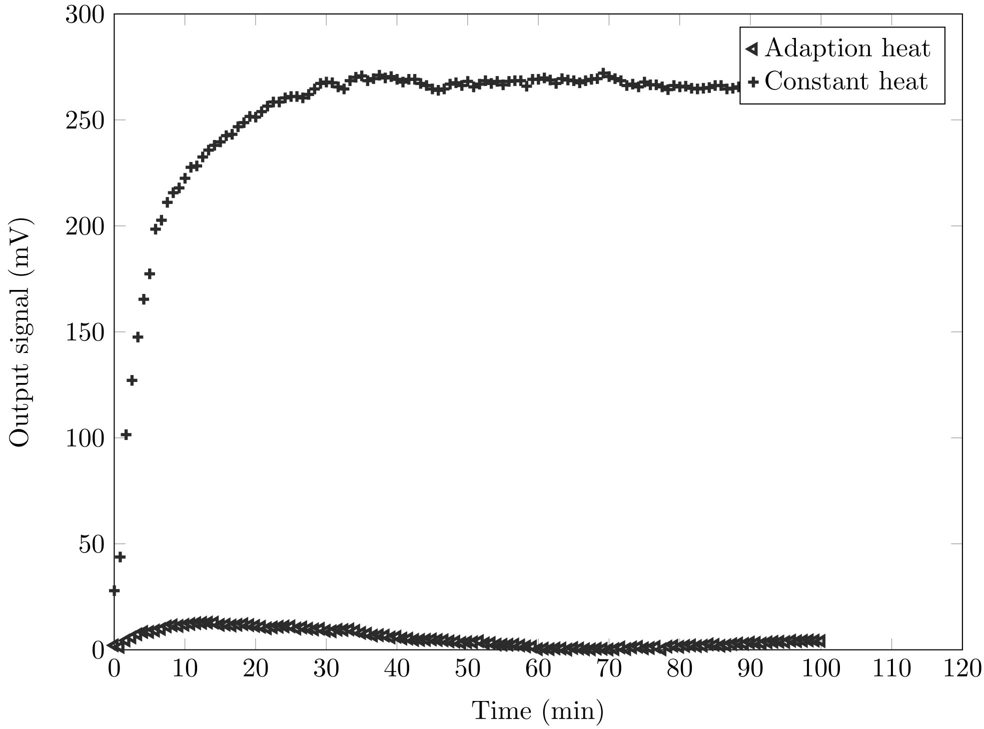

Figure I.4: Horizontal sensor 2

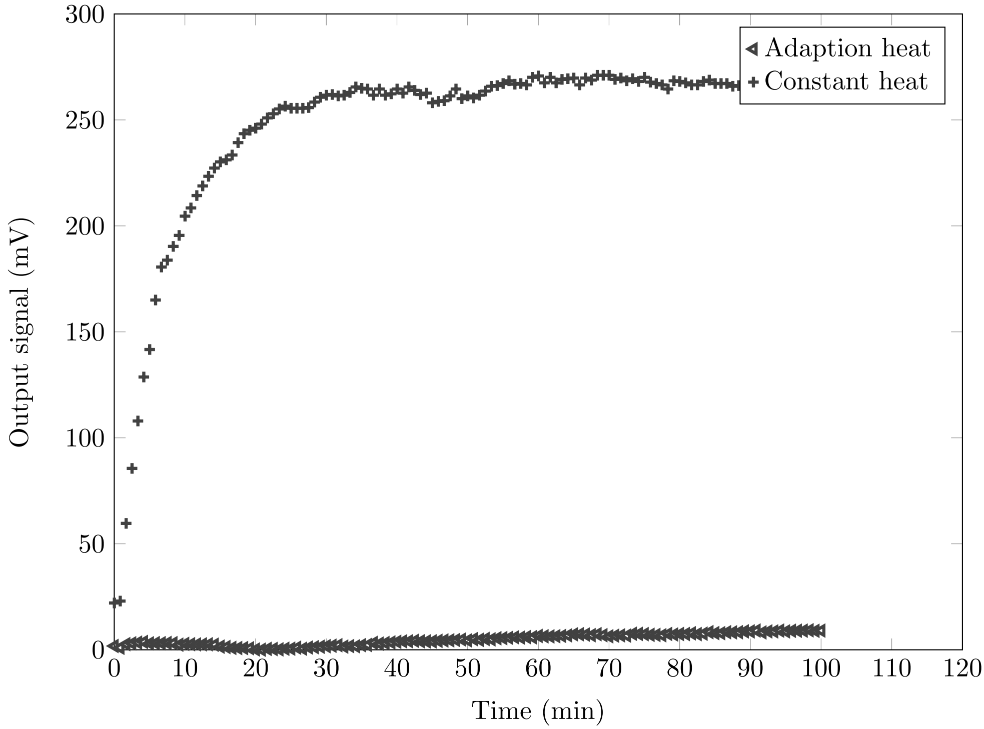

Figure I.5: Horizontal sensor 3

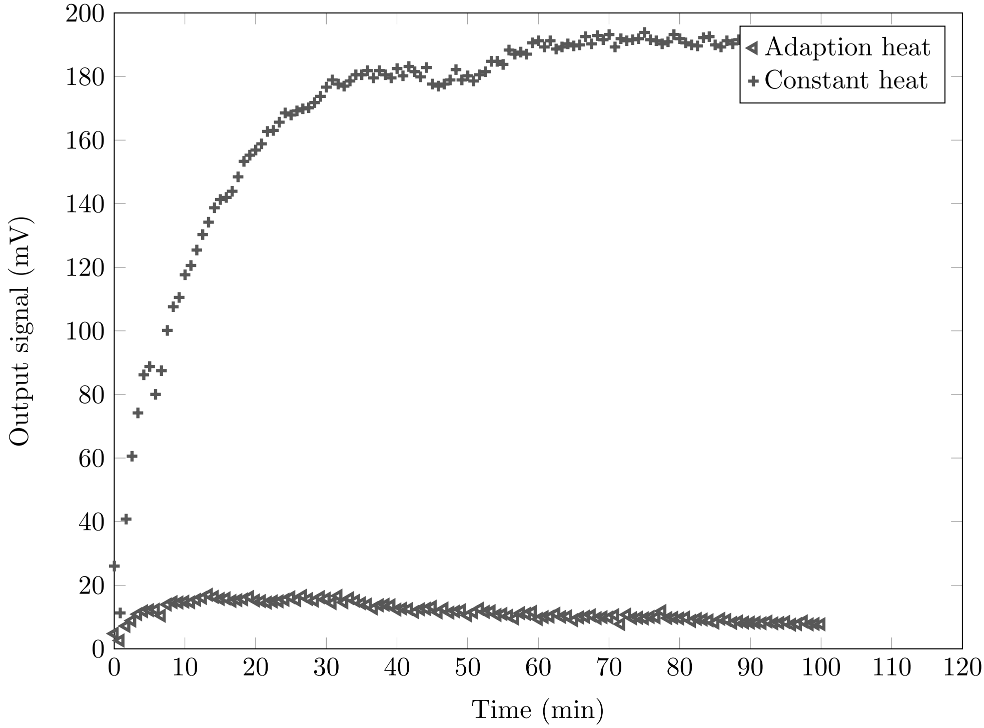

Figure I.6: Horizontal sensor 4

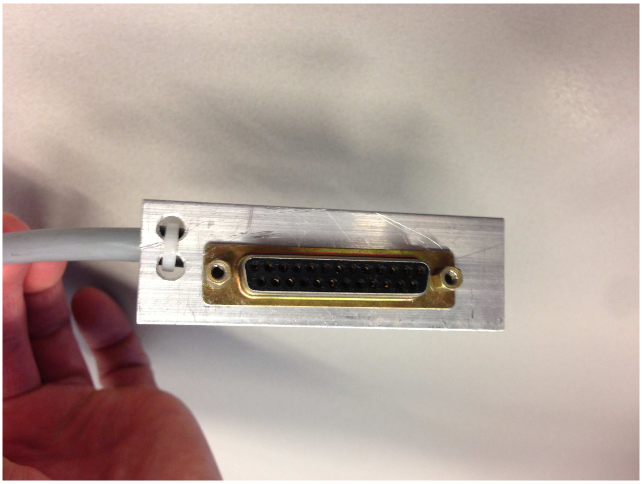

Figure I.7: Connection of alternate voltage supply system to the instrumented model pile

I.3 Connection to the instrumented model pile

The electric circuit was installed inside a small electric cable which was attached to the instrumented model pile, and is shown in Figure I.7, and which was attached to the data acquisition system. The system could therefore conveniently be added to the model.

Appendix J

Calibration of the model pile in the pressure vessel

J.1 Measurements in the calibration vessel

The measurements conducted in the calibration vessel are shown here in detail. For all the sensors, a series of four calibration measurements were carried out. Figure J.1 shows the calibration set-up and pressure distribution during the calibration. The stress distribution consisted of isotropic pressure, which was provided by the water pressure in the calibration vessel. Figure J.1a shows a load cycle in the calibration vessel for Sensor 1.

Figure J.2 - J.5 shows the calibration measurements for the horizontal stress sensors 1-4. The calibration series consisted of four different measurements. In between these measurements the pile was released fromt eh calibration vessel, and the seal between the vessel and the pile was inspected to assure that the vessel was sealed.

Figure J.6 shows the calibration of the axial stress sensors in the calibration vessel. There are relatively large variations of measurements, which may be explained by the very small level of the measurements compared to the full range of the sensors, whcih was much larger.

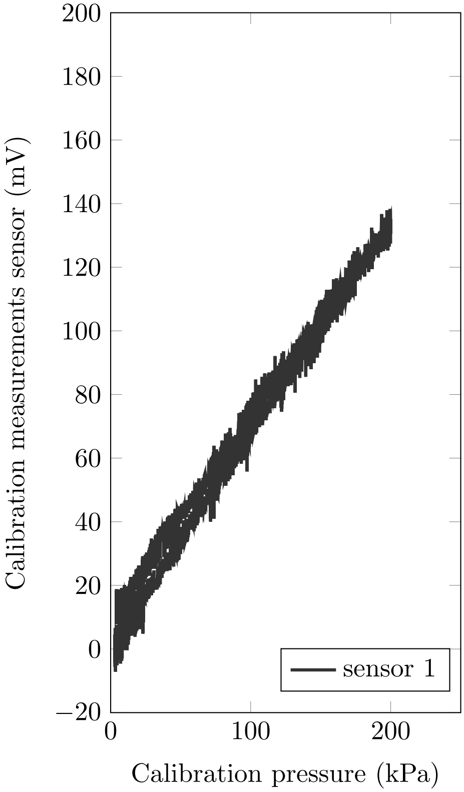

(a) Calibration cycle from the calibration vessel.

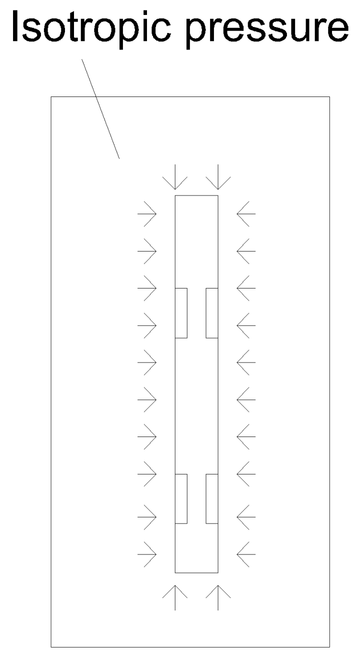

(b) Diagram of the horizontal calibration.

Figure J.1: Calibration of the model pile in the horizontal calibration system.

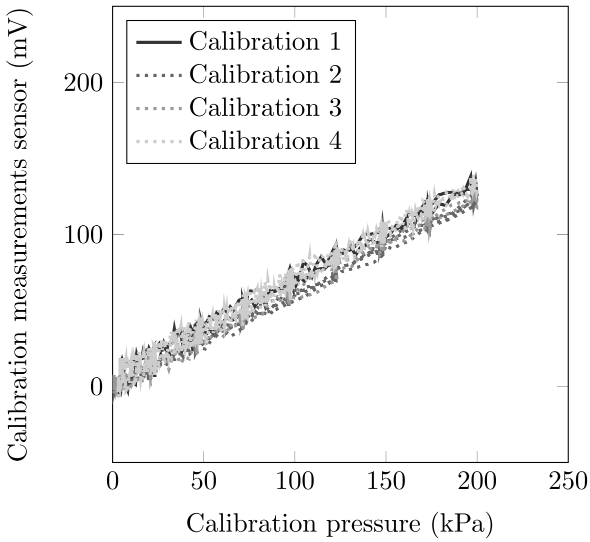

Figure J.2: Calibration of the horizontal normal stress sensor 1.

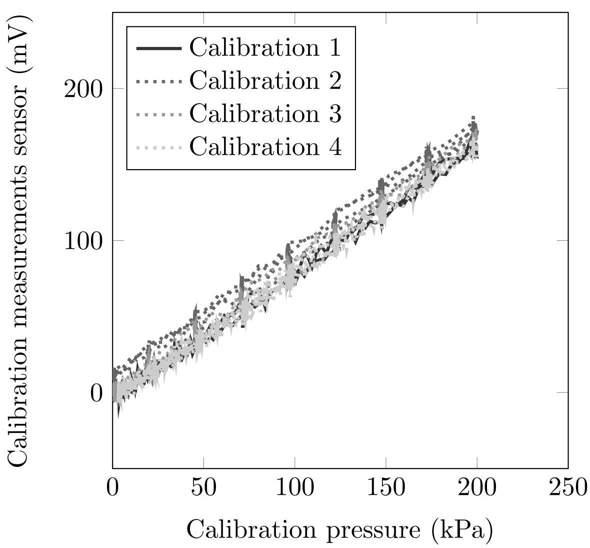

Figure J.3: Calibration of the horizontal normal stress sensor 2.

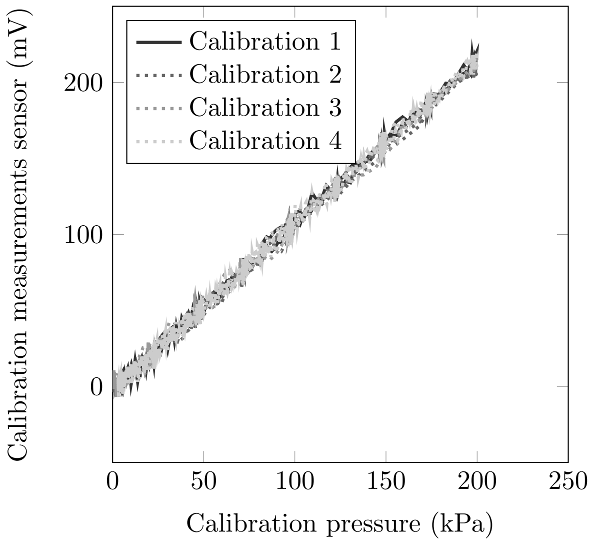

Figure J.4: Calibration of the horizontal normal stress sensor 3.

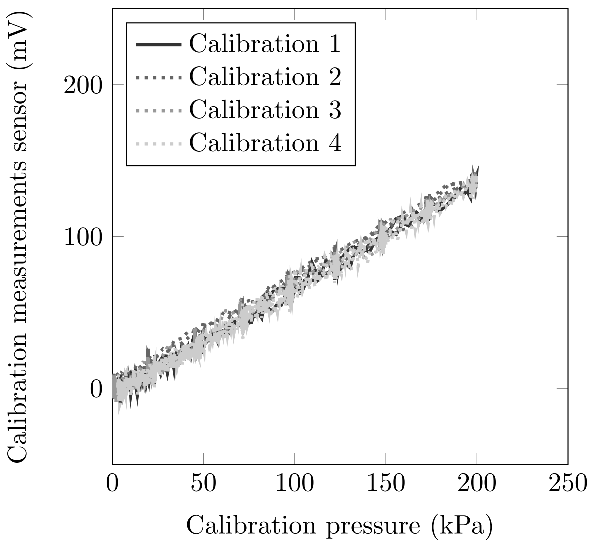

Figure J.5: Calibration of the horizontal normal stress sensor 4.

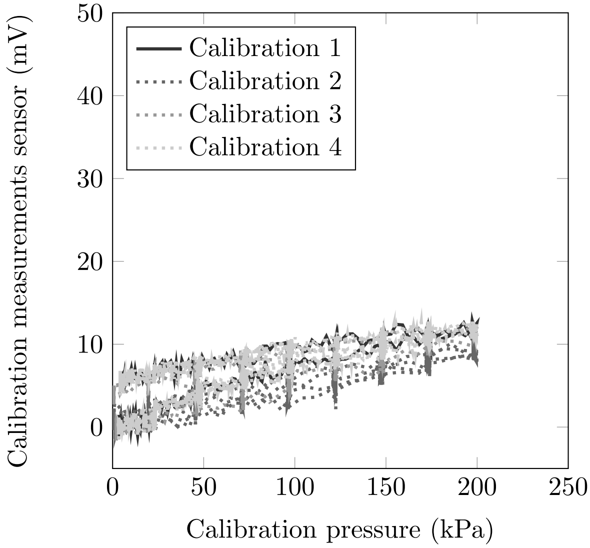

Figure J.6: Calibration of the axial stress sensor in the calibration vessel.

J.2 Calibration coefficients for isotropic stress

The calibration measurements were calculated as a $y = kx$ calibration factor k with MATLAB. The calibration coefficients were calculated from each test, and the average calibration coefficients were out into the data interpreptation program.

Table J.1 shows the calibration coefficients from loading of the vessel. Figure J.2 shows the calibration coefficients for calibration vessel stress decrease. The sensor calibration factors are relatively similar for the horizontal stress sensors. The axial stress sensors shows more variation.

Sensor nr	Cal. 1	Cal. 2	Cal. 3	Cal. 4	Average cal.
sensor 1	1.515	1.581	1.627	1.570	1.573
sensor 2	1.155	1.145	1.186	1.179	1.166
sensor 3	0.9403	0.9474	0.9403	0.9430	0.9427
sensor 4	1.4334	1.444	1.438	1.425	1.435
axial	14.18	21.00	21.34	17.21	18.43

Table J.1: Calibration coefficients from the calibration vessel stress calibration for incremental stress increase.

Sensor nr	Cal. 1	Cal. 2	Cal. 3	Cal. 4	Average cal.
sensor 1	1.594	1.588	1.603	1.604	1.597
sensor 2	1.180	1.227	1.186	1.180	1.193
sensor 3	0.9294	0.9440	0.9412	0.9548	0.9423
sensor 4	1.425	1.458	1.447	1.440	1.442
axial	26.99	21.95	22.96	23.44	23.83

Table J.2: Calibration coefficients from the calibration vessel stress calibration for incremental stress decrease.

Appendix K

Correlation factor c_a for the axial correlation coefficient

K.1 Effect of shaft friction and the pile diameter on the axial measurements

The axial stress sensor consists of two strain gauges mounted on opposite interior walls inside the model pile. Here some factors that govern the axial stress measurements are discussed.

The aim of the axial stress sensor is to measure the pile base stress σ_b. Since the axial stress sensor is mounted around 10 mm from the pile base, the extra area distanced by the boundary soil will also influence effective area, and some shaft friction will also be measured as the load registered in the axial stress sensor, P_{tot}/d^2. This configuration results in extra load from the shaft friction during loading. This is illustrated in Figure K.1, which shows the axial measurements during tension.

The first part of the correlation c_a, $c_{a,1}$, results from the increase in area of the pile when the load is mobilized resulting from the grain size. The extra length mobilized is assumed to be $D_{Pile} + 2d_{50}$. The correction factor $c_{a,1}$ is then:

$$c_{a,1} = \frac{(D_{Pile})^2}{(D_{Pile} + 2d_{50})^2} = 0.902 \tag{K.1.1}$$

The measurement of P_{tot}/D^2 is consequently first multiplied with the correction factor $c_{a,1}$, to get $P_{tot,corr,1}/D^2$.

The other axial correction factor $c_{a,2}$ results from the shear load of the pile, since the sensor measured the axial stress including the shaft friction.

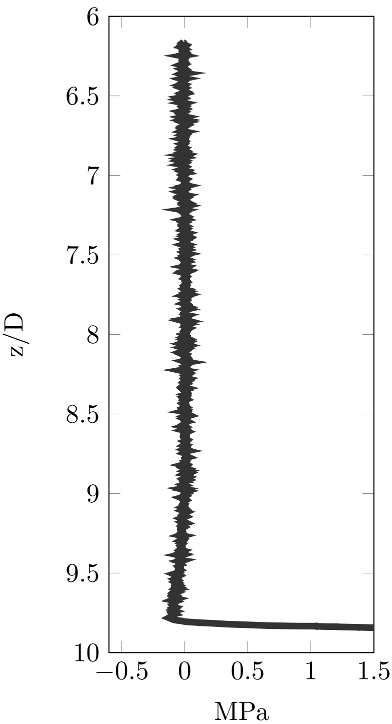

Figure K.1: Measurements of axial sensor during extraction test by tension.

$$P_{tot,corr,1}/D^2 = 1/D^2 \left(\sigma_b A_b + C_{Pile} \int_{z_{base}}^{z_{sensor}} \tau_s(z) dz \right) \tag{K.1.2}$$

where σ_b is the base stress, A_b is the base area, C_{Pile} is the circumference of the pile, z_{sensor} is the location of the sensor, and z_{base} is the location of the base, and $\tau_s(z)$ is the magnitude of the shaft friction τ_s at the location z along the pile.

If the z-axis is defined to start at the pile base, the location of the sensor i z_{sensor}, and $\Delta z = z_{sensor} - z_{base} = 10$ mm.

According to some of the empirical axial pile design methods, e.g. [121], [138], [150], the shaft friction is distributed in an exponential curve, with a maximum value around the pile base of around 3% to 8% of the cone resistance q_c.

In the following reasoning, the value of 4% of cone resistance is estimated to be relatively accurate for the shaft friction. The correlated measurement $P_{tot,corr,1}/D^2$ is then simplified to:

$$P_{tot,corr,1}/D^2 = 1/D^2 \left(\sigma_b D^2 + 4D^2 0.04 \sigma_b \right) \tag{K.1.3}$$

And

$$\sigma_b = P_{tot,corr,1}/D^2 1/1.16 \tag{K.1.4}$$

which results in the correction factor $c_{a,2} = 1/1.16 = 0.862$. The total correction factor c_a is then:

$$P_{tot,corr,1} c_{a,2} = P_{tot} c_{a,1} c_{a,2} = P_{tot} c_a \tag{K.1.5}$$

The total correction factor is then 0.78.

The calculation of the correction factor c_a depends on the assumption of the average shaft friction over the initial part of the pile, which is complicated to estimate, and is consequently not very exact.

Appendix L

Calibration of model pile in the lever system

L.1 Measurements in the axial lever system

The instrumented model pile was also calibrated in the axial lever system. The principles of the system are shown in Figure L.1. The counterweight was provided by 0.5 kg steel weights which were mounted on the lever by hand.

Figure L.1a shows a load cycle in the axial calibration system for sensor 1. Measurements of both axial and horizontal stress sensors were carried out with the axial calibration system. Figure L.2 L.5 shows the measurements of the horizontal stress sensor system loaded within the axial compression lever system. There is wide variation in measurements between the sensors.

Figure L.6 shows the axial stress sensors, and shows a relatively straight calibration curve.

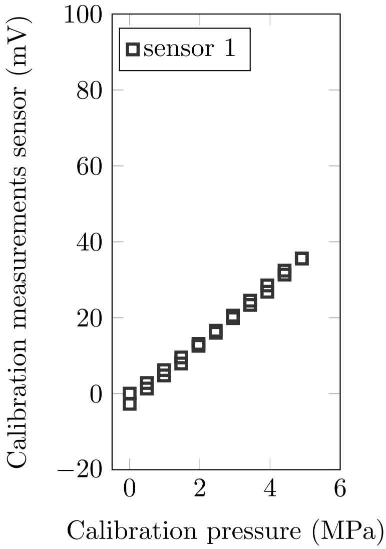

(a) Calibration cycle in the lever system.

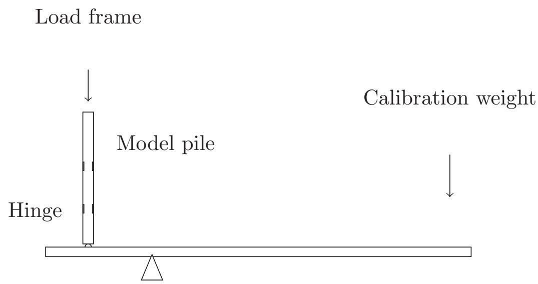

(b) Calibration principle.

Figure L.1: Calibration of the axial stress sensor including calibration cycle.

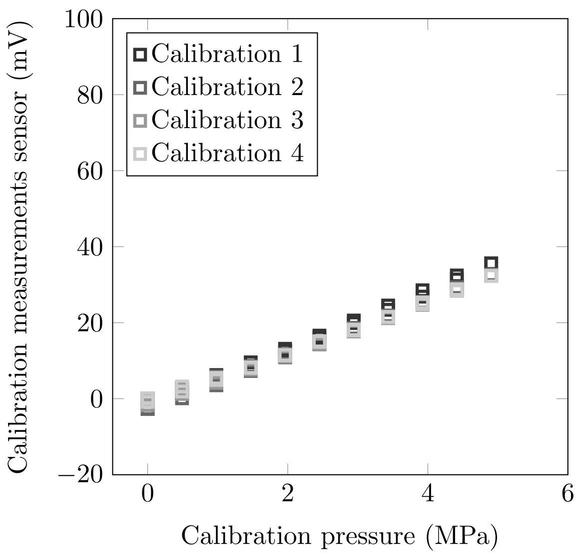

Figure L.2: Sensor 1.

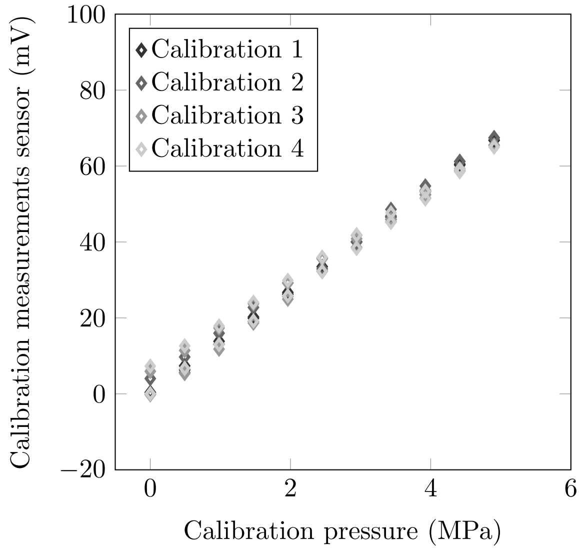

Figure L.3: Sensor 2.

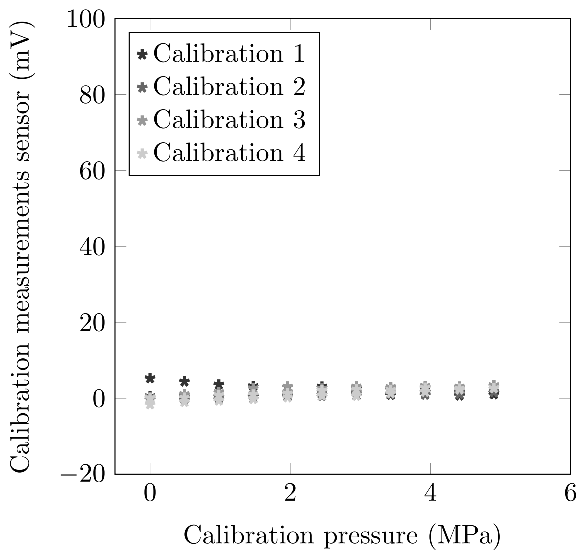

Figure L.4: Sensor 3.

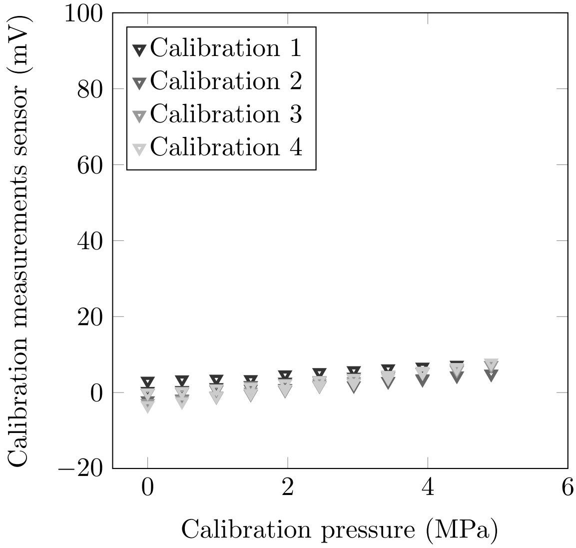

Figure L.5: Sensor 4.

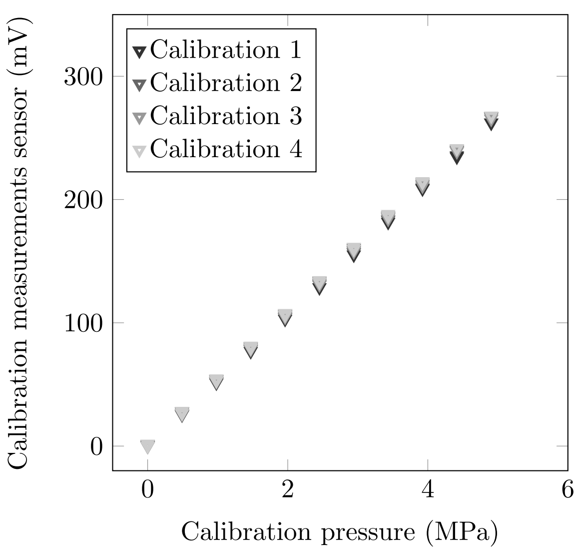

Figure L.6: Calibration of the axial stress sensor in the axial calibration system.

L.2 Calibration coefficients from the axial compression lever system

Table L.1 and L.2 show the calibration coefficients calculated from the calibration measurements. There is relatively small deviation from the averaged coefficients from the calibration.

Sensor nr	Cal. 1	Cal. 2	Cal. 3	Cal. 4	Average Cal.
sensor 1	7.197	6.710	6.645	6.544	6.774
sensor 2	13.62	13.92	13.50	13.19	13.56
sensor 3	0.108	0.3052	0.5727	0.5883	0.3935
sensor 4	1.400	1.031	1.439	1.608	1.370
axial	0.01872	0.01839	0.01847	0.01830	0.01847

Table L.1: Calibration coefficients from the axial stress calibration for incremental stress increase.

Sensor nr	Cal. 1	Cal. 2	Cal. 3	Cal. 4	Average Cal.
sensor 1	7.924	7.320	6.998	6.814	7.264
sensor 2	13.49	13.04	12.06	11.86	12.61
sensor 3	-0.7106	0.3861	0.6843	0.8284	0.2970
sensor 4	0.9709	1.514	2.049	2.213	1.687
axial	0.01874	0.01844	0.01861	0.01841	0.01854

Table L.2: Calibration coefficients from the axial stress calibration for incremental stress decrease.

Appendix M

Measurements of horizontal stress during incremental installation

The locations of the sensors are shown in Figure M.1, which shows the model pile with the sensors and the instrumentation levels. The measurements show mean value in solid line, and outer limits in dotted lines.

The horizontal stress measurements during incremental installation (including load reversal during installation) are presented in this appendix for the soil samples.

Figure N.1a and the N.1b show the measurements in initial loose soil samples for incremental installation method.

Figure N.2a, Figure N.2b and Figure N.2c show the measurements in the medium dense sample.

Figure N.3a and Figure N.3b show the measurements in the dense sample.

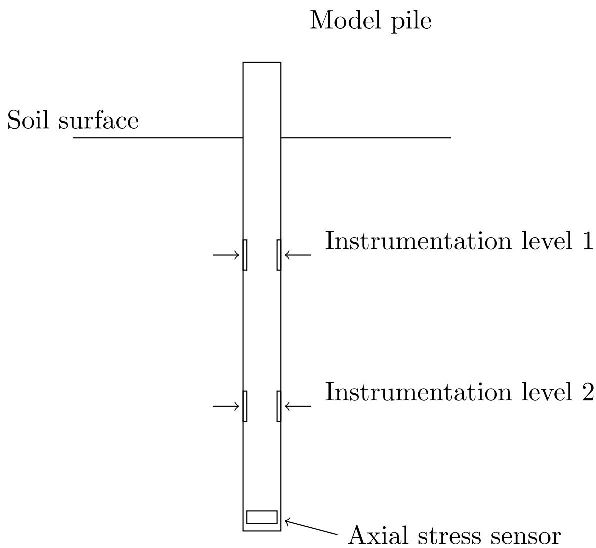

Figure M.1: Instrumentation level 1 and 2 on the instrumented model pile.

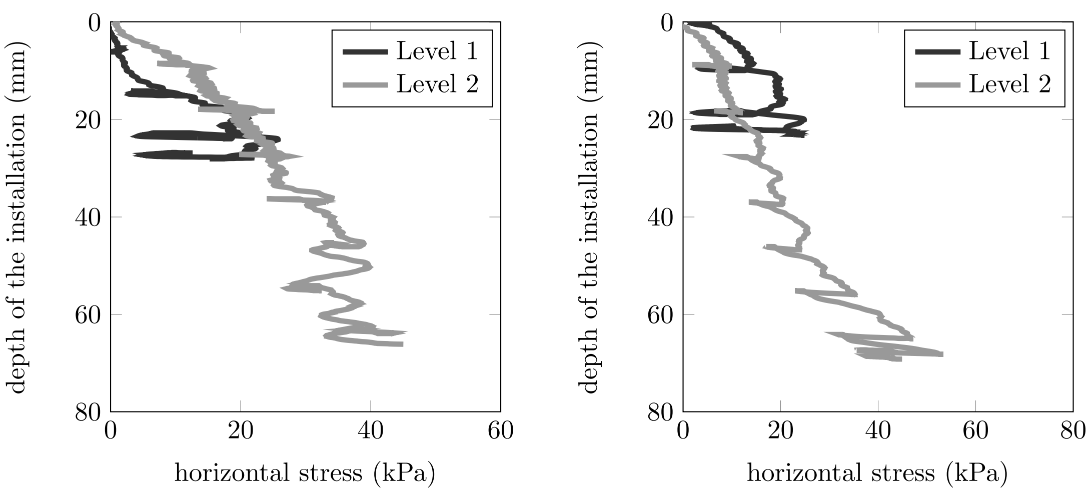

(a) Measurements of total horizontal stress $\sigma'_{tot,h}$ in loose sample 1 during incremental installation.

(b) Measurements of total horizontal stress $\sigma'_{tot,h}$ in loose sample 2 during incremental installation.

Figure M.2: Measurements of total horizontal stress $\sigma'_{tot,h}$ in loose sample during incremental installation.

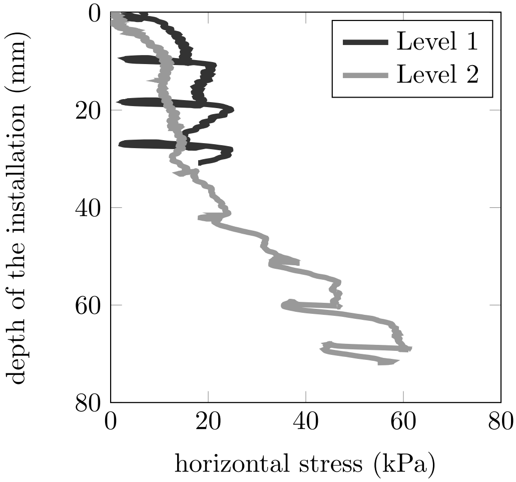

(a) Measurements of total horizontal stress $\sigma'_{tot,h}$ in medium dense sample 1 during incremental installation.

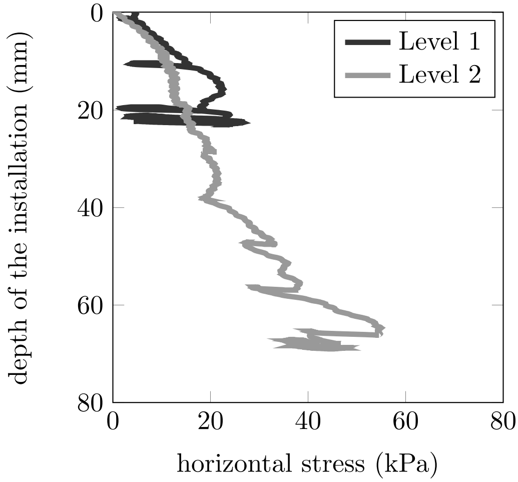

(b) Measurements of total horizontal stress $\sigma'_{tot,h}$ in medium dense sample 2 during incremental installation.

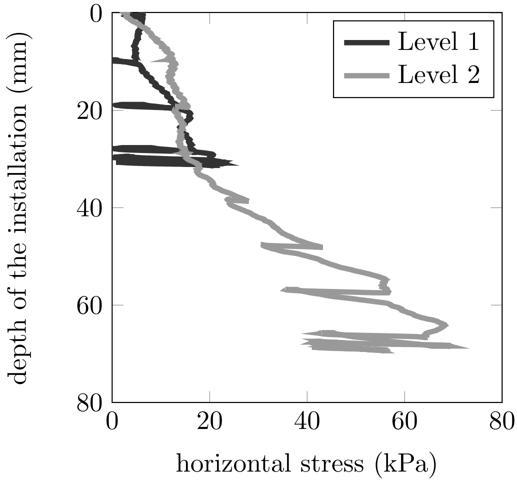

(c) Measurements of total horizontal stress $\sigma'_{tot,h}$ in medium dense sample 3 during incremental installation.

Figure M.3: Measurements of total horizontal stress $\sigma'_{tot,h}$ in medium dense sample during incremental installation.

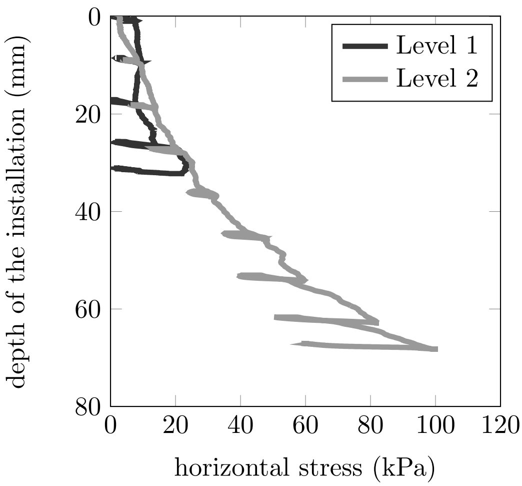

(a) Measurements of total horizontal stress $\sigma'_{tot,h}$ in dense sample 1 during incremental installation.

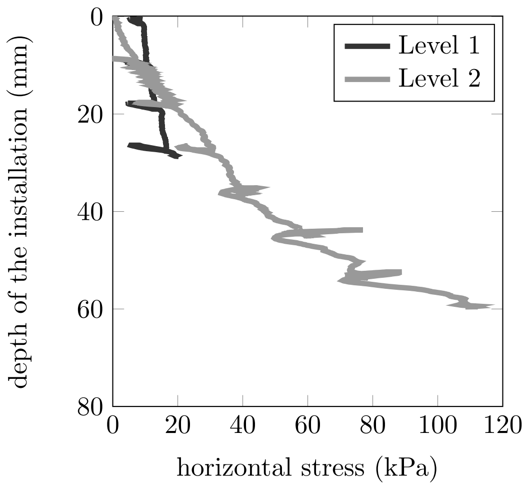

(b) Measurements of total horizontal stress $\sigma'_{tot,h}$ in dense sample 2 during incremental installation.

Figure M.4: Measurements of total horizontal stress $\sigma'_{tot,h}$ in dense sample during incremental installation.

Appendix N

Measurements of horizontal stress during incremental installation

The horizontal stress measurements during incremental installation (including load reversal during installation) are presented in this appendix for the soil samples.

Figure N.1a and the N.1b show the measurements in initial loose soil samples for incremental installation method.

Figure N.2a, Figure N.2b and Figure N.2c show the measurements in the medium dense sample.

Figure N.3a and Figure N.3b show the measurements in the dense sample.

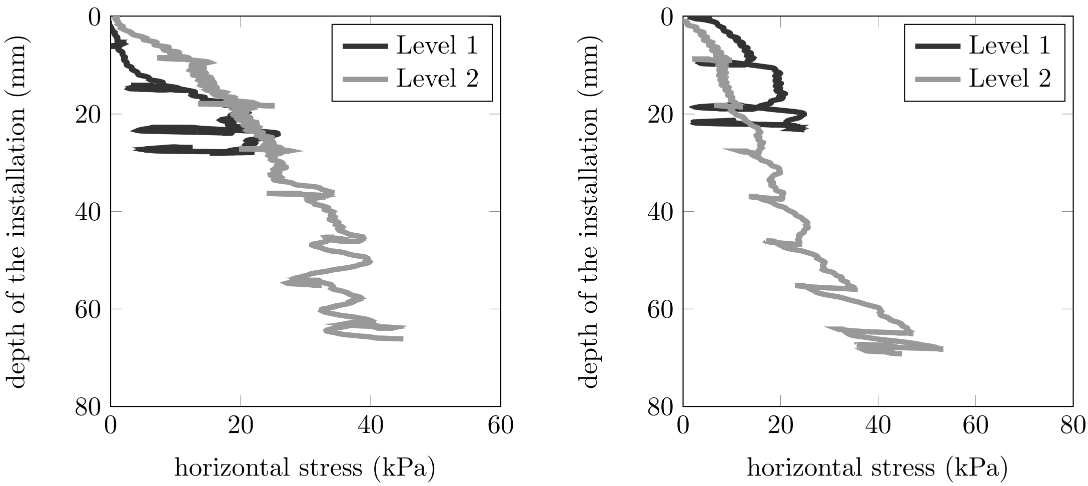

(a) Measurements of total horizontal stress $\sigma'_{tot,h}$ in loose sample 1 during incremental installation.

(b) Measurements of total horizontal stress $\sigma'_{tot,h}$ in loose sample 2 during incremental installation.

Figure N.1: Measurements of total horizontal stress $\sigma'_{tot,h}$ in loose sample during incremental installation.

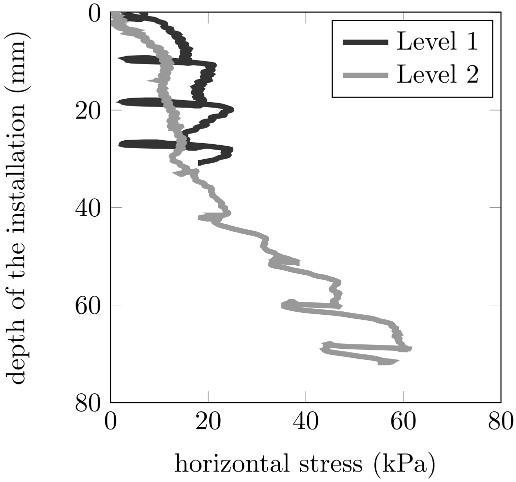

(a) Measurements of total horizontal stress $\sigma'_{tot,h}$ in medium dense sample 1 during incremental installation.

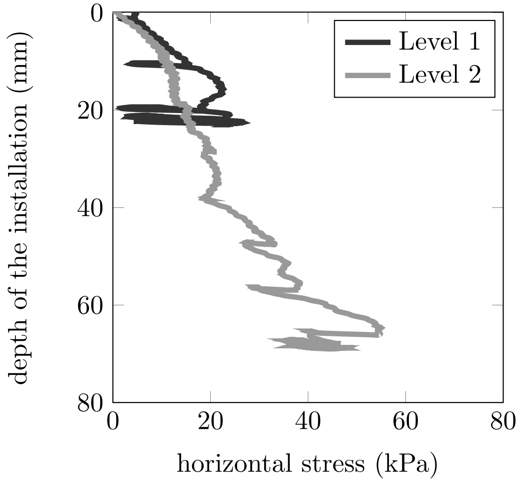

(b) Measurements of total horizontal stress $\sigma'_{tot,h}$ in medium dense sample 2 during incremental installation.

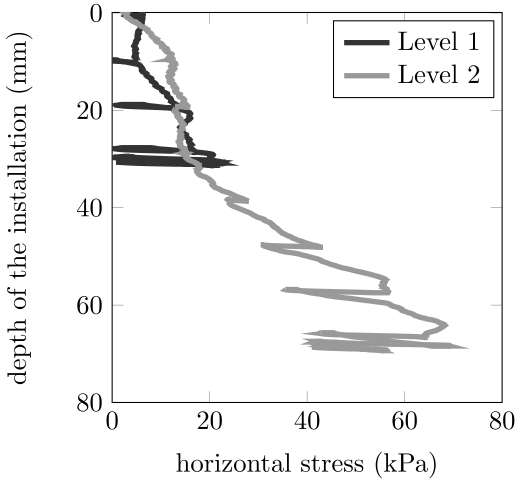

(c) Measurements of total horizontal stress $\sigma'_{tot,h}$ in medium dense sample 3 during incremental installation.

Figure N.2: Measurements of total horizontal stress $\sigma'_{tot,h}$ in medium dense sample during incremental installation.

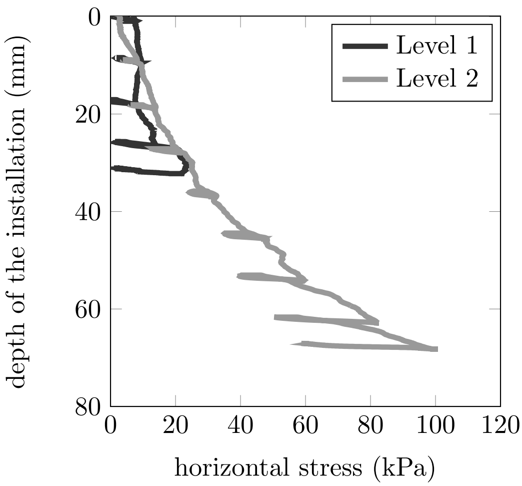

(a) Measurements of total horizontal stress $\sigma'_{tot,h}$ in dense sample 1 during incremental installation.

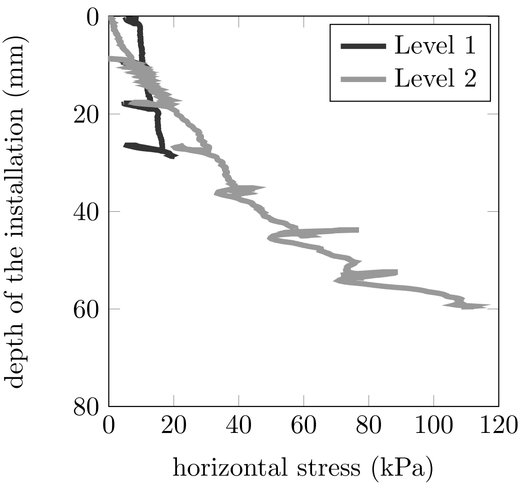

(b) Measurements of total horizontal stress $\sigma'_{tot,h}$ in dense sample 2 during incremental installation.

Figure N.3: Measurements of total horizontal stress $\sigma'_{tot,h}$ in dense sample during incremental installation.

Appendix O

Measurements of horizontal stress during extraction pile extraction

The horizontal stress was measured during pull tests after the installation.

Figure O.1a, Figure O.1b, and Figure O.1c show horizontal stress measurements after continouous installation in the loose soil sample.

Figure O.2a and O.2b show the horizontal stress measurements during pull tests after incremental installation in loose soil sample.

Figure O.3a, O.3b and O.3c show the horizontal stress measurements during pull tests after continuous installation in medium dense soil.

Figure O.4a and Figure O.4b show the horizontal stress measurements during pull tests after incremental installation in medium dense soil.

Figure O.5a and Figure O.5b show the horizontal stress measurements during pull tests after incremental installation in dense soil.

Figure O.6a and Figure O.6b show the horizontal stress measurements during pull tests after incremental installation in dense soil.

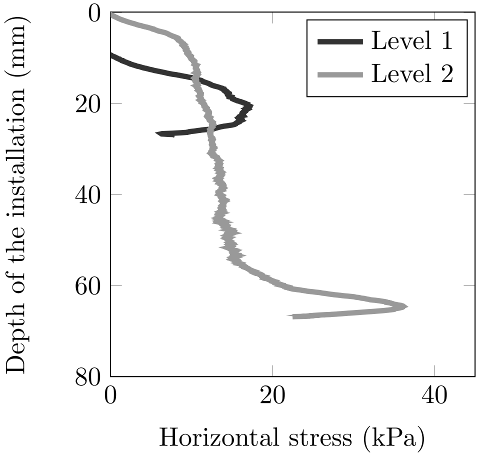

(a) Measurements of total horizontal stress $\sigma'_{tot,h}$ in loose sample 1 during pull tests after continuous installation.

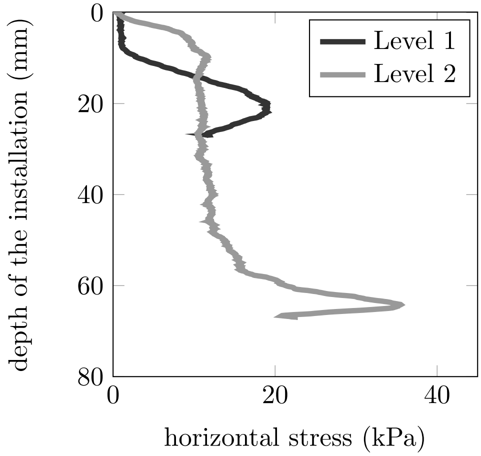

(b) Measurements of total horizontal stress $\sigma'_{tot,h}$ in loose sample 2 during pull tests after continuous installation.

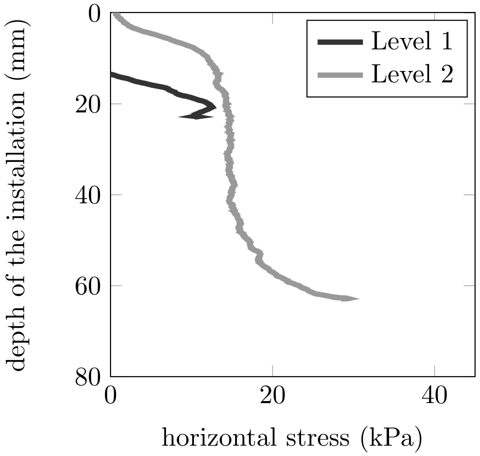

(c) Measurements of total horizontal stress $\sigma'_{tot,h}$ in loose sample 3 during pull tests after continuous installation.

Figure O.1: Measurements of total horizontal stress $\sigma'_{tot,h}$ in loose sample during pull tests after continuous installation.

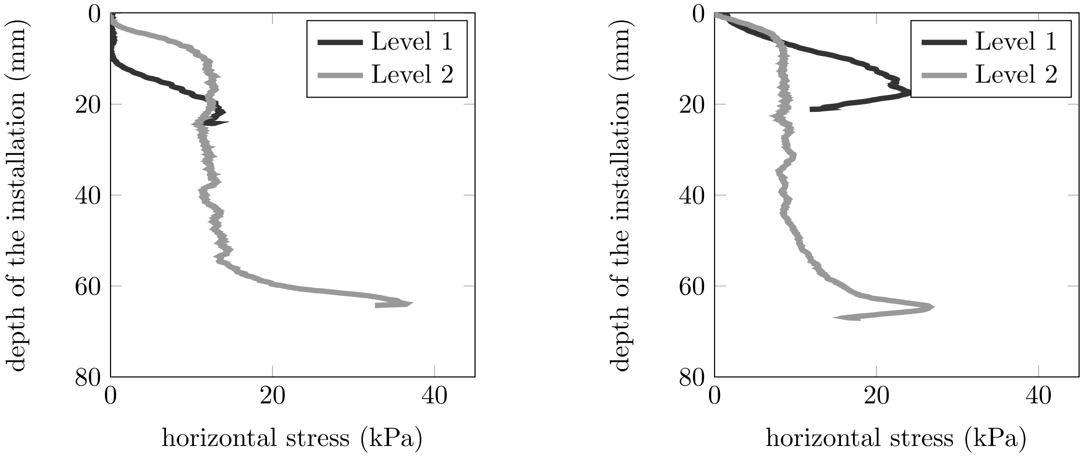

(a) Measurements of total horizontal stress $\sigma'_{tot,h}$ in loose sample 1 during pull tests after cyclic installation.

(b) Measurements of total horizontal stress $\sigma'_{tot,h}$ in loose sample 2 during pull tests after cyclic installation.

Figure O.2: Measurements of total horizontal stress $\sigma'_{tot,h}$ in loose sample during pull tests after incremental installation.

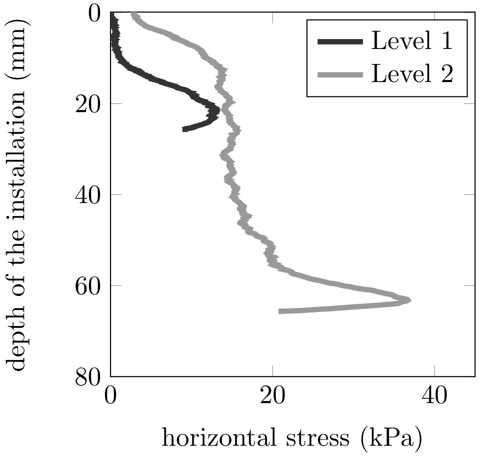

(a) Measurements of total horizontal stress $\sigma'_{tot,h}$ in medium sample 1 during pull tests after continuous installation.

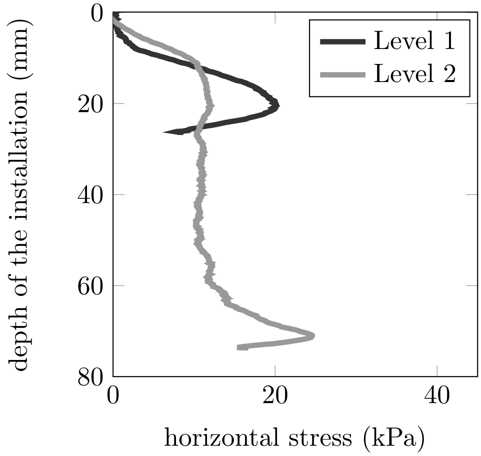

(b) Measurements of total horizontal stress $\sigma'_{tot,h}$ in medium sample 2 during pull tests after continuous installation.

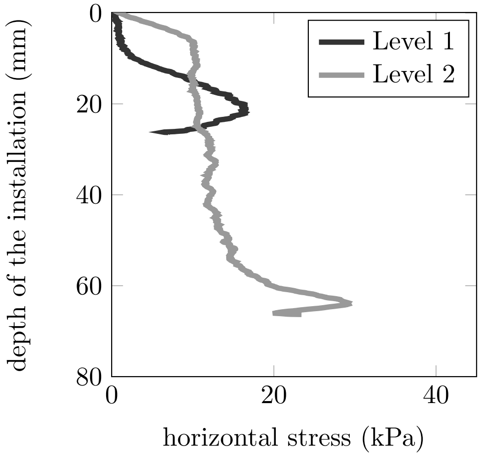

(c) Measurements of total horizontal stress $\sigma'_{tot,h}$ in medium sample 3 during pull tests after continuous installation.

Figure O.3: Measurements of total horizontal stress $\sigma'_{tot,h}$ in medium dense sample during pull tests after continuous installation.

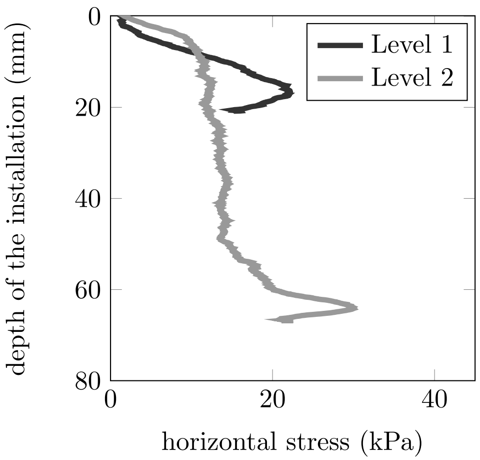

(a) Measurements of total horizontal stress $\sigma'_{tot,h}$ in medium sample 2 during pull tests after cyclic installation.

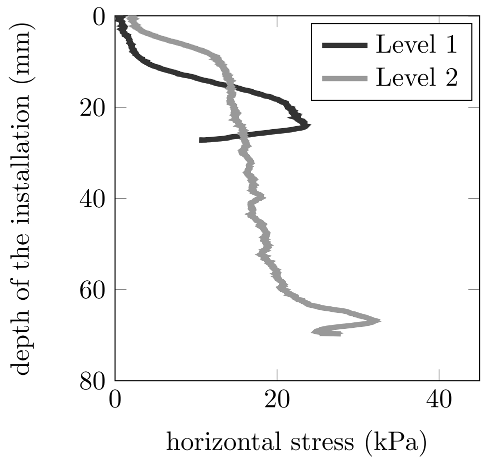

(b) Measurements of total horizontal stress $\sigma'_{tot,h}$ in medium sample 3 during pull tests after cyclic installation.

Figure O.4: Measurements of total horizontal stress $\sigma'_{tot,h}$ in medium dense sample during pull tests after cyclic installation.

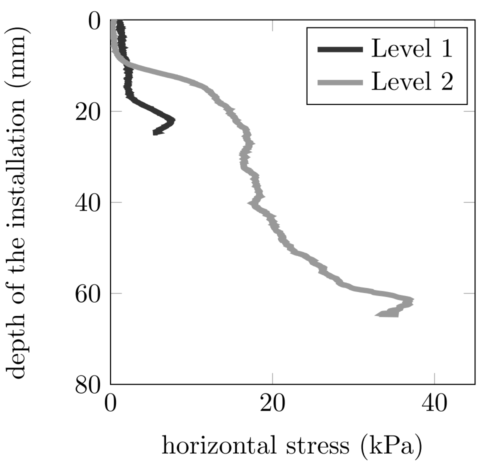

(a) Measurements of total horizontal stress $\sigma'_{tot,h}$ in dense sample 1 during pull tests after continuous installation.

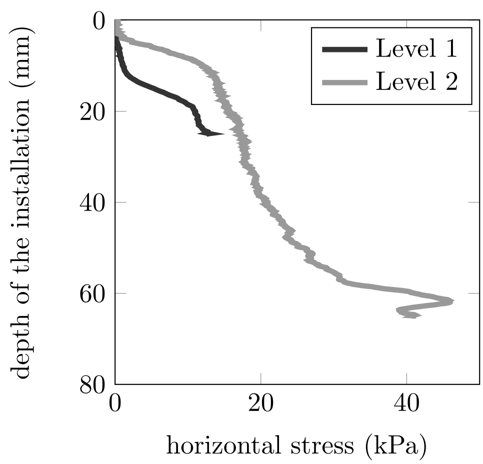

(b) Measurements of total horizontal stress $\sigma'_{tot,h}$ in dense sample 2 during pull tests after continuous installation.

Figure O.5: Measurements of total horizontal stress $\sigma'_{tot,h}$ in dense sample during pull tests after continuous installation.

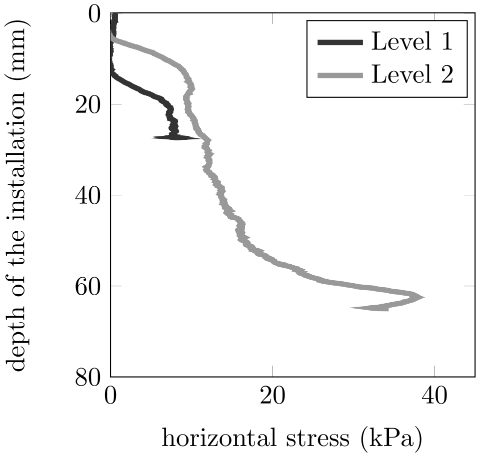

(a) Measurements of total horizontal stress $\sigma'_{tot,h}$ in dense sample 1 during pull tests after incremental installation.

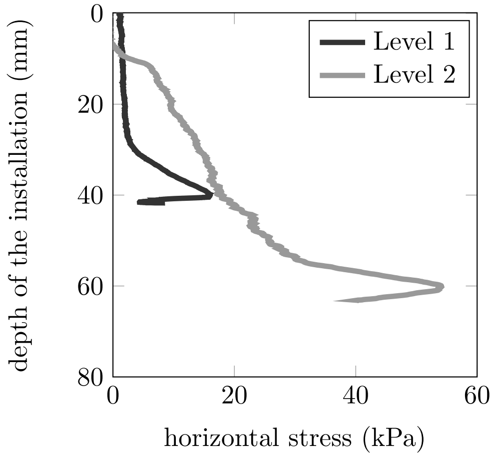

(b) Measurements of total horizontal stress $\sigma'_{tot,h}$ in dense sample 2 during pull tests after incremental installation.

Figure O.6: Measurements of total horizontal stress $\sigma'_{tot,h}$ in dense sample during pull tests after incremental installation.

Appendix P

Measurement of pile head load during static pile load test

Static load tests were carried out after the installation. The pile head load was measured with the load cell mounted on the pile, Figure P.1. The modelpile was first unloaded (excluding self-weight and a small extra weight for stability in the actuator control system). A continuous quasi-static pile load test with an installation rate of 0.01 mm/s was then carried out to $0.2D_{Pile}$ (= 2 mm).

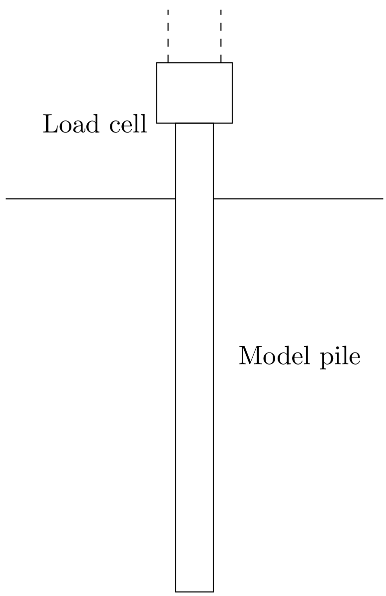

Figure P.1: Measurements of pile head load with load cell.

The measurements of pile head head for the pile load test after continuous and incremental installation are shown in Figure P.2, Figure P.3, and Figure P.4 for loose, medium dense,

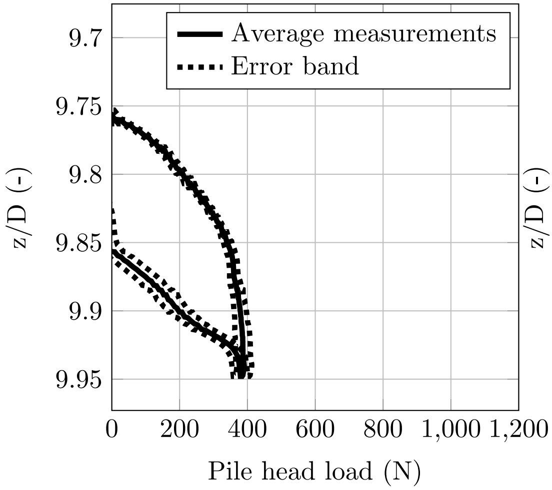

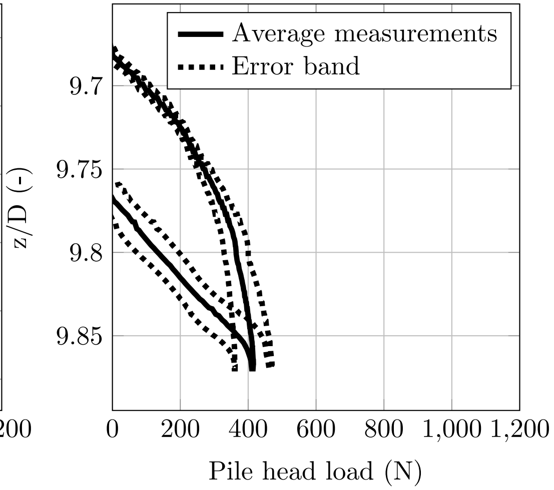

(a) Pile head load measurements during static pile load test in loose soil sample and continuous installation.

(b) Pile head load measurements during static pile load test in loose soil sample and incremental installation.

Figure P.2: Pile head load measurements in loose soil sample for static pile load test.

and dense soil sample, respectively.

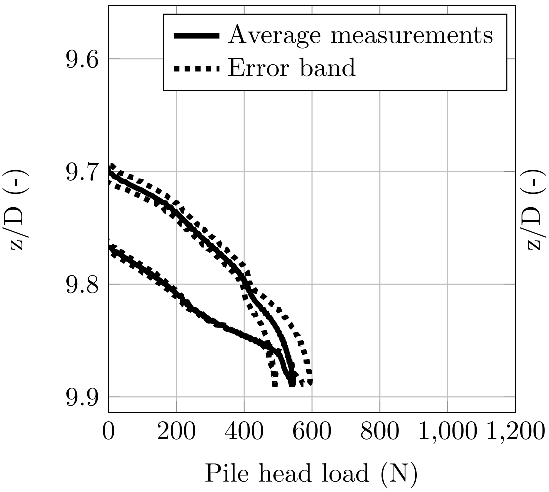

(a) Pile head load measurements during static pile load test in medium dense soil for continuous installation.

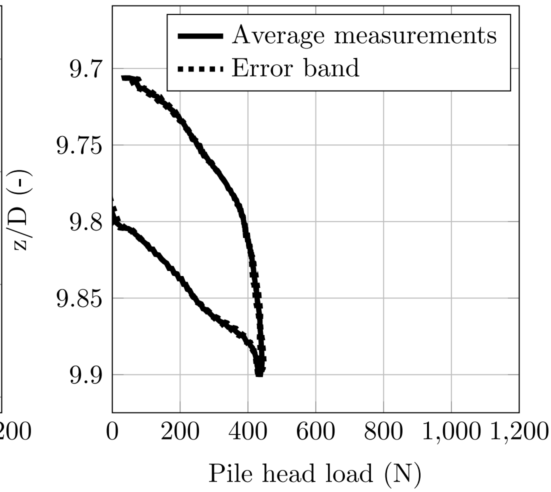

(b) Pile head load measurements during static pile load test in medium dense soil for incremental installation.

Figure P.3: Pile head load measurements in medium dense soil sample for static pile load test.

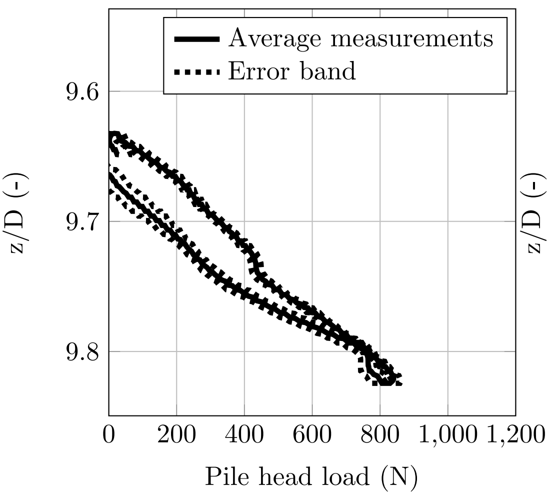

(a) Pile head load measurements during static pile load test in dense soil sample for continuous installation.

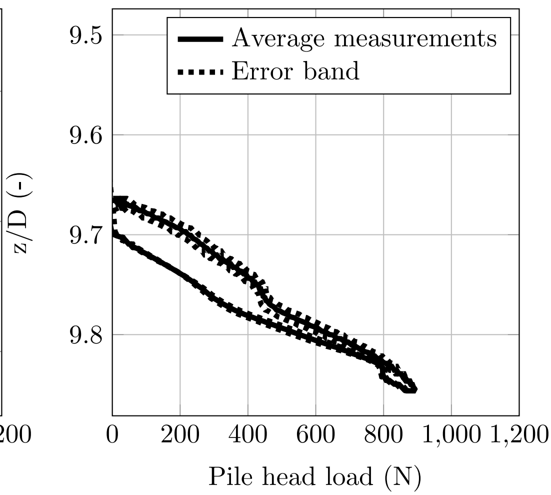

(b) Pile head load measurements during static pile load test in dense soil sample for incremental installation.

Figure P.4: Pile head load measurements in dense soil sample for static pile load test.

Appendix Q

Correlation for shear modulus

Q.1 Dilational stress $\Delta\sigma'_h$

The shear modulus should be estimated for the calculation of stress increase from dilation at the soil-pile interface:

$$\Delta\sigma'_h = \frac{4G}{D_{pile}}\Delta h \tag{Q.1.1}$$

where $\Delta\sigma'_h$ is the stress increase from dilation, G is the shear modulus, D_{Pile} is the pile diameter, and Δh is the volumetric increase from dilation during shear. Δh is assumed to be 0.005 mm, which is lower than the values in design, since the pile surface is much smoother, and the scaled size of the grains are larger, thereby creating less interlocking between the grains and the surface, [124], [150].

G is here estimated with three different methods, based on the cone penetration test, [12], a Duncan-Chang hyperbolic method, [75], and the Janbu modulus, [117]. The value of peak shear modulus is then adjusted, since the soil is disturbed around the pile, [151].

Q.2 Shear modulus from cone penetration test

The cone penetration correlation is formulated as:

$$G = q_c[A + B\eta - C\eta^2]^{-1} \tag{Q.2.1}$$

where

$$\eta = q_c/\sqrt{(}P_a\sigma'_v) \tag{Q.2.2}$$

where q_c is the cone resistance, P_a is the atmospheric pressure, $\sigma_v textquoteright$ is the effective vertical stress, and A, B, C are correlation coefficient. Here $A = 0.0203$, $B = 0.00125$ and $C = 1.216\text{x}10^{-3}$, [12], [125].

Q.3 Shear modulus from Duncan-Chang hyperbolic correlation

The Young's modulus $E(z)$ is calculated from:

$$E(z) = E_{500kPa}\left(\frac{z\gamma'}{E_{500kPa}}\right)^n \quad \text{(Q.3.1)}$$

where z is the scaled depth of the model, γ' is the weight of the sand, n is a constant, and E_{500kPa} is the tangent stiffness of the soil att 500 kPa, [75].

In the calculations $n = 0.5$ for sand, [75], and $E_{500kPa} = 1500$ kPa from triaxial test in the same sand, [2].

The shear modulus G is then calculated with the Poisson's ratio v:

$$G = \frac{E(z)}{2(1+v)} \quad \text{(Q.3.2)}$$

Q.4 Shear modulus from Janbu stiffness modulus

The constrained modulus $M_d(z)$ is formulated as, [117]:

$$M_d(z) = k_m P_a (p'/P_a)^{0.5} \quad \text{(Q.4.1)}$$

where k_m is the Janbu modulus, P_a is the atmospheric pressure, and p' is the mean stress level.

The shear modulus G is then calculated with the Poisson's ratio v:

$$G(z) = M_d(z)\frac{1-2v}{2(1-v)} \quad \text{(Q.4.2)}$$

The Janbu stiffness modulus which has been fitted to the experimental measurements is relatively low, [117]. This could result from the change in stiffness because of the cyclic loading. Since the Janbu formulation is derived from experimental triaxial testing, the stress and strain paths are probably different from those in the soil during displacement pile installation. The other correlations ([12], [75]) also depends on the experimental basis of the formulation.

Q.5 Change in shear modulus

Experimental measurements on tension piles in the centrifuge with known interface friction show that the shear modulus is significantly lower than the G_{max}, [147]. The correlation discussed in the current Appendix predict the maximum or small strain stiffness G_{max}, [12], [75], [117], which should be modified for correct description.

Appendix R

Strain measurements

The strain components ε_{xx}, ε_{yy}, γ_{yx} and ε_v were calculated according to the cross-triangular strain triangle method presented in Appendix H from the displacement paths. The strain was calculated for the loose, medium dense, and dense soil samples at three different depths A, B and C.

The sample area within $0.5D$ was very distorted, and consequently resulted in very noise and also oscillating strain measurements. In the following presentation of strain, a black mask with $0.5D$ length has been extended from the plot of the model pile in the Figures.

The strain components are here defined in the mechanical system in which tensile strain is positive, and compressive strain is negative.

Figure R.1, Figure R.2 and Figure R.3 show the horizontal ε_{xx} at three different depths A, B and C.

Figure R.4, Figure R.5 and Figure R.6 show the vertical strain ε_{xx} at three different depths A, B and C.

Figure R.7, Figure R.8 and Figure R.9 show the shear strain γ_{xx} at three different depths A, B and C.

Figure R.10, Figure R.11 and Figure R.12 show the volumetric strain ε_v at three different depths A, B and C.

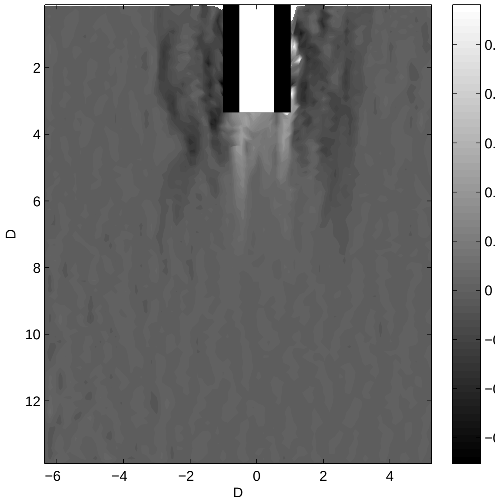

(a) ε_{xx} in the loose soil sample.

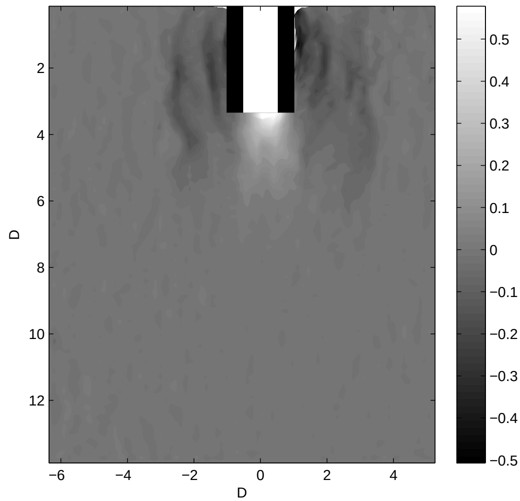

(b) ε_{xx} in the medium dense soil sample.

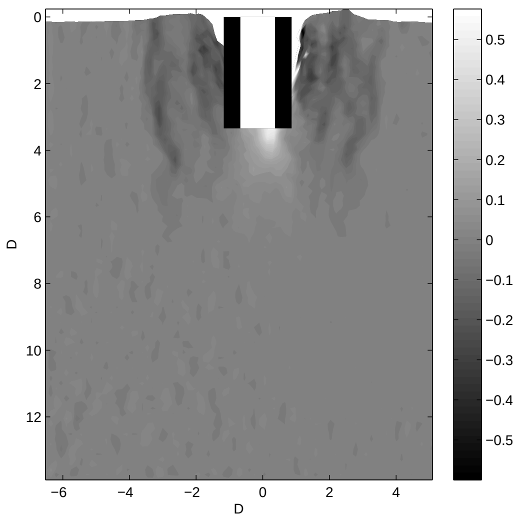

(c) ε_{xx} in the dense soil sample.

Figure R.1: The horizontal strain ε_{xx} at installation position A.

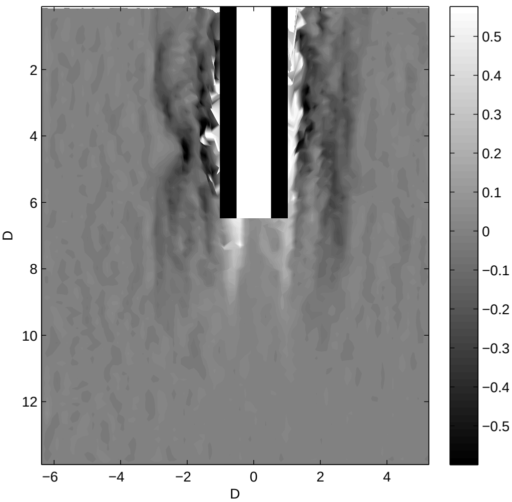

(a) ε_{xx} in the loose soil sample.

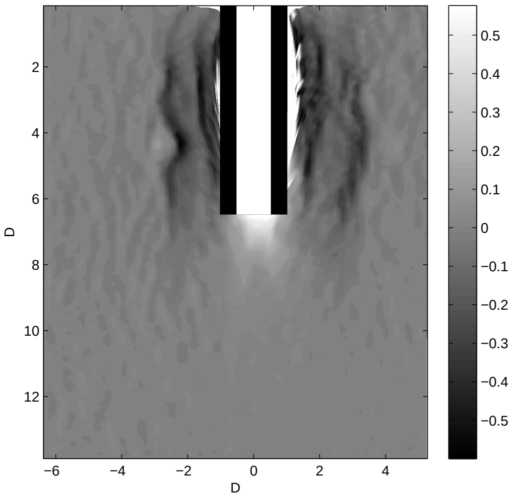

(b) ε_{xx} in the medium dense soil sample.

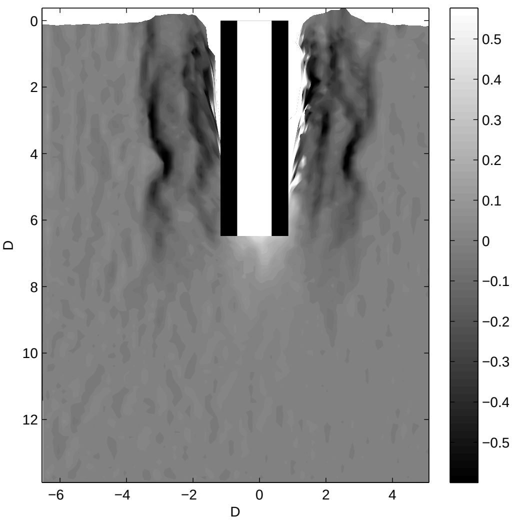

(c) ε_{xx} in the dense soil sample.

Figure R.2: The horizontal strain ε_{xx} at installation position B.

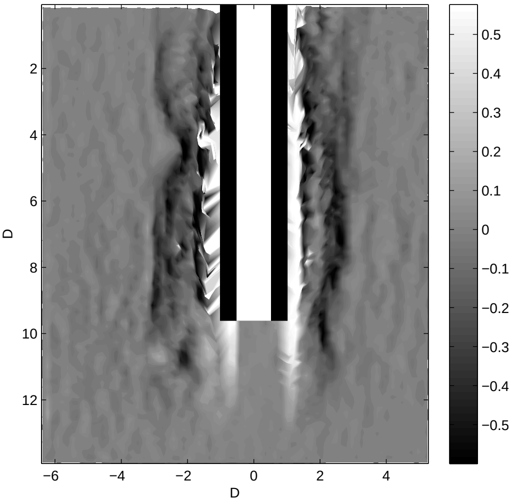

(a) ε_{xx} in the loose soil sample.

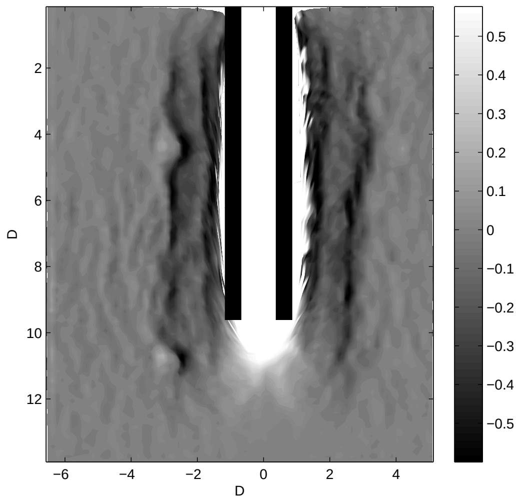

(b) ε_{xx} in the medium dense soil sample.

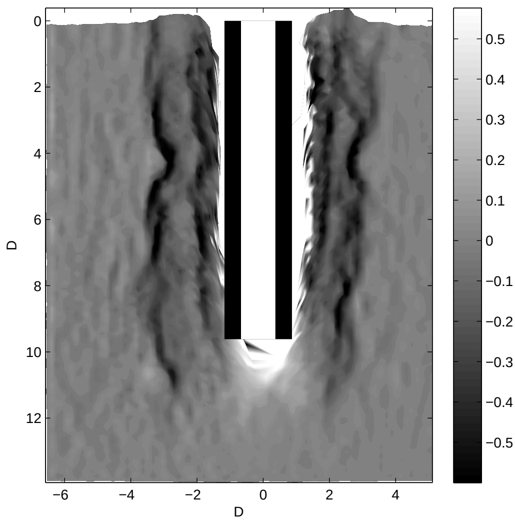

(c) ε_{xx} in the dense soil sample.

Figure R.3: The horizontal strain ε_{xx} at installation position C.

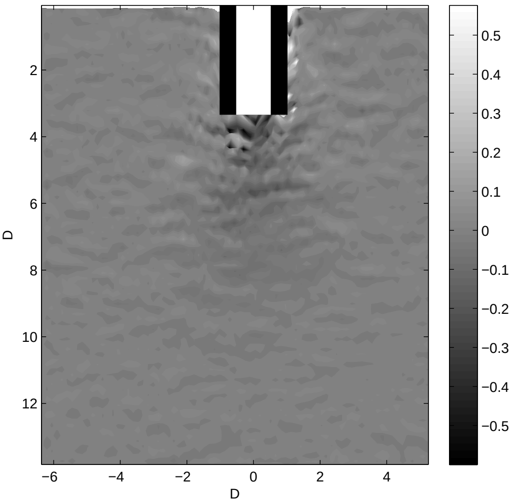

(a) ε_{yy} in the loose soil sample.

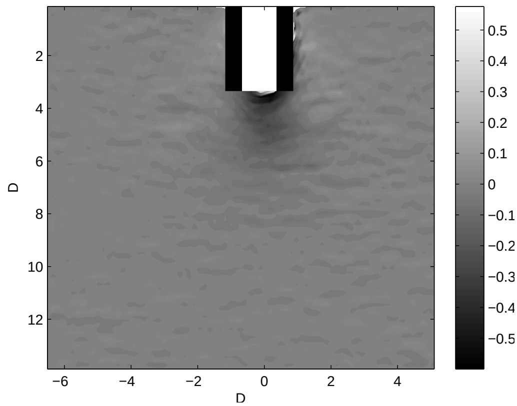

(b) ε_{yy} in the medium dense soil sample.

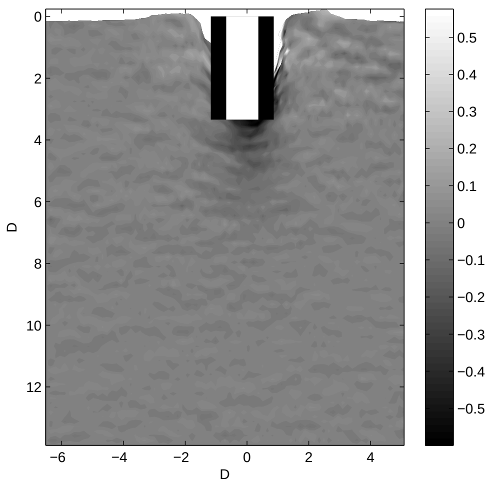

(c) ε_{yy} in the dense soil sample.

Figure R.4: The vertical strain ε_{yy} at installation position A.

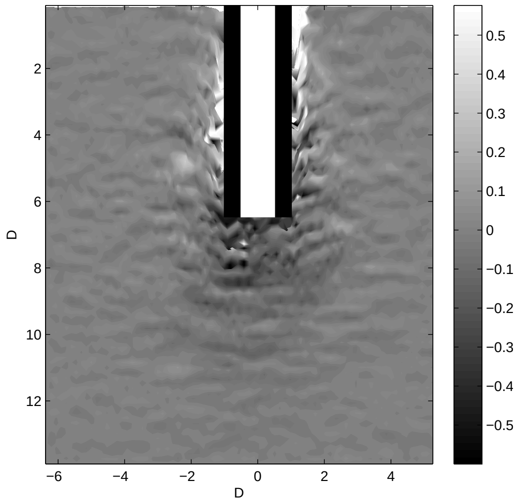

(a) ε_{yy} in the loose soil sample.

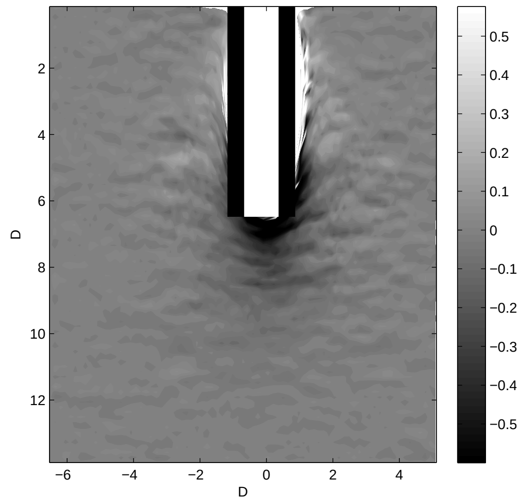

(b) ε_{yy} in the medium dense soil sample.

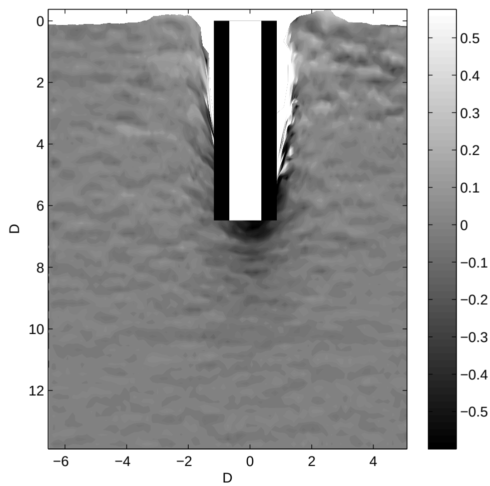

(c) ε_{yy} in the dense soil sample.

Figure R.5: The vertical strain ε_{yy} at installation position B.

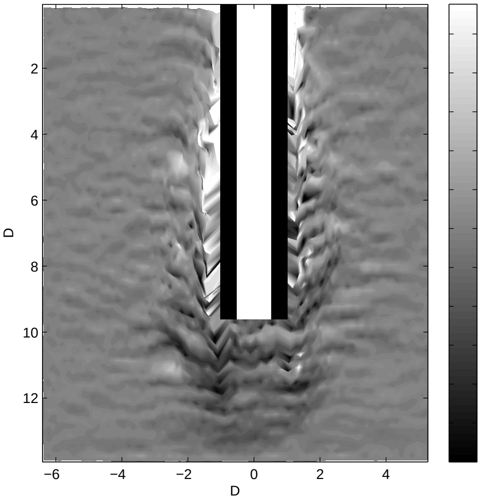

(a) ε_{yy} in the loose soil sample.

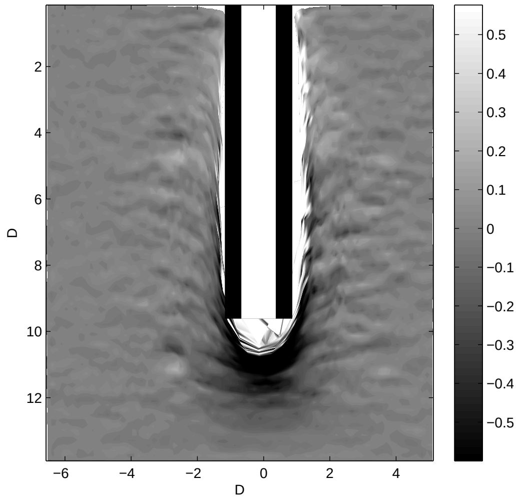

(b) ε_{yy} in the medium dense soil sample.

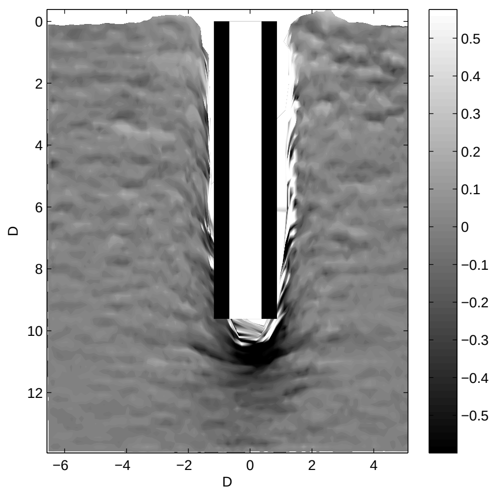

(c) ε_{yy} in the dense soil sample.

Figure R.6: The vertical strain ε_{yy} at installation position C.

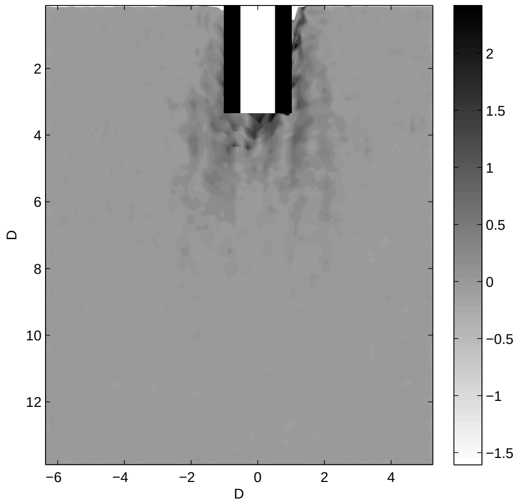

(a) γ_{yx} in the loose soil sample.

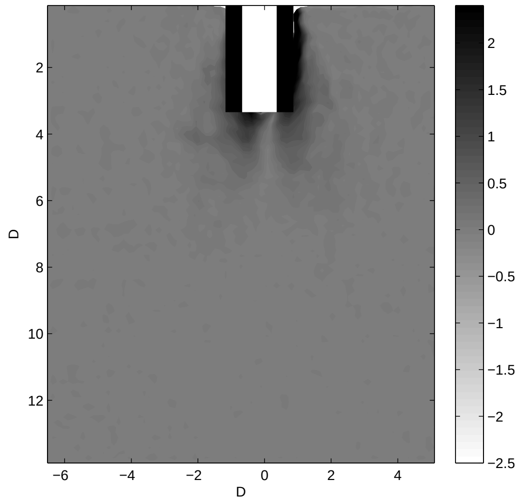

(b) γ_{yx} in the medium dense soil sample.

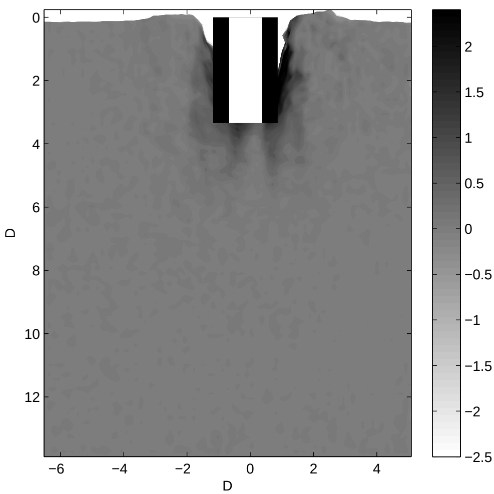

(c) γ_{yx} in the dense soil sample.

Figure R.7: The shear strain γ_{yx} at installation position A.

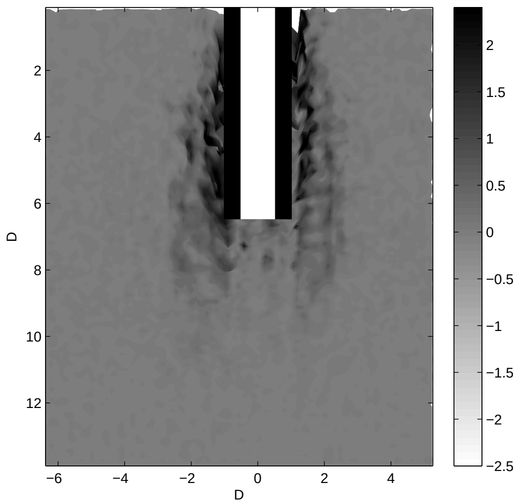

(a) γ_{yx} in the loose soil sample.

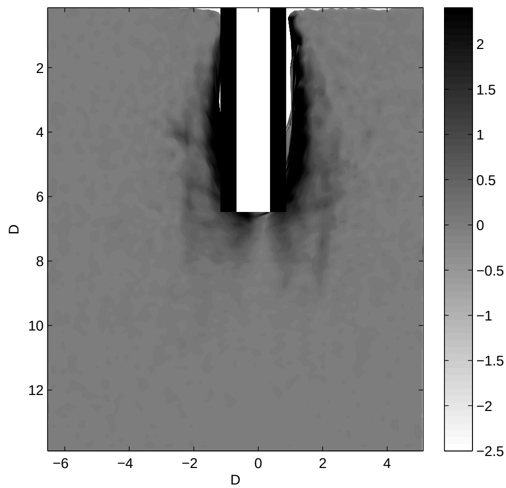

(b) γ_{yx} in the medium dense soil sample.

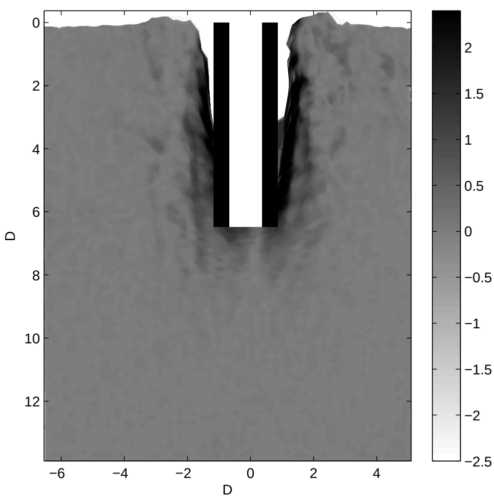

(c) γ_{yx} in the dense soil sample.

Figure R.8: The shear strain γ_{yx} at installation position B.

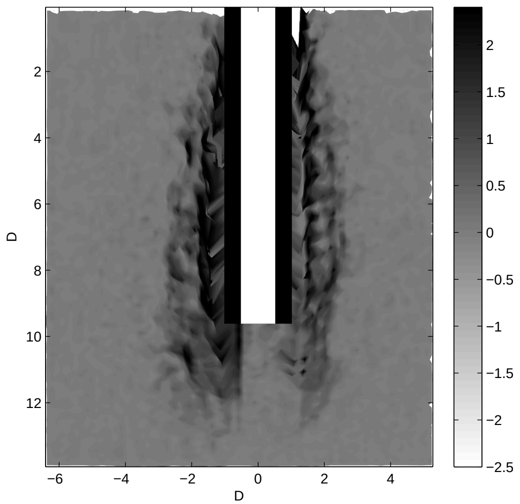

(a) γ_{yx} in the loose soil sample.

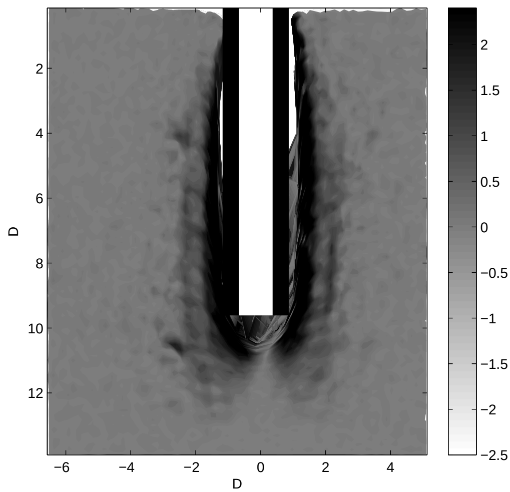

(b) γ_{yx} in the medium dense soil sample.

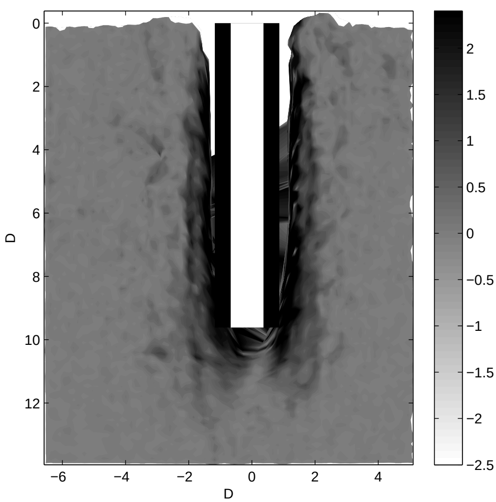

(c) γ_{yx} in the dense soil sample.

Figure R.9: The shear strain γ_{yx} at installation position C.

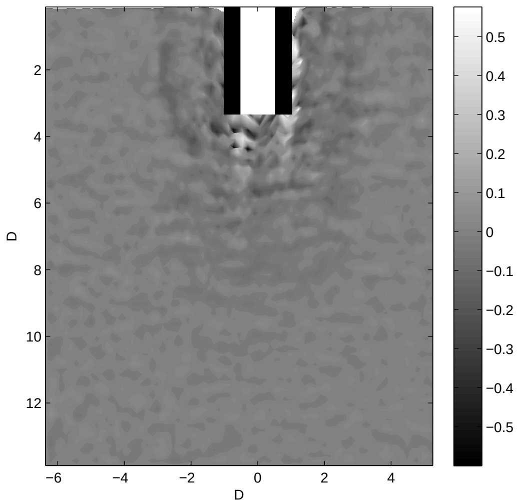

(a) ε_v in the loose soil sample.

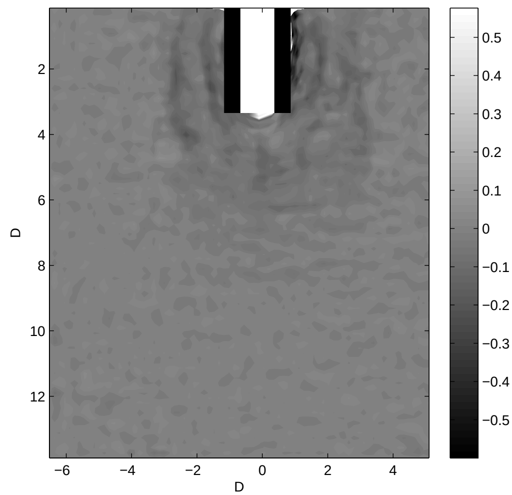

(b) ε_v in the medium dense soil sample.

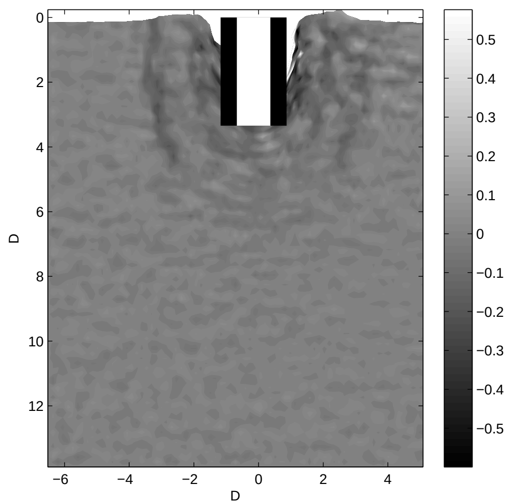

(c) ε_v in the dense soil sample.

Figure R.10: The volumetric strain ε_v at installation position A.

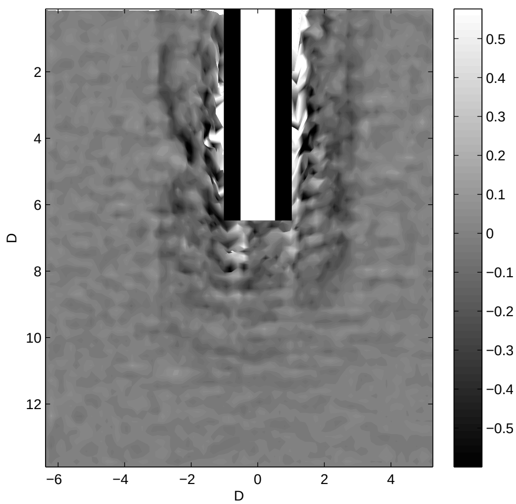

(a) ε_v in the loose soil sample.

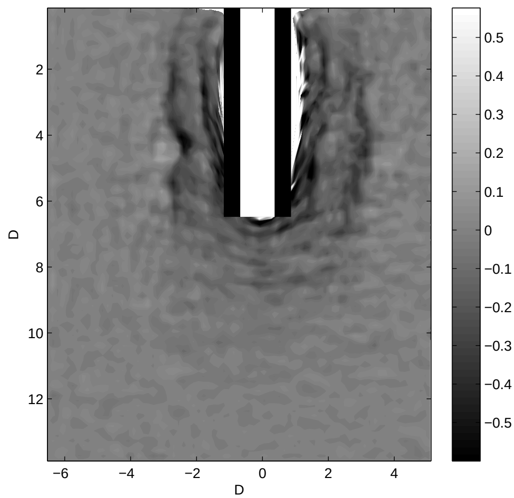

(b) ε_v in the medium dense soil sample.

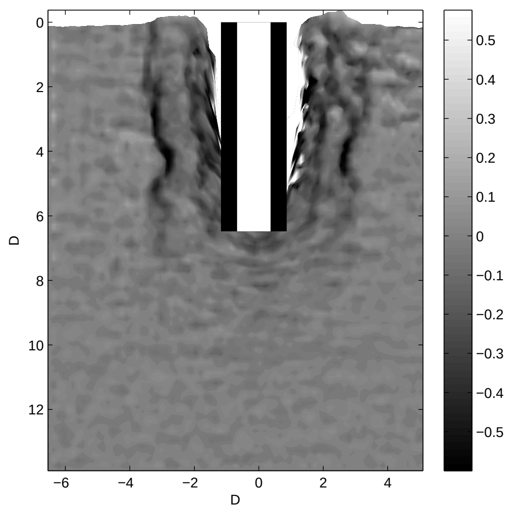

(c) ε_v in the dense soil sample.

Figure R.11: The volumetric strain ε_v at installation position B.

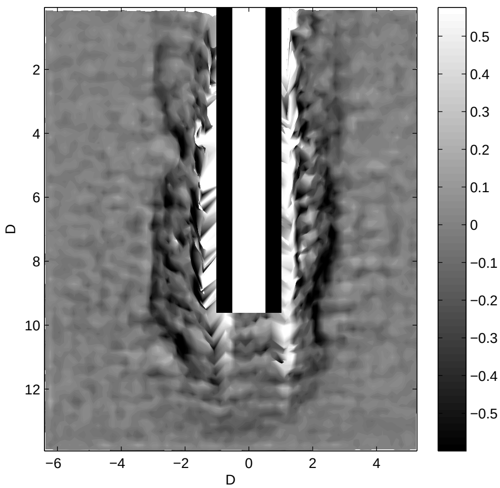

(a) ε_v in the loose soil sample.

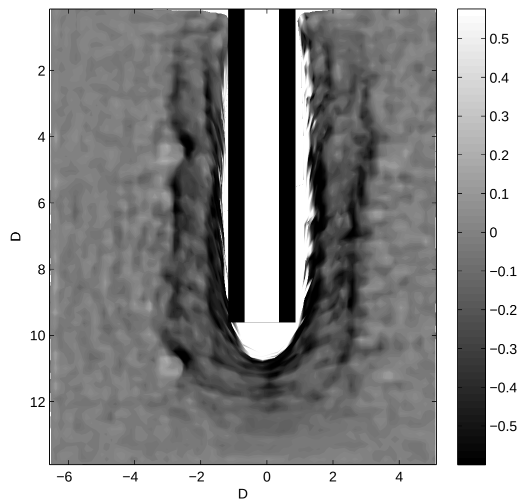

(b) ε_v in the medium dense soil sample.

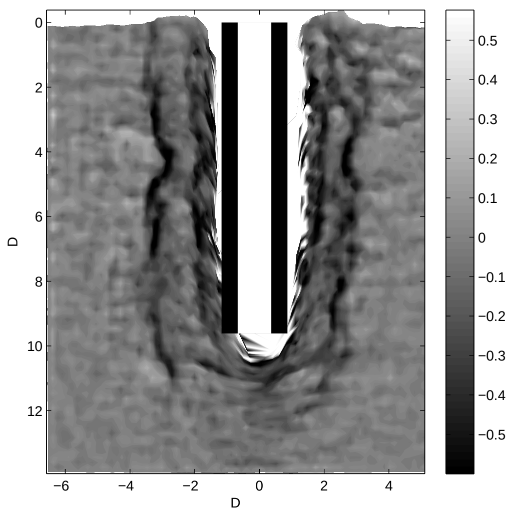

(c) ε_v in the dense soil sample.

Figure R.12: The volumetric strain ε_v at installation position C.

Appendix S

Strain calculation method A and B

The stress-strain paths were calculated both with the cross-triangular method A and B. Here a comparison of these is made for the loose soil sample.

Figures S.1, S.2, S.3 and S.4 show the strain calculation methods A and B for strain components ε_{xx}, ε_{yy}, γ_{yx} and ε_{vv} for the loose soil sample.

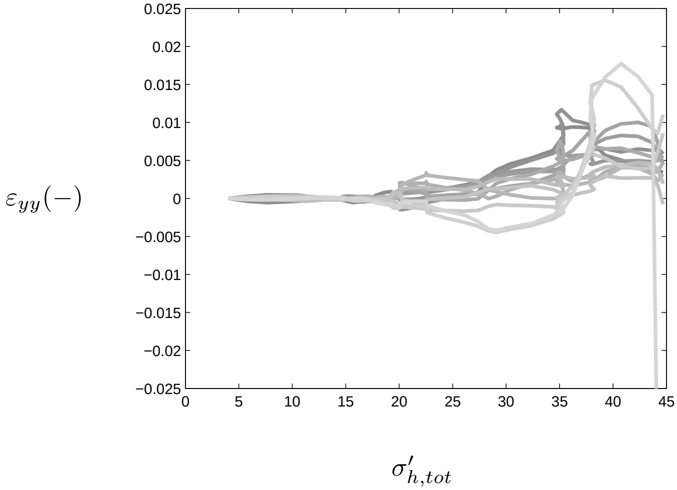

(a) Method A.

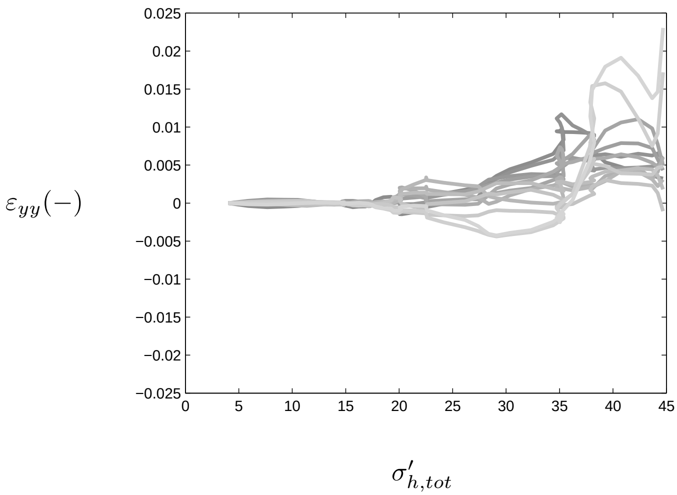

(b) Method B.

Figure S.1: Method A and B for the ε_{xx} strain component.

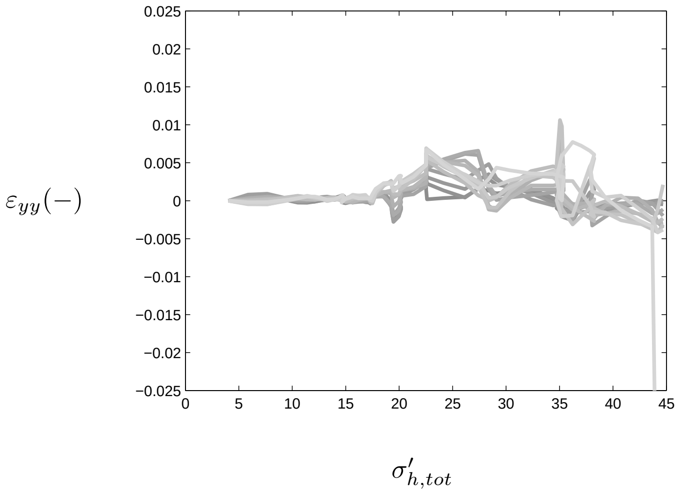

(a) Method A.

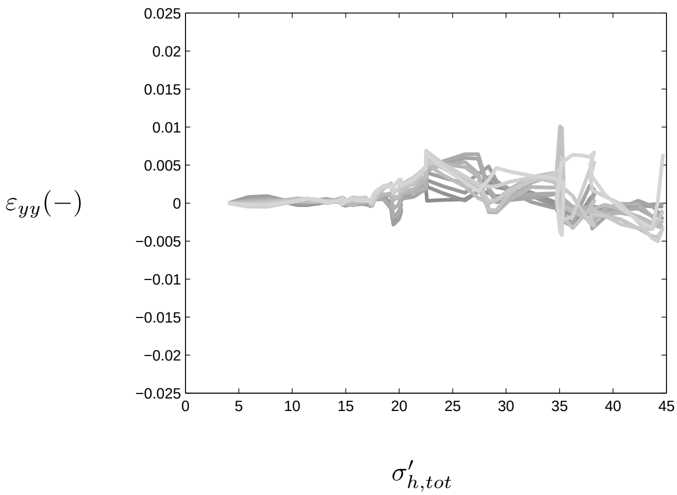

(b) Method B.

Figure S.2: Method A and B for the ε_{yy} strain component.

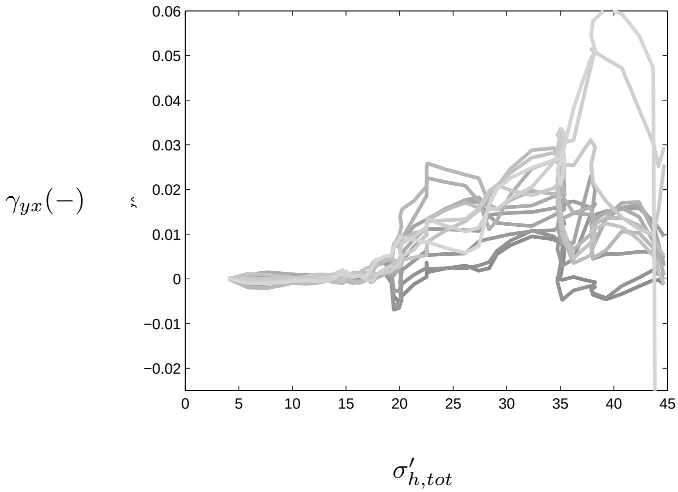

(a) Method A.

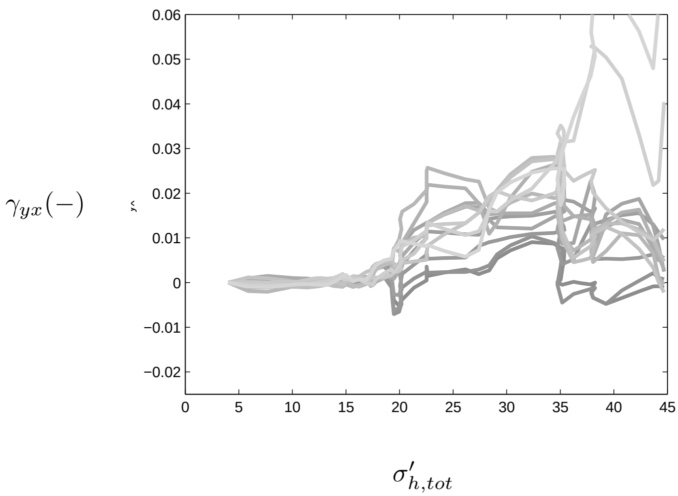

(b) Method B.

Figure S.3: Method A and B for the γ_{yx} strain component.

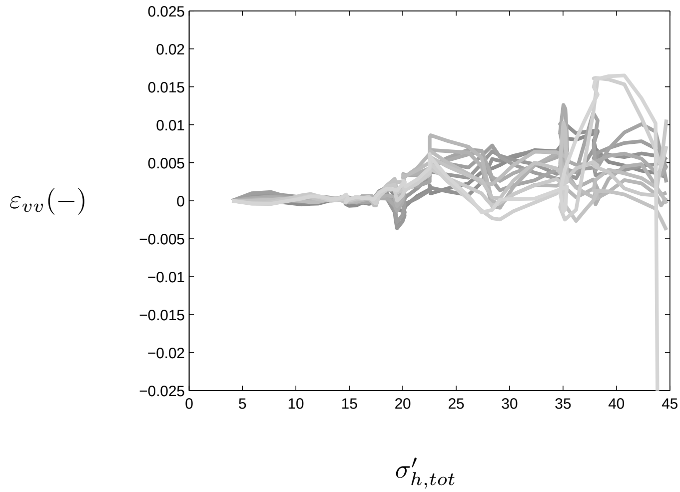

(a) Method A.

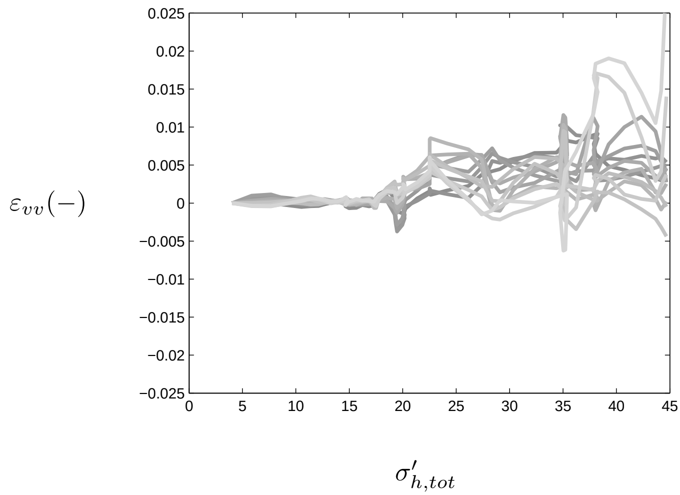

(b) Method B.

Figure S.4: Method A and B for the ε_{vv} strain component.

Appendix T

Strain change during installation

In this appendix the change in strain $\Delta\epsilon_{ij}$ with installation stress is plotted for all strain component ε_{xx}, ε_{yy}, γ_{yx} and ε_{vv}.

Figures T.1, T.2, T.3 and T.4 shows these plots for the strain components ε_{xx}, ε_{yy}, γ_{yx} and ε_{vv} for the loose, medium dense, and dense soil sample. The strain direction is the same as the stress direction, and compression is consequently shown as a positive volumetric strain. The total value of the shear strain was calculated in the measurements.

The strain change shown in Figures T.1, T.2, T.3 and T.4 is related to installation stage 2, in which the soil is sheared against the pile, [241]. This phenomena has previously been studied in continuously installed models in the calibration chamber (in which the installation cycles and stress gradient were not included), [243], and in shear box tests (in which installation phase 1 was not included), e.g. [65]. The measurements display some noise, but suggests the soil behaviour during the shearing stage of installation.

Figure T.1 suggest a relatively large volumetric expansion close the model pile in the denser soil samples. The loose soil sample in Figure T.1 does not display the same type of behaviour. The current approach to analysis of pile installation in empirical design methods does not explicitly account for the difference in behaviour because of of the initial relative density, [241]. Instead the total response as guided from the Cone resistance is governing the behaviour, e.g. [40], [50], [64]. Figure T.1 shows that the shearing mechanism is also dependent on the initial relative density, and consequently the friction fatigue mechanism. It would therefore be interesting to analyse this effect within the current general framework, [241].

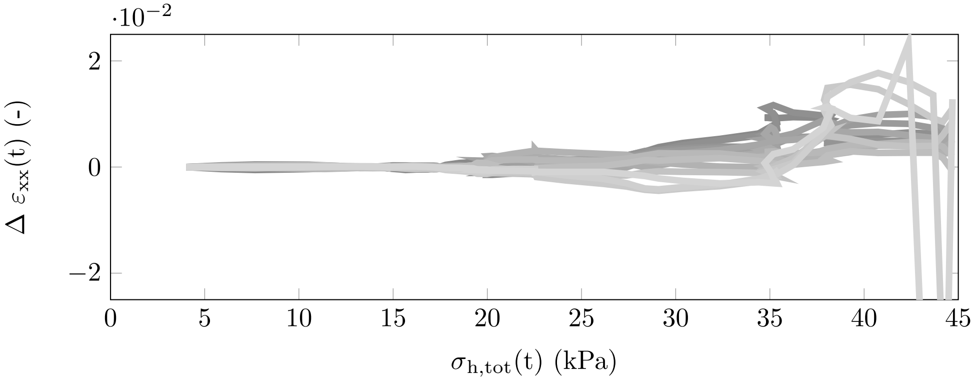

(a) The loose soil sample.

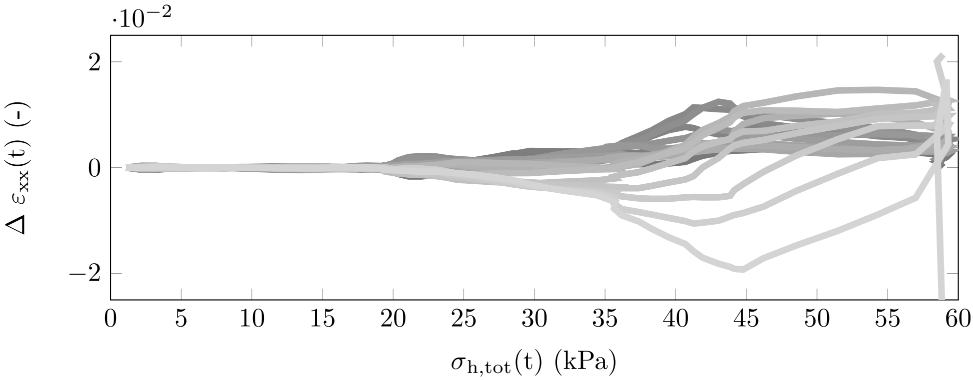

(b) The medium dense sample.

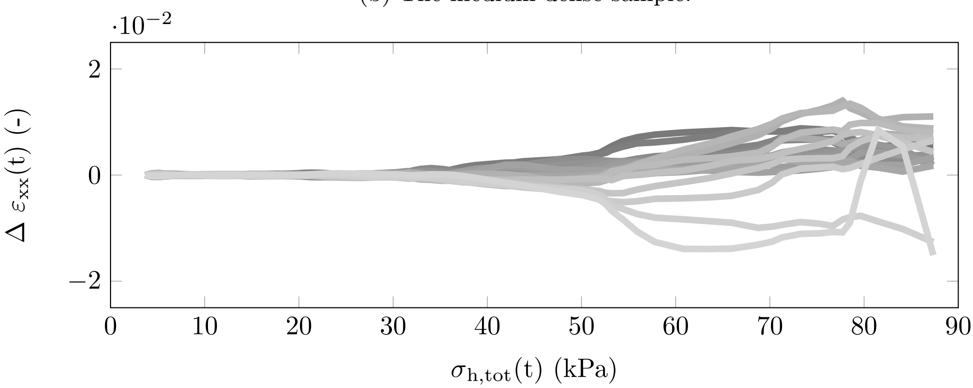

(c) The dense soil sample.

Figure T.1: The ϵ_{xx} strain component.

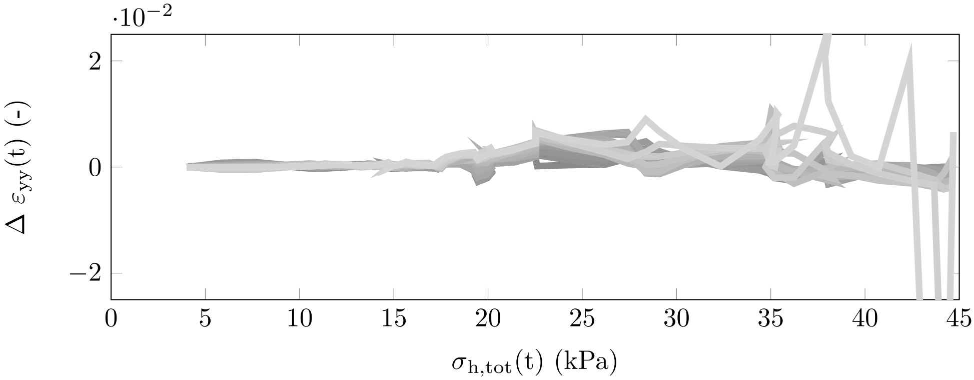

(a) The loose soil sample.

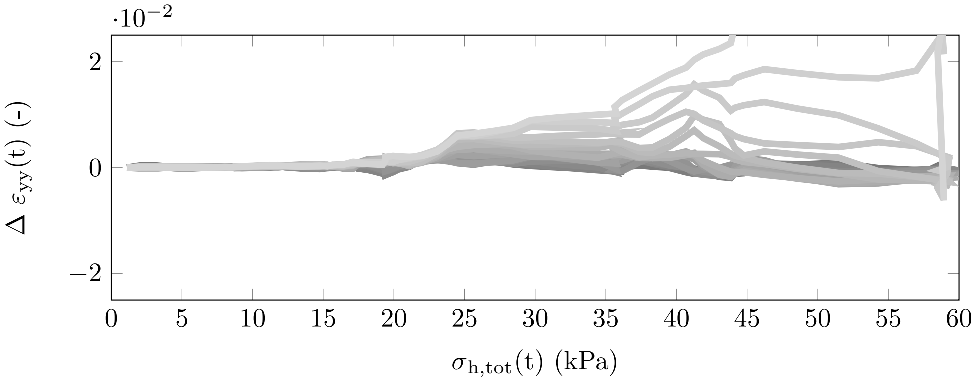

(b) The medium dense sample.

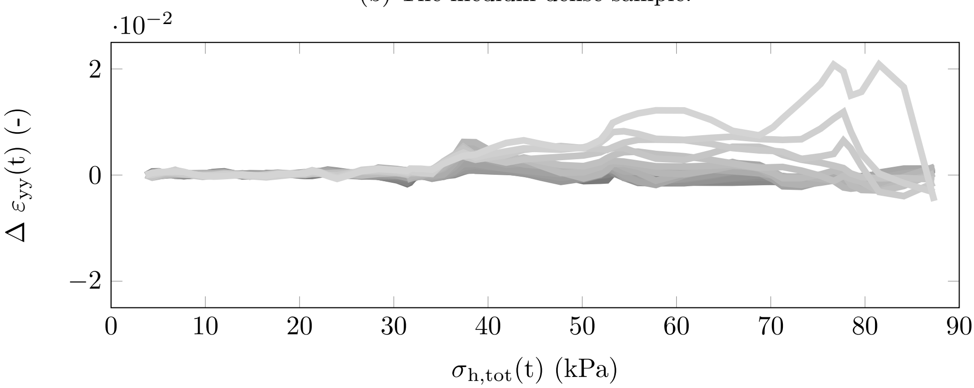

(c) The dense soil sample.

Figure T.2: The ϵ_{yy} strain component.

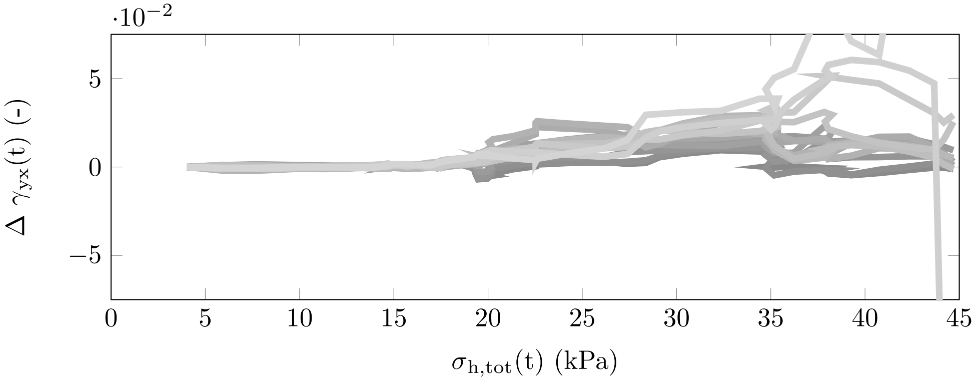

(a) The loose soil sample.

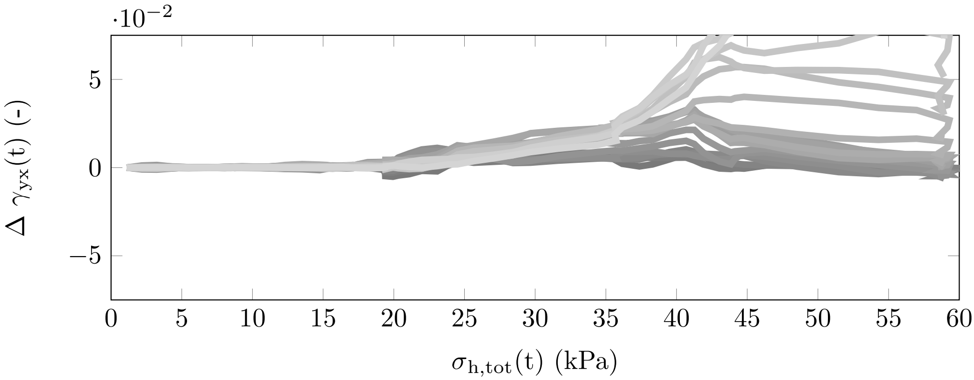

(b) The medium dense sample.

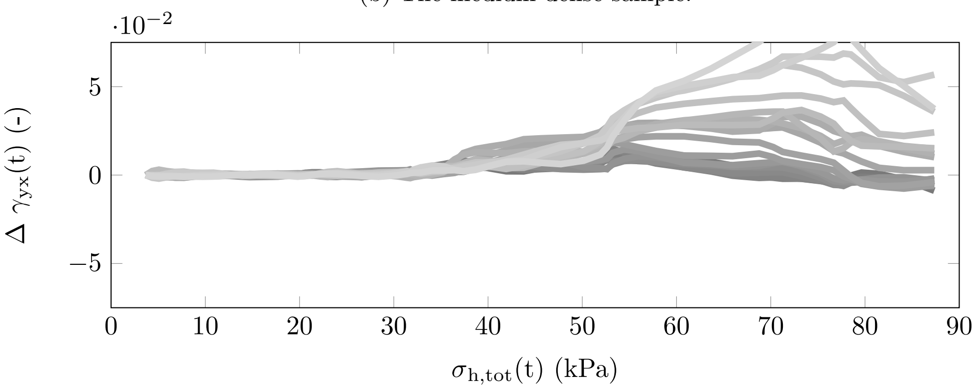

(c) The dense soil sample.

Figure T.3: The γ_{yx} strain component.

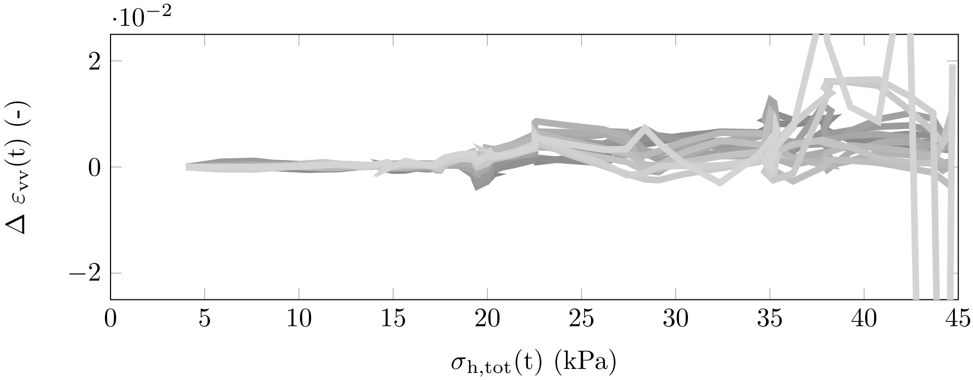

(a) The loose soil sample.

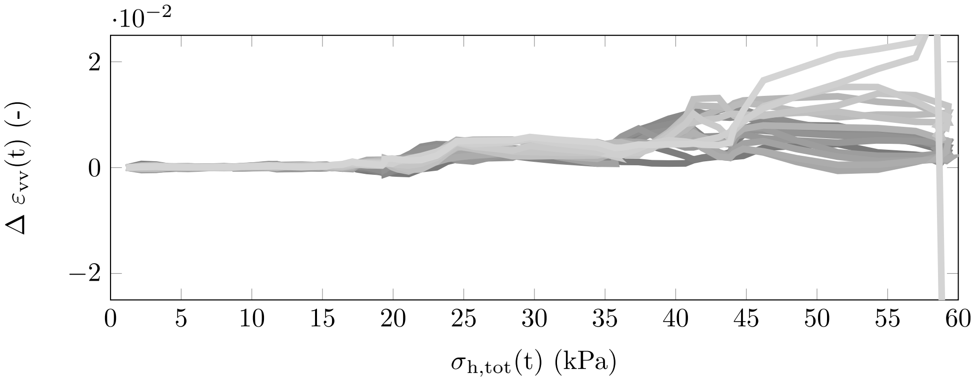

(b) The medium dense sample.

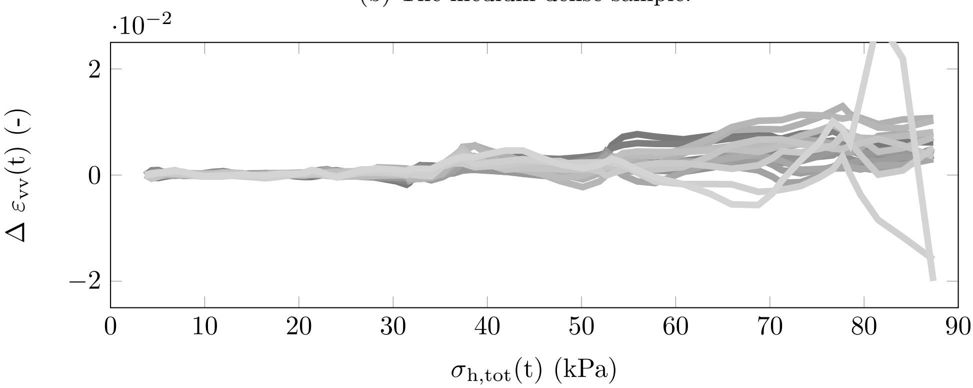

(c) The dense soil sample.

Figure T.4: The ε_{vv} strain component.

Acknowledgments

I am very grateful for the very kind support from my promotor Frits van Tol, who has been very helpful during the whole research project.

I am also very grateful for having the opportunity to have had Jelke Dijkstra as a co-promotor. I have probably learned more from him than almost any other person in my life.

The research would not have been possible without the enormously kind help from Kees van Beek and Han de Visser. I am really grateful for your time and patience, and it has always been a pleasure to learn from you!

I would also like to thank all the other laboratory technicians and other people who have helped me with the research. This includes Ron, Arno, Martin and Paul, and Taco Dijkstra, who helped us with the software design. I am very grateful for the support of STW. I have also appreciated the assistance and moral support from my senior colleagues. Among these Wout Broere, Leon van Paassen and Phil Vardon have been very supportive. My colleagues in Delft have made daily life a pleasure. I am very grateful for your help and kindness. I especially want to thank Master Li, Etienne, Alex, Richard, Chi, Boss Yao and Patrick for their help.

During my period at Keller, Peter, Paul, Justin, Julian, Sam, Dan and Harry were very pleasant to talk to, and I learned at lot from them.

I would like to thank Minna Karstunen for the possibility to stay with her group at Chalmers, and also Claes, Johan, Maria, Johan, Mats, Åsa, Göran, Aaro and Peter.

My colleagues at ELU have also been very supportive, so I would like to thank Sebastian, Almut, Pia, Annika, Jocke, Nadia, Ola, Lars, Mehras, Gabbe, Gary, Viveca, Jimmie, Katarina, Johan, Jakobsson, Fredrik, Therese and Costin for their help.

I would also like to thank my family (and the Bernadotte family) for their help and thoughtfulness, especially Evelina who was kind enough to help me, both with the text and with the layout of the thesis.

Finally, I also want to thank Håkan Stille, Anders Ansell and Jonas Holmgren for their inspiring lectures, and Olof and Christer P. i Himlen.

Curriculum vitae

Anders Beijer-Lundberg
Born in 1984 in H a

Stockholms kommunala gymnasium
Civil Engineering KTH 2005-2010

Teacher in skolhjlp 2007-2008